UNIVERSIDAD COMPLUTENSE DE MADRID

FACULTAD DE CIENCIAS FÍSICAS
DEPARTAMENTO DE ASTROFÍSICA Y CIENCIAS DE LA ATMÓSFERA

El origen de las galaxias enanas de primeros tipos

The Origin of Dwarf Early-Type Galaxies

Dirigida por:

Dr. Alessandro Boselli
Director de Investigación del CNRS
Laboratoire d'Astrophysique de Marseille

Dr. Javier Gorgas
Profesor Titular
Universidad Complutense de Madrid

Memoria presentada por
Dña. Elisa Toloba Jurado
para aspirar al grado de
Doctor en Ciencias Físicas
Madrid, Febrero 2011

Pauca sed matura.

Johan Carl Friedrich Gauss.

Research Lab: the physics is theoretical, but the fun is real.

Sheldon Cooper, PhD.

We must be playing it wrong...

Leonard Hofstadter, PhD.

A mi familia.

Contents

Agradecimientos

Esta tesis es el más claro ejemplo de ser el resultado de las circunstancias. Comenzó en el año 2005 cuando Javier Gorgas me ofreció la increíble oportunidad de formar parte de la colaboración europea MAGPOP, poniendo a mi disposición los datos que observaríamos en diferentes campañas ya concedidas en el INT y el WHT en La Palma. La primera campaña de observación coincidió con Nochebuena, para empezar a saborear lo que significa ser astrónomo: el cielo no entiende de vacaciones o festivos. Al poco tiempo de regresar de estas observaciones el Decanato de la Facultad de CC. Físicas ofreció a Javier un puesto como vicedecano de ordenación académica, todo un reto para generar los nuevos planes de estudio de Grado que ya están funcionando en nuestra facultad. Como no podía ser de otra manera, ya que Javier no conoce otro trabajo que no sea el bien hecho, tuvo que dedicarle más del 100 % de su tiempo, llevándole fines de semana, festivos, vacaciones. Afortunadamente Javier Cenarro acababa de regresar de su estancia en la Universidad de California Santa Cruz y se estaba reincorporando a la vida en el departamento. Esto nos llevó a trabajar codo con codo en la reducción de los datos y así pude aprender de primera mano el paquete REDUCE que tan útil ha sido a lo largo de esta tesis, y que por supuesto lo será en los trabajos futuros. Desafortunadamente la situación laboral de Javier Cenarro se fue complicando y tuvo que marcharse con un puesto postdoctoral Juan de la Cierva al Instituto de Astrofísica de Canarias, que al final ha terminado siendo un gran éxito para su carrera científica pero que todo el departamento, y yo en especial, lamentamos profundamente. En esta etapa, que podemos llamar de transición, a Javier Gorgas se le ocurrió la idea de realizar un estudio, sin precedentes, del nitrógeno en galaxias elípticas. Esta idea me llevó a la Universidad de Lancashire en Preston, Inglaterra, donde pasé un mes analizando los datos con Patricia Sánchez-Blázquez y Brad Gibson, dos anfitriones estupendos que, además de hacerme trabajar duro, hicieron que mi estancia allí fuese inolvidable. Al regresar de esta estancia Alessandro Boselli estaba en nuestro departamento como invitado para las clases del máster. Como parte de MAGPOP, Alessandro se interesó muchísimo por el estatus de los datos de las galaxias enanas y de esta forma retomé estos datos que se habían quedado un poco aparcados durante el estudio del nitrógeno, comenzando así una colaboración que se ha ido estrechando hasta terminar siendo también mi supervisor de tesis. Armando Gil de Paz y Juan Carlos Muñoz Mateos pusieron el punto fotométrico a este trabajo de tesis fundamentalmente espectroscópico, enseñándome a analizar todo tipo de imágenes. El papel que ha jugado Reynier Peletier en todos estos años ha sido absolutamente esencial, ha estado ahí desde el primer momento, como investigador principal de la parte observacional del proyecto MAGPOP, y siempre se ha ofrecido a echar una mano en todo lo necesario. Por todo esto, he tenido la excepcional suerte de que tanta gente importante en el mundo de la astrofísica se haya involucrado en mi trabajo y de haber hecho tantos amigos por el camino.

Como no podía ser de otra manera, mi agradecimiento va dirigido a todas estas personas y, en general, a todo el departamento de Astrofísica y CC. de la Atmósfera, que ha puesto a mi

disposición los medios necesarios para realizar esta tesis. A todos ellos, que de una forma u otra me han ayudado a que este trabajo llegase a buen término, gracias.

Madrid, Febrero de 2011

1

Introducción

1.1 Formación y evolución de galaxias

El estudio de cómo las galaxias se forman y evolucionan nos proporciona información esencial acerca de la creación y evolución del Universo mismo. Estudiando galaxias locales y con alto desplazamiento al rojo nos encontramos en una situación privilegiada para analizar su evolución a través del tiempo, lo que nos permite recomponer las piezas del puzzle para comprender el Universo desde su nacimiento hasta hoy.

Históricamente, dos escenarios se han propuesto para explicar las propiedades de las galaxias observadas en el Universo local: *el colapso monolítico* (Eggen et al. 1962; Arimoto & Yoshii 1987; Bressan et al. 1994) y *el modelo jerárquico de fusiones de galaxias* (Toomre 1977; White & Rees 1978; White & Frenk 1991).

En el colapso monolítico, los sistemas esferoidales se forman en una época muy temprana del Universo como resultado del colapso de gas primordial seguido de un estallido de formación estelar. Desde ese momento evolucionan de forma pasiva hasta la época actual. La formación estelar sucede en todas partes y el gas enriquecido en metales, que se eyecta al medio interestelar en los últimos estadios de la evolución de las estrellas, cae hacia el centro de la galaxia. La mayor parte del gas se transforma en estrellas por el colapso gravitacional y el resto es expulsado por supernovas, explicando así la poca cantidad de gas que se encuentra en las galaxias de tipo temprano (Es).

Por otro lado, en el escenario jerárquico, las estructuras más pequeñas como las galaxias enanas, son los primeros sistemas que se forman, después colapsan para construir estructuras más grandes como son las galaxias masivas o los cúmulos. Las fusiones que dan lugar a la formación de galaxias masivas pueden ser, dependiendo de si las galaxias progenitoras son ricas en gas o no, de dos tipos: *fusiones húmedas y secas* (Faber et al. 2007). En el primer tipo, la colisión entre galaxias ricas en gas provoca nuevos eventos de formación estelar que dan lugar a una galaxia con una población estelar distinta de la de sus progenitores. Tras la fusión, si la formación estelar está activa, consume la mayor parte del gas y el restante es expulsado de la galaxia a través de vientos galácticos. Las fusiones secas consisten en la fusión de galaxias pobres en gas, como consecuencia las poblaciones estelares sólo se mezclan sin dar lugar a nuevas estrellas. Estos dos tipos de fusiones consiguen reproducir las propiedades observadas en galaxias locales. Debido a que las fusiones son más probables a alto desplazamiento al rojo, la mayoría de las fusiones tuvieron su último evento de formación estelar hace ya mucho tiempo, lo que explica el color rojo de las galaxias elípticas en comparación con los sistemas de tipo tardío. Dado que las fusiones se

producen preferentemente en regiones de alta densidad y éstas colapsan antes, el modelo jerárquico también predice una dependencia de las poblaciones estelares con la masa y el entorno, de forma que se espera que las galaxias más masivas sean las más metálicas y las que se encuentran en regiones densas presenten poblaciones estelares más viejas.

El acuerdo entre el modelo jerárquico y el modelo cosmológico de materia oscura fría (ΛCDM) ha propiciado que este escenario sea el mecanismo de formación de galaxias más aceptado. Además es capaz de reproducir tanto la distribución a gran escala de las galaxias como la distribución general de las estructuras observadas en el fondo cósmico de microondas.

El modelo cosmológico de materia oscura fría y energía oscura (ΛCDM) se basa en que la materia bariónica que observamos, que son las partículas que forman el gas, las estrellas, el polvo, etc., sólo representa el $5\,\%$ de la masa total del Universo, lo que significa que el $95\,\%$ de la materia no es luminosa. Esta gran cantidad de materia desconocida se divide en materia oscura fría (CDM) y energía oscura (Λ). La CDM representa el $25\,\%$ de la masa total del Universo y consiste en partículas no bariónicas que sólo interaccionan a través de la gravedad. Estas partículas son necesarias para explicar las curvas de rotación de las galaxias espirales y el movimiento relativo de las galaxias dentro de los cúmulos. El $70\,\%$ restante, la energía oscura, es necesaria para explicar la expansión del Universo. En este modelo cosmológico ΛCDM, las simulaciones numéricas predicen la formación y evolución del Universo a través de la fusión de halos de materia oscura que actúan como anclas de la materia luminosa. Esta materia luminosa colapsa más tarde como consecuencia de las inestabilidades gravitacionales que genera la materia oscura.

El análisis detallado de las propiedades de las galaxias en el Universo local han aportado nuevas evidencias de cómo las galaxias se forman y evolucionan:

- En vez de tratarse de los objetos más viejos del Universo, como en principio sugiere el modelo jerárquico, las galaxias enanas quiescentes presentan poblaciones estelares que en ocasiones son más jóvenes que las de las elípticas gigantes (ver por ejemplo Mateo 1998; Grebel et al. 2003; Michielsen et al. 2008; Koleva et al. 2009a). Esto sugiere que el proceso evolutivo de las galaxias sufre un efecto de *downsizing*. Este efecto implica que la masa de las galaxias es el parámetro que determina la evolución galáctica, siendo las galaxias de baja masa las que presentan historias de formación estelar más extendida en el tiempo que las galaxias masivas (Cowie et al. 1996; Gavazzi et al. 1996; Boselli et al. 2001; Caldwell et al. 2003; Nelan et al. 2005; Bundy et al. 2006). A pesar de que esta evidencia no está en contra del modelo jerárquico, ha propiciado que el colapso monolítico vuelva a considerarse.

- Se ha obsevado una segregación morfológica en la distribución de las galaxias: las galaxias enanas de tipo temprano dominan la población de galaxias en cúmulos y las galaxias de tipo tardío dominan en el campo (ver por ejemplo Dressler 1980; Binggeli et al. 1988; Ferguson & Binggeli 1994). Esta segregación sugiere que el entorno tiene una gran influencia en la formación y/o evolución de las galaxias.

- Las simulaciones que se enmarcan en el escenario de fusión jerárquica predicen una función de luminosidad (número de galaxias por intervalo de magnitud) mucho más pronunciada que la observada, por lo tanto el número de galaxias enanas observadas es mucho menor que el esperado por estos modelos. Este hecho se conoce como *the missing satellite problem* (Kauffmann et al. 1993; Mateo 1998; Moore et al. 1999; Simon & Geha 2007).

- Los modelos semi-analíticos de De Lucia et al. (2006), los cuales se basan en el escenario de fusión jerárquica, encuentran que, mientras que las galaxias masivas de primeros tipos se pueden formar a través de un número finito de fusiones, las galaxias elípticas enanas tienen una probabilidad nula de ser el resultado de un evento de fusión.

1.1.1 Galaxias enanas

Para poder comprobar los diferentes mecanismos de formación y evolución de galaxias, las galaxias enanas se han convertido en un objetivo importante, ya que, además de ser la población dominante del Universo (Ferguson & Binggeli 1994), su baja masa y su pozo de potencial poco profundo nos ayudan a entender el papel de la masa y el entorno en la evolución galáctica. Para comprender la importancia de la masa en los mecanismos físicos que generan a las galaxias, lograr el régimen de baja luminosidad que alcanzan las galaxias enanas y comparar sus propiedades con las de las galaxias más masivas, nos da una visión única de este efecto. Su pozo de potencial poco profundo las convierte en sistemas fácilmente perturbables por el entorno, por lo tanto, si la densidad del medio en el que se encuentran juega algún papel en su formación y evolución, entonces, las galaxias enanas serán los objetos más afectados. Además, exploraciones de galaxias enanas enfocadas específicamente en la búsqueda de sistemas estelares con luminosidades en los límites de detección, son esenciales para resolver el *missing satellite problem*.

Trabajos anteriores basados en el estudio de estos sistemas enanos han encontrado importantes similitudes en las propiedades estructurales de las galaxias enanas con formación estelar y quiescentes en el Universo cercano. Por ejemplo, ambas poblaciones de objetos tienen perfiles de luminosidad exponenciales (Lin & Faber 1983; Binggeli et al. 1984; Ferrarese et al. 2006). Este hecho sugiere que las elípticas enanas son el resultado de la pérdida del gas y posterior truncamiento de la formación estelar en galaxias de baja luminosidad ricas en gas. Varios escenarios se han propuesto para explicar esta transformación a partir de galaxias enanas de los últimos tipos.

El escenario más simple consiste en considerar que la extinción del gas, y por lo tanto el enrojeciemiento de las galaxias, sucede a través de procesos internos. Las explosiones de supernova que se producen en una galaxia como consecuencia de la evolución estelar es el mecanismo más fácil para barrer el gas interestelar (ver por ejemplo Yoshii & Arimoto 1987). Otro procedimiento posible es a través de los siguientes episodios de formación estelar que agotan el gas de la galaxia (Davies & Phillipps 1988). Estos mecanismos son independientes del entorno en el que se encuentran las galaxias.

El entorno donde habitan las galaxias puede alterar también la apariencia de las mismas (un resumen de los efectos del entorno sobre la evolución de las galaxias puede verse en Boselli & Gavazzi 2006). *Starvation* es un fenómeno típico del entorno: en una región densa la caída del material necesario para alimentar la formación de estrellas se detiene, de forma que una vez que el gas frío se consume, la galaxia se hace más ténue (Larson et al. 1980). Existen dos mecanismos puramente ambientales que están en álgida discusión: *galaxy harassment*, o acoso entre galaxias, y *ram-pressure stripping*, pérdida de gas como consecuencia de la presión de choque generada al entrar la galaxia en un medio intergaláctico denso. En el primer escenario las galaxias enanas se ven afectadas por múltiples interacciones con galaxias vecinas y como consecuencia sufren una transformación completa convirtiéndose en enanas de tipo temprano (Moore et al. 1998). Este proceso requiere que las galaxias estén ubicadas en regiones donde el número de vecinos sea muy elevado, como sucede en el centro de los cúmulos (Mastropietro et al. 2005). Simulaciones

recientes han demostrado que las galaxias enanas con formación estelar que están entrando ahora en los cúmulos prácticamente no van a sufrir ningún *harassment*. Los únicos casos que podrán dar lugar a una elíptica enana son aquellos que adquieran una órbita con un apocentro pequeño ($<$ 250 kpc). Sin embargo, estas órbitas son muy improbables para galaxias que estén cayendo ahora debido al profundo pozo de potencial del cúmulo (Smith et al. 2010). Por otro lado, en el escenario de *ram-pressure stripping*, el gas de las galaxias enanas que entran en el cúmulo es extirpado parando de forma abrupta la formación estelar en unas escalas de tiempo muy cortas ($\leq$ 150 millones de años), pero este proceso no afecta al momento angular de la galaxia (Boselli et al. 2008a).

En resumen, el estudio de las galaxias de primeros tipos es importante para entender la formación y evolución de las galaxias en general. Al ser la población dominante en cúmulos, nos ofrecen una visión privilegiada sobre los efectos del entorno, y cómo el estar rodeado de muchas otras galaxias afecta a su evolución. Además, el estudio de sus poblaciones estelares aporta una información crucial acerca de cuándo se formaron y cómo han evolucionado.

1.2 Objetivos del trabajo

Este trabajo pretende proporcionar nuevos conocimientos sobre las galaxias enanas y gigantes de primeros tipos situadas en diferentes entornos. Estas dos poblaciones de galaxias han sido elegidas por las siguientes razones:

- El estudio de galaxias elípticas masivas es un método excelente para analizar los modelos monolítico y jerárquico de formación de galaxias, ya que, mientras que la fusión jerárquica de sistemas predice que las regiones de mayor densidad son las que colapsan primero y se fusionan más rápidamente (Thomas et al. 2005; Renzini 2006), el colapso monolítico no depende de la densidad del medio. Por lo tanto, el estudio de las poblaciones estelares de galaxias masivas situadas en diferentes entornos nos da información acerca de la escala de tiempo de su formación y de su dependencia con la densidad de la zona donde habitan. Un procedimiento eficaz, y casi inexplorado, para analizar estas escalas de tiempo es el estudio de las abundancias químicas presentes en las galaxias, ya que los diferentes elementos se producen en escalas de tiempo distintas actuando así como relojes cosmológicos.

- Las galaxias enanas son los candidatos perfectos para estudiar los efectos del entorno sobre la evolución galáctica debido a que su pozo de potencial es poco profundo, lo que las convierte en objetos fácilmente perturbables por cualquier tipo de interacción.

- La comparación entre elípticas masivas y enanas es esencial para comprobar del escenario de fusiones jerárquicas. Si las galaxias enanas fueron los constituyentes originales de las galaxias más masivas entonces uno esperaría que ambas poblaciones tuviesen propiedades similares, siendo entonces las galaxias enanas la contrapartida a baja luminosidad de las gigantes.

Para abordar estos estudios hemos dividido la tesis en los siguientes apartados:

En el Capítulo 3 se describen las propiedades básicas de las galaxias de primeros tipos y hacemos una introducción a los diferentes métodos utilizados para su estudio. Explicamos la información fotométrica y espectroscópica que se puede obtener de la observación de galaxias elípticas, presentando sus problemas y soluciones, así como las ventajas de realizar estudios espectrofotométricos para obtener una visión más completa de las propiedades de estas galaxias. Este Capítulo describe los conocimientos necesarios para analizar galaxias masivas y enanas con los métodos empleados en los Capítulos 5 y 6. En el Capítulo 4 se presentan las herramientas utilizadas en los estudios de espectros de objetos de los primeros tipos caracterizados por líneas de absorción. Este Capítulo está dedicado a la presentación de la biblioteca estelar MILES. El objetivo de este Capítulo es resumir el papel que las bibliotecas estelares jugan en cualquier estudio espectroscópico, haciendo especial hincapié en los puntos fuertes y débiles de las bibliotecas estelares empíricas actualmente disponibles. Aunque no fuí parte del equipo de MILES en el momento en que se definió el proyecto, tuve la oportunidad de participar en él a través de mi colaboración en el segundo artículo de MILES (Cenarro et al. 2007). Este Capítulo 4 termina con una descripción de mi contribución a la biblioteca estelar MILES y la importancia que ha tenido, como herramienta, en el desarrollo de esta tesis.

Los Capítulos 5 y 6 presentan el análisis de una muestra de galaxias elípticas masivas y enanas. Los resultados científicos que se encuentran en estos Capítulos han sido publicados en diferentes artículos en revistas con árbitro.

El Capítulo 5 presenta una nueva técnica para analizar la abundancias de carbono y nitrógeno en los sistemas de líneas de absorción. Hemos utilizado por primera vez un índice espectroscópico que mide únicamente abundancias de N y nos ha ayudado a desentrañar las contribuciones de C y N en galaxias masivas de tipo temprano localizadas en diferentes entornos (en los cúmulos de Coma y Virgo, y en el campo). Este método lo hemos utilizado para estudiar el modelo jerárquico de formación de galaxias, para ello hemos buscado diferencias en las historias de formación estelar de galaxias ubicadas en regiones de densidad distinta. Las observaciones, la reducción y el análisis de estos datos los he realizado yo misma con la ayuda de los coautores del artículo Toloba et al. (2009b). El Capítulo 4 también incluye un resumen de los resultados presentados en Serven et al. (2010), donde soy coautora. Este estudio posterior fue motivado por los resultados encontrados en Toloba et al. (2009b), y pretende ahondar en las conclusiones obtenidas a través de la comparación de los datos con una serie de modelos desarrollados específicamente para ese fín.

El Capítulo 6 presenta el estudio espectrofotométrico de una muestra de galaxias enanas de primeros tipos (dEs) localizadas principalmente en el cúmulo de Virgo. En este Capítulo pretendemos comprobar si las galaxias elípticas enanas son la contrapartida a baja luminosidad de la más masivas, esto implica que las dEs se formaron y evolucionaron siguiendo la fusión jerárquica, o si, por el contrario, se trata de objetos que han tenido su propio camino evolutivo y la única característica en común con las galaxias gigantes es que a simple vista presentan un aspecto muy similar. Para comprobar la hipótesis de fusión jerárquica en este contexto, hemos realizado un estudio muy detallado de las características fotométricas y espectroscópicas de dEs en Virgo. En primer lugar, hemos hecho un análisis de su contenido estelar basado en observaciones espectroscópicas a baja resolución. Los resultados de este primer estudio fueron publicados en Michielsen et al. (2008), donde soy coautora. Todo el análisis posterior se ha realizado usando espectroscopía de resolución intermedia que he observado, analizado y reducido, esta información la hemos combinado con una serie de parámetros fotométricos en diferentes bandas que yo he calculado. El estudio cinemático de la muestra de dEs ha incluido el desarrollo de simulaciones de Monte-Carlo para comprobar la

calidad de las medidas. Tanto los perfiles de rotación como de dispersión de velocidades han sido publicados en (Toloba et al. 2011). Al final de este artículo y en (Toloba et al. 2009a) profundizamos en las características cinemáticas de galaxias enanas de primeros tipos combinándolas con parámetros fotométricos y compararándolas con elípticas masivas y galaxias espirales. Por último, en este Capítulo se incluye el estudio que estamos desarrollando sobre las relaciones de escala de las galaxias enanas en comparación con elípticas masivas.

Los dos últimos Capítulos, el 8 y el 9, presentan las conclusiones obtenidas de los estudios realizados en los Capítulos 5 y 6 y el trabajo futuro que se plantea. Debido a la naturaleza de esta tesis, donde se han estudiado de forma independiente dos muestras de galaxias masivas y enanas de primeros tipos, las conclusiones se dividen en dos partes, cada una dedicada específicamente a la descripción de los principales resultados y conclusiones obtenidas para cada muestra. Después hemos incluido unas conclusiones finales integrando los estudios anteriores anteriores en el contexto general del estudio de la formación y evolución de galaxias, que es el objetivo principal de esta tesis.

El trabajo futuro descrito en el Capítulo 9 discute los proyectos a corto y largo plazo que estoy actualmente desarrollando, que tengo previsto realizar en un futuro cercano y que se proponen como un reto para el futuro de los grandes telescopios.

2

Introduction

2.1 Formation and evolution of galaxies

The study of how galaxies form and evolve provides us essential information about the creation and evolution of the Universe itself. Studying high-redshift and local galaxies we have a privileged look at the Universe as a function of time that enables us to assemble the pieces of the puzzle that lead to the understanding of the Universe from its birth to today.

Historically, two main scenarios have been proposed to explain the properties of the galaxies observed in the local Universe: the so-called *monolithic collapse model* (Eggen et al. 1962; Arimoto & Yoshii 1987; Bressan et al. 1994) and the *hierarchical merging model* (Toomre 1977; White & Rees 1978; White & Frenk 1991).

In the monolithic collapse scenario, spheroids form at a very early epoch as a result of a primordial cloud collapse followed by a starburst, and then passively evolve to the present epoch. The star formation processes occur everywhere in the galaxy and the metal-enriched gas, expelled in the last stages of the stellar evolution, falls towards the center of the galaxy. Most of the gas is transformed into stars by the gravitational collapse and the rest is expelled by supernovae, explaining the low gas content found in early-type galaxies (Es).

On the other hand, in the hierarchical scenario, small structures, like dwarf galaxies, are the first systems formed, and later they collapse to build larger structures like massive galaxies or clusters. The mergers that lead to the formation of massive galaxies can be, depending on whether the galaxies are gas-rich or not, of two types: *wet and dry mergers* (Faber et al. 2007). In the former type, the collision between gas-rich galaxies triggers new events of star formation generating a galaxy with a stellar population content distinct from its progenitors. After the merger, if any star formation is ongoing, it consumes the gas while the remaining is expelled from the galaxy via galactic winds. The latter type of mergers consists of the fusion of gas-poor galaxies and the stellar populations are just mixed, without new stars being formed. These two types of mergers are able to reproduce the observed appearance of the local galaxies. Due to the fact that mergers were more probable at high redshift, most merger remnants have had their last star formation event long ago, which explains the redder colours of the elliptical galaxies in comparison with late-type systems. Since mergers occur preferentially in high density regions and these dense environments collapse earlier, the hierarchical scenario also predicts a dependence of the stellar populations on mass and environment, expecting more massive galaxies to be more metallic and galaxies inhabiting dense clusters to present older stellar populations.

Since it agrees with the Lambda-Cold Dark Matter (ΛCDM) cosmological paradigm, this

hierarchical scenario became the most accepted formation mechanism. It reproduces both the large scale distribution of galaxies and the general distribution of structures observationally detected in the cosmic microwave background.

This ΛCDM model is based on the fact that the baryonic matter that we observe, the ordinary particles that builds the gas, stars, dust, etc., comprises only the 5% of the total mass of the Universe, which means that 95% of the matter is non-luminous. This enormous fraction of unknown matter is divided in cold dark matter (CDM) and dark energy (Λ). The CDM represents the 25% of the total mass of the Universe and consists on non-baryonic particles, thus they are collisionless, interacting only through gravity. These dark particles are needed to explain the rotation curves of spiral galaxies and the relative motion of the galaxies within clusters. The remaining 70%, the dark energy, is required to explain the accelerating expansion of the Universe although its nature is yet unknown. In this ΛCDM context, numerical simulations predict the formation and evolution of the Universe through the creation and merging of dark matter haloes that are the anchors of the luminous matter which, as a consequence, collapse following the gravitational instabilities generated by the dark matter.

Detailed analyses of the properties of galaxies in the local Universe have provided new evidences of how galaxies form and evolve:

- Instead of being the oldest objects of the Universe as, in principle, suggested by the hierarchical scenario, dwarf quiescent galaxies exhibit stellar populations that sometimes are younger than those of giant ellipticals (e.g., Mateo 1998; Grebel et al. 2003; Michielsen et al. 2008; Koleva et al. 2009a) which suggests a *downsizing* effect in the evolutionary process of galaxies. This downsizing implies that it is the mass of the galaxies the parameter that drives galaxy evolution, being low-mass galaxies those with star formation histories more extended than massive galaxies (Cowie et al. 1996; Gavazzi et al. 1996; Boselli et al. 2001; Caldwell et al. 2003; Nelan et al. 2005; Bundy et al. 2006). Although this evidence is not contrary to the hierarchical scenario, it has led to a reconsideration of the monolithic collapse.

- A morphology segregation has also been observed, being dwarf early-type galaxies the main population of clusters and late-type galaxies those dominating the field (e.g., Dressler 1980; Binggeli et al. 1988; Ferguson & Binggeli 1994). This segregation suggests that the environment highly influences the formation and/or the evolution of galaxies.

- The simulations under the hierarchical merging scenario predict a luminosity function (number of galaxies per magnitude bin) much steeper than observationally found, therefore the number of observed dwarf galaxies is much lower than that expected from the models. This fact is called *the missing satellite problem* (Kauffmann et al. 1993; Mateo 1998; Moore et al. 1999; Simon & Geha 2007).

- In the semi-analytic models of De Lucia et al. (2006), based on the hierarchical merging scenario, it is found that whereas massive early-type galaxies can be formed through a finite number of mergers, dwarf elliptical galaxies have a null probability of being the result of a merging event.

2.1.1 Dwarf galaxies

In order to test the different mechanisms of galaxy formation and evolution, dwarf galaxies are, therefore, an excellent target of study as suggested by the evidences described above since, apart from being the dominant population of the Universe (Ferguson & Binggeli 1994), their low mass and shallow potential well provide the clues to understand the role of the mass and the environment in galaxy evolution. To comprehend the importance of the mass of the galaxies in the physical mechanisms that originate them, achieving the low luminosity regime of dwarf galaxies and comparing their properties with those of more massive galaxies gives us a unique insight of this effect. Their shallow potential well make them fragile systems easily perturbed by the environment, thus if the density of the area where galaxies are located plays any role on their formation and evolution, then, dwarf galaxies are expected to be the most affected objects. Moreover, surveys of dwarf galaxies, specifically seeking for the lowest luminosity dwarfs, are essential to solve the missing satellite problem.

Previous works based on the study of these dwarf systems have found strong similarities in the structural properties of star-forming and quiescent dwarf galaxies in the nearby Universe. For instance, both of them have similar exponential light profiles (Lin & Faber 1983; Binggeli et al. 1984; Ferrarese et al. 2006). This fact suggests that dwarf ellipticals are the result of gas removal and subsequent suppression of star formation in gas-rich low-luminosity galaxies. Several scenarios have been proposed to explain this transformation from late-type to early-type dwarfs.

The simplest scenario consists of just considering the removal of the gas through internal processes and, hence, the fading of the galaxies. The supernova explosions that occur in a galaxy as a consequence of the stellar evolution is the easiest mechanism to sweep away the interestellar gas (e.g., Yoshii & Arimoto 1987). Another plausible procedure is through the subsequent episodes of star formation that exhausts the gaseous content of a galaxy (Davies & Phillipps 1988). These mechanisms are independent from the environment where the galaxies are located.

External perturbations induced by the hostile environment in which galaxies evolve can also alter the appearance of a galaxy (for a review of the effects of the environment on galaxy evolution see Boselli & Gavazzi 2006). *Starvation* is a typical environmental phenomenon: in a dense region the infall of fresh material needed to feed star formation is stopped, thus, once the cold gas reservoir of the galaxy is consumed, the galaxy fades (Larson et al. 1980). There exist two more fully environmental mechanisms that are widely debated nowadays: *galaxy harassment* and *ram-pressure stripping*. In the former scenario dwarf galaxies are perturbed via multiple galaxy-galaxy interactions suffering a complete transformation into an early-type galaxy (Moore et al. 1998). In order to be affected, this process requires that galaxies must be located in regions of high density of neighbours, like in the center of clusters (Mastropietro et al. 2005). More recent simulations have probed that new star-forming dwarfs infalling in a cluster experience from little to no harassment processes. As a consequence, the transformation to dwarf elliptical galaxies does not occur unless the dwarf star-forming galaxy acquires an orbit with a small apocentric distance (< 250 kpc). However, such orbits are highly improbable for newly infalling galaxies due to the deep potential well of the cluster (Smith et al. 2010). On the other hand, in the ram-pressure stripping scenario, the gas of the dwarf galaxies that enter the cluster is blown away quenching their star formation in short time scales (≤ 150 Myr) but conserving the angular momentum of the progenitor galaxy (Boselli et al. 2008a).

To summarise, the study of early-type galaxies is an important approach to disentangle the formation and evolution of galaxies since, as they are the dominating population in clusters, they provide a privileged insight into the effect of the environment, and how being surrounded by many other galaxies affect their evolution. Furthermore, the study of their stellar populations yields crucial information about when they were formed and how they have evolved.

2.2 Aims of this work

This work is devoted to provide new insights into the study of dwarf and giant early-type galaxies in different environments. Those populations have been chosen for the following reasons:

- The study of massive elliptical galaxies is an excellent approach to test the monolithic and hierarchical scenarios. Due to the fact that the hierarchical merging scenario predicts, in contrast to the monolithic collapse, that those regions with the highest density of material collapse earlier and merge more rapidly (Thomas et al. 2005; Renzini 2006). Therefore, the study of the stellar populations of massive galaxies located in different environments gives us information about the time scale of their formation and its dependence on density. An efficient and almost not explored procedure to analyse these time scales is to study the abundances of the chemical species present in the galaxies. In fact, since the different elements are produced in different time scales, they can act as cosmological clocks of the galaxy evolution.
- Being fragile objects due to their shallow potential well, thus easily perturbed by any kind of interactions, dwarf galaxies are ideal candidates to study the effects of the environment on galaxy evolution.
- The comparison between Es and dEs is essential as a final test of the hierarchical merging scenario. If dwarf galaxies were the building blocks of more massive galaxies then one would expect them to have similar properties as giant galaxies, being in this sense their low luminosity counterparts.

To develop these topics, this thesis has been arranged as follows:

In Chapter 3 we describe the basic properties of early-type galaxies and an introduction to the different methods used to study them. I explain separately the photometric and spectroscopic information that can be obtained from the observation of elliptical galaxies, presenting the problems and successes in each case as well as the advantages of performing spectrophotometric studies that combine both regimes to give a deeper insight in the properties of these galaxies. This Chapter establishes the necessary knowledge to develop the study of massive and dwarf early-type galaxies performed in Chapters 5 and 6, whereas in Chapter 4 I present the essential tools to analyse any absorption features that characterise the early-type spectra. This Chapter is devoted to the presentation of the MILES stellar library. The objective of this Chapter is to summarise the role that stellar libraries play in any spectroscopic study, giving special emphasis to the usual strengths and weaknesses of the empirical stellar libraries available in comparison with other methods to accomplish the same analysis, such as theoretical stellar libraries or fitting functions. Although I was not part of the MILES team when it was defined and observed, I had the opportunity to participate in the

project through my collaboration to the second paper of the library (Cenarro et al. 2007). Therefore, this Chapter 4 finishes with a description of my contribution to the MILES stellar library and the importance that it has had, as a tool, in the development of this thesis.

Chapters 5 and 6 contain the scientific analysis of a sample of massive elliptical galaxies and of dwarf early-types. The scientific results found have been published in different papers in refereed journals.

Chapter 5 introduces a new technique to analyse carbon and nitrogen abundances in absorption-line systems. The usage of an index that measures purely N abundances has been used for the first time to disentangle C and N abundances in early-type galaxies located in different environments (Coma and Virgo clusters and in the field), which has also helped us to test the hierarchical merging scenario looking for differences in the star formation histories of galaxies located in areas of different density. The observations, data reduction and analysis of these data was performed by myself guided by the coauthors of the paper that resulted from this study (Toloba et al. 2009b). Also in Chapter 5 I include a summary of the results presented in Serven et al. (2010), where I am coauthor. This posterior study was motivated by the results found in Toloba et al. (2009b) with the aim of further investigating them with the help of models specifically developed for that goal.

Chapter 6 consists of a spectrophotometric study of a sample of dEs mainly inhabiting the Virgo cluster. This Chapter is aimed to test if dwarf elliptical galaxies are the low luminosity extension of more massive early-types, in such a case dEs were formed and evolved in the hierarchical merging cosmology, or, on the contrary, they were objects that have had their own evolving path and the only common characteristic with the bigger early-type galaxies was their similar appearance. To test the hierarchical merging scenario in this context we have performed a very detailed study of the photometric and spectroscopic characteristics of dEs in Virgo. Firstly, we made an analysis of their stellar content based on low-resolution observations. The results were published in Michielsen et al. (2008), where I am coauthor. From this point, all the analysis was done using medium-resolution spectroscopic data that I observed, reduced and analysed and photometric data in different bands where I measured all the necessary parameters involved in the study presented here. Secondly, we made a kinematic study that we improved developing Monte-Carlo simulations in order to test the quality of the data in our hands and to establish their limitations. The kinematic profiles of the sample of galaxies and these simulations were published in (Toloba et al. 2011). At the end of this paper and in (Toloba et al. 2009a) we dig into the kinematic characteristics of dwarf early-type galaxies combining them with some photometric parameters and comparing the observed results with massive ellipticals and spiral galaxies. Finally, in this Chapter I include the study that we are about to finish about the scaling relations of dwarf early-type galaxies in comparison with massive ellipticals.

The last two Chapters, numbered 8 and 9, present the conclusions obtained from the studies of Chapters 5 and 6 and the future perspectives of this work. Due to the nature of this thesis, where we have studied independently two samples of massive and dwarf early-type galaxies, the conclusions are divided in two parts, each one specifically devoted to the description of the main results and conclusions obtained for each sample. To this separate summaries, we have included a final remarks where we integrate all the previous conclusions in the general context of the study of the formation and evolution of galaxies, which is the main goal of this thesis.

The future work described in Chapter 9 discuss the immediate and long-term projects that I am currently developing, that I have planned to accomplish in a nearby future and that I propose

to perform as a challenge for the next era of large telescopes.

3

Early-type galaxies

Este Capítulo pretende ser una introducción general al estudio de las galaxias de primeros tipos. Después de una breve discusión sobre el descubrimiento de estos objetos y sus propiedades básicas, he detallado los diferentes métodos de estudio aplicados históricamente al análisis de galaxias elípticas, desde los estudios fotométricos a los espectroscópicos.

He diferenciado entre dos grupos de técnicas de estudio. Un primer grupo cuyo objetivo es analizar el contenido estelar de las galaxias, es decir, sus edades, metalicidades, si la mayor parte de las estrellas son jóvenes, viejas, etc., y un segundo grupo enfocado al análisis de los parámetros estructurales de las galaxias, es decir, aquellos que se basan principalmente en la forma matemática que describe el perfil de brillo superficial de las galaxias, como son el radio efectivo, la magnitud absoluta, brillo superficial efectivo.

Para cada método presentado en este Capítulo, además de describir en qué consiste y qué información se puede sacar de él, he intentado resumir el estado actual del método en concreto, es decir, cuáles han sido los avances más novedosos en esa dirección.

Debido a que las galaxias enanas de primeros tipos son también objetos caracterizados por espectros de líneas de absorción, los métodos descritos para las galaxias masivas pueden aplicarse igualmente a estos sistemas de bajo brillo superficial. Y lo que es más, de su comparación entre gigantes y enanas es posible extraer información muy valiosa acerca de la formación y evolución de galaxias que pone restricciones importantes a los modelos cosmológicos.

La última Sección de este Capítulo hace un resumen del esfuerzo realizado por diferentes investigadores por analizar las galaxias enanas y deja abiertas muchas preguntas, algunas de ellas son las que se han intentado dar respuesta en este trabajo de tesis.

3.1 Definition

On 1749 the first early-type galaxy was observed by Le Gentil, M32. This galaxy, a companion of Andromeda (M31), is the nearest early-type galaxy and, for that reason, also the brightest elliptical galaxy in the sky. However, it was not until 1926 that Edwin Hubble introduced the concept of elliptical galaxy. The so-called 'Hubble Sequence' is a fork-shaped diagram where different types of galaxies are defined according to their morphological appearance (see Figure 3.1). Two main groups of galaxies were introduced by Hubble, a possible evolution from one to another provoked the definition of *early-types* and *late-types*. The early-type galaxies (*ellipticals* and *lenticulars*) are designated with an E or S0 plus a number (e.g., E0, E3, E7) that describes the flattening of the galaxy, being E0 nearly spherical and E7 remarkably flattened. The late-type galaxies (*spirals* and *irregulars*) are divided in two groups: those with and without bars. Those spiral galaxies without bars are called Sa, Sb and so on. This sequence is in decreasing order of importance of the bulge in relation to the disk of the galaxy. The barred late-type galaxies are categorized as SBa, SBb and so on according to the importance of the bar.

Of the total baryonic mass of the local Universe elliptical galaxies represent the $\sim$22$\%$, a fraction amounting to $\sim$75$\%$ when all spheroids are considered (i.e., including S0 and spiral bulges). On the other hand, disks contribute only $\sim$25$\%$ and dwarfs are an irrelevant fraction in mass (Fukugita et al. 1998). However, when the number of galaxies is considered instead of the mass, dwarfs are by far the dominant objects (Ferguson & Binggeli 1994, see Figure 3.2). The range in masses covered by the family of elliptical galaxies goes from dwarfs ($M \simeq 10^6 M_\odot$) to cD galaxies ($M \simeq 10^{13} M_\odot$) and they are characterised by an ellipsoidal shape, red colours in comparison to late-type galaxies (Tinsley 1978; Aaronson 1978), almost purely stellar absorption-line spectra and a low content of dust and gas. These spheroids are, in addition, preferentially found in clusters (Dressler 1980; Sandage et al. 1985; Ferguson & Binggeli 1994; Blanton et al. 2005; Croton et al. 2005) and the massive ones follow a de Vaucouleurs surface brightness profile, also called $R^{1/4}$ *law* due to the typical radial behaviour.

All these characteristics have favored the common use of "early-type" to refer to red galaxies or galaxies with absorption spectra rather than only to pure E's or S0's (ellipsoids). However, samples selected using only one criterion (morphology, spectra or colours) do not fully overlap (see Table 3.1). This fact was found by Bernardi et al. (2006), who selected $\sim$123,000 galaxies with $14.5 \leq r_{\rm Pet} \leq 17.75$ ($r_{\rm Pet}$, the Petrosian ratio, is defined as the ratio of the local surface brightness in an annulus of radius r to the mean surface brightness within that same radius, Blanton et al. 2001) and $0.004 < z < 0.08$ from the Sloan Digital Sky Survey (SDSS, York et al. 2000) Data Release 1 (DR1, Abazajian et al. 2003). Adopting in turns morphology, spectra and colour criteria for early-type galaxies, the number of Es fulfilling each criterion is different in each case, as it can be seen in the diagonal numbers of Table 3.1 from Bernardi et al. (2006). Out of the diagonal are the fractions of galaxies that satisfy two criteria. For example, out of the colour selected Es, 58$\%$ satisfy also the morphological selection. This emphasizes the fact that when the term "early-type" is used it must be specified the selection criterion used.

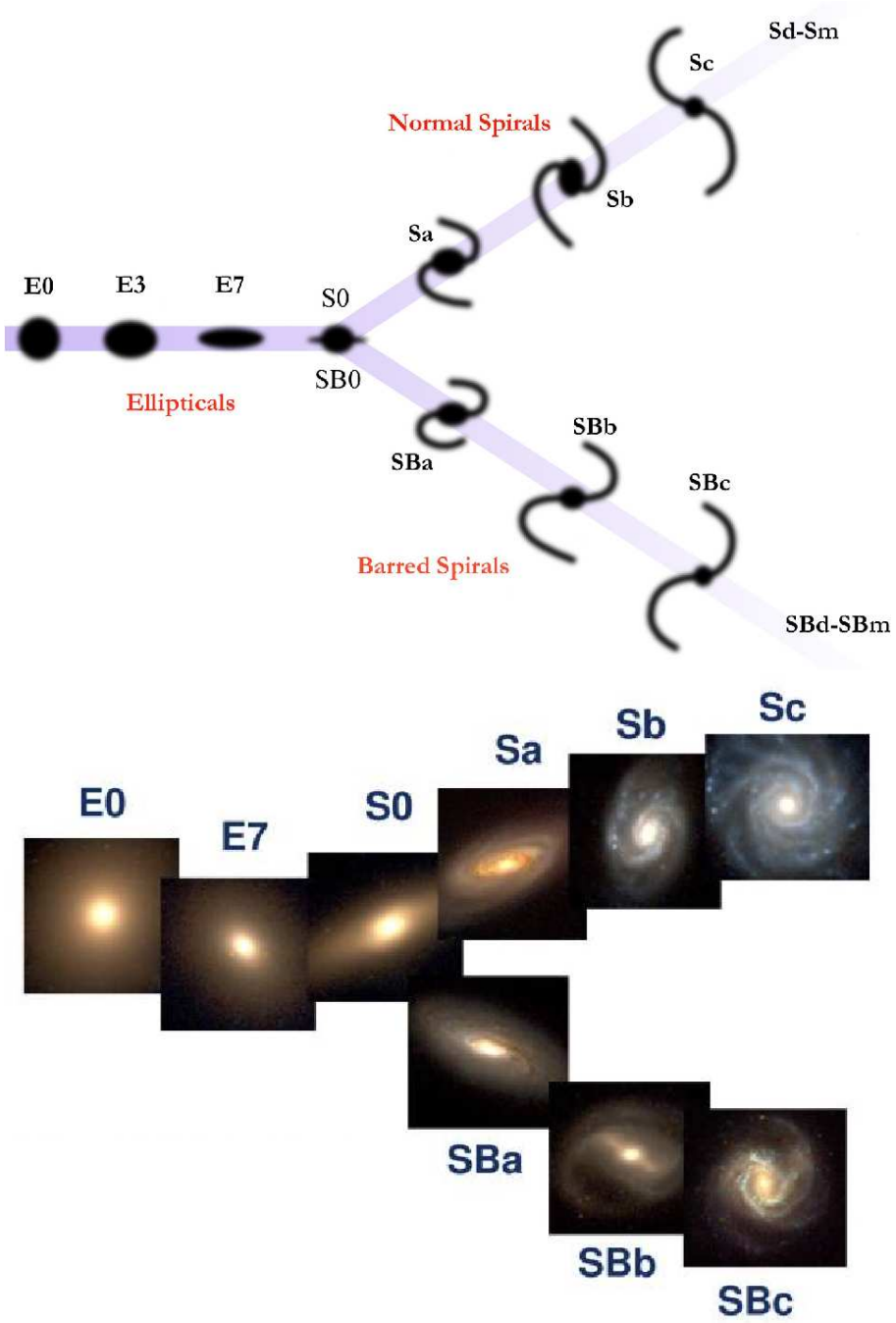

Figure 3.1: Hubble tunning-fork diagram. In the upper diagram it is shown a drawing scheme of the classification of the galaxies. In the lower diagram, some examples of real galaxies are plotted for comparison.

	MOR	COL	SPE
MOR	37151	70%	81%
COL	58%	44618	87%
SPE	55%	70%	55134

Table 3.1: Morphology versus colour versus spectrum-selected samples from Bernardi et al. (2006).

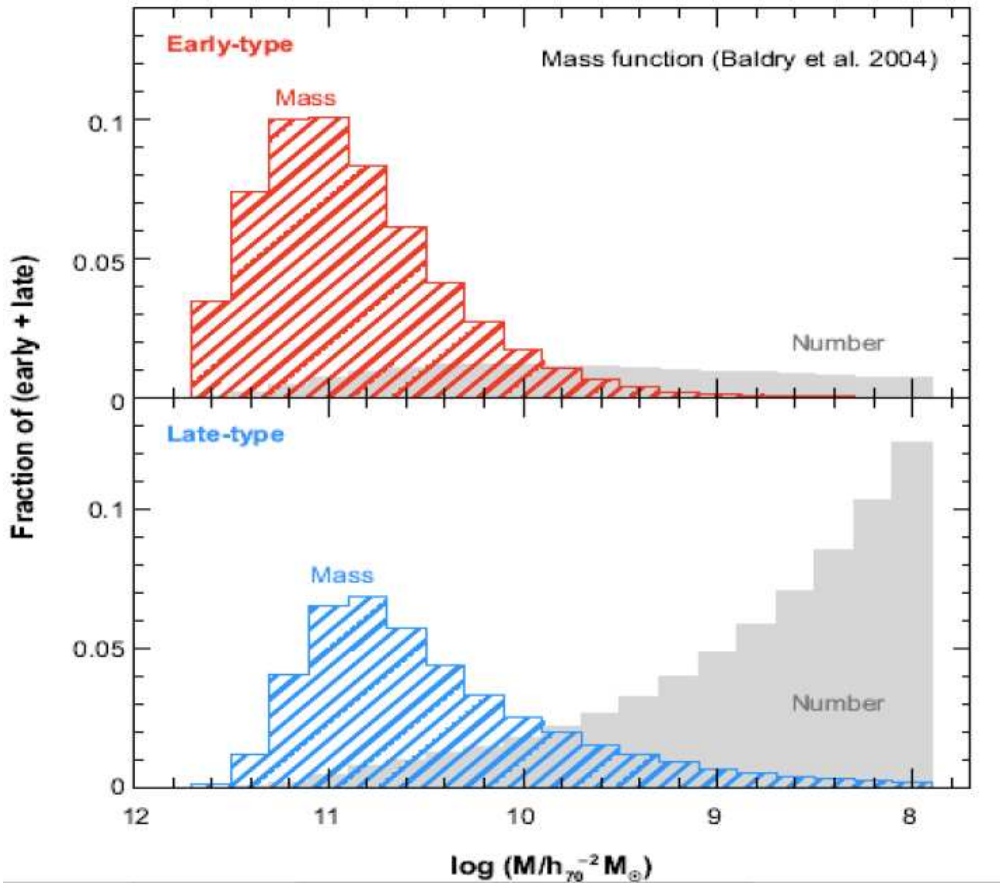

Figure 3.2: Contributions to the total stellar mass (coloured dashed areas) and to the number of galaxies (grey regions) by early-type (upper panel) and late-type (lower panel) galaxies as a function of galaxy mass, from Renzini (2006). The different mass bins are derived from the best-fit mass functions of Baldry et al. (2004).

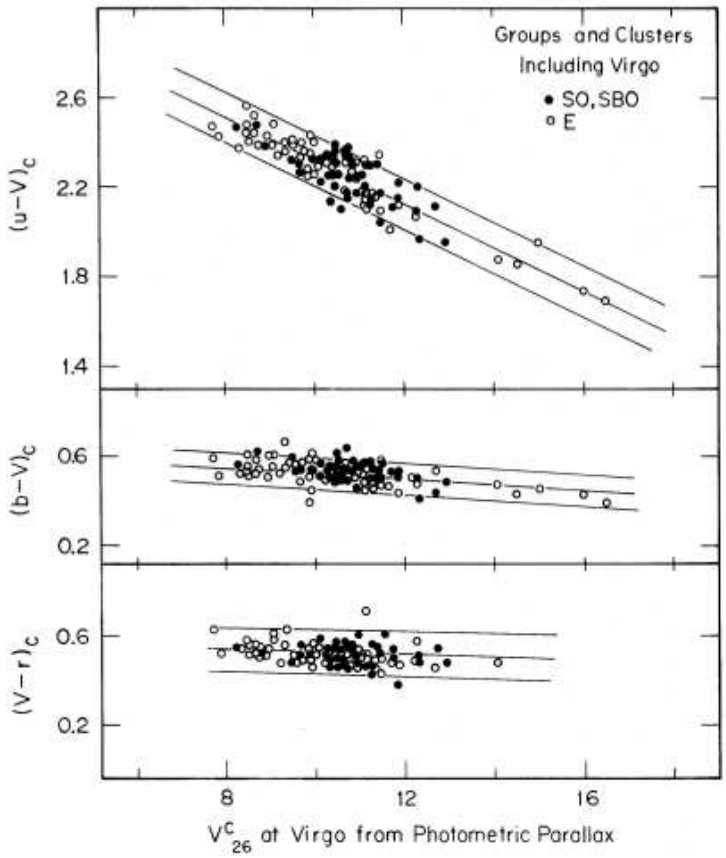

Figure 3.3: Figure from Visvanathan & Sandage (1977). It shows the tightness of the colour-magnitude diagram for all the galaxies in their sample as well as how closely both S0s and Es follow the relation. The ridge line is the best fit solution for Virgo galaxies, and the boundary lines are at $\pm 2\sigma$ in the colour residuals.

3.2 Stellar content

The study of the stellar content of galaxies provides information about their formation and evolution. Analysing the colours or the absorption line features present in their integrated spectra using the techniques described below, gives us the age and metallicity of the dominant stellar population of the galaxy, two key parameters to learn about their evolution through the cosmological time.

3.2.1 The Colour-Magnitude and Colour-Mass Relations

A powerful tool to analyse the stellar populations of galaxies is to study the shape of their Spectral Energy Distribution (SED). Usually it is not possible to obtain the complete SED of a galaxy since it requires to acquire its complete spectrum covering all the wavelength ranges or, at least, its magnitudes in adjacent photometric bands. A way to solve this problem is to use colours, the difference between two different luminosities within specific windows in two different wavelength ranges. These colours are tightly related to the shape of the SED between the two photometric bands analysed, and they are generally used to quantitatively characterise the underlying stellar population of a galaxy. Roughly speaking, if the colour is blue or red the target galaxy is young/metal-poor or old/metal-rich depending on the colours in study.

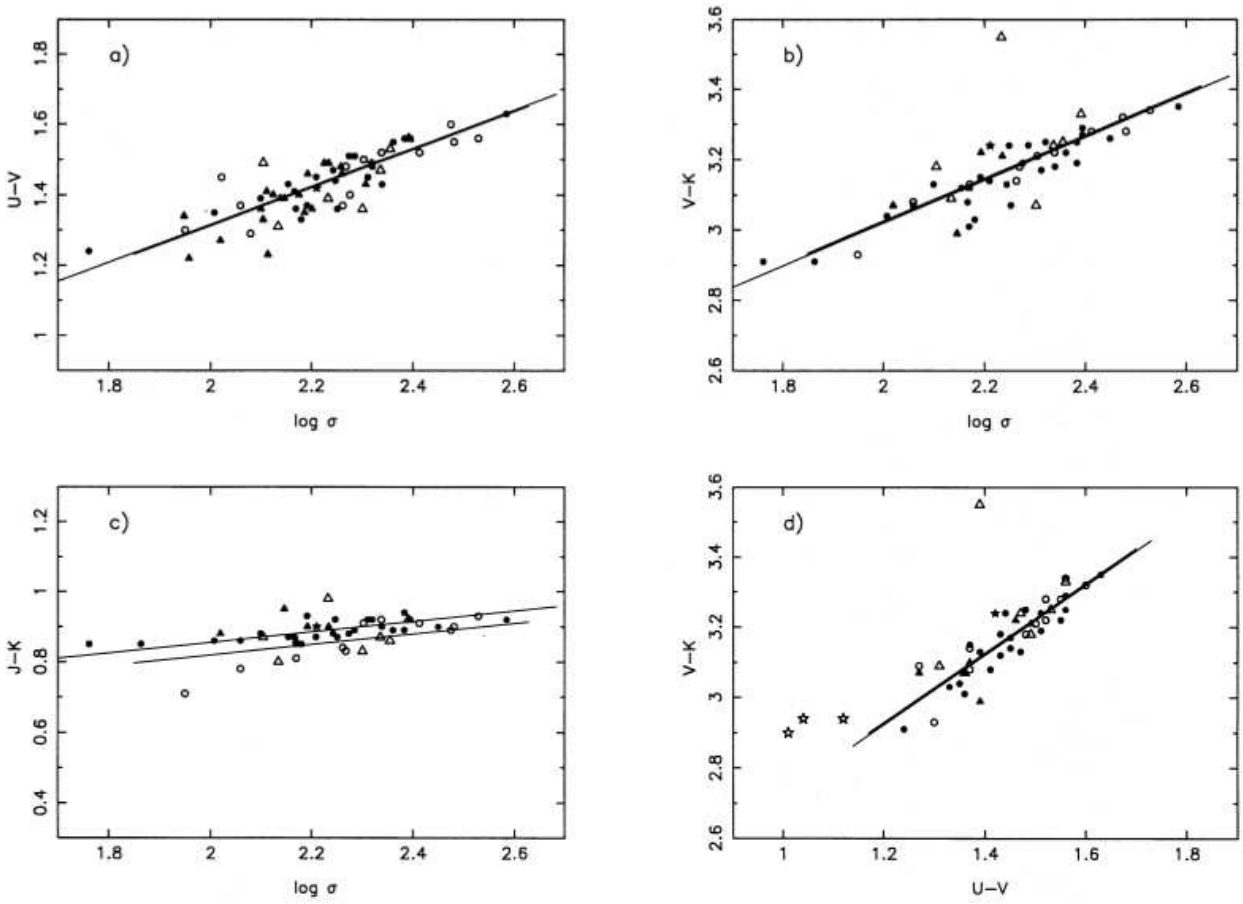

Figure 3.4: Figure from Bower et al. (1992). Panel (a) presents $U - V$ colour versus the velocity dispersion; panel (b) $V - K$ colour versus velocity dispersion; panel (c) $J - K$ colour versus velocity dispersion; panel (d) $V - K$ versus $U - V$, colour-colour diagram. Open symbols denote galaxies in the Virgo cluster; filled symbols, galaxies in the Coma cluster. Circles denote ellipticals; triangles, S0; stars S0a or $S0_3$. Solid lines show median fits to the data.

The colour-magnitude relation (CMR) was first found by Baum (1959) (see Figure 3.3). Faber (1973) used differences between absorption lines instead of broad-band colours and concluded that more luminous elliptical galaxies had stronger absorption lines. Visvanathan & Sandage (1977) and Sandage & Visvanathan (1978a,b) established that the CM diagram is universal, meaning that it looks the same independently of the environment where early-type galaxies are located. This fact indicates that this relation can be used, in principle, as a distance indicator and that the stellar content of the galaxies is roughly uniform. As a consequence, this uniformity in the stellar populations of elliptical galaxies suggests that these objects must have suffered a passive evolution, at least in the last few Gyrs.

Bower et al. (1992) found also a tight relation between colour and σ (the central velocity dispersion of the galaxies, see Figure 3.4). The scatter found in the colours is determined by both the scatter in the ages and in the metallicities, but it is generally interpreted that the scatter in the ages is the dominant driver, at least in $U - V$ in quiescent galaxies (Bower et al. 1992; Gallazzi et al. 2006). As a result, Bower et al. (1992) argued that the colour scatter observed in the colour-σ relation should be equal to the time scatter in the formation epochs of the elliptical galaxies, concluding that ellipticals in clusters formed the bulk of their stars at $z \geq 2$. This approach provided for the first time a robust probe that cluster ellipticals are made of very old stars.

Interpreting colours of galaxies is difficult due to the *age-metallicity degeneracy*. One can mimic the effects of a change in age to integrated galaxy colours by changing the metallicity of the galaxy by a certain amount, making it impossible to distinguish if a blue/red colour is a purely effect of age or metallicity. The problem has been tried to be solved through spectroscopic studies, where specific line-strengths can be studied.

3.2.2 Line-strength indices

The absorption lines that characterise the spectra of early-type objects are the result of the combination of the individual spectra of the stars that populate the system, thus the strength of the lines gives insight into the stellar population of the galaxy.

In order to exploit this idea, Burstein et al. (1984) defined the Lick/IDS system: a compilation of indices defined to measure the strength of an absorption feature by comparing the flux in a specific line and two continuum regions at both sides of it used as reference levels. A total of 21 indices were defined and thoroughly studied by Burstein et al. (1986); Faber et al. (1985); Gorgas et al. (1993); Worthey (1994) and Worthey & Ottaviani (1997). Nowadays they still are the most widely used index system to analyse the stellar populations of galaxies.

From this collection of 21 indices, three of them are widely used to study age and metallicity effects on early-type galaxies: Mg_2 (or Mgb), <Fe> and H_β. These three indices measure respectively the strength of MgH+MgI at $\lambda \simeq 5156 - 5197$ Å, the average of two FeI lines at $\lambda \simeq 5248 - 5315$ Å and the Balmer line H_β located at $\lambda \simeq 4861$ Å. The first two indices are mainly sensitive to metallicity and the last one to age (O'Connell 1980; Gunn et al. 1981; Rabin 1981, 1982).

3.2.2.1 Mgb − <Fe> diagram

The first diagnostic considered was the comparison of the strengths of Mgb and <Fe>. This diagram is an indirect indication of the time scale for the evolution of galaxies because these two

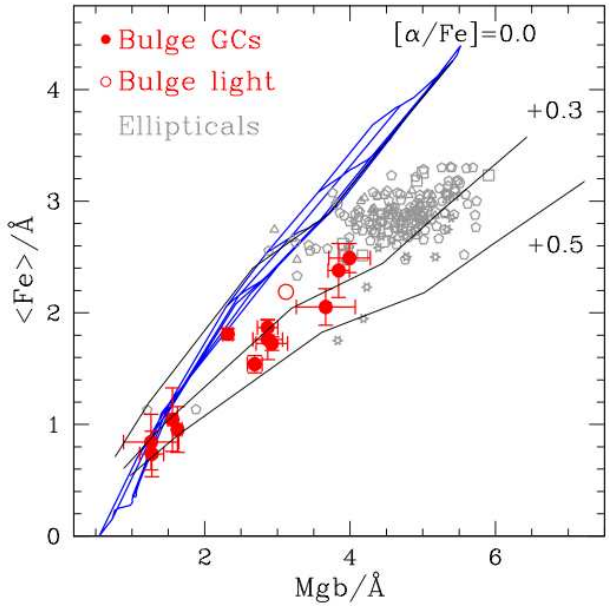

Figure 3.5: <Fe> vs. Mgb diagram from Maraston et al. (2003). The red filled symbols show galactic and bulge globular clusters. The open circle is the average value of 15 bulges. Small open grey symbols show the central values of the indices for ellipticals: field and cluster Es from Beuing et al. (2002, pentagons); Coma Es from Mehlert et al. (2002, stars); Fornax Es from Kuntschner (1998, squares); field and Virgo Es of González (1993, triangles). Standard SSP (simple stellar population) models in blue, metallicities $[\mathrm{Z/H}] = (-2.25, -1.35, -0.55, -0.33, 0.00, +0.35, +0.67)$ from bottom to top, and ages 3, 5, 10, 12 and 15 Gyr from left to right. The black lines show 12 Gyr SSP models with the same total metallicities and various $[\alpha/\mathrm{Fe}] = 0, +0.3, +0.5$ from Thomas et al. (2003).

elements are produced in different evolutionary processes: Type II and Type Ia supernovae (SN) respectively. These two kinds of SN are the last stages of the evolutionary process of stars of different masses and occur on distinct time scales. The Type Ia SN is the result of the evolution of a binary system formed by two typical main sequence stars ($\sim 1-2\ M_{\odot}$) that evolve slowly in time, whereas the Type II SN is the final stage of the evolution of the most massive stars ($M > 8M_{\odot}$) that evolve very quickly. As a consequence the Type II SN, where Mg is predominantly produced, is a much rapid process than Type Ia SN, where Fe is mainly generated.

The measurement of these two indices in elliptical galaxies showed that while the low-luminosity Es had Mg/Fe consistent with the solar neighbourhood, the most luminous galaxies presented an enhancement (Peletier & Valentijn 1989; Gorgas et al. 1990; Faber et al. 1992; Davies et al. 1993; Jorgensen 1997). This implies that the mass drives the formation and evolution of galaxies: the most massive Es experienced a shorter star formation and as a result they suffered an enrichment in Mg from Type II SN, or equivalently, their star formation was not long enough as to incorporate the Fe, and, as a consequence, their content in Fe is smaller in comparison with lower luminosity Es, which experienced a more extended star formation and had the time to incorporate Fe through Type Ia SN (e.g., Trager et al. 2000; Sánchez-Blázquez et al. 2003).

Thomas et al. (2003) introduced α-enhanced models to reproduce the properties of the most massive ellipticals through the increase of α-elements (O, Mg, Si, Ca, Ti) with respect to the solar neighbourhood. These models were first tested in Maraston et al. (2003, see Figure 3.5), finding that massive ellipticals as well as globular clusters are α-enhanced objects.

3.2.2.2 H_β − *Mgb and* H_β − <*Fe*> *diagrams*

Measuring ages and metallicities of early-type systems has been a problem throughout the years because these two parameters appear degenerated in their spectra. This means that an increase in the metallicity produces a similar effect in the colours and most indices as an increase in the age (Faber 1972, 1973; O'Connell 1980; Rose 1985). In particular, when Worthey (1994) used his Single Stellar Population models (SSPs, those considering only one burst of star formation) to quantify this degeneracy, he found the so-called *3/2 law*. This law implies that an increase in the age by a factor of 3 produces the same effects in the colours as an increase in the metallicity by a factor of 2. The key to solve this degeneracy was provided by Worthey models (although is was suggested before by Rabin (1982) and Gunn et al. (1981). A Balmer index plotted versus a metal line or colour yields a two-dimensional theoretical grid where the equivalent single-burst age and metallicity for a population can be directly read. This method has extensively been tested (e.g., González 1993; Fisher et al. 1995; Kuntschner & Davies 1998; Jørgensen 1999; Trager et al. 2000) and it is nowadays the most used procedure to obtain ages and metallicities of the stellar populations of evolved stellar systems. The most common diagrams used are those that plot the Balmer line H_β versus Mgb or <Fe> because, for this combination of indices, the models appear nearly orthogonal, i.e. the degeneracy is almost broken. However, it must be noted that a small amount of young stars dominate the strength of H_β, making the galaxy appear younger although the bulk of stars may be old. As a result the ages obtained from Balmer lines has to be taken as *luminosity-weighted ages*.

When the line-strengths of elliptical galaxies are plotted over SSP models on H_β − Mgb and H_β − <Fe> diagrams, an anticorrelation between age and metallicity can be detected, where young galaxies tend to be more metallic than the old ones (Trager et al. 2000). However, it must be noted that the H_β − Mgb and H_β − <Fe> are not fully orthogonal: thus H_β is primarily sensitive to age, but also to $[\mathrm{Fe/H}]$ and $[\alpha/\mathrm{Fe}]$, <Fe> is sensitive to $[\mathrm{Fe/H}]$, but also to age and $[\mathrm{Mg/Fe}]$, etc. Hence, the resulting errors in age, $[\mathrm{Fe/H}]$ and $[\mathrm{Mg/Fe}]$ are tightly correlated (Trager et al. 2000).

3.2.2.3 *Index* − σ *relations*

The index-velocity dispersion diagrams can be used to study the trends of the stellar population properties with the mass of galaxies. Thus, if the mass is the parameter that drives the formation and evolution of the galaxies, then it should be manifested in these index-σ relations.

Sánchez-Blázquez (2004) found that all three parameters, age, metallicity ($[\mathrm{Z/H}]$) and α-enhancement ($[\alpha/\mathrm{Fe}]$), correlate strongly with σ: low mass ellipticals ($\leq 10^{10} M_\odot$) present intermediate-age stellar populations with nearly solar Mg/Fe, while massive galaxies ($\geq 10^{11} M_\odot$) appear dominated by old stellar populations and are α-enhanced. The same test was performed in high and low density environments finding that galaxies in clusters formed the bulk of their stars at redshift between ~ 2 and 5 and galaxies in low density regions were delayed to $z \sim 2$ to 1. This trends were also confirmed by Nelan et al. (2005); Thomas et al. (2005) and Sánchez-Blázquez et al. (2006b) (see Figure 3.6).

Therefore, the utility of these diagrams resides on the fact that the comparison of an index with the velocity dispersion of the galaxies gives us the clues of their star formation histories as a function of their masses. The $[\mathrm{Mg/Fe}] - \sigma$ diagram indicates that the duration of the star

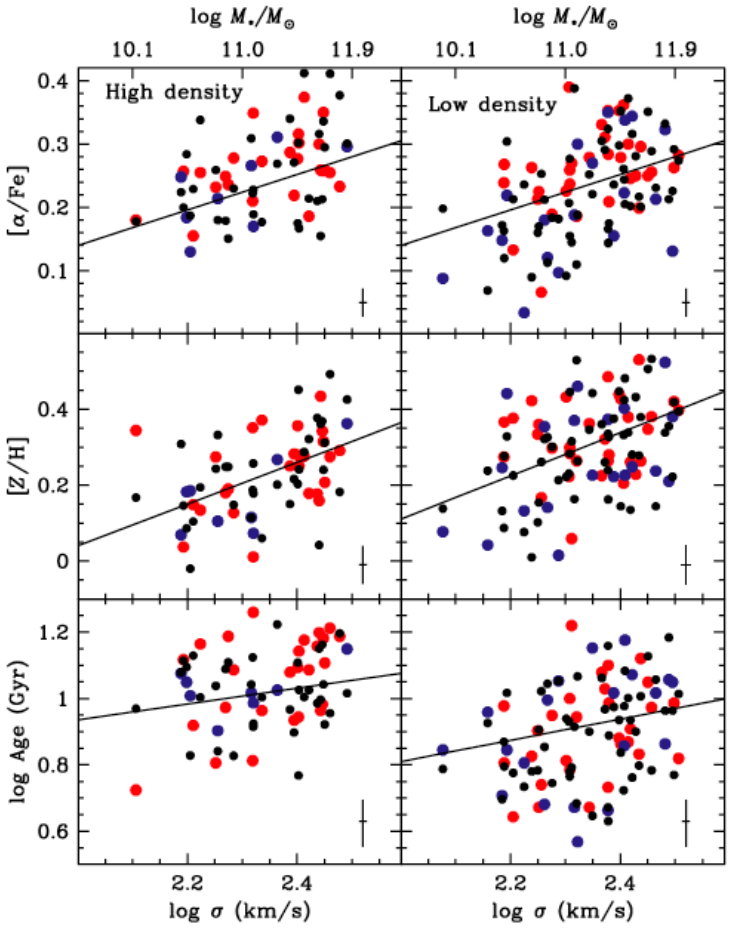

Figure 3.6: Age, metallicity and α-enhancement relation with the masses of the galaxies in different environments from Thomas et al. (2005). Ages and element abundances are derived with the $[\alpha/\mathrm{Fe}]$ enhanced SSP models from Thomas et al. (2003). Red circles are elliptical galaxies whereas blue circles are S0s. Black circles are Monte Carlo simulations taking into account the observational errors and an intrinsic scatter. Typical error bars are given in the bottom right corners.

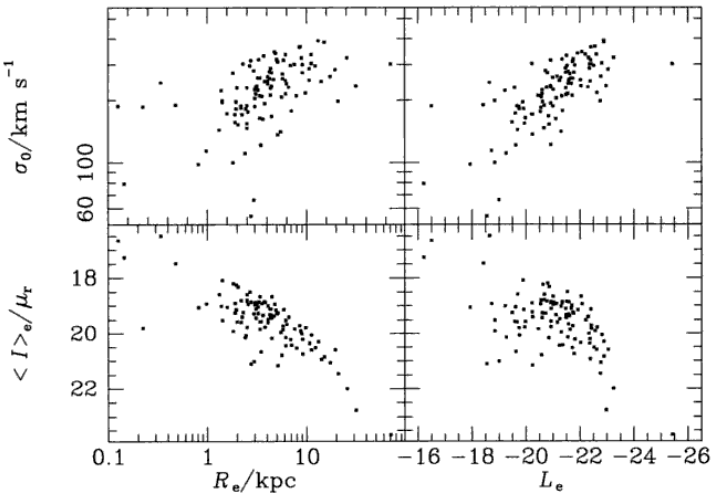

Figure 3.7: Correlations between different parameters of elliptical galaxies. R_e is the effective radius measured in kpc, $< I_e >$ the mean surface brightness within the R_e in mag arcsec^{-2}, σ_0 is the central velocity dispersion expressed in km s^{-1} and L_e is the luminosity in G band (from Djorgovski & Davis (1987)) interior to R_e in magnitudes, from Binney & Merrifield (1998) based on the data of Djorgovski & Davis (1987).

formation activity decreases with increasing mass and the $\mathrm{H}_\beta - \sigma$ plot evidences the downsizing effect, because the star formation activity extends to younger ages for decreasing mass.

3.3 Structural Properties

The structural properties of the galaxies are measured through some parameters that are based on their light distribution. These structural properties correlate strongly with other physical characteristics of the galaxies, such as mass, size and luminosity. These correlations are called *scaling relations* and among them, the most studied ones for early-type galaxies are the *Kormendy relation*, the *Faber-Jackson relation* and the *Fundamental Plane*. These relations are independent of the environment of the galaxies in the Universe, therefore their mere existence provides insights into both the formation and evolution of galaxies. Moreover, they are also used as distance indicators.

3.3.1 Kormendy relation

Kormendy (1977) found a correlation between the effective radius, ($R_{\rm eff}$, radius that contains half the total luminosity of the galaxy) and the effective surface brightness ($\mu_{\rm eff}$, originally defined as the surface brightness measured at the $R_{\rm eff}$ but nowadays alternatively measured as the averaged surface brightness within the $R_{\rm eff}$, $< \mu >_{\rm eff}$). This correlation, shown in the left lower panel of Figure 3.7 (where $< I_e > /\mu_r$ gives the mean surface brightness within the effective radius in mag arcsec^{-2}), indicates that larger early-type galaxies have fainter effective surface brightnesses. Defining the effective luminosity inside the $R_{\rm eff}$ as $L_{\rm eff} = \pi < \mu >_{\rm eff} R^2_{\rm eff}$, from the $\mu_{\rm eff}$-$R_{\rm eff}$ relation it is inferred that more luminous early-type galaxies have lower surface brightnesses (lower right panel of Figure 3.7).

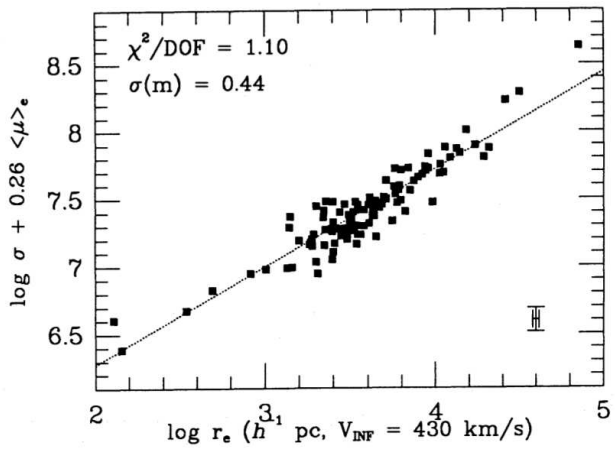

Figure 3.8: Fundamental Plane from Djorgovski & Davis (1987). The dotted line represent the least-square fit. Median errors are indicated by the error bars in the right lower corner. Reduced chi-squares, χ^2/DOF, and the estimated error of the relation when used as distance predictor, expressed in magnitudes, $\sigma(m)$, is shown in the left upper corner.

3.3.2 Faber-Jackson relation

The Faber-Jackson relation (right upper panel of Figure 3.7), called after its discoverers (Faber & Jackson 1976a), relates the effective luminosity ($L_{\rm eff}$) with the central velocity dispersion (σ_0) finding that more luminous elliptical galaxies have larger central velocity dispersions. Quantitatively this relation indicates $L_{\rm eff} \sim \sigma_0^4$. Since σ_0 is correlated with $L_{\rm eff}$ and $L_{\rm eff}$ is correlated with $R_{\rm eff}$, it follows that σ_0 must be correlated with $R_{\rm eff}$ (left upper panel of Figure 3.7).

3.3.3 $D_n - \sigma$ relation

Dressler et al. (1987) defined D_n (the diameter within which the mean surface brightness is 20.75 μ_B), a photometric parameter based on the mean surface brightness in the B band that shows a very tight relation with a very small scatter with the central velocity dispersion of early-type galaxies. This strong relation is found to be independent of the cluster the early-type galaxies are inhabiting (Dressler et al. 1987; Jorgensen et al. 1993; Kelson et al. 2000), which means that when D_n is measured in kpc for a reference object for which its distance is known, the offset between the rest of the systems and this reference object provides the distances to all of them. As a consequence, the $D_n - \sigma$ diagram is considered as a good distance indicator.

Comparing spiral bulges and elliptical galaxies in the $D_n - \sigma$ plane, it is seen that both populations present the same trend, suggesting that their inner structures are very similar. This fact was found and interpreted by Dressler et al. (1987) as an indication of both populations having a common origin.

3.3.4 Fundamental Plane

In all the correlations of Figure 3.7 the scatter of the points from the mean relations is larger than what can be accounted by the observational errors. Moreover, this scatter is correlated between the different diagrams. For example, galaxies which lie above the mean Faber-Jackson relation in the right upper panel tend to lie above the mean surface brightness-luminosity relation in the

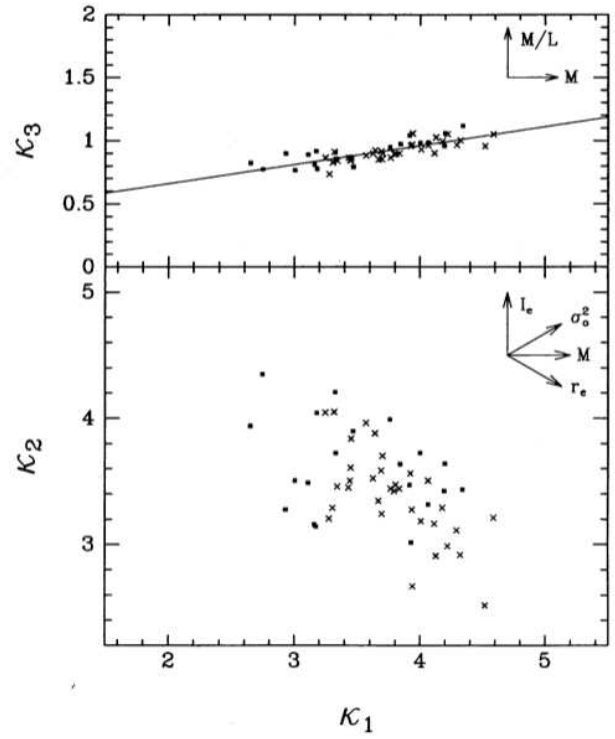

Figure 3.9: Fundamental Plane plotted in the κ-space as defined in Bender et al. (1992). Virgo ellipticals are the closed squares and Coma Es are the crosses.

right lower panel. To understand the meaning of these diagrams and the correlations between their residuals it is useful to create a three-dimensional space that represents all the parameters together. The effective luminosity can be excluded because it is related to $\mu_{\rm eff}$ and $R_{\rm eff}$ as described above. As a result, a three-dimensional space of $R_{\rm eff}$, $< \mu_{\rm eff} >$ and σ can be generated. It relates the structural and dynamical properties of the galaxies to their stellar content. In such diagram the early-type galaxies lie in a tight surface known as the *Fundamental Plane* (FP; Djorgovski & Davis 1987; Dressler et al. 1987, see Figure 3.8).

The most common representation of the FP in a two-dimension diagram is its edge-on view, commonly expressed as:

$$\log(R_{\rm eff}) = \alpha \log(\sigma_{\rm eff}) + \beta < \mu_{\rm eff} > +\gamma \tag{3.1}$$

where the velocity dispersion is now measured inside the effective radius to have all the magnitudes coherently measured, and α, β and γ are the coefficients that minimise the scatter of the plane and determine its tilt.

The FP can be understood as a manifestation of the virial theorem for relaxed systems, under the assumption that dynamical galaxy mass-to-light ratios ($M_{\rm dyn}/L$) are constant, or at least smoothly varying, for all galaxies. The physical characteristics that involve the virial theorem, the total mass (M), root-mean square speed of the stars (V_0) and the gravitational radius (r_g), can be substituted by the observables $< \mu_{\rm eff} >$, $\sigma_{\rm eff}$ and $R_{\rm eff}$, leading to the coefficients for the edge-on view (Equation 3.1) of $\alpha = 2.0$ and $\beta = 0.4$ while γ is just the offset that depends on the distance to the objects plotted in the FP. Therefore it can also be used as a distance indicator. The

existence of the FP implies that elliptical galaxies: (a) are virialised systems, (b) all of them have homologous structures (e.g., the shape of the mass distribution) or their structural characteristics vary along the plane, and (c) they form a homogeneous family in terms of ages and metallicities.

The observed FP presents a certain inclination with respect to the virial theorem prediction (e.g., see the coefficients in Figure 3.8), and it also presents a finite thickness (e.g., Jorgensen et al. 1996; Forbes et al. 1998; Wuyts et al. 2004; Hyde & Bernardi 2009; Gargiulo et al. 2009), in contrast to the infinitely thin prediction of the virial theorem. Faber et al. (1987) and Prugniel & Simien (1996) proposed that this tilt could be due to differences in the stellar populations. They suggested that when the luminosity of the galaxies increases, systematic differences in their stellar populations appear. Other authors, like Pahre et al. (1998a) and Trujillo et al. (2004), have proposed that the tilt is a consequence of early-type galaxies not having homogeneous structural properties. For example, the content and/or distribution of the stars and dark matter could vary with the luminosity as well as the anisotropy and rotational support (Ciotti et al. 1996; Prugniel & Simien 1996; Ciotti & Lanzoni 1997). The origin of this inclination is still an open question and many efforts are yet being devoted to its analysis (see e.g., Graves & Faber 2010a).

In order to represent almost perfectly the edge-on projection of the FP, Bender et al. (1992) defined an orthogonal coordinate system (κ_1, κ_2, κ_3) in which each new variable is a linear combination of $\log \sigma^2$, $\log R_{\rm eff}$ and $\log \mu_{\rm eff}$ (see Figure 3.9). The κ-space FP is defined as follows:

$$\kappa_1 \equiv (\log \sigma^2 + \log R_{\rm eff})/\sqrt{2} \tag{3.2}$$

$$\kappa_2 \equiv (\log \sigma^2 + 2\log \mu_{\rm eff} - \log R_{\rm eff})/\sqrt{6} \tag{3.3}$$

$$\kappa_3 \equiv (\log \sigma^2 - \log \mu_{\rm eff} - \log R_{\rm eff})/\sqrt{3} \tag{3.4}$$

The main advantage of this κ-FP is that each variable is physically meaningful. Specifically, $\kappa_1 \sim M$, $\kappa_2 \sim \mu_{\rm eff}$ and $\kappa_3 \sim M/L$. Bender et al. (1992) found that when the FP was analysed in this new space of parameters, luminous ellipticals, bulges of spiral galaxies and most compact ellipticals define a smooth continuous plane. In particular, they found that, defining the FP as the region covered by the luminous ellipticals, bulges have somewhat lower M/L while dwarf early-type galaxies have slightly higher M/L. They also found that some of the dwarf spheroidals present an extreme excess of M/L setting them apart from the rest of the dynamically hot systems, which they interpreted as the consequence of being dominated by dark matter.

3.4 Dwarf early-type galaxies

Although they are the most numerous galaxies in clusters (see Figure 3.10; Sandage et al. 1985; Binggeli et al. 1988; Ferguson & Binggeli 1994; Blanton et al. 2005; Croton et al. 2005) dwarf early-type galaxies (ellipticals and spheroidals, hereafter dEs) have not been studied as extensively as massive ellipticals due to their low luminosity ($M_B > -18$). As far as kinematic parameters are concerned it was not until the first decade of the 21st century when a systematic study of dwarf galaxies has begun and the first comparisons with giant ellipticals has been performed in order to determine if dEs and Es are the same family of objects (Gorgas et al. 1997; Pedraz et al. 2002; Geha et al. 2002, 2003; van Zee et al. 2004b; Lisker et al. 2006a,b, 2007, 2008, 2009; Ferrarese

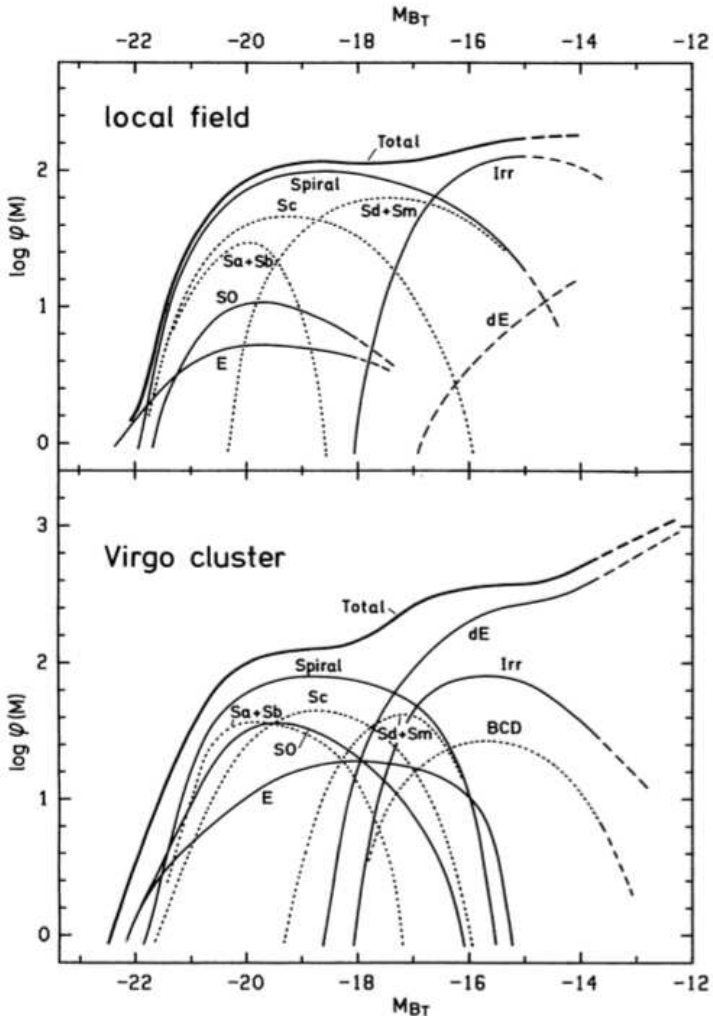

Figure 3.10: Luminosity Function (LF, number of galaxies per bin in magnitude) of field galaxies and Virgo cluster members from Binggeli et al. (1988). Extrapolations are marked by dashed lines. In addition to the LF of all spirals, the LFs of the subtypes Sa+Sb, Sc and Sd+Sm are also shown as dotted curves. The LF of Irr galaxies comprises the Im and BCD galaxies in the case of the Virgo cluster, the BCDs are also shown separately.

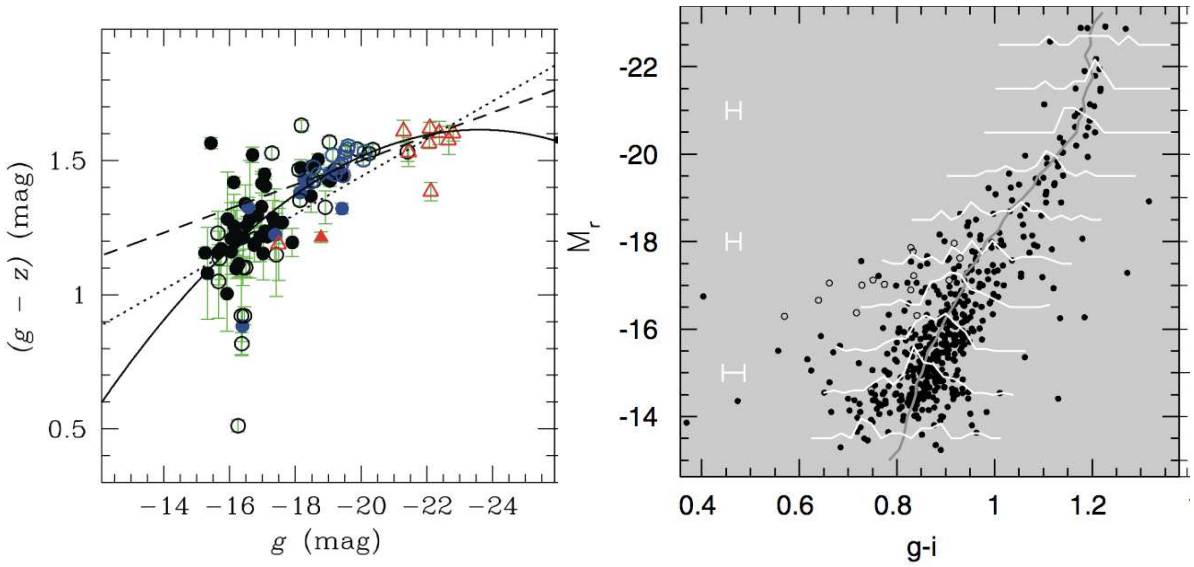

Figure 3.11: Colour-magnitude diagram for the early-type galaxies that comprise the ACSVCS (left panel Ferrarese et al. 2006) and those from SDSS analysed by Janz & Lisker (2009) (right panel). *Left panel:* Black open circles are galaxies fitted with a Sersic profile that are not nucleated, black filled symbols those with a Sersic profile that are nucleated. Red open triangles are those fitted with a core-Sersic profile non-nucleated and filled red triangles core-Sersic nucleated. Blue dots are those fitted with multiple components. The dashed and dotted line correspond to least-squares fits to galaxies fainter and brighter than $M_g = -18$ mag, respectively, while the curved line represents the best quadratic fit to the entire sample. *Right panel:* Open circles show dEs with blue cores and filled circles the remaining galaxies. The grey line indicates the "running histogram" as found in successive magnitude bins with a width of 1 mag and steps of 0.25 mag, clipped one time at 3σ. The white histograms show the distributions in bins of the same width, normalized to the square root of the number of galaxies in the bin. The white error bars show indicate typical photometric errors at the respective brightness.

et al. 2006; Michielsen et al. 2008; Janz & Lisker 2008, 2009; Chilingarian 2009; Koleva et al. 2009a; Paudel et al. 2010).

3.4.1 Colour-Magnitude Diagram

Regarding the CM diagram, it is still an open question if Es and dEs follow the same trend and whether this trend is linear.

The most recent survey made in Virgo (ACSVCS - ACS Virgo Cluster Survey, Ferrarese et al. 2006) reported a parabolic curve to describe the CM relation from dwarfs to giant early-type galaxies. However, Andreon et al. (2006) indicated that this parabolic curve could be linearised if the intrinsic scatter in the statistical analysis was considered. In contrast, Janz & Lisker (2009) fitted an S-like shape for this diagram (see Figure 3.11).

Although the discussion about the best curve that fits simultaneously massive and dwarf elliptical galaxies still remains open, there are two conclusions in common to all the studies: *(1)* there is no gap between dEs and Es and *(2)* the CM relation is still well defined for faint magnitudes ($M_B \sim -14$ mag).

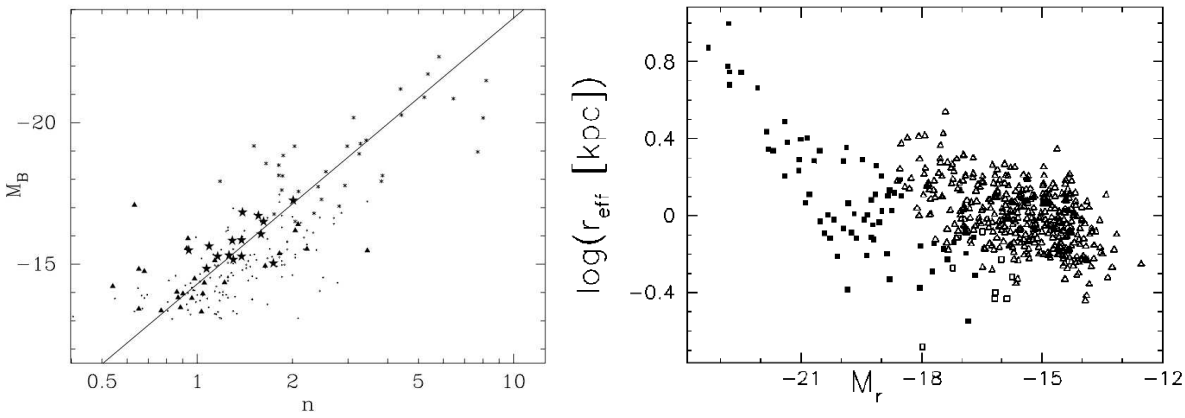

Figure 3.12: Left panel: Absolute B-band magnitude vs. logarithm of the Sérsic index n from Graham & Guzmán (2003a). Dots are dEs from Binggeli & Jerjen (1998), triangles dEs from Stiavelli et al. (2001), stars Coma dEs from Graham & Guzmán (2003a), asterisks intermediate-to-bright Es from Caon et al. (1993); D'Onofrio et al. (1994), open circles represent the power-law Es from Faber et al. (1997) and filled circles represent the core-E from Faber et al. (1997). Right panel: Absolute r-band magnitude vs. logarithm of half light radius from Janz & Lisker (2008). dEs are shown with open triangles and E and S0 with filled squares. M32-type candidates are drawn with open squares.

3.4.2 Stellar Populations

The analysis of the Lick/IDS indices has revealed that dEs contain intermediate to old ages ($\sim$ 5 Gyr, with a rather large scatter), subsolar metallicities ($-1 \leq [\mathrm{Fe/H}] \leq 0$), and around solar α-element abundances (Gorgas et al. 1997; Geha et al. 2003; van Zee et al. 2004b; Michielsen et al. 2008; Chilingarian 2009; Koleva et al. 2009a; Paudel et al. 2010), evidencing that their stellar content is remarkably different from those of massive ellipticals.

An important question still under debate is whether their ages are correlated with their luminosities. Poggianti et al. (2001) found that the ages decrease with decreasing luminosity while Geha et al. (2003) found the same trend with velocity dispersion. However, Michielsen et al. (2008) did not find any correlation with luminosity within the dwarf regime and Paudel et al. (2010) found indications of an anticorrelation.

The gradients of the stellar populations have been studied only for the brightest dEs. The pioneer study on this topic was Gorgas et al. (1997) studying a sample of 6 dEs in Virgo, nothing else has been conducted in this direction until Chilingarian (2009) and Koleva et al. (2009a) for Virgo and Fornax dEs respectively. Concerning the metallicity it has been found that the gradients decrease with the radius or they remain constant. With respect to the age, the gradients usually stay constant with the radius or exhibit a small increase with radius. These results are consistent with the picture of dEs having their last star formation activity at their centers, specifically those with blue cores (Lisker et al. 2006a).

3.4.3 Structural Characteristics

Dwarf early-type galaxies have surface brightness profiles which are less steep than massive ellipticals, (exponential profiles versus de Vaucouleurs profiles Lin & Faber 1983; Binggeli et al. 1984; Ferrarese et al. 2006), but both populations can be described by a Sérsic profile (Sérsic 1968; Ciotti 1991):

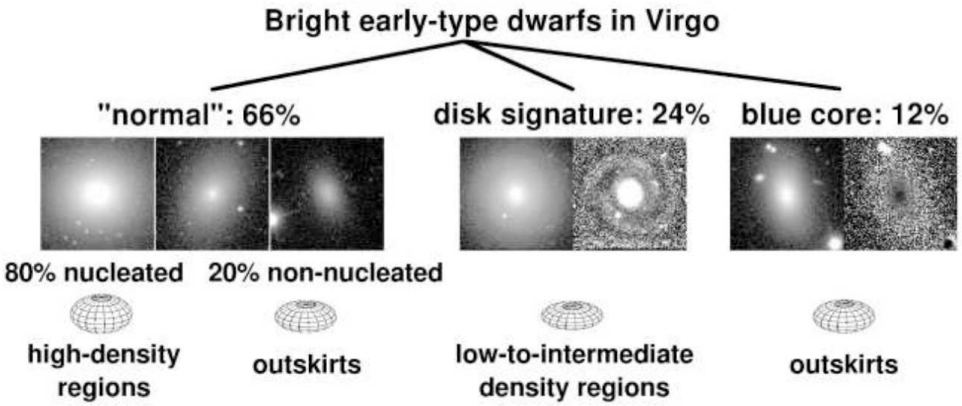

Figure 3.13: Scheme of dE subclasses from Lisker (2009).

$$I(R) = I_{\rm eff} 10^{-b_n[(R/R_{\rm eff})^{1/n}-1]} \tag{3.5}$$

where $I(R)$ is the intensity measured in the isophote of radius R, $I_{\rm eff}$ is the intensity measured at the $R_{\rm eff}$, b_n is a constant chosen such that half the total luminosity predicted by this law comes from $R < R_{\rm eff}$. Es and dEs have light distributions described by this Sérsic profile where the index n changes linearly with their luminosity (Graham & Guzmán 2003a, see Figure 3.12).

According to the sizes of dEs in comparison to Es, it has been shown that in the magnitude were both families overlap, there are two trends in sizes: one trend is the extrapolation of the Es relation all the way to compact Es (cEs), being M 32 the prototype of this kind of galaxies, and another independent trend for dEs (Janz & Lisker 2008, see Figure 3.12). Therefore, in the low-luminosity regime, dEs appear larger than their cEs counterparts.

By using SDSS images, a morphological subclassification of dwarf early-type galaxies has been introduced. Lisker et al. (2006b) systematically analysed the residual shapes that appear after removing the smooth surface brightness profiles of dEs in the Virgo cluster. It was found that a non-negligible number of dEs present disk-like structures (see Figure 6). This study provided a new insight into the nature of dE galaxies suggesting that these galaxies are not as simple as they were originally thought.

4

MILES stellar library

Resumen

En este Capítulo se explica la importancia y el uso de las bibliotecas estelares, que no son más que una colección de espectros de estrellas observados o generados teóricamente.

El uso de estas bibliotecas es muy diverso dentro del campo de la espectroscopía. Por un lado son el ingrediente principal de los modelos de síntesis de poblaciones estelares. Por otro lado se utilizan como plantillas para el cálculo de dispersiones de velocidades y velocidades radiales de objetos estelares. Una biblioteca bien calibrada en flujo es además muy útil para calibrar espectros observados.

Pese a su gran importancia, las bibliotecas estelares aun presentan ciertos problemas. El cubrimiento del espacio de parámetros que caracterizan a las estrellas (temperatura efectiva, gravedad y metalicidad) es insuficiente, de forma que en este espacio tridimensional hay huecos e incluso áreas completamente vacías. Estos huecos se suelen rellenar haciendo interpolaciones entre estrellas con parámetros similares, con las consecuentes incertidumbres que esto acarrea. Para evitar estas interpolaciones se utilizan bibliotecas teóricas (como por ejemplo Coelho et al. 2007), que cubren todo el espacio de parámetros completo. El principal inconveniente de este método es que estos espectros teóricos se obtienen modelando la evolución estelar, y no todos los pasos de dicha evolución son conocidos, de forma que los espectros teóricos así obtenidos no se corresponden al 100 % con los observados. Otra forma de cubrir estos huecos en el espacio de parámetros es la utilización de funciones de ajuste. Estas funciones relacionan los índices de intensidad de líneas con los parámetros atmosféricos de las estrellas, de forma que en vez de interpolar entre espectros estelares similares, se interpola dentro de una función suave.

Vista la importancia del cubrimiento de parámetros estelares, la Dra. Patricia Sánchez Blázquez empleó buena parte de su trabajo de tesis en la elaboración de la biblioteca estelar denominada MILES (Medium-resolution Isaac Newton Telescope Library of Empirical Spectra) con el objetivo de incrementar sustancialmente este cubrimiento (como puede verse en la Figura 4.1).

En el momento de mi incorporación a este grupo de investigación la biblioteca MILES ya estaba completada, pero se me dió la oportunidad de formar parte del equipo y colaborar en el desarrollo del segundo artículo de MILES dedicado al cálculo de los parámetros estelares de esta biblioteca (Cenarro et al. 2007).

He creído necesaria la incorporación de un Capítulo de esta tesis enteramente dedicado a esta biblioteca estelar ya que se trata de una herramienta muy valiosa que ha estado presente en

todo momento en el desarrollo de todos los análisis espectroscópicos realizados en los siguientes Capítulos. Para especificar un poco más, en todas las campañas de observación se han obtenido espectros de estrellas de esta biblioteca que después se han utilizado para calibrar en flujo las galaxias observadas y para calcular sus parámetros cinemáticos. Además, los modelos de poblaciones estelares utilizados en ciertos análisis de esta tesis se basan en MILES (Vazdekis et al. 2010).

4.1 Introduction

A stellar library is a collection of stars generated (if it is theoretical) or observed (if it is empirical) with the same resolution and spectral coverage. Having a good quality stellar library is essential in any spectroscopic analysis because they are used as tools for different kinds of studies.

Firstly, the stellar libraries are the main ingredient in stellar population synthesis models that are used to derive ages, metallicities and/or abundances of stellar objects. Secondly, a properly flux calibrated stellar library is also used to flux calibrate the observed spectra by comparing the general shape of the spectrum of a star in common between the library and the sample of observed objects under study. Finally, the stellar libraries are also used as radial velocity templates to obtain the redshift of the objects observed.

In the analysis of star formation epoch of early-type galaxies and their subsequent evolution, the usage of stellar population synthesis models has several advantages over other methods. As we discussed in Chapter 3, the colours can give us some information about the stellar populations of the galaxies, but they present an age-metallicity degeneracy that is not possible to break. Using index-index diagrams (see Section 3.2.2) it is possible to break this degeneration and, therefore, a luminosity-weighted age and metallicity for a given galaxy can be obtained (see Section 3.2.2.2). Another advantage of using absorption lines instead of photometric colours is that they offer the possibility to study the chemical abundances of the elements present in the spectrum of a stellar object. The different abundances provide good insight into the evolution of the underlying stellar population of galaxies since they act as cosmological clocks, due to the fact that they are generated in different stages of the evolution of the stars that populate the galaxies (see Section 3.2.2 and Chapter 5).

One source of uncertainty in the measurement of ages and metallicities through stellar population synthesis models comes from the stellar libraries employed in their computation. The main problem of the empirical stellar libraries is the usual small coverage of the atmospheric parameters of the stars. These parameters (metallicity, effective temperature $T_{\rm eff}$, and gravity) represent the main properties that characterise different stars. The lack of stars with all kind of atmospheric characteristics is generally overcome by interpolating between stars with similar parameters to generate those missing. Therefore the uncertainties increase dramatically with the decrease of the coverage of the atmospheric parameters space.

One way to solve this problem is to use theoretical stellar libraries based on stellar atmospheres models (e.g., Kurucz 1992; Lejeune et al. 1997). The main advantage of these theoretical stellar libraries is that they provide model spectra of stars covering the complete space of atmospheric parameters, thus avoiding any interpolations. However, due to the fact that the complete physical mechanisms involved in the stellar evolution are not well-known, the strength of the absorption lines predicted by the synthesis models based on these theoretical libraries are not always observed afterwards in the galaxies. This is the reason why these theoretical stellar libraries are ”specialised” in some spectral characteristics that are better understood (as it is the case e.g. of Coelho et al. 2007, specialised on Fe and α elements, whereas C and N are less accurately predicted). Another way to overcome this problem of the coverage of the atmospheric parameters is to use fitting functions. These functions relate the line-strength indices with the fundamental atmospheric parameters, thus the interpolations in these polynomials are much smoother than interpolating within the stellar libraries. The most widely used fitting functions are those based on

the Lick/IDS library (Gorgas et al. 1993; Worthey 1994). Using fitting functions has the disadvantage of providing just a limited amount of information because they are restricted to line-strength indices, and as a consequence the synthesis models based on do not provide synthetic Spectral Energy Distributions (SED), as can be made when they are fed with stellar libraries.

As it can be inferred from this discussion, the best way to improve the stellar population synthesis models is to observe high quality spectra of a large number of stars that cover as much as possible the atmospheric parameter space.

4.2 MILES (Medium-resolution Isaac Newton Telescope Library of Empirical Spectra)

In order to have an improved stellar library specially designed for stellar population modeling (Sánchez-Blázquez et al. 2006c) developed MILES (Medium-resolution Isaac Newton Telescope Library of Empirical Spectra), a spectral library in the complete optical range with medium-resolution and an improved coverage of the atmospheric parameter space (Table 4.1) in order to cover stellar properties never reached before or with a poor coverage due to the low number of stars. In particular, the number of cool and super-metal-rich stars, metal-poor stars, and hot stars ($T_{\rm eff} > 6500$ K) was greatly enhanced with respect to previous works (see Figure 4.1 for a comparison of the coverage of the atmospheric parameter space in comparison to the most widely used optical empirical stellar libraries). The observations comprised a total of 25 nights in five different observing runs during the years 2000 and 2001 using the 2.5m Isaac Newton Telescope (INT) at the Roque de los Muchachos observatory (La Palma, Spain). The stellar spectra were observed at the paralactic angle, favouring to have flux calibrated spectra, one of the weakest points of previous works (such as e.g., Worthey 1994). The result was an empirical library that consists of around 1000 stars observed with a resolution of 2.3 Å (FWHM) in the wavelength range $\lambda\lambda 3525-7500$Å. This library is up to now one of the best empirical stellar libraries because it successes simultaneously in several aspects: (i) MILES provides a large number of stars; (ii) it also covers the complete optical region; (iii) it is flux calibrated, advantaging INDO-US (Valdes et al. 2004) in this last step; and (iv) it presents the best coverage of the stellar atmospheric parameters available.

To derive ages and metallicities of stellar systems it is necessary to plot index-index diagrams (see Section 3.2.2) where the theoretical grid is the result of measuring the indices under study in the population synthesis models fed with the stellar library. Historically, the reference resolution used to measure the indices has been the so-called Lick/IDS system. This spectrophotometric system consists of the measurement of each index at a specific broadening that changes with wavelength, between 10.4 Å to 9 Å (200 km s^{-1} to 325 km s^{-1}) for Lick/IDS indices. MILES, which resolution is constant as a function of wavelength and much higher than that of Lick/IDS stellar library (Table 4.1), has led to the definition of a new reference system, *LIS* (Line Index System, Vazdekis et al. 2010), that avoids the large broadening imposed by the Lick/IDS system when measuring stellar objects of small velocity dispersion, such as globular clusters or dwarf early-type galaxies. This LIS system consists of 3 different spectral resolutions (5.0, 8.4 and 14.0 Å, FWHM) and it is not restricted to the Lick/IDS set of indices but can be used for any index in the literature (e.g., Rose 1994; Serven et al. 2005). The main advantage of the LIS system is that indices in high-resolution spectra can be measured without losing the spectral resolution achieved in the observations. MILES is also the core of the stellar population synthesis models of Vazdekis

Table 4.1: Some of the previous libraries in the optical region devoted to stellar population studies. Compiled by Sánchez-Blázquez et al. (2006c).

Reference	Resolution FWHM (Å)	Spectral range (Å)	Number of stars	Comments
Spinrad (1962)				Spectrophotometry
Spinrad & Taylor (1971)				Spectrophotometry
Gunn & Stryker (1983)	20-40	3130-10800	175	
Kitt Peak (Jacoby et al. 1984)	4.5	3510-7427	161	Only solar metallicity
Pickles (1985)	10-17	3600-10000	200	Solar metallicity except G-K giants
Lick/IDS (Worthey 1994)	9-11	4100-6300	425	Not flux calibrated, variable resolution
Kirkpatrick et al. (1991)	8-18	6300-9000	39	No atmospheric correction
Silva & Cornell (1992)	11	3510-8930	72 groups	Poor metallicity coverage
Serote Roos et al. (1996)	1.25	4800-9000	21	
Pickles (1998)		1150-10620	131 groups	Flux calibrated
Jones (1999)	1.8	3856-4476	684	Flux calibrated
		4795-6800		
ELODIE (Prugniel & Soubiran 2001)	0.1	4100-6800	709	Echelle
STELIB (Le Borgne et al. 2003)	3.0	3200-9500	249	Flux calibrated
INDO-US (Valdes et al. 2004)	1.0	3460-9464	1273	Poor flux calibrated
MILES (Sánchez-Blázquez et al. 2006c)	2.3	3525-7500	985	

et al. (2010). These models are therefore provided in the 3 spectral resolutions defined by the LIS system as well as at the resolution of the stellar library itself (2.3 Å, FWHM).

During the course of this thesis I have contributed to the construction of the empirical MILES stellar library by being coauthor of Paper II (Cenarro et al. 2007). This paper is devoted to generate a homogeneous dataset of atmospheric parameters for all the stars in the MILES library. Specifically I have helped in the compilation of the literature available for each one of the stars of the library, homogenising them, looking for the last and best updates. These are essential steps to calculate the final values of effective temperature, gravity and metallicity that will be used, for example, in the generation of the fitting functions. We decided to use Soubiran et al. (1998) as reference system, to obtain the fundamental parameters presented in that Paper II of MILES, due to the fact that it computes self-consistent atmospheric parameters for a total of 211 echelle spectra covering a wide rage of effective temperatures and gravities. Those stars not included in Soubiran et al. (1998) are calibrated and corrected for systematic differences. In the case of stars not available in the literature, both $T_{\rm eff}$ and gravity were estimated from its spectral type and luminosity class.

MILES has been an important tool throughout this thesis. In our observing campaigns we selected several calibration stars from the MILES stellar library to be observed under the same conditions as our target galaxies. Comparing the observed stars with the same ones in MILES we obtained the flux calibrating curve that we applied to our galaxies. These observed stars, instrumentally affected in the same way as the galaxies, were also used as kinematic templates. Instead of using a single template, we made a linear combination of the observed stars in order to have a spectrum that resembled the target galaxy. Then, we compared this linear combination of stars with the galaxy in study, shifting and broadening it until it fitted the target galaxy. The result of applying this procedure for the spectra of each galaxy along their radius is the radial velocity and velocity dispersion profiles. These two kinematic curves are essential to analyse the rotation of the galaxies and their dark matter content, together with other parameters that will be described in Chapter 6.

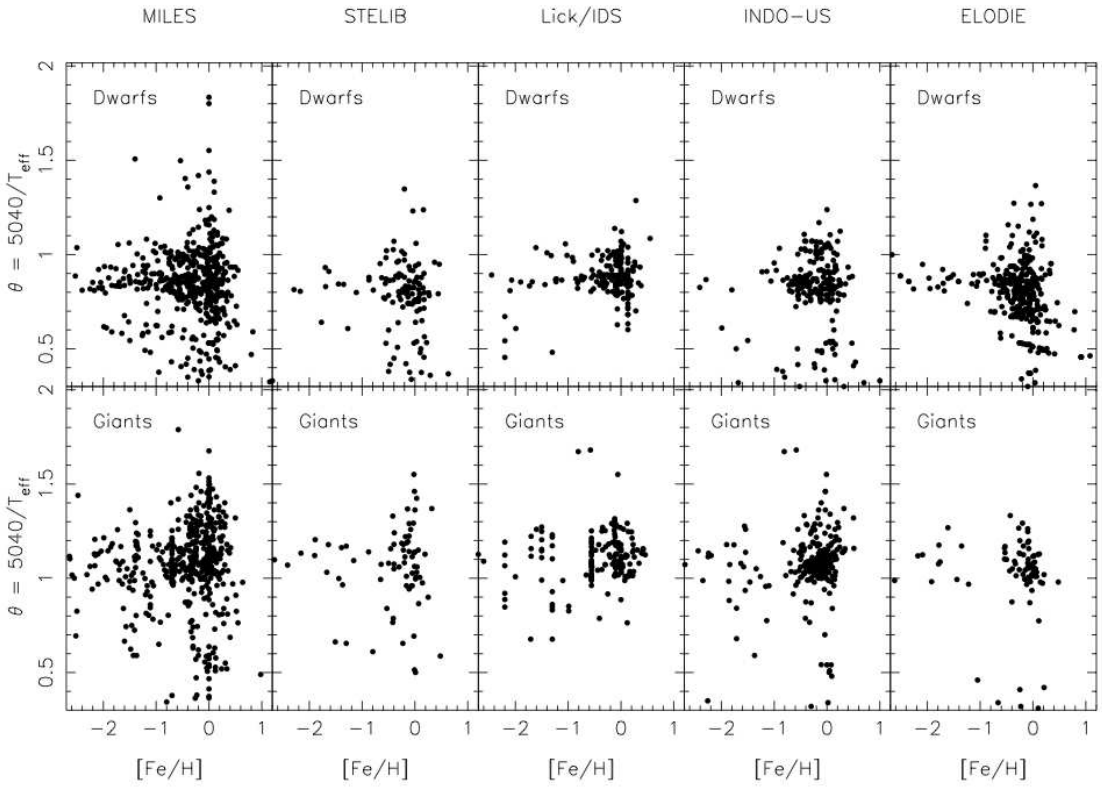

Figure 4.1: Effective temperature vs. metallicity for MILES stars in comparison with other stellar libraries (Sánchez-Blázquez et al. 2006c).

5

Chemical abundances of early-type galaxies in different environments

Resumen

Como ya vimos en el Capítulo 2, el modelo de formación jerárquica de galaxias predice que la historia de formación estelar depende de la densidad del entorno en el que se encuentran las galaxias (por ejemplo Kauffmann & Charlot 1998; De Lucia et al. 2006), de forma que será más rápida para aquellos objetos que se originen en zonas de alta densidad. Mientras que el modelo de colapso monolítico no predice ninguna dependencia con el medio que las rodea.

En este Capítulo hemos comparado la historia de formación estelar de galaxias masivas de primeros tipos localizadas en entornos de alta y baja densidad. Para hacer este estudio hemos medido abundancias de elementos químicos presentes en los espectros de estas galaxias. Hemos escogido este método porque los elementos químicos actúan como relojes cosmológicos, es decir, cada elemento se eyecta al medio interestelar en un momento determinado que viene caracterizado por el proceso evolutivo de la estrella que lo eyecta, caracterizado a su vez por la masa de la estrella.

Estudios anteriores (por ejemplo Sánchez-Blázquez et al. 2003, 2006b) ya demostraron que la historia de formación estelar en galaxias en cúmulos densos, como el de Coma, es más rápida que en cúmulos de menor densidad o en galaxias que se encuentran en el campo. Para este análisis utilizaron como elementos de referencia el magnesio, el hierro, el carbono y el nitrógeno. Mientras que el magnesio es generado en las supernovas de tipo II (Faber et al. 1992; Worthey et al. 1992; Matteucci 1994, la última etapa en la evolución de estrellas masivas, $M > 8M_{\odot}$), el hierro se genera en supernovas de tipo Ia (Nomoto et al. 1984; Woosley & Weaver 1995; Thielemann et al. 1996, la última etapa en la evolución de estrellas de masa intermedia). Sin embargo, en cuanto al carbono y al nitrógeno no está tan claro aun el tipo de estrellas que dan lugar a estos dos elementos.

Del estudio del magnesio y el hierro sabemos que la escala de tiempo en que se eyecta el primero es mucho más corta que la necesaria para eyectar el segundo. Esto es la consecuencia directa de que uno proviene de las estrellas más masivas y el otro de las menos masivas. Pero sólo usando estos dos elementos no podemos saber qué sucede en el tiempo intermedio entre los dos. Aquí es donde entran en juego el carbono y el nitrógeno, porque estos elementos podrán datar entonces estadios intermedios de la formación estelar.

Los estudios realizados hasta el momento sobre el carbono y el nitrógeno utilizaban índices de intensidad de líneas donde las contribuciones de estos dos elementos están mezcladas junto con el oxígeno (Worthey 1998; Burstein 2003; Sánchez-Blázquez et al. 2003; Kelson et al. 2006;

Sánchez-Blázquez et al. 2006b; Schiavon 2007; Graves & Schiavon 2008). Mientras que el índice C4668 es básicamente carbono (Serven et al. 2005), el nitrógeno se ha estudiado hasta este momento utilizando las bandas de CN, donde contribuyen los tres elementos simultáneamente. En este Capítulo hemos introducido por primera vez el estudio del nitrógeno independientemente de cualquier otro elemento a través del índice NH3360.

El procedimiento que hemos seguido para realizar este análisis ha consistido en la observación de una muestra de 35 galaxias que se encuentran en los cúmulos de Coma y Virgo y en el campo. Las galaxias seleccionadas son una submuestra de Sánchez-Blázquez et al. (2006b), con el objetivo de poder tener el rango óptico ya observado, de forma que sólo es necesario observar el ultravioleta cercano para poder medir este índice NH3360. El método de estudio ha consistido en analizar los índices que detallamos en la tabla 5.1 en función de la densidad del entorno de las galaxias y en comparación con modelos de síntesis de poblaciones estelares.

Los resultados obtenidos en este estudio, y que fueron publicados como una carta al editor en Toloba et al. (2009b) nos permitieron afirmar que el carbono está generado, casi en la misma proporción, por estrellas masivas y de baja masa, mientras que el nitrógeno es eyectado al medio interestelar por estrellas también masivas y con una cierta contribución de estrellas de masas intermedias. Esta conclusión nos ha permitido saber que el magnesio es el elemento que se genera antes, seguido del nitrógeno, del carbono y por último del hierro por este orden.

En la última Sección previa a las conclusiones de este Capítulo presento un trabajo que realizé en colaboración con el Dr. Guy Worthey, su estudiante Jedidiah Serven y con la Dra. Patricia Sánchez Blázquez que ha sido publicado como artículo en Serven et al. (2010). Este estudio pretende ahondar más en la naturaleza del nitrógeno a través de su estudio con modelos generados por el Dr. Worthey y el Sr. Serven. Al realizar un estudio más profundo del índice NH3360 con los modelos vimos que este índice está contaminado por magnesio, de modo que procedimos a redefinir el índice en NH3375 donde el magnesio dejaba de intervenir. También definimos un nuevo índice de magnesio que comprendía la contaminación mencionada anteriormente, Mg3334. Y aprovechando los datos que yo misma observé para mi trabajo del NH3360, hicimos un estudio de estos dos índices nuevos en función de las metalicidad de las galaxias, utilizando para ello el índice Fe4383.

5.1 Introduction

As discussed in Section 2, there are two main formation scenarios to explain the star formation history of elliptical galaxies observed in the local Universe: the *monolithic collapse* and the *hierarchical merging*. The natural outcome of the hierarchical merging scenario is that the regions with the highest density of dark matter collapse earlier and merge more rapidly (e.g., Kauffmann & Charlot 1998; De Lucia et al. 2006). If star formation follows this merging scenario galaxies in high density environments have older underlying stellar populations. On the contrary, the monolithic collapse do not predict any distinction as a function of the environment.

Our strategy to analyse the star formation history of galaxies located in different regions of the local Universe is to study the chemical species present in their stars. This is justified by the fact that chemical elements are ejected into the interstellar medium on different time scales as a consequence of being generated in different evolutionary processes. Whereas magnesium (Mg) is mainly produced in type II supernovae (Faber et al. 1992; Worthey et al. 1992; Matteucci 1994, the last stage in the evolution of the most massive stars, $M > 8M_{\odot}$), iron (Fe) is mainly released by type Ia supernovae (Nomoto et al. 1984; Woosley & Weaver 1995; Thielemann et al. 1996, the last stage in the evolution of intermediate-mass stars in some binary systems). On the other hand, carbon (C) and nitrogen (N) are mainly produced in low and intermediate mass stars (Renzini & Voli 1981; Chiappini et al. 2003), although there are suggestions that C can also be produced in massive stars (e.g., Carigi et al. 2005). The pioneer studies on this topic which began in the 1970s, have shown that abundance ratios in early-type galaxies are ofter non-solar (O'Connell 1976; Peterson 1976). Later on, it was found that $[\mathrm{Mg/Fe}]$ was overabundant in massive elliptical galaxies with respect to the solar ratio, whereas the low-luminosity early-type galaxies were consistent with the solar neighbourhood (e.g., Peletier & Valentijn 1989; Gorgas et al. 1990; Worthey et al. 1992; Vazdekis et al. 1997). These evidences prove that galaxies of different mass underwent a different star formation history (Greggio & Renzini 1983; Matteucci & Greggio 1986; Gibson et al. 1997; Thomas et al. 1998), with low-luminosity galaxies being characterised by an extended star formation history necessary to release the elements produced by low mass stars into the interstellar medium and the consequent incorporation of those elements in the next generation of stars, while massive galaxies experienced such a rapid star formation that only the elements generated in massive stars had the time to be incorporated (Worthey 1998). Several authors (Worthey 1998; Vazdekis et al. 2001) also noted a strengthening in other absorption-line indices, in particular C4668 and CN_2, suggesting also an enhancement of C and N relative to Fe when compared with the solar values.

This last evidence has made C and N an alternative to the studies based on Mg and Fe to characterise the star formation history of early-type galaxies (e.g., Worthey 1998; Burstein 2003; Sánchez-Blázquez et al. 2003; Kelson et al. 2006; Sánchez-Blázquez et al. 2006b; Schiavon 2007; Graves & Schiavon 2008). These two elements appear in the spectrum of a galaxy almost exclusively in molecular species, such as NH, CN, C_2, CH and CO, making the study of a single element at a time a very difficult task. In the work presented in this Chapter we try to disentangle the contribution of these two elements (C and N) using, for a sample of 35 early-type galaxies, the following near-ultraviolet (NUV) and optical indices: NH3360, defined by Davidge & Clark (1994) and principally dependent on N (Bessell & Norris 1982; Tomkin & Lambert 1984), and CNO3882, CNO4175 and CO4685, three new optical indices defined by Serven et al. (2005), where the contribution of C, N and O varies as indicated in Table 5.1.

In order to study the star formation history of galaxies in different environments we select

Index	NH3360	NH3375	Mg3334	CNO3862	CNO4175	CO4685	Mgb
elements	N, (-Mg)	N, (-Ti)	Mg, (-O)	N, (C, -O)	C, N, -O	C, (-O)	Mg, (-Fe)

Table 5.1: Dependence of each index on the abundances of different elements (Serven et al. 2005, 2010). The elements appear in importance order. Brackets mean much lower contribution and negative symbol means that an increase in the abundance of that element makes the index weaker. NH3360 was defined in Davidge & Clark (1994), NH3375 and Mg3335 in Serven et al. (2010), CNO3862, CNO4175 and CO4685 in Serven et al. (2005) and Mgb in Burstein et al. (1984).

classical elliptical galaxies in Coma, Virgo and the field as examples of Es located in high and low density regions. The methodology we follow to approach the problem consists of two different techniques. In the first place we make a direct comparison of the indices under analysis with stellar population synthesis models with typical ages of massive early-type galaxies, and solar and supersolar metallicities. The goal of this procedure is to check the contribution of each element to the absorption feature within the C and N indices, as well as to analyse any sign of a different star formation history for galaxies inhabiting high and low density environments. The technical procedure conducted to achieve this goal is based on the stacking of all the spectra of the galaxies in two different groups defined according to their environment. This technique provides a high S/N spectrum representative of a high and low density region respectively, that we compare with the SSP models. The second technique used in this study is the analysis of the indices as a function of the velocity dispersion of the galaxies. These index-σ diagrams give additional information about the dependence of the abundances of these elements with the mass of the galaxies (see Section 3.2.2.3), and conducted with the previously mentioned analysis is a powerful tool for understanding the role of mass and environment on galaxy evolution.

The missing piece of this study is the lack of specific models that investigate the effect of N, and any other chemical species, in the NH3360 index in the same way as it has been done in Serven et al. (2005) for all the optical indices. For this reason, we developed a new set of models that covers the near-ultraviolet of NH3360 in order to make a further investigation of N abundances in early-type galaxies (Serven et al. 2010). The analysis of these models suggests the definition of two new near-ultraviolet indices, Mg3334 and NH3375. The inferred influence of the different elements to these indices is presented in Table 5.1. With the aim of trying to understand the N abundances observed in elliptical galaxies we present in Section 5.3 the analysis of the three near-ultraviolet indices, NH3360, NH3375 and Mg3334, in addition to some other optical indices, in the same sample of galaxies as the one presented in Section 5.2.

We end this Chapter (Section 5.4) presenting final remarks of all the results found, emphasizing those aspects that are new in this thesis with respect to previous works in the same topic.

Appendix A includes a table presenting the sample of galaxies used in this Chapter, a summary of the reduction procedure followed, and some extra tables that contain the indices measured in Toloba et al. (2009b) and Serven et al. (2010) as well as the rest of Lick/IDS indices and those defined by Serven et al. (2005).

I would like to emphasize that the study developed in this Chapter for massive early-type galaxies is a pilot analysis that can be applied to dwarf galaxies. Due to the difficulty of observing such a blue wavelength, as it is 3300Å, using a optical spectrograph as ISIS, we decided to test this technique in massive galaxies and assure that it is possible to be conducted at the WHT. In our run at La Palma, apart from the sample of 35 massive ellipticals analysed in this Chapter, we

observed one of the dwarf galaxies that will be presented in Chapter 6, and we proved that the William Herschel Telescope is capable of gathering enough S/N to extend this same study to low luminosity early-types.

5.2 Toloba et al. (2009) ApJ, 691 L95

Carbon and Nitrogen Abundances in Early-type Galaxies

E. Toloba[a], P. Sánchez-Blázquez[b], J. Gorgas[a], B. K. Gibson[b]

[a]Universidad Complutense de Madrid, 28040, Madrid, Spain
[b]Centre for Astrophysics, University of Central Lancashire, Preston, PR1 2HE, UK

Abstract—For the first time, we undertake a systematic examination of the nitrogen abundances for a sample of 35 early-type galaxies spanning a range of masses and local environment. The nitrogen-sensitive molecular feature at 3360Å has been employed in conjunction with a suite of atomic- and molecular-sensitive indices to provide unique and definitive constraints on the chemical content of these systems. By employing NH3360, we are now able to break the carbon, nitrogen, and oxygen degeneracies inherent to the use of the CN-index. We demonstrate that the NH3360 feature shows little dependency upon the velocity dispersion (our proxy for mass) of the galaxies, contrary to what is seen for carbon- and magnesium-sensitive indices. At face value, these results are at odds with conclusions drawn previously using indices sensitive to both carbon and nitrogen, such as cyanogen (CN). With the aid of stellar population models, we find that the N/Fe ratios in these galaxies are consistent with being mildly-enhanced with respect to the solar ratio. We also explore the dependence of these findings upon environment, by analyzing the co-added spectra of galaxies in the field and the Coma cluster. We confirm the previously found differences in carbon abundances between galaxies in low- and high-density environments, while showing that these differences do not seem to exist for nitrogen. We discuss the implications of these findings for the derivation of the star formation histories in early-type galaxies, and for the origin of carbon and nitrogen, themselves.

5.2.1 Introduction

Uncovering the star formation histories of early-type galaxies has proved to be a challenging endeavor for several decades now. Perhaps the most common approach to date has been via the comparison of Lick/IDS spectral indices, each with varying degrees of sensitivity to age and metallicity (Worthey 1994). Alas, the lack of indices which are *purely* sensitive to age and/or metallicity has limited the uniqueness of the claimed results. Despite a rich literature, there remains fundamental disagreement on the magnitude and even veracity of important trends, including those linking age, metallicity, and relative elemental abundances, with mass and environment. A further limitation to this technique is its sensitivity to the youngest stellar component in a given galaxy, as opposed to the more representative underlying population.

An alternative approach, and one employed successfully for our own Galaxy, is to use our knowledge of galactic chemical evolution to inform our derivation of star formation histories. In massive early-type galaxies O'Connell (1976) first noticed that Mg abundance was enhanced relative to Fe; Other works confirmed this by comparing absorption line indices with isochrone-based stellar population models. Because Mg is predominantly produced in Type II supernovae

while Fe production is dominated by Type Ia supernovae, this enhancement is often interpreted as the result of very short timescales for the formation of stars in these galaxies. Apart from Mg, other elements (eg. C, N, Na) have been claimed to be enhanced in large ellipticals (Worthey 1998; Burstein 2003; Kelson et al. 2006, Sánchez-Blázquez et al. 2003, 2006a (SB03 and SB06a hereafter); Schiavon 2007; Graves et al. 2008) and to be strongly correlated with their velocity dispersions (although see Kelson et al. 2006; Clemens et al. 2006) for an alternate perspective regarding Mg and C).

Claims have been made for a strong N/Fe correlation with mass (SB06a, Kelson et al. 2006; Schiavon 2007; Graves & Schiavon 2008). Nitrogen is produced during hydrogen burning via the CNO and CN cycles, and it is created as both, primary and secondary element. In primary nucleosynthesis N is produced at the same time as C and O and it is independent of metallicity while in secondary production nitrogen is synthesized from the carbon and oxygen already present in the star, and its abundance is therefore proportional to the heavy elements abundance. The correlation of N/Fe with mass have been interpreted as a correlation between N/Fe and metallicity (through the mass-metallicity relation) and has lead the authors above to conclude that most of the N produced in ellipticals is of secondary origin. To derive nitrogen abundances, the CN-band at 4175Å has typically been used; however, disentangling the effects of C, N, and O using the CN-band is difficult (Burstein 2003). Direct observation of the NH feature at 3360Å offers a more direct, and robust estimator as the NH-feature is insensitive to C and O (Sneden 1973; Norris et al. 2002) and it is directly measuring N abundances (Bessell & Norris 1982; Tomkin & Lambert 1984). In addition, the near-UV light is produced primarily by dwarf stars (Davidge & Clark 1994, , DC94), while the optical cyanogen indices result from a more complex mix of both dwarf and giant star light. This avoid the variation in the stellar atmospheric abundances due to mixing during the first dredge-up.

There are fewer than 15 early-type galaxies with published values of NH3360 in the literature (Ponder et al. 1998; Boulade et al. 1988; Davidge & Clark 1994), due in large part to the relative insensitivity of detectors in the near-UV. We present here observations of the NH feature in a sample of 35 early-type galaxies in the field, Virgo, and Coma clusters. We show that previous claims of correlations between nitrogen and velocity dispersion are incorrect and that the NH3360 index-σ relation is almost flat.

5.2.2 Observations and Data Reduction

Long slit spectroscopic data for 35 ellipticals were obtained at the 4.2m William Herschel Telescope at Roque de los Muchachos Observatory, using the ISIS spectrograph. The instrumental configuration provided and spectral coverage from 3140 to 4040Å in the blue arm with an spectral resolution of 2.3Å (FWHM) and a typical sigmal to noise per Å of 40. Our sample is a subset of those presented in SB06a, allowing us to supplement our near-UV data with the associated optical indices ($3500-5250$Å). We measure the NH3360 index in our new data, and the Serven, Worthey & Briley (2005, SWB05 hereafter) optical indices in our SB06a optical spectra.

In SB03, we claimed that galaxies in the Coma cluster had much lower CN and C4668 indices than those in lower-density environments. We were unable then to conclude whether the differences were due exclusively to differences in carbon or if nitrogen was also overabundant in galaxies in lower-density environments. With the aim of resolving this issue, we selected our sample to include field, Virgo and Coma ellipticals, spanning a range in velocity dispersions

Table 5.2: Index definitions

Name	Blue passband (Å)	Index passband (Å)	Red passband (Å)	Reference
NH3360	3320-3350	3350-3400	3415-3435	DC94
CNO3862	3768.1-3812.3	3840.3-3883.4	3896.4-3916.2	SWB05
CNO4175	4082.5-4123.3	4129.4-4219.8	4243.3-4284.2	SWB05
CO4685	4557.3-4589.5	4626.4-4743.3	4805.1-4835.3	SWB05
Mgb	5142.6-5161.4	5160.1-5192.6	5191.4-5206.4	Lick

(130$<\sigma<$330 km s^{-1}). Following the nomenclature of SB03, we denote our Coma cluster sample as High-Density Environment Galaxies (HDEG), while galaxies in the field and Virgo are denoted Low-Density Environment Galaxies (LDEG).

We have followed the standard reduction procedure for long-slit spectra, using REDUCE (Cardiel 1999). Galaxy spectra were extracted within a central equivalent aperture of 4″ at the distance of NGC 6703 (corresponding to a physical aperture of 0.76 kpc). We measured the NH3360 index using the definition of Davidge & Clark (1994) (see 5.2)[1] and the CNO3862, CNO4175, and CO4685 indices, as defined by SWB05. All indices were measured at a dispersion of σ=200 km s^{-1} and corrected for the effects of velocity dispersion broadening using a combination of synthetic spectra from Bruzual & Charlot (2003, BC03 hereafter) and Vazdekis et al. (2008, V08 hereafter).

5.2.3 Results

Figure 5.1 shows the co-added spectra in different wavelength regions of LDEG (blue) and HDEG (red), with velocity dispersions in the range 150$<\sigma<$250 km s^{-1}. Before being added, the spectra were shifted to the same radial velocity and broadened to the maximum σ of all spectra (250 km s^{-1}). The spectral regions correspond to the bands of four different indices: NH3360, CNO3862, CNO4175, and CO4685.

Overplotted in these diagrams are the models by BC03 for the NH3360 and the models of V08 for the remainder of the indices. We could not use V08 for the comparison of the NH index because the spectra start at 3500 Å. However, we prefer to use it for the other regions of the spectra as the stellar library used in the BC03 models suffers from wavelength calibration problems. Nevertheless, we have checked and ensured that the results obtained are independent of the models employed. All synthetic spectra were degraded to the same broadened resolution as the galactic spectra. We have plotted four models in each figure, with ages $\sim$6 and 15 Gyr, and metallicities solar and supersolar ([M/H]=+0.4 for BC03 and [M/H]=+0.2 for V08).

Comparing the empirical spectra with the models in Fig. 5.1 and taking into account the element dependence of the indices (see inset of the figure) we can see: NH3360 is slightly overabundant with respect to the scaled-solar models; CNO3862 is compatible with the scaled-solar models at lower metallicities (for older ages) or higher metallicities (for younger ages); CNO4175 and CO4682 are overabundant in the field galaxies, but not for the cluster galaxies. In consort,

[1] A case could be made to amend the Davidge & Clark (1994) definition somewhat, in light of Carbon et al. (1992; Fig 13). Specifically, the NH3360 continua sit within the broad wings of the NH feature itself, reducing its optimal sensitivity to nitrogen. Redefining the red continuum to be 3480$-$3520Å would mitigate this effect to some degree, but for consistency with the canonical definition, we have not pursued this approach.

these data require nitrogen-based indices be overabundant with respect to solar, carbon-based indices be overabundant with respect to solar only for LDEG, and oxygen be similarly overabundant.

5.2.3.1 The index-velocity dispersion relations

In Fig. 5.1 we present the behavior of the four indices analyzed, in addition to Mgb, as a function of the velocity dispersion of the galaxies. We distinguish between three different groups of plots, depending on the chemical element dominating the intensity of the index: N-based indices (CO3862 and NH3360), C-based indices (CNO4175 and CO4685), and Mgb. Indices dependent on C show a strong dependency upon velocity dispersion, in a similar way to Mgb. However, the trends between the N-sensitive indices and velocity dispersion are much flatter; indeed, they are even flatter than that found for <Fe> (see SB03).

Differences in the slope of the index-σ diagram could appear due to a different sensitivity of the indices to age and/or metallicity and do not necessarily reflect differences in the chemical abundance ratios. Figure 5.2 shows the variation of the indices with age for different metallicities. It can be seen that each of the SWB05 indices show a strong dependence on metallicity, particularly CO4685. The Lick/IDS index Mgb also shows a strong metallicity dependence. On the other hand, for metallicities relevant for elliptical galaxies ($Z > 0.004$), NH3360 is essentially constant with age and overall metallicity. This behavior allows NH3360 to be used successfully to derive nitrogen abundances in integrated spectra, with Boulade et al. (1988) confirming its strong sensitivity to nitrogen abundance .

Can we explain the relations between the other indices and σ as the consequence only of a relation between the overall metallicity and/or age with σ? To answer this question we have parametrized the models of BC03 and V08 as a function of age and metallicity, in the age and metallicity restricted to the range covered by our sample, $\sim$4-$\sim$17 Gyrs and -0.70<[M/H]<0.40. If we allow for the same age variation with σ (from 5-12 Gyr in the σ range 125-350 kms^{-1}) for all the indices, we need $\sim$0.13 dex more metallicity variation to explain the CNO4175- and CO4685-σ relations – the most C-sensitive indices – while and extra $\sim$ 0.3 dex variation in metallicity is needed to explain the relation of the Mgb-σ slope. At a face value, this would be indicating that [C/M], [Mg/M] and [Mg/C] increase with σ. The conclusions, however, remain very speculative until the oxygen abundance and its variation with σ is calculated in these galaxies. In addition, the indices strongly dependent on C show a systematic offset between LDEG and HDEG, with the indices for HDEG systematically weaker than those for LDEG. [2]

5.2.4 Discussion

We present here the NH3360 indices for a sample of 35 early-type galaxies. Unlike the ambiguities which exist when inferring nitrogen abundances from cyanogen indices in the optical (due to contamination from carbon and oxygen in the bands and associated continua), the near-UV molecular feature of NH isolates the nitrogen abundance. The main conclusions of this work are: (1) a flat relation exists between the NH3360 index and the velocity dispersion of the galaxies, contrary to what has been previously claimed by other authors from their analysis of the more ambiguous CN-

[2]This behavior is also visible in the near-IR C-sensitive indices (Mármol-Queraltó, in preparation).

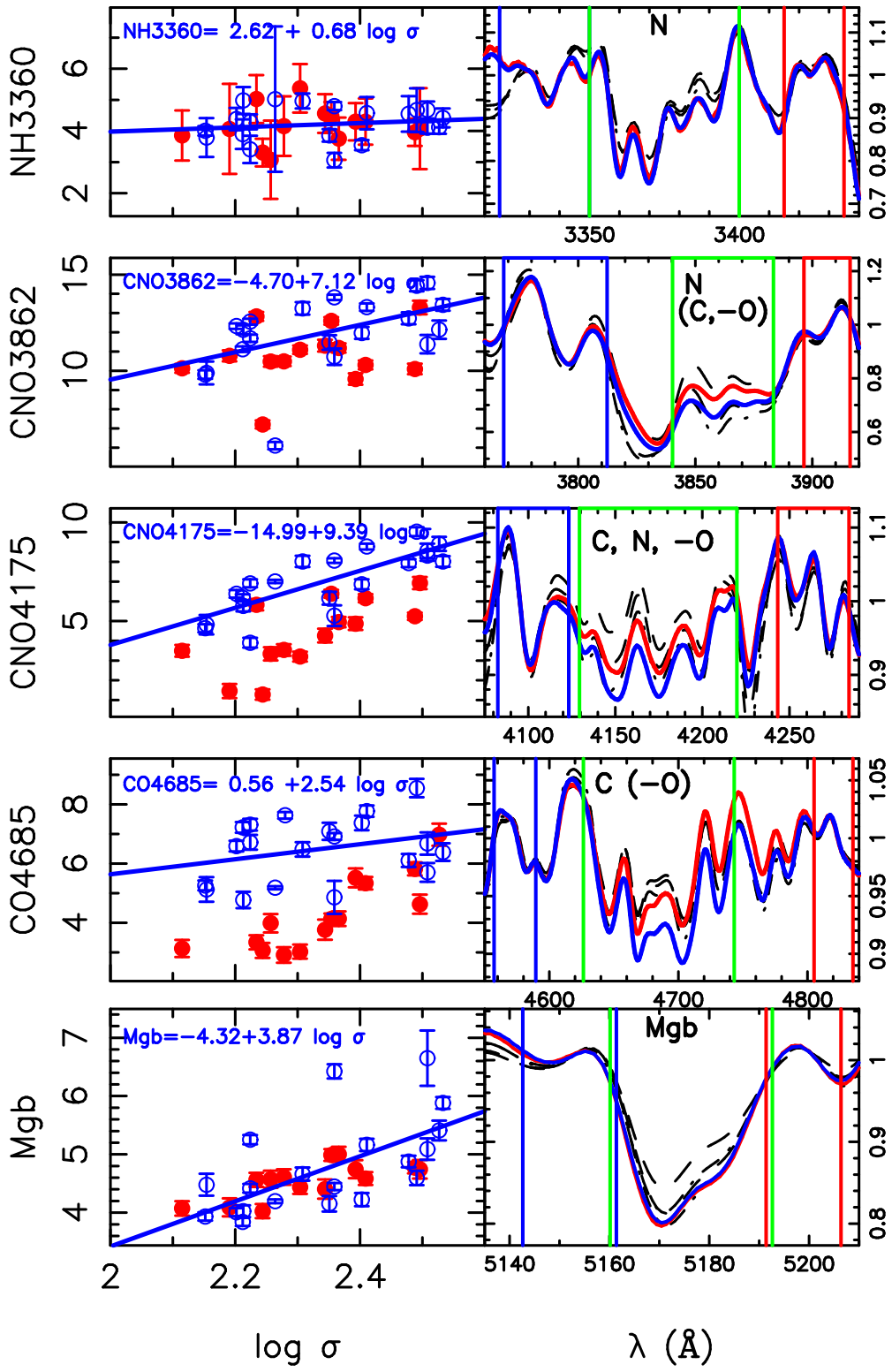

Figure 5.1: Left column: Line-strength indices versus velocity dispersion. Red solid circles correspond to HDEG, while blue open circles are LDEG. Right column: Blue, green, and red boxes represent the bandpass of the index definition: In blue and red are the two-bands used to define the pseudocontinua. The flux in both, the data and the models have been normalized to these bands. The central band where the feature is located is indicated in green. Black lines represent stellar population models. Only models with solar (dashed lines) and supersolar (dotted lines) metallicity are plotted; 6 and 15 Gyr models are plotted for each metallicity. The stacked spectra for LDEG are plotted in blue, while the HDEG are represented in red. Dominant species and other important species (within brackets) contributing to the indices defined by SWB05 are shown in the inset of the panels. A - symbol indicates that an increase in the abundance of that element makes the index weaker.

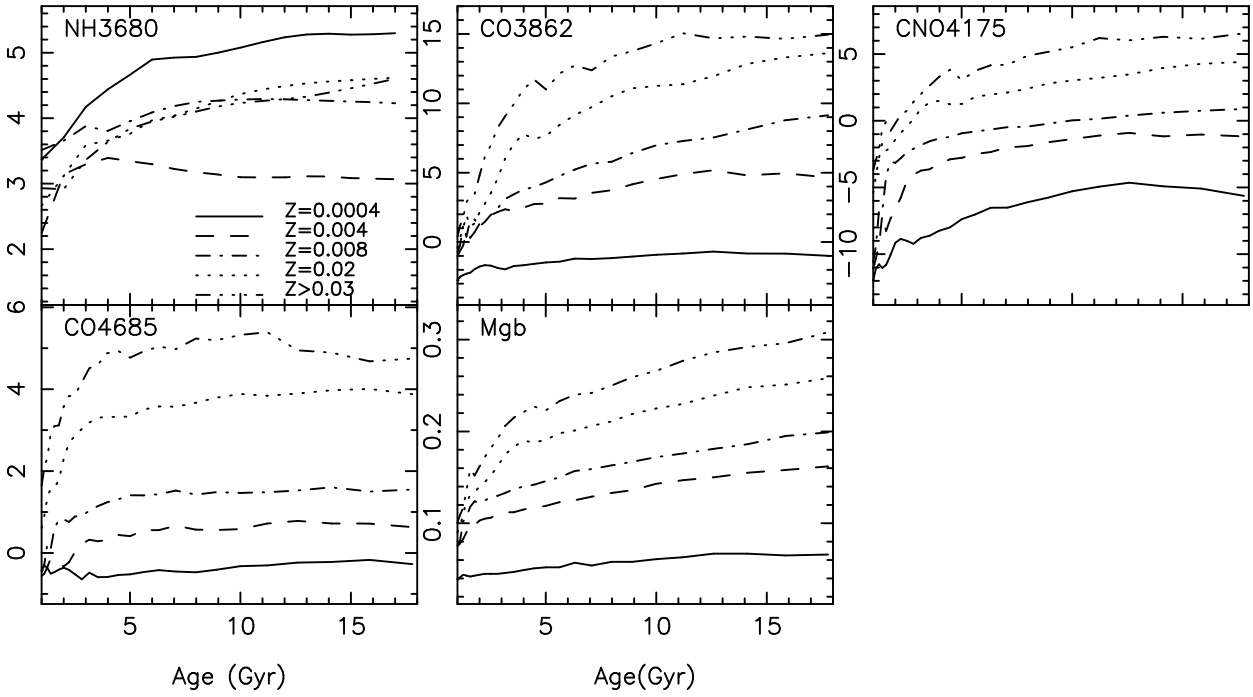

Figure 5.2: Variations of the analyzed indices with age at different metallicities as indicated in the inset. BC03 models are used for the NH3360 while V08 models are employed for the remainder of the plots.

index; (2) N is independent of local environment, whereas C appears stronger for LDEG relative to HDEG. In this sense, carbon and nitrogen production appear to be essentially decoupled from one another.

Our results can be useful for constraining the origin of C and N. Nitrogen is produced in both intermediate-mass and massive stars, and it can have a primary and secondary origin (Carigi et al. 2005; Chiappini et al. 2006). The abundance ratio of a secondary element is predicted to increase with metallicity. If elliptical galaxies show a mass-metallicity relation, as it has been claimed by many authors (eg., Kodama & Arimoto 1998), then we should expect the secondary N to increase with the mass of the galaxies, as suggested in previous works based upon cyanogen-inferred nitrogen abundance determinations (eg., Kelson et al. 2006; Schiavon 2007). However, we have shown here that when a more "pure" nitrogen-sensitive indicator is used, there is no relation between the nitrogen abundance and the mass of the galaxies. This lack of correlation may be indicating primary production of nitrogen.

Nucleosynthesis studies predict that primary N can be produced both in the third dredge-up along the Asymptotic Giant Branch (AGB) phase, if nuclear burning at the base of the convective envelope is efficient (Renzini & Voli 1981, hot-bottom burning), and recent yields, including rotationally-induced mixing, also predict significant production of N in massive stars (Meynet & Maeder 2002). Chiappini et al. (2003, 2006) has shown that the inclusion of these yields in a Galactic chemical evolution model of the Milky Way predicts an N/O gradient consistent with observations. Having said that, this primary nitrogen production pathway is apparently only significant at low metallicities and is not predicted to be particularly relevant for systems such as elliptical galaxies that can reach supersolar metallicities very rapidly. In a system more similar to elliptical galaxies – that of the bulge of our galaxy – Ballero et al. (2007) (see also Matteucci 1986) need to include primary N from massive stars of *all* metallicities (and all masses), in order

too explain the data from planetary nebulae.

In elliptical galaxies, the offsets between LDEG and HDEG favor massive stars as the main contributors to primary nitrogen, because for the elements produced by intermediate mass stars, no offsets are detected. However, if that is the case, then we would expect a similar correlation between N and σ, as seen for Mg and σ. As we have shown though, the N–σ correlation appears flat from our new data and analysis. A possible solution is that the contribution from *both* massive and intermediate mass stars is shaping the N–σ relation in ellipticals. The delay in the N release from intermediate mass ($4<$M <8 M$_{\odot}$) stars is $\sim$100 Myr, so even in a relatively short star formation burst, some contribution from these stars is expected. It is believed that the star formation in ellipticals is both more efficient and of a shorter timescale with increasing galactic mass. If this is the case, N would be produced increasingly more prominently by massive stars in the most massive galaxies, while the less-massive galaxies with their more protracted star formation history would have an additional contribution from intermediate mass stars. As mentioned, the delay in the release of N from intermediate mass stars is $\sim$100 Myrs (the lifetime of $5-6$ M$_{\odot}$ solar metallicity stars); intermediate mass stars do not release significant amounts of Mg at high metallicities [3], which would explain the different behavior of the Mg$-\sigma$ relation compared with the N-σ relation.

Carbon is another controversial element. While some authors argue that it is mainly produced in intermediate mass stars (Chiappini et al. 2003) (with masses between $1-4$ M$_{\odot}$) others suggest that massive stars are the main contributors (eg., Carigi et al. 2005). The offset between galaxies in different environments that is not seen in other elements produced mainly in massive stars, such as Mg, favors the suggestion that C is produced mainly in lower mass stars. However, if low- and intermediate-mass stars *are* the main producers of C, it is difficult to explain the strong correlation between C and σ and the overabundance of C/Fe with respect to the Sun. One possibility is that C is produced in both, massive and lower mass stars in comparable proportions. The significant slope in the relation would be the consequence of C production in massive stars while the offset would come from a different production in lower mass stars. This latter C release would increase the C budget in LDEG while in the HDEG, star formation ceases before this can happen.

Of course these are very simplified scenarios. The relative importance of the different N-sites and the origin of C in elliptical galaxies will be explored in a future paper using our `GEtool` chemical evolution code (eg., Hughes et al. 2008).

In summary, we report the first determination of "pure" nitrogen abundances for a sample of early-type galaxies and compare these with stellar population models. Contrary to what has been claimed previously, the nitrogen abundances do not vary with the velocity dispersion of the galaxies. The environmental differences found for C and N abundances impose an important constraint on chemical evolution and galaxy formation models. It will be critical to independently constrain the oxygen abundance and its dependence upon galaxy mass, in part because of the obvious synergies between CNO in low- and intermediate-mass stars, and in part because oxygen is simply the most dominant component ($\sim$50%) of global metallicity.

We thank Francesca Matteucci and Reynier Peletier for several very useful discussions. The expert guidance of the referee, Judy Cohen, is gratefully acknowledged. This work has been partially supported by the Spanish research project AYA2007-67752-C03-03, the Marie Curie Intra-European Fellowship scheme within the 6th European Community Framework Programme (PSB),

[3] note that significant contribution from AGB stars to the heavy isotopes ^{25}Mg and ^{26}Mg is predicted at metallicities lower than [Fe/H]< -0.5 (Fenner et al. 2003)

UK's Science & Technology Facilities Council (BKG). E.T. acknowledges the support of the University of Central Lancashire's Livesey Award scheme (PSB).

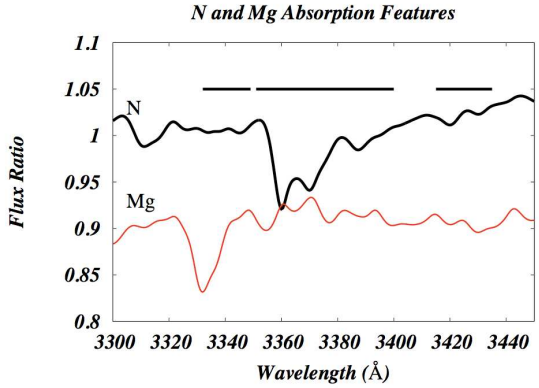

Figure 5.3: NH3360 bandpasses are shown with horizontal lines. Black and red lines present, respectively, the relative spectral responses due to 0.3 dex increase in N and Mg in the same spectral region. Here it is seen that the Mg absorption line is partially introduced in the definition of the blue passband of NH3360.

5.3 NH and Mg trends in elliptical galaxies (Serven, Worthey, Toloba, Sánchez-Blázquez, 2011, in press)

The previous analysis has shown that early-type galaxies located in different environments do not present any difference in purely N-based indices, in contrast to C-based indices. It has also shown that NH3360 is nearly independent of the velocity dispersion of the galaxies. These results constrain the formation time scales for these two elements, imposing that N must be formed on time scales longer than C. These findings are, however, contrary to previous works based on the analysis of CN-indices, where C and N contributions are mixed up (e.g., Sánchez-Blázquez et al. 2006b; Kelson et al. 2006; Schiavon 2007; Graves & Schiavon 2008). In an attempt to explain the differences observed in the time scale production of N determined through the analysis of the near-ultraviolet (NUV), using NH3360, or the optical, using CN-bands, in a work in collaboration with Dr. G. Worthey and his PhD student J. Serven we developed a new set of simple stellar population models specially tailored to vary individual abundances of elements and analyse their effects on the absorption features present in the spectrum of early-type galaxies.

Specifically, the PhD student Jedidiah Serven developed the models that we describe below this paragraph. The data presented on this publication is the same spectra of the 35 massive elliptical published in Toloba et al. (2009b). In this regard, the observation and reduction of these galaxies was conducted by myself as well as the measurement of the indices needed for the analysis described below.

The new set of models presented in Serven et al. (2010) is a new version of those of Worthey (1994) and Trager et al. (1998) with the improvement of using a grid of synthetic spectra in the optical (Lee et al. 2009). These models allow us to vary independently the age, overall metallicity Z, and 23 individual elemental abundances to synthesise single-burst stellar population spectra. The method for determining the response of the indices to the different element abundances is the same as the one presented in Serven et al. (2005) with the improvement that now, instead of using a G dwarf star and a K giant to simulate a typical spectrum of an elliptical galaxy, single stellar population models are employed, thus better to represent a galaxy. This method consists of taking one base model of solar metallicity and then 23 variations, each one with a particular abundance doubled. Then, the ratios of these spectra were taken to find any spectral influence due to any

Index	Blue Passband	Index Passband	Red Passband	Reference
NH3360	3332-3350	3350-3400	3415-3435	Davidge & Clark (1994)
NH3375	3342-3352	3350-3400	3415-3355	Serven et al. (2010)
Mg3334	3310-3320	3328-3340	3342-3335	Serven et al. (2010)

Table 5.3: Definition of the near-ultraviolet indices. The passbands are measured in Å.

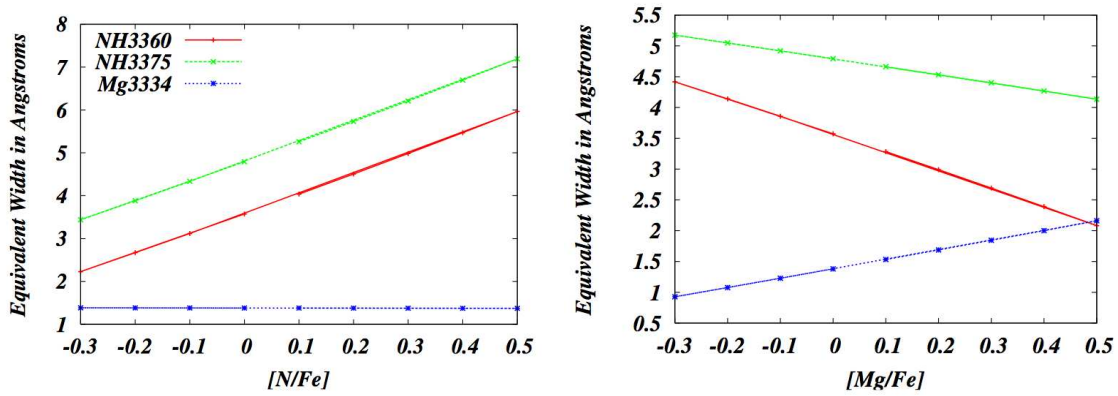

Figure 5.4: N and Mg abundances from Serven et al. (2010). This Figure illustrates the sensitivity of these indices to changes in N and Mg abundances at fixed metallicity $[Z/H] = [Fe/H] = 0.0$ and age ($8Gyr$), with $[Mg/Fe] = 0.0$ for the left panel and $[N/Fe] = 0.0$ for the right panel.

particular element.

We analysed the contribution of the 23 individual elements to the index NH3360 and we found that it is contaminated by Mg. Due to the fact that the Mg feature is located only in the blue continuum of NH3360 (see Figure 5.3), it was possible to isolate this contamination in the definition of the new index Mg3334, and redefine the NH index avoiding the Mg contribution in NH3375, thus this new NUV index is nearly only dependent on N (see Table 5.1 for the contribution of the different chemical species into these indices and Table 5.3 for their definition). Figure 5.4 shows the sensitivity of these three indices (NH3360, NH3375 and Mg3334) with N and Mg abundances.

Now that we had a new index, NH3375, that measures almost pure N abundances without any important contribution from other elements, we study its dependence on the velocity dispersion of the 35 galaxies from Toloba et al. (2009b). We found that this new index presents a slight dependence on σ in contrast to NH3360 (see Figure 5.5), which was expected because the Mg line is contaminating the blue passband of NH3360, thus galaxies with stronger Mg were more affected.

In order to dig more into the origin of that lack of trend, we analyse the behaviour of the indices used in Toloba et al. (2009b) in addition to the two new index definitions, Mg3334 and NH3375, as a function of metallicity, using Fe4383 as a metallicity ($[\mathrm{Fe/H}]$) indicator. The aim of these index-index diagrams is to disentangle the time scale of the formation of the elements in the same way as the Mgb-$<\mathrm{Fe}>$ diagram discussed in Section 3.2.2.1. If a strong correlation is found, the element analysed versus Fe is formed in a shorter time scale than Fe. In this regard, we found that both NH3360 and NH3375 show an anticorrelation with Fe4383, thus their behaviour as a function of the metallicity is similar, as expected because their contribution of N is equivalent.

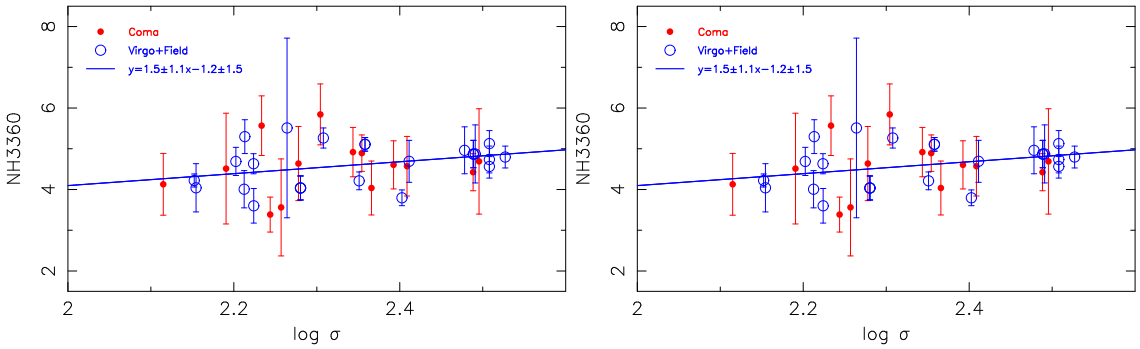

Figure 5.5: Index-σ relation for NH3360 as shown in Toloba et al. (2009b) and NH3375, the new index defined in Serven et al. (2010). Red solid circles are galaxies inhabiting a high density environment and blue open circles are galaxies in a low density environment. The fits shown have been done for the blue symbols.

On the contrary, CN1 is strongly correlated with Fe4383. In the case of magnesium, while Mgb is strongly correlated with Fe4383, Mg3334 present a lack of trend (see Figure 5.6). This seems to indicate that the Mg contribution measured in these two different regions of the spectrum comes from different stellar populations inhabiting the galaxies. With the aim of studying this possibility we analyse the effect of a metal-poor subpopulation coexisting with the typical underlying population of an elliptical galaxy, that present old ages ($\sim$12 Gyr) and solar metallicities ([Fe/H] $=$ 0.0). The subpopulation considered is old (12 Gyr) and metal-poor ([Fe/H] $= -1.5$) because it is photometrically bluer than an old population with solar [Fe/H], and it does not require the existence of emission lines, not seen in elliptical galaxies, as in the case of a young stellar population. We show in Figure 5.6 the effects of this subpopulation over the different indices when it represents the 10% of the total mass of the galaxy (blue line), the 5% of the total mass (green line) or when this metal-poor subpopulation does not exist (red line). Comparing these three colour lines with the fit to the data (black line) we find that the increase of the contribution of a metal-poor subpopulation to the total mass of the galaxy flattens the behaviour of Mg3334 as a function of Fe4383, which is more similar to what is observed in the target galaxies than considering alone an old and solar metallicity population. In the case of NH indices, the presence of a metal-poor subpopulation changes the slope NH-Fe4383 from positive to negative, which is what it is seen in the observed galaxies. However, there is a significant offset appreciable between the metal-poor subpopulation and the black line. In fact, this offset increases when increasing the amount of metal-poor stars in the galaxy. As a result, this metal-poor subpopulation can not completely explain the NH-Fe4383 anticorrelation, as we suspected because of the inherent complex nature of the NUV spectra (Burstein et al. 1988).

From this exercise we have learnt that the light in the NUV is probably highly affected by the existence of an old, metal-poor subpopulation. To quantify the contribution that this population has in the NUV may be helpful to compare abundances of different chemical species in the visible and NUV. This could be done by calibrating the old and metal-poor subpopulation until the Mg3334 abundance agrees with that of Mgb. Then we could apply this calibration to NH3375 and derive the N abundances that, in comparison to the N measured from carbon and nitrogen indices in other wavelength regions, should provide the same N enhancement in elliptical galaxies.

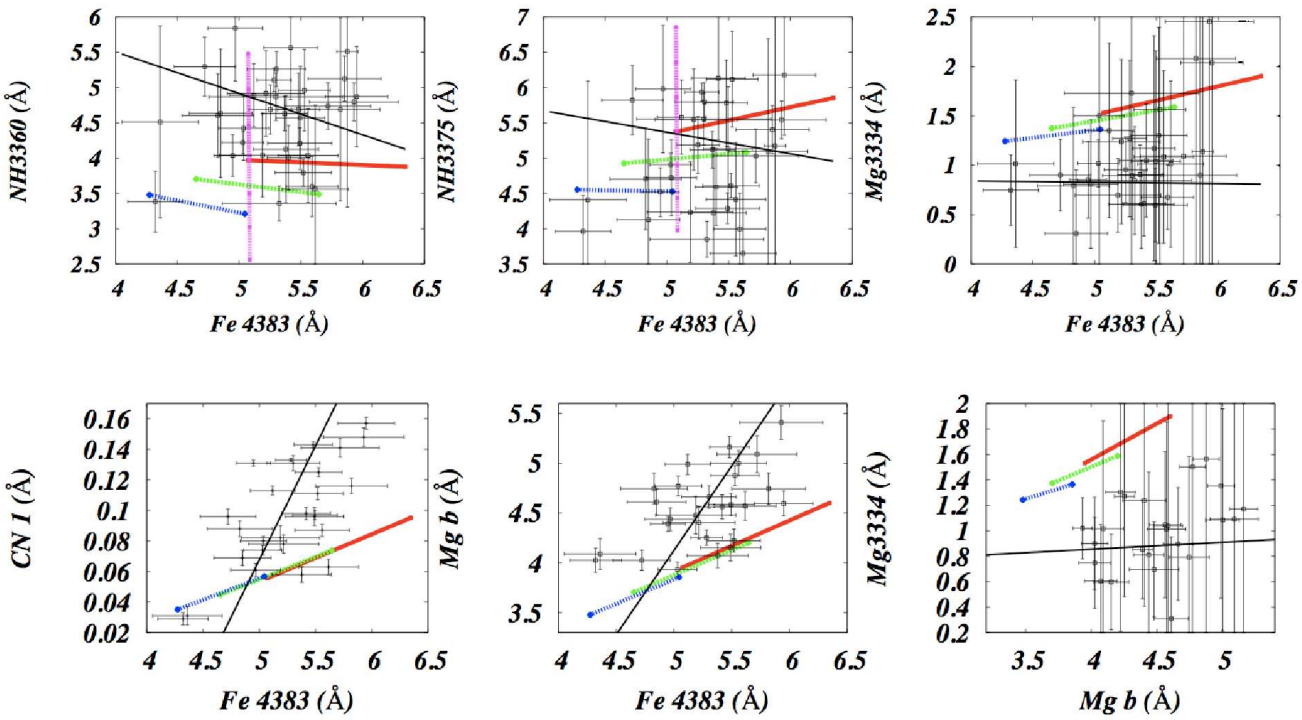

Figure 5.6: Index-metallicity relations from Serven et al. (2010). Black points are the early-type galaxies from Toloba et al. (2009b). The black line represents the best fit for the galaxies. The red line represents a galaxy model of 12 Gyr and metallicity varying from solar metallicity to [Fe/H] = 0.25. The green line is the same model of 12 Gyr and solar metallicity with 5% of the galaxy mass consisting of a 12 Gyr metal-poor ([Fe/H] = −1.5) subpopulation. The blue line is the same model except that the subpopulation is now 10 % of the total mass. The pink line represents the galaxy model of 12 Gyr and solar metallicity where the N abundance varies, that is why these pink lines appear parallel to the Y-axis. In addition, the relation Mg3334-Mgb is plotted with the same code of colours and symbols to visualize that these two indices do not follow the line X = Y.

5.4 Conclusions

This Chapter has been devoted to the study of the star formation history of massive early-type galaxies located in different environments. This work has been done by using the C and N abundances determined from different spectral indices as proxies of the time scale of the stellar evolution. This has been accomplished through the analysis of the indices in a sample of 35 early-type galaxies located in Coma, Virgo and in the field. Our analysis has been focused on some new optical indices defined in Serven et al. (2005) that provide a clean measurement of the C abundance. We confirm that this chemical element depends on the mass of the galaxies and the environment they inhabit, as previously claimed by other authors (e.g., Sánchez-Blázquez et al. 2006b; Schiavon 2007).

From the innovative analysis of the index NH3360 defined in the NUV we have learned that N abundances do not depend on the mass of the galaxies, and do not present any differences as a function of the environment. These results are in contrast to the strong correlation of CN indices with the velocity dispersion (σ) of the galaxies found by Sánchez-Blázquez et al. (e.g., 2006b); Schiavon (e.g., 2007); Graves & Schiavon (e.g., 2008). Note that in all of these previous works C and N abundances were completely mixed and could not be disentangled. To better understand

these results, we have quantified the effect produced by an old metal-poor subpopulation on the indices. Although a test using NUV and optical Mg indices indicates that this metal-poor subpopulation must be present in the galaxies, the same analysis performed for N do not provide such a clear conclusion. It seems that a population of 12 Gyr and $[Fe/H] = -1.5$ is contributing to the light observed in the NH index but it can not fully explain the observed anticorrelation with metallicity.

All the results obtained in this Chapter point out that C must be produced both in massive and low mass stars in comparable proportions in order to simultaneously explain the steep slope found with σ and the offset that appears for galaxies situated in high and low density environments. In regard to N, early-type galaxies in high and low density regions do not present any offset when an index based on pure N abundances, such as NH3360, is studied as a function of galaxy mass. Moreover, N abundances are independent of the mass of the galaxies. As a consequence, in order to understand simultaneously these two facts, N must be produced in massive and intermediate-mass stars. These new results establish that magnesium is the first element formed, being generated exclusively in type II supernovae, after the magnesium the next chemical specie formed is nitrogen, ejected by both massive and intermediate-mass stars, then it comes carbon, incorporated to the interstellar medium in the last stages of the evolution of massive and low-mass stars, and the last element in being released to the interstellar medium is iron, originated exclusively when low-mass stars explode in type Ia supernovae, a process with a time scale much longer than any of the previous ones.

6

Spectrophotometric study of dwarf early-type galaxies in the Virgo cluster

Resumen

En este Capítulo presento el estudio espectrofotométrico de una muestra de galaxias enanas de primeros tipos que yo misma he observado en espectroscopía de resolución intermedia y he analizado tanto en espectroscopía como en fotometría.

Bajo el modelo cosmológico ΛCDM las galaxias enanas son una pieza esencial en la formación y evolución de galaxias, ya que son los componentes primarios de los sistemas estelares más masivos (White & Rees 1978; White & Frenk 1991). Esto ha provocado que en los últimos años, coincidiendo también con las mejoras instrumentales que permiten observar esta población de objetos estelares de bajo brillo superficial, muchos esfuerzos se hayan concentrado en explorar la naturaleza de estos sistemas (Gorgas et al. 1997; Pedraz et al. 2002; Geha et al. 2002, 2003; Guzmán et al. 2003; van Zee et al. 2004b; Matković & Guzmán 2005; de Rijcke et al. 2005; Ferrarese et al. 2006; Michielsen et al. 2008; Koleva et al. 2009a; Chilingarian 2009).

Su apariencia similar a las elípticas gigantes (ver Ferguson & Binggeli 1994) ha hecho pensar que las enanas son la contrapartida a bajo brillo superficial de las gigantes. Sin embargo, los estudios más recientes han revelado que se trata de una población muy heterogénea (Lisker et al. 2006-2009) con indicios de tratarse de galaxias de los últimos tipos que se han transformado debido a su interacción con el entorno.

Con el objetivo de arrojar un poco de luz sobre el origen de las galaxias enanas de primeros tipos se inició la colaboración MAGPOP (Multi-wavelength Analysis of Galaxy POPulations), proyecto en el que se enmarca el trabajo realizado en este Capítulo.

Además de las observaciones espectroscópicas de resolución intermedia, simultáneamente, y dentro de este mismo proyecto, se observó la misma muestra de galaxias a baja resolución. El análisis de la muestra a baja resolución fue liderado por el Dr. Dolf Michielsen y tuve el placer de colaborar estrechamente con él en la elaboración del artículo al que dió lugar tal análisis.

En este artículo (Michielsen et al. 2008) hemos calculado las poblaciones estelares centrales de la muestra de galaxias y hemos analizado sus parámetros estructurales. Para el estudio de las edades y metalicidades se han utilizado los modelos de síntesis de poblaciones de Vazdekis et al. (2010) y el método de diagramas índice-índice descrito en la Sección 3.2.2. El estudio de las características estructurales se ha basado en el análisis de los denominados parámetros CAS (Conselice

et al. 2003), que miden la concentración, la asimetría y el "clumpiness" de las galaxias, siendo este último también un parámetro de asimetría.

El resto del Capítulo está dedicado a la espectroscopía de resolución intermedia y a su estudio junto con la fotometría en diferentes bandas. Con el objetivo de poder discernir el proceso de formación que han sufrido las galaxias elípticas enanas nos hemos centrado en el estudio cinemático de la muestra en buena parte de esta Sección. Utilizando la técnica de comparación del ensanchamiento de las líneas de absorción de las galaxias y de su desplazamiento por efecto Doppler con las mismas líneas en las estrellas observadas con este fín, hemos obtenido las curvas de rotación y de dispersión de velocidades para toda la muestra de galaxias.

Estas curvas cinemáticas han sido analizadas de differentes formas. En primer lugar hemos comparado su forma general con la de galaxias de los últimos tipos de luminosidades similares a las de nuestras enanas. También hemos analizado, ya que algunas de estas galaxias presentan una cierta rotación, cómo encaja ésta en la relación de Tully-Fisher típica de las galaxias espirales. Y como última parte del trabajo presentado en la Sección 6.2 hemos hecho un estudio del contenido de materia oscura en comparación con galaxias esferoidales del Grupo Local y galaxias elípticas masivas.

En la Sección 6.3, publicada en Toloba et al. (2009a), hemos desarrollado el análisis del comportamiento cinemático de estas galaxias. Tras medir las elipticidades de las galaxias en las imágenes fotométricas utilizando la técnica descrita en la Sección 6.2, hemos comparado el cociente entre la velocidad de rotación y la dispersión de velocidades (v/σ) con la elipticidad, y, utilizando el modelo de Binney (1978), hemos visto que parte de la muestra está soportada por rotación y el resto por los movimientos aleatorios de las estrellas. En la imágenes fotométricas obtenidas dentro de la colaboración MAGPOP, he medido el parámetro C_4 denominado *diskyness/boxymess*, que mide cómo de diferentes son las isofotas de las galaxias con respecto a una elipse perfecta. Este parámetro ha resultado ser coincidente con la subclasificación en galaxias de disco y no disco realizado por Lisker et al. (2006a) con una técnica completamente diferente. Encontrando que las galaxias clasificadas como de disco, efectivamente tienen las isofotas de tipo *disky* y las no disco son *boxy*. Para completar este análisis centrado en el soporte cinemático de esta muestra de galaxias enanas, hemos estudiado v/σ en función de la edad de las galaxias, sacadas del estudio a baja resolución de Michielsen et al. (2008), y de la distancia al centro del cúmulo de Virgo.

La Sección 6.4 está dedicada al estudio de las relaciones de escala que describimos en el Capítulo 3. Con el objetivo de estudiar si estas relaciones están governadas por las poblaciones estelares de las galaxias o por sus parámetros estructurales, las hemos analizado en una banda óptica (la banda B), altamente influenciada por la edad y metalicidad de las galaxias, y por primera vez para galaxias enanas, en una banda infraroja (la banda K), escogida por no estar influenciada por las estrellas jóvenes que puedan estar presentes en la galaxia. En este Capítulo, que actualmente está en desarrollo, estudiamos las propiedades dinámicas y estructurales de las galaxias en comparación con galaxias masivas de primeros tipos, e incluyendo, cuando ha sido posible, galaxias enanas esferoidales del Grupo Local.

6.1 Introduction

In the study of the formation and evolution of galaxies in the Universe, dwarf galaxies have been identified as a key piece in the puzzle. This is because under the ΛCDM scenario they thought to be the building blocks of more massive objects (e.g., White & Rees 1978; White & Frenk 1991). In addition, due to their resemblance to massive elliptical galaxies, e.g. elliptical appearance, red colours, absorption-line spectra (for a review see Ferguson & Binggeli 1994), they have been thought to be the low luminosity extension of massive early-types. However, this scenario is in contrast to new observational analyses that have probed that dEs are an heterogeneous class of objects with properties sometimes in between spiral and elliptical galaxies (Lisker et al. 2006-2009) suggesting that dEs could be dwarf late-type galaxies that have been transformed.

Many efforts have been made to unravel the origin of dwarf early-type galaxies (Gorgas et al. 1997; Pedraz et al. 2002; Geha et al. 2002, 2003; Guzmán et al. 2003; van Zee et al. 2004b; Matković & Guzmán 2005; de Rijcke et al. 2005; Ferrarese et al. 2006; Michielsen et al. 2008; Koleva et al. 2009a; Chilingarian 2009), but the question is still open. With the aim of solving this fundamental question in extragalactic astronomy, researchers from several European countries joined their wide expertise in the MAGPOP collaboration. MAGPOP (Multi-wavelength Analysis of Galaxy POPulations) was a Marie Curie Research Training Network funded under the Sixth Framework Programme of the European Union and leaded by Dr. Guinevere Kauffmann. This programme run from December 2004 to December 2008. During that time this collaboration was awarded with a two-year International Time Progamme (ITP) at La Palma telescopes. This ambitious observational proposal was led by Dr. Reynier F. Peletier with the co-PIs Dr. Alessandro Boselli and Dr. Javier Gorgas.

The overall objectives of the MAGPOP network were to use multi-wavelength data to study the star formation history of galaxies of different nature through the analysis of their stellar population and metal content, as well as the role of supermassive black holes in their evolution. These are the principal ingredients in any models of galaxy evolution. Within this network, the ITP focuses on the study of a sample of star-forming and quiescent dwarf galaxies selected to belong to high (the Virgo cluster) and low (the field) density regions.

The MAGPOP-ITP team decided to restrict this analysis to the local Universe, where dwarf galaxies can be spatially resolved, are well catalogued (Binggeli et al. 1985), and there are available data at different wavelengths, such as HST-ACS survey (Ferrarese et al. 2006), SDSS (Lisker et al. 2006a,b, 2007, 2008, 2009), ALFALFA survey in HI (Giovanelli et al. 2005), etc. For all these reasons, the ITP team chose the closest cluster, Virgo, as an example of high density environment, and some field dwarfs located within a distance no much further away than Virgo ($\sim$ 17 Mpc, Boselli & Gavazzi 2006) as galaxies in low density regions. All the dwarfs considered by the team are present within the GALEX MIS fields (Boselli et al. 2005) and in the Sloan Digital Sky Survey (SDSS, York et al. 2000).

The Virgo cluster sample was selected from the Virgo Cluster Catalog (VCC) of Binggeli et al. (1985). We identified 50 star-forming candidates with $m_B < 15.5$ and 43 quiescent dwarfs (classified as dE or dS0) with $m_B < 15$.

The field sample was selected querying SDSS for nearby (5−25 Mpc in distance) dwarf galaxies ($-18.5 < M_{r\prime} < 15$ mag, using a Hubble constant of $H_0 = 70$ km s^{-1} Mpc^{-1}). They were

required to have a declination in between -10^o and $+75^o$ to be observed in the Northern hemisphere. The total field sample consisted of 50 dwarf galaxies. A colour criterion in the ultraviolet (UV) using GALEX photometry (Martin et al. 2005) was applied to classify the candidates into star-forming and quiescent dwarfs. Those galaxies with a near ultraviolet colour of FUV$-$NUV < 0.9 were classified as star-forming and those with FUV$-$NUV > 0.9 as quiescent. For those galaxies without FUV magnitude, we adopted a cut u$-$g $= 1.2$. The resulting field sample is then composed by 24 star-forming and 10 quiescent dwarf galaxies.

A total of 53 nights were awarded to this project through the ITP at La Palma telescopes. These nights were distributed within the 4 largest telescopes (INT 2.5 m; NOT 2.5 m; TNG 3.6 m and WHT 4.2 m). Very different instrumental configurations were used in each observing facility to cover the selected samples of star-forming and quiescent dwarfs both in photometry and in spectroscopy. The observational campaigns for the quiescent dwarfs were by far the most successful ones and have provided long-slit spectroscopy in low ($R \sim 650$) and medium ($R \sim 3800$) resolution as well as near infrared (NIR) imaging. Among the sample of galaxies, we selected with high priority those with the highest surface brightness to make the observations accessible for the kind of telescopes we had access to (between 2.5 m and 4 m of diameter). A total of 23 dEs were observed in low-resolution spectroscopy. This sample completely overlaps with the 21 dEs observed in the medium-resolution campaings except for NGC3073, a field dE observed only at $R \sim 3800$. The NIR imaging sample consists of a total of 33 dEs. 67$\%$ of the optical spectroscopic sample overlaps with the NIR (H- and/or K-band) sample. For the remaining 33$\%$, H-band images were drawn from the GOLDMine database (Gavazzi et al. 2003a).

The analysis of the low-resolution spectroscopy was leaded by Dr. Dolf Michielsen (Michielsen et al. 2008). A summary of the most important results are presented in Section 6.1.1. The medium-resolution spectroscopy was leaded by myself. I also conducted the measurement of the photometric parameters needed to complete the spectrophotometric analysis (Sections 6.2, 6.3 and 6.4).

6.1.1 Low-resolution spectroscopy of dwarf early-type galaxies in the Virgo cluster (Michielsen, Boselli, Conselice, Toloba, et al. 2008, MNRAS, 385, 1374)

We observed a sample of 18 dEs in the Virgo cluster and 5 in the field at the NOT telescope. These observations were done using the spectrograph ALFOSC with the grism number 14 and a slit width of 1.2″ oriented along the major axis of the galaxies. The obtained spectra had a resolution of $R \sim 650$. The analysis conducted with these data consists of the measurement of their stellar populations inside their central 4″ through the analysis of Lick/IDS indices (see Section 3.2). We combine this information with some structural parameters measured in SDSS (York et al. 2000) g-band images.

My specific contribution to this study began with the observations, that were simultaneous for the low and medium-resolution spectroscopy. I helped to establish the priority list of galaxies to be followed during these observing campaigns. In particular, I flux calibrated the spectra presented in this work following the technique described in Section 6.2. Regarding the index measurements, I made a comparison of all the indices in common between the two wavelength ranges in order to check that all the values obtained were in complete agreement (these comparisons can be seen in Appendix B). Thus this work was performed in a very close collaboration between Dr. Dolf

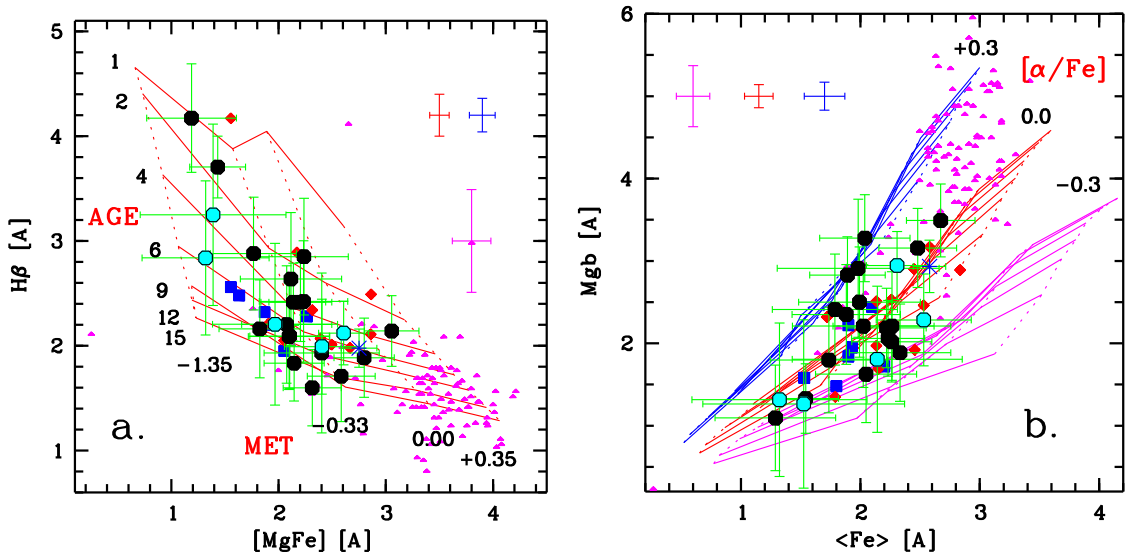

Figure 6.1: Ages, metallicities and α-enhancement from Michielsen et al. (2008). Comparison of our dEs (Virgo: black filled circles, field: cyan filled circles, M32: blue asterisk) with dE samples of Geha et al. (2003) (red diamonds) and van Zee et al. (2004b) (blue squares), and with the massive early-type galaxies from Sánchez-Blázquez et al. (2006b) (magenta triangles). The average error bars for these other samples are plotted with the same colour code. Overlaid are Thomas et al. (2003) models with different ages, metallicities and abundance ratios, as indicated on the left Figure: H_β-[MgFe] diagram overlaid with $[\alpha/\mathrm{Fe}] = 0$ model grid. Figure on the right: Mgb$-<\mathrm{Fe}>$ diagram with different $[\alpha/\mathrm{Fe}]$ models.

Michielsen and myself, being part also of the development of the discussion and conclusions of this analysis.

From the study of the stellar content of these galaxies we found that dEs, on average, are younger and less metal-rich than more massive Es (see left panel of Figure 6.1). Moreover, their $[\alpha/\mathrm{Fe}]$ abundance ratios scatter around the solar value ($[\alpha/\mathrm{Fe}] = 0.0$), some of the galaxies are even consistent with having sub-solar abundance ratios ($[\alpha/\mathrm{Fe}] = -0.3$, see right panel of Figure 6.1). Field dEs are found to be generally young, and their metallicities and abundance ratios are not very different from those of Virgo dwarfs. These evidences point to an extended star formation history in dEs that is in accordance with the downsizing scenario where dwarf galaxies have a longer star formation history than massive ellipticals (Cowie et al. 1996; Gavazzi et al. 1996; Boselli et al. 2001; Caldwell et al. 2003; Nelan et al. 2005; Bundy et al. 2006). Specifically, the fact that metallicity and $[\alpha/\mathrm{Fe}]$ do not depend on the location of the galaxy (surrounding the cluster, near its center or isolated in the field) suggests that the chemical evolution of dEs is an internally governed process of slow enrichment. However, preliminary truncation of the star formation by a hostile environment can stop this process.

By analysing the properties of dEs with the Virgocentric distance we have detected that galaxies with old stellar populations tend to be located in the central parts of the cluster (see right panel of Figure 6.2). If a transformation from a star-forming irregular galaxy has occurred, then we would expect a correlation between some structural parameters and the clustercentric distance. To investigate this possibility, the structural parameters (C, A, S) as defined in Conselice et al. (2003) were analysed as a function of the distance to M87, considered the center of Virgo. These structural parameters were measured in the SDSS g-band images of our galaxies. The C, A, S parameters have a well-defined range of values and are computed using simple techniques. The

concentration index (C) is the logarithm of the ratio of the radius that contains 80% of the total light of the galaxy to the radius which contains 20% of the light. The range in C varies from 2 to 5, with higher C values for more concentrated galaxies, such as massive ellipticals, and $C \sim 2$ for exponential discs. The asymmetry (A) is measured by rotating the image of the galaxy by 180 degrees and subtracting this rotated image from the original one. Then the residuals obtained are compared with the original flux of the galaxy. The A parameter ranges from 0 to 1 with merging galaxies typically found at $A > 0.35$, and unperturbed symmetric objects with $A = 0$. Finally, the clumpiness S is defined in a similar way as the asymmetry, with the difference that the amount of light in high frequency clumps is compared to the total light of the galaxy. The S values range from 0 to 2, with star-forming galaxies dominated by HII regions found at $S > 0.3$, while smooth ellipticals present $S \sim 0$ (see Conselice et al. 2003, for a more complete description of the CAS parameters).

The left panels of Figure 6.2 present the CAS parameters measured in our sample of dEs as a function of the Virgocentric distance. Whereas the concentration (C) and the clumpiness (S) do not show any clear correlation with the distance from M87, the A parameter, the large-scale asymmetry, seems to have larger values for those galaxies in the outer parts of the Virgo cluster. This suggests that galaxies in the outskirts of the cluster are slightly more structurally distorted than those in the core, but this asymmetry is smaller than that observed in star-forming galaxies, where $S > 0.3$.

6.1.2 Kinematics: a key parameter

These stellar population properties and asymmetries found in Michielsen et al. (2008) and described above, in addition to other observed properties such as the disky structures observed underneath their elliptical appearance (Lisker et al. 2006-2009), suggest that dEs are transformed late-type galaxies as a consequence of the interaction of the galaxies with the hostile environment. As we discussed in Chapter 2, there are two proposed mechanisms that can be responsible of such a transformation: ram-pressure stripping and harassment (for a review see Boselli & Gavazzi 2006).

Galaxy harassment was first defined by Moore et al. (1996, 1998, 1999) as the combined effect of high speed galaxy-galaxy close ($\sim$ 50 kpc) encounters with the interaction with the potential of the cluster as whole. Their simulations predict that the strength of the perturbation depends on the potential wells of the galaxies. This is the reason why bright disk galaxies are relatively stable to galaxy harassment, suffering only a small increase of the central surface brightness (around 0.5 mag arcsec^{-2}), an increase of the disk scale height (by a factor of $2-4$), a positive increment of the central velocity dispersion and the consequent fading of the spiral features (Moore et al. 1998). The resulting structural and kinematic properties resemble those of bright lenticulars. However, due to their low potential well, low surface brightness spiral galaxies are strongly perturbed by their interaction. These galaxies are expected to lose most of their stars, up to $50-90$%, increase their central velocity dispersion and, consequently, their central surface brightness by $\sim$ 2 mag arcsec^{-2} (Moore et al. 1999). The resulting kinematic and structural properties resemble would those of dEs.

Gunn & Gott (1972) first proposed that the interstellar medium (ISM) of the galaxies could be removed if they were moving at $\sim$ 1000 km s^{-1} through the hot ($\sim 10^{7}-10^{8}$ K) and dense ($\sim 10^{-3}-10^{-4}$ atoms cm^{-3}) intergalactic medium (IGM) by the ram-pressure mechanism. This physical process is based on the fact that galaxies crossing an IGM as described above suffer a

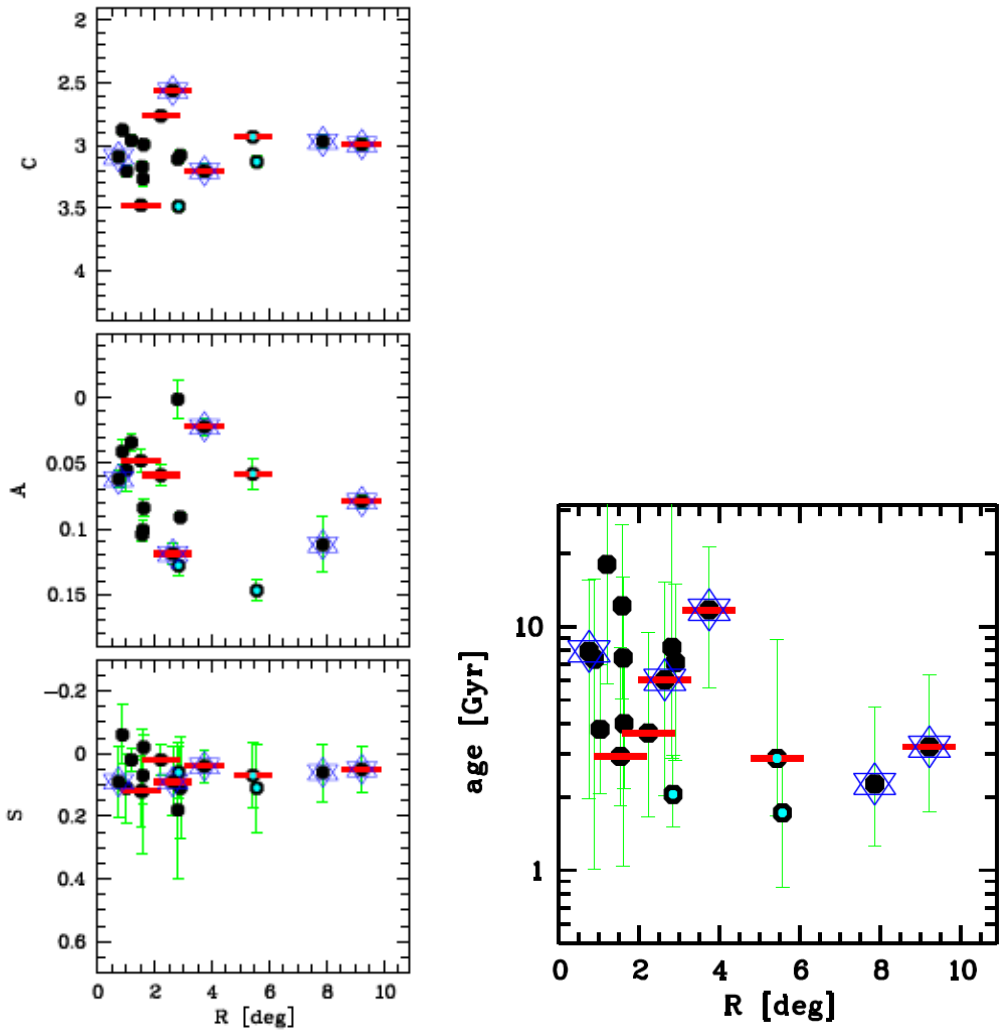

Figure 6.2: Structural parameters (C, A and S) and age vs. the projected Virgocentric distance (R, in degrees) from Michielsen et al. (2008). The symbols with a cyan center are dEs with a blue nucleus (Lisker et al. 2006a). Those with a red horizontal bar are dEs in which disks or spiral structures have been found (certain and probable disks from Lisker et al. (2006b). Finally the stars highlight those dEs with known rotation (Geha et al. 2003; van Zee et al. 2004b)).

significant compression ahead of them as a consequence of the increase of the external pressure due to the distinct density of the IGM with respect to the ISM that can form a bow-shock and a low density gaseous tail behind, giving to the galaxy a cometary shape (Balsara et al. 1994; Stevens et al. 1999; Murakami & Babul 1999; Quilis et al. 2000; Mori & Burkert 2000). The most recent models developed to analyse the consequences of this mechanism on the physical properties of the galaxies (Boselli et al. 2008a) show that, because of the shallow potential well of dwarf galaxies, most of their gas is efficiently removed on very short time scales ($\sim$ 150 Myr), leading to the formation of extremely gas-deficient objects. As a consequence of this lack of gas, star formation abruptly decreases by a factor of $\sim$10$-$100 and continues at a very low level afterwards. Obviously, stopping the star formation makes galaxies redder. Since the decrease of the star formation activity is rapid, the younger stellar populations, those emitting in the ultraviolet, are the most affected, e.g., $FUV - H$ colour increases by $\sim$ 4.5 mag in 1 Gyr, while $B - H$ by only 1 mag.

These two mechanisms, harassment and ram-pressure stripping, can explain the red colours and smooth structural properties of dwarf early-type galaxies. However, in terms of kinematics, they predict very different effects: from a ram-pressure stripping event, where the gas in the galaxy is easily removed just by the interaction with the IGM, the rotation of the progenitor galaxy must be conserved. On the contrary, in the harassment process, where the transformation is via galaxy-galaxy interactions and, therefore, much more violent than in ram-pressure, the system is rapidly heated, the stars migrate from the disk losing the rotation and increasing the velocity dispersion of the galaxy, so nearly no rotation should be found if the galaxies are transformed via harassment. This makes kinematic parameters a key parameter to try to disentangle how this galaxies have been formed and have evolved along the cosmological time.

However, the measurement of the kinematics is not an easy procedure due to the spectral resolution needed (at least 40 km s^{-1}), the signal-to-noise required (a minimum of 10), and the radial coverage (the largest the better) to obtain reliable kinematic values, such as the maximum rotation velocity, that are representative of the internal behaviour of the galaxy. The combination of these parameters with the low surface brightness of the galaxies ($\mu_{B,\rm eff} > 22$ mag arcsec^{-2}) requires large exposure times (a minimum of one hour in a 2$-$4m telescope) to get acceptable signal-to-noise (around 40$-$60 in the center of the brightest and most concentrated dEs). This is the reason why only a few results have been published on this topic (Pedraz et al. 2002; Simien & Prugniel 2002; Geha et al. 2002, 2003; van Zee et al. 2004b).

In Bender & Nieto (1990) it was found for the first time that, at least, some early-type dwarfs have significant rotation. This result arose several questions: what fraction of dEs rotate?, are they a significant population?, how strong is this rotation?, what is the origin of the rotation?. These questions have been addressed by several studies (Pedraz et al. 2002; Simien & Prugniel 2002; Geha et al. 2002, 2003; van Zee et al. 2004b; de Rijcke et al. 2005; Chilingarian 2009). The conclusion that is common to all these works is that some, but not all, dEs present significant rotation. The reasons of why this is the case still remain unknown. With the aim of answering these questions and, more generally, of understanding the origin of such a heterogeneous population we began a spectrophotometric analysis of a sample of 21 dEs mainly in the Virgo cluster. The results of this work are presented in the following Sections of this Chapter.

First of all, in Section 6.2 we have conducted an extensive analysis of the parameters that influence the kinematic measurements through the development of a series of Monte-Carlo sim-

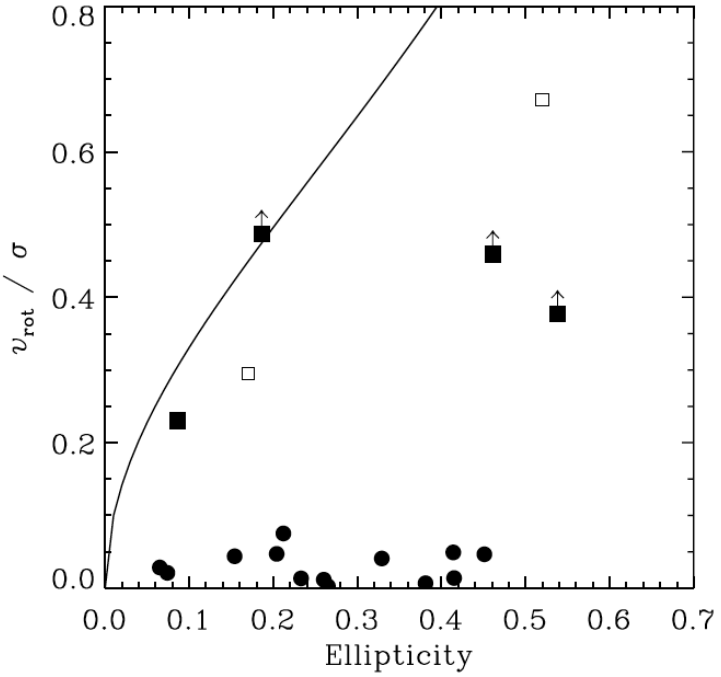

Figure 6.3: Ratio of the rotation velocity ($v_{\rm rot}$) over the velocity dispersion (σ) vs. the mean isophotal ellipticity from Geha et al. (2003). The solid line is the expected relation for an oblate, isotropic galaxy flattened by rotation (Binney 1978). Solid symbols indicate Virgo cluster dEs from Geha et al. (2003) and open symbols are two dEs from Simien & Prugniel (2002); dEs are plotted as circles if $v_{\rm rot}/\sigma \leq 0.1$ and as squares otherwise.

ulations. The parameters investigated are the minimum signal-to-noise (S/N) needed to rely on the results, the accuracy of measuring velocity dispersions (σ) below the instrumental resolution, the advantages of having a wide range of stars of different spectral types and luminosity classes as templates to measure σ, and the effects of the stellar populations of the galaxies in the determinations of the radial velocities and velocity dispersions. In order to perform this exhaustive study we have used the single stellar population (SSP) models of PEGASE.HR (Le Borgne et al. 2003) to create model dwarf early-type galaxies where their parameters were controlled at all times (ages, metallicities, radial velocities, σ). In the first part of Section 6.2 we have investigated the influence of all these parameters as a function of the S/N.

After this technical and detailed report on how to measure kinematics in the most accurate way, we have analysed the shapes of the rotation curves of the rotating dEs of our sample. This analysis has been done by comparing them with the rotation curves of spiral galaxies of similar luminosity from Catinella et al. (2006). We have also compared the rotation velocity measured in our dEs with the rotation of normal spiral galaxies through the Tully-Fisher relation. With this analysis we have tried to understand the similarities in the kinematics between today's star-forming galaxies and our rotating dEs. The aim of this study was to give some insight on the possibility of dEs being transformed late-type galaxies through a ram-pressure stripping event or through harassment. The dark matter content of these systems is another controversial topic intimately related to the dynamics of the galaxies. If they are dark matter dominated systems their rotation curves should continue increasing with the radius of the galaxy, while, if they are luminosity dominated, the rotation velocity achieves a radius where it begins to decrease due to the lack of dark matter that maintains the star rotation at larger radii. At the end of Section 6.2 we have studied the dynamical and stellar mass-to-light ratios in comparison to dSphs (mainly dark matter

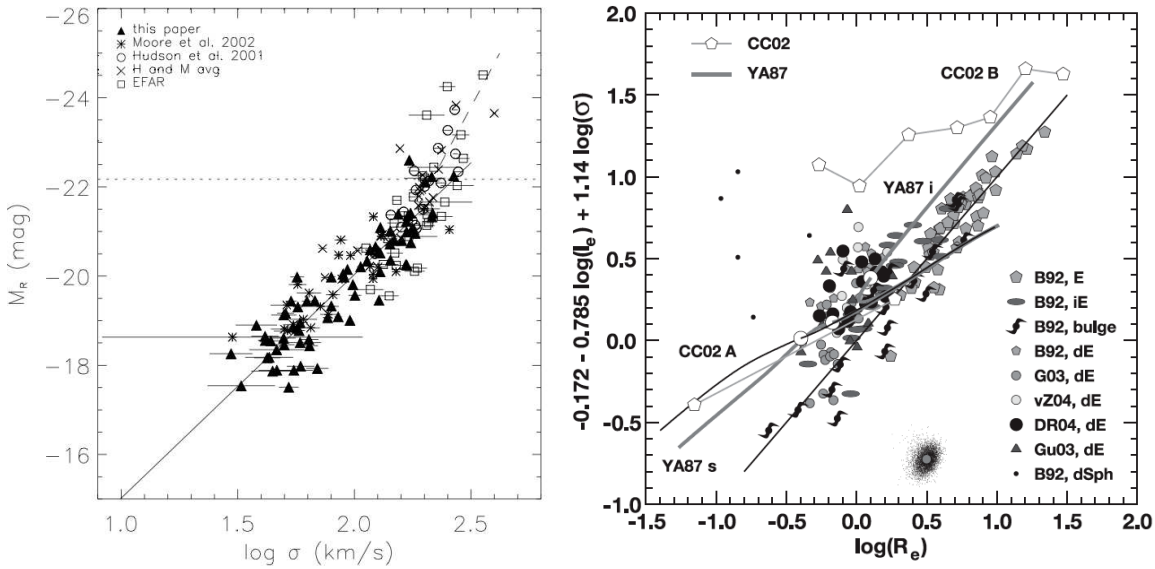

Figure 6.4: Left Panel: Faber-Jackson relation for Coma cluster galaxies by Matković & Guzmán (2007). This plot combines the data from Matković & Guzmán (2007) with the measurements from Hudson et al. (2001); Moore et al. (2002) and the EFAR sample by Colless et al. (2001). The dotted line corresponds to $M_B = -20.50$ mag and separates bright from faint early-type galaxies (Graham & Guzmán 2003a). The dashed line is the traditional Faber-Jackson relation $L \propto \sigma^4$ (Forbes & Ponman 1999). The solid line is the least squares fit to all the faint early-type galaxies ($L \propto \sigma^{2.01\pm0.36}$). **Right panel:** Edge-on view of the FP by de Rijcke et al. (2005, DR04). The straight black line traces the FP indicated in the y-axis of the plot. The dEs observed by Guzmán et al. (2003, Gu03) have been added to the DR04, Geha et al. (2003, G03) and Bender et al. (1992, B92) datasets. The curved black line traces the FP of zero mass-loss models by Yoshii & Arimoto (1987, YA87). The thick grey lines give the locus of the YA87 models after slow (bottom thick grey line) or fast (top thick grey line) gas removal. The white circles show the expected evolution of a m_B =16 Fornax dE.

dominated systems) and Es (systems dominated by the baryonic matter).

In Section 6.3 we present the study of the rotational support of dwarf early-type galaxies. This analysis is made quantifying the importance of the rotation (v) over the velocity dispersion (σ). This v/σ parameter is called *anisotropy* parameter and quantifies the motions that govern the galaxy (ordered versus random motions). The classical method to analyse the kinematic support of galaxies is to compare the anisotropy parameter with the model of Binney (1978). This model is developed from the virial theorem tensor and describes the theoretical curve of v/σ vs. ϵ (the measured ellipticity of the galaxy) for an isotropic oblate spheroid flattened by rotation. Those galaxies with v/σ consistent with or above the model are rotationally supported and those below the model are pressure supported. Figure 6.3 shows an example of this diagram by Geha et al. (2003).

If dEs are transformed late-type galaxies then we should find differences in the kinematics of the dEs located in different regions within the cluster. In particular, those that are falling in now should be less perturbed than those that fell some Giga-years ago. To investigate this possibility we have combined the kinematic information that the anisotropy parameter provides with the Virgocentric distance. We have also studied this scenario as a function of luminosity-weighted ages of our dEs from Michielsen et al. (2008), an estimation of the age of the last starburst in the galaxy, and the morphological classification of Lisker et al. (2006a), that informs us if the galaxy has any underlying disky structure. On the contrary, if dEs, instead of being transformed late-type galaxies, are the small pieces that have merged along the cosmological time to form the massive

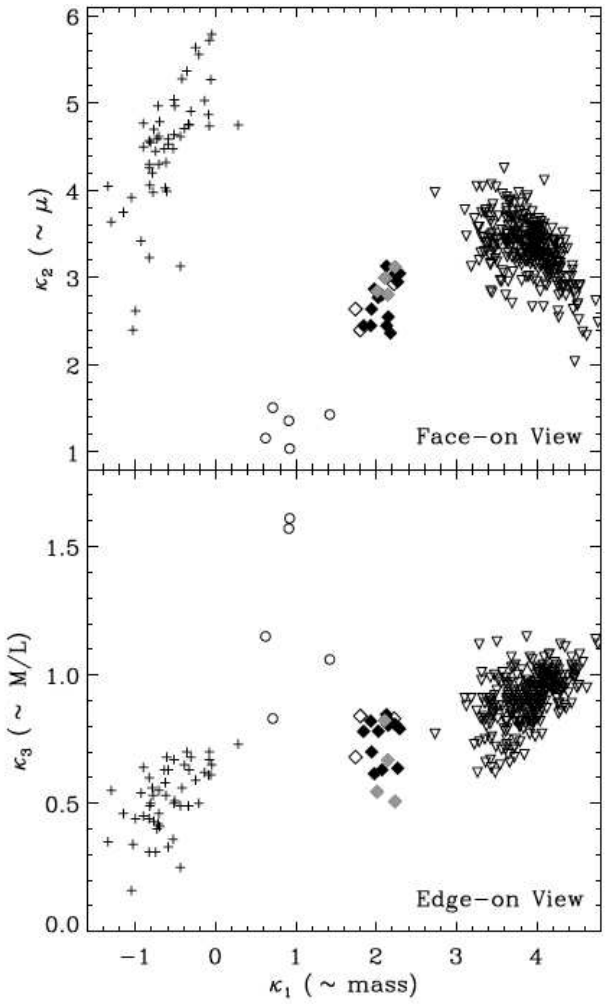

Figure 6.5: Face-on and edge-on projections of the κ-FP for dynamically hot systems from Geha et al. (2003). Black diamonds are nonrotating dEs, grey diamonds rotating dEs. Data from Burstein et al. (1997) are: classical ellipticals and spiral bulges (open triangles), Local Group dEs (open diamonds), Local Group dSphs (open circles) and Galactic globular clusters (plus signs).

elliptical galaxies, as suggested by the hierarchical merging formation, then dEs are expected to be the low-luminosity extension of Es. In Section 6.4 we analyse this possibility through the scaling relations followed by dEs in comparison to massive Es.

This possible connection between dEs and more massive ellipticals is still in its infancy. After the early work by Nieto et al. (1990); Bender et al. (1992) and Guzmán et al. (1993), relatively little attention has been paid to the relation between the internal kinematics and the structural parameters of these faint, small galaxies. The main reason for this is, as discussed above, the low surface brightness of dwarf galaxies, which makes spectroscopy very time-consuming. The most recent studies in this direction are based on the analysis of relations such as the Fundamental Plane (FP) and their projections over different axis (see Chapter 2).

In Matković & Guzmán (2005, 2007) the Faber-Jackson relation was studied and it was found that dwarf galaxies appear more luminous than they should be for their velocity dispersion if they follow the same Faber-Jackson relation as massive ellipticals (see Figure 6.4). Bender et al. (1992) was the first noting that dEs appear above the FP defined by massive early-type galaxies.

More recently, de Rijcke et al. (2005) gathering all the available spectrophotometric measurements for dEs, adding some of their own for the Fornax cluster, and comparing them to Bender et al. (1992), also found that dEs lie above the FP defined by bright ellipticals, with fainter galaxies lying progressively higher above the FP (see Figure 6.4). When the FP is studied in the κ-space, as in Geha et al. (2003), it has been found that dEs populate a different area of the FP in their face-on and edge-on projections (see Figure 6.5) but with no differences between rotating and non-rotating dwarf systems. The different trends followed by Es and dEs in their scaling relations has been interpreted as a fundamental difference between the galaxy formation processes of dEs and more luminous elliptical galaxies (e.g., Bender et al. 1992; Geha et al. 2003; Kormendy et al. 2009), although not all the authors agree with this view. Groups like Guzmán et al. (2003) and de Rijcke et al. (2005) explain this difference as a natural consequence of dEs being the low-luminosity extension of giant Es because, claiming that mergers do not equally affect massive and low-mass galaxies. To test this possible origin of dEs as the progenitors of more massive Es we have analysed in Section 6.4 some scaling relations such as the Kormendy, Faber-Jackson and the Fundamental Plane as a function of the kinematic properties of dwarf galaxies and in comparison to Es.

At the end of this Chapter (Section 6.5) we summarise the main results and conclusions achieved during the spectrophotometric analysis developed in Sections 6.2, 6.3 and 6.4.

6.2 Toloba et al. (2011) A&A, 526, 114

Formation and evolution of dwarf early-type galaxies in the Virgo cluster I. Internal kinematics

E. Toloba[a], A. Boselli[b], A. J. Cenarro[c], R. F. Peletier[d], J. Gorgas[a], A. Gil de Paz[a], J. C. Muñoz-Mateos[a,e]

[a]Departamento de Astrofísica y CC. de la Atmósfera, Universidad Complutense de Madrid, 28040, Madrid, Spain
[b]Laboratoire d'Astrophysique de Marseille, UMR 6110 CNRS, 38 rue F. Joliot-Curie, F-13388 Marseille, France
[c]Centro de Estudios de Física del Cosmos de Aragón, E-44001, Teruel, Spain
[d]Kapteyn Astronomical Institute, Rijksuniversiteit Groningen, Postbus 800, 9700 AV Groningen, the Netherlands
[e]National Radio Astronomy Observatory, 520 Edgemont Road, Charlottesville, VA 22903-2475

Abstract—We present new medium resolution kinematic data for a sample of 21 dwarf early-type galaxies (dEs) mainly in the Virgo cluster, obtained with the WHT and INT telescopes at the Roque de los Muchachos Observatory (La Palma, Spain). These data are used to study the origin of the dwarf elliptical galaxy population inhabiting clusters. We confirm that dEs are not dark matter dominated galaxies, at least up to the half-light radius. We also find that the observed galaxies in the outer parts of the cluster are mostly rotationally supported systems with disky morphological shapes. Rotationally supported dEs have rotation curves similar to those of star forming galaxies of similar luminosity and follow the Tully-Fisher relation. This is expected if dE galaxies are the descendant of low luminosity star forming systems which recently entered the cluster environment and lost their gas due to a ram pressure stripping event, quenching their star formation activity and transforming into quiescent systems, but conserving their angular momentum.

6.2.1 Introduction

The processes involved in galaxy formation and evolution through cosmic time are still poorly understood. It is indeed still unclear how matter assembled to form the present day galaxy population, whether it followed a passive evolution after the collapse of the primordial density fluctuations (secular evolution), through a subsequent merging of growing structures (hierarchical formation) or a combination of the two. A way of quantifying the relative role of these different mechanisms is to study dwarf galaxies, the most numerous objects in the universe (Ferguson & Binggeli 1994). Their importance resides in the fact that these low-luminosity systems are expected to be the building blocks of massive galaxies in lambda cold dark matter (ΛCDM) hierarchical merging scenarios (e.g., White & Rees 1978; White & Frenk 1991).

Among dwarf galaxies, quiescent dwarfs (which we here define to be all quiescent galaxies with $M_B > -18$, including both dwarf ellipticals and spheroidals, hereafter indicated as dEs) are of particular interest since they are the most numerous population in clusters (Ferguson & Binggeli 1994). These objects were originally thought to be the low luminosity extension of giant ellipticals (Es). Since the 1990s it is known that dEs are composed of several families of objects (e.g. compact and low surface brightness dwarfs) (Bender et al. (1992);Kormendy et al. (2009)). Later on, it was shown that dEs were no longer small Es with simple, old and metal-poor stellar populations, but much more complex objects exhibiting a wide range of stellar contents. For

example, in the Virgo cluster, they have stellar populations ranging from very young (around 1 Gyr old) luminosity-weighted ages to as old as the oldest Es galaxies (14 Gyr) (Michielsen et al. 2008). Their proximity allowed detailed studies of their structural properties which indicated that, behind their elliptical appearance, dEs show a great variety of underlying structures, like discs, spiral arms, irregular features, etc, making them a very heterogeneous class of galaxies (Lisker et al. 2006a,b, 2007).

These evidences indicate a complex formation process shaping the evolution of dEs in clusters. Two main different processes have been proposed in the literature: the first mechanism is based on the idea that dEs are formed through internal processes, like supernova feedback, where the interstellar medium (ISM) of the progenitor star forming galaxy is swept away by the kinetic pressure generated by supernovae (Yoshii & Arimoto 1987), although it seems highly unlikely in dark-matter dominated systems (Silich & Tenorio-Tagle 2001); the second mechanism rests upon external processes induced by the interaction with the hostile environment in which dEs reside (Sandage et al. 1985; Blanton et al. 2005). In a dense environment several mechanisms are affecting galaxies. This might happen through interactions with the intergalactic medium (IGM), as ram-pressure stripping (Boselli et al. 2008a,b), galaxy-galaxy interactions (e.g., Byrd & Valtonen 1990) and galaxy harassment (e.g., Moore et al. 1998; Mastropietro et al. 2005). It has been shown that all these interactions are able to reproduce some of the observational properties of local dEs in clusters, like their structural parameters (Lisker et al. 2006b, 2007) or their stellar populations (Geha et al. 2002, 2003; van Zee et al. 2004b; Michielsen et al. 2008; Paudel et al. 2010), but none of them have been tested versus the kinematic properties. In this regard, whereas in the harassment scenario the system is rapidly heated, leading to an increase of the velocity dispersion of the galaxy and a decrease of its rotation (Mastropietro et al. 2005), in a ram-pressure stripping event the angular momentum is conserved (Boselli et al. 2008a,b).

With the aim of using kinematic data to constrain dwarf galaxy evolution, we recently started an ambitious observational program at the Observatory El Roque de los Muchachos (La Palma, Spain) to gather medium resolution spectroscopic data of dEs in the Virgo cluster. In this paper we present a detailed analysis of the internal kinematics focusing our attention into the most rapidly rotating systems. In Toloba et al. (2009a) we have studied the kinematics as a function of local environment inside the Virgo cluster. Several typical scaling relations of pressure supported systems, such as the Fundamental Plane as well as their stellar population properties will be analysed in a forthcoming communication.

This paper is structured as follows: in Sections 2, 3 and 4 we describe the sample selection, the observations and the data reduction process. In Section 5 we report the kinematic measurements paying special attention to the method employed and the stellar templates used. We also describe the procedure followed to obtain the radial kinematic profiles (Section 5.1), the central velocity dispersion and the maximum rotational speed of the selected galaxies (Section 5.2), making comparisons with previous works (Section 5.3). Combined with photometric data (Section 6), the present kinematic observations are used to study the properties of rotationally supported systems in the framework of various models of galaxy evolution (Sections 7, 8 and 9).

6.2.2 The sample

The sample analysed in this work is composed of galaxies with $M_r > -16$ classified as dE or dS0 in the Virgo Cluster Catalog (VCC) by Binggeli et al. (1985). All galaxies have been selected to

have SDSS imaging and to be within the GALEX MIS fields (Boselli et al. 2005), thus to have a measured UV magnitude or an upper limit. To these we added a few field quiescent dwarfs (originally used as fillers in our observing runs) useful for comparison in a statistical study. Out of the 43 Virgo galaxies satisfying these requirements in the VCC, 18 have been observed for this work. To make the observations accessible to 2.5-4.2m telescopes, we chose those objects with the highest surface brightness.

The field sample consists of early-type dwarfs in low density regions with magnitudes between $-18.5 < M_r < -14.5$ and distances similar to Virgo (375 km s^{-1}$< v <$ 1875 km s^{-1}, 5-25 Mpc). Quiescent objects have been selected assuming the colour criterion FUV-NUV > 0.9 or $u - g > 1.2$ when UV detections were not available. We observed only 3 out of 10 field dEs candidates. To these 18 Virgo and 3 field dEs we added M32, selected to test the setup of the instruments. Thanks to the large amount of available data, M32 is also an ideal target for comparison with other data available in the literature.

Although we can consider it representative of the bright end of the Virgo Cluster dE population, the observed sample is not complete in any sense.

6.2.3 Observations

The observing time that we obtained for this work was part of the International Time Program (ITP 2005-2007) at El Roque de los Muchachos Observatory. Here we focus on the medium resolution ($R \simeq 3800$), long-slit spectroscopy carried out during three observing runs. In runs 1 and 3 (December 2005, February 2007) we used the ISIS double-arm spectrograph at the 4.2m WHT, and in run 2 (January 2007) we used the IDS spectrograph at the INT (2.5m telescope).

The advantage of ISIS over IDS is that it allows us to use a dichroic (*5300 dichroic* in our case) to split the light into two beams to observe simultaneously two wavelength ranges, one in the blue optical part of the spectra and another in the red. This technique allowed us to cover, in 3 settings in the first run, the full wavelength range from 3500 Å to 8950 Å, using a mirror to cover 5000-5600 Å, the only range that we could not cover with this dichroic. In the third run we used 2 settings to cover the same wavelength range except for the dichroic gap.

The wavelength range covered by the IDS was smaller (4600-5960 Å), since detector and grating are the same as on the blue arm of ISIS, the data obtained had similar resolution. The spectral resolution ($R \simeq 3800$) is high enough to obtain reliable kinematics for dwarf galaxies.

All the details of the configurations used in each run are specified in Table 6.1.

In Table 6.2 we list the observed sample. Column 5 presents the morphological type classification according to Lisker et al. (2006a) and Lisker et al. (2006b): dE(di) indicates dwarf ellipticals with a certain, probable or possible underlying disk (i.e. showing spiral arms, edge-on disks and/or a bar) or other structures (such as irregular central features (VCC21)); dE(bc) refers to galaxies with a blue center; dE to galaxies with no evident underlying structure. Four out of our 21 dwarf galaxies were not in the Lisker et al. sample (NGC3073, PGC1007217, PGC1154903 and VCC1947), therefore we classified them as described in Section 6 attending only to their boxyness/diskyness. Column 6 gives the Virgo substructure to which the galaxy belongs, taken from GOLDMine Database (Gavazzi et al. 2003a) and defined as in Gavazzi et al. (1999a). Columns 7 and 8 refer to the observational campaign (see Table 6.1) and the exposure time for each setting,

Table 6.1: Observational configurations

	Run 1		Run 2	Run 3	
Date	Dec.24-27 2005		Jan.21-23 2007	Feb.10-12 2007	
Telescope	WHT 4.2m		INT 2.5m	WHT 4.2	
Spectrograph	ISIS		IDS	ISIS	
Detector	EEV12(blue)	Marconi(red)	EEV10	EEV12(blue)	RedPlus(red)
Grating	R1200B(blue)	R600R (red)	R1200B	R1200B(blue)	R600R(red)
Wavelength range 1 (Å)	3500-4300	5500-6700	3700-4790	3500-4300	5500-6700
Wavelength range 2 (Å)	4100-4900	7750-8950	4600-5690	4100-4900	7750-8950
Wavelength range 3 (Å)	4800-5600	—	—	—	—
Dispersion (Å/pixel)	0.44	0.87	0.48	0.44	0.97
Spectral Resolution (FWHM, Å)	1.56	3.22	1.80	1.56	3.23
Instrumental Resolution (km s^{-1})	40	58	46	40	58
Spatial scale (”/pix)	0.40	0.44	0.40	0.40	0.44
Slit width (”)	1.95	1.95	1.94	1.91	1.91

which allowed us to get a typical signal-to-noise ratio[1] for the central spectra of $\sim$60 $^{-1}$, enough to obtain reliable central kinematics. The galaxies were observed along their major axis. Their position angles (PA) from the HyperLEDA Database (Paturel et al. 2003) are given in column 9. Column 10 gives the Galactic colour excess from Schlegel et al. (1998).

A total of 37 B to M stars in common with the MILES library (Sánchez-Blázquez et al. 2006c) and the CaT library (Cenarro et al. 2001) were observed to flux-calibrate our data and to use them as templates for velocity dispersion measurements.

6.2.4 Data reduction

The data reduction was performed with REDUCE (Cardiel 1999), a package specially designed to reduce long-slit spectroscopy with particular attention to the treatment of errors. This package is ideal for treating in parallel the data and error frames, producing an error spectrum associated with each individual data spectrum, which means that the errors are controlled at all times.

Due to the similar instrumental configurations used on all observing runs, the reduction process for both telescopes was the same. The standard procedure for long-slit spectroscopy data reduction consists of bias and dark current subtraction, flat-fielding (using observations of tungsten lamps and twilight sky to correct for high and low frequency variations respectively), cosmic ray cleaning, C-distortion correction, wavelength calibration, S-distortion correction, sky subtraction, atmospheric and interstellar extinction correction and flux calibration. We give below some comments on steps of particular importance:

Flat-fielding. The flat-fielding correction is a delicate step at near infrared wavelengths due to the fringing effects. In the first run, the Marconi CCD suffered from significant fringing that varied with the telescope position. Since complete removal of the fringing in run 1 was not possible, we did not use the red Marconi-CCD data to determine the galaxy kinematics. The fringing produced

[1]The S/N per $^{-1}$ is obtained dividing the S/N per pixel by the square root of the spatial scale along the slit. These measurement is therefore independent of the instrument used.

Table 6.2: The observed galaxies.

Galaxy	Other name	RA(J2000) (h:m:s)	Dec.(J2000) (°:':")	Type	Env.	Run	t_{exp} (sec)	PA (°)	E(B-V) (mag)
M 32	NGC 221	00:42:41.84	+40:51:57.4	cE2	M31 group	1	1350	170	0.062
NGC 3073	UGC 05374	10:00:52.10	+55:37:08.0	dE(di)	Field	1	3200	120	0.010
PGC 1007217	2MASX J02413514-0810243	02:41:35.8	-08:10:24.8	dE(di)	Field	1	3600	126	0.024
PGC 1154903	2MASX J02420036+0000531	02:42:00.3	+00:00:52.3	dE	Field	1	3600	126	0.031
VCC 21	IC 3025	12:10:23.14	+10:11:18.9	dE(di,bc)	Virgo N Cloud	2	3600	99	0.021
VCC 308	IC 3131	12:18:50.77	+07:51:41.3	dE(di,bc)	Virgo B Cluster	3	2400	109	0.021
VCC 397	CGCG 042-031	12:20:12.25	+06:37:23.6	dE(di)	Virgo B Cluster	3	3600	133	0.020
VCC 523	NGC 4306	12:22:04.13	+12:47:15.1	dE(di)	Virgo A Cluster	1	3400	144	0.044
VCC 856	IC 3328	12:25:57.93	+10:03:13.8	dE(di)	Virgo B Cluster	2	2740	72	0.024
VCC 917	IC 3344	12:26:32.40	+13:34:43.8	dE	Virgo A Cluster	3	3600	57	0.032
VCC 990	IC 3369	12:27:16.91	+16:01:28.4	dE(di)	Virgo A Cluster	2	3000	135	0.028
VCC 1087	IC 3381	12:28:17.88	+11:47:23.7	dE	Virgo A Cluster	3	3600	106	0.026
VCC 1122	IC 3393	12:28:41.74	+12:54:57.3	dE	Virgo A Cluster	3	3600	132	0.021
VCC 1183	IC 3413	12:29:22.49	+11:26:01.8	dE(di)	Virgo A Cluster	2	3600	144	0.031
VCC 1261	NGC 4482	12:30:10.35	+10:46:46.3	dE	Virgo A Cluster	2	6930	133	0.028
VCC 1431	IC 3470	12:32:23.39	+11:15:47.4	dE	Virgo A Cluster	2	3000	135	0.054
VCC 1549	IC 3510	12:34:14.85	+11:04:18.1	dE	Virgo A Cluster	2	3300	13	0.030
VCC 1695	IC 3586	12:36:54.79	+12:31:12.3	dE(di)	Virgo A Cluster	3	3600	39	0.045
VCC 1861	IC 3652	12:40:58.60	+11:11:04.1	dE	Virgo E Cloud	3	3600	109	0.030
VCC 1910	IC 809	12:42:08.68	+11:45:15.9	dE(di)	Virgo E Cloud	2	3800	135	0.030
VCC 1912	IC 810	12:42:09.12	+12:35:48.8	dE(bc)	Virgo E Cloud	2	3600	166	0.032
VCC 1947	CGCG 043-003	12:42:56.36	+03:40:35.6	dE(di)	Virgo S Cloud	2	3060	126	0.027

by RedPlus, the new CCD optimised to avoid these patterns, was much lower, with an amplitude of only $\sim 1\%$ independent of position.

Wavelength calibration. The wavelength calibration was performed using between 65-100 arc lines depending on the instrumental configuration. They were fitted with a 5^{th} order polynomial that led to a typical RMS dispersion of 0.1-0.25 Å.

S-distortion, alignment of the spectra. During the spectroscopic observations, the galaxies were not perfectly aligned with the rows of the detector. This effect is crucial when measuring gradients of any type (rotation curves, velocity dispersion profiles or line-strength indices). The correction of this effect was performed using a routine that found the position of the galaxy center as a function of wavelength, fitted all these positions with a low order polynomial and straightened the spectra using that polynomial. This alignment was done with a technique that minimised the errors due to the discretization of the signal. This technique consists of adopting a more realistic distribution of the light in each pixel than just assuming it to be constant. To achieve this the signal in each pixel is fitted with a second order polynomial using the available information in the adjacent pixels.

Sky subtraction. The sky subtraction is critical for studies where the spectra are analysed at light levels corresponding to only a few per cent of the sky signal, as in our case. For each galaxy observation a sky image was generated fitting the data at each wavelength with a first order polynomial in regions at both sides of the galaxy close to the ends of the slit (which has a length of 3.7 arcmin on the WHT and 3.3 arcmin on the INT). This was possible since for all targets except M32 the galaxy filled only a small region of the slit, so this synthetic sky image was free from contamination from the galaxy. For M32, we observed a separate sky frame moving the telescope from the coordinates of the galaxy to a position $\Delta\alpha$ =-416" (West), $\Delta\delta$ =-459" (South) far enough from M32 to avoid its light but with the same level of contamination from M31.

Extinction correction. Atmospheric extinction was calculated using the extinction curve for El Roque de los Muchachos Observatory (www.ing.iac.es/Astronomy/observing/manuals/ps/tech_notes/tn031.pdf). The Galactic extinction was corrected using the curve of Fitzpatrick (1999) and the reddening from Schlegel et al. (1998) listed in Table 6.2.

Flux calibration. The relative flux calibration of the spectra was performed using the observed stars in common with the MILES library (Sánchez-Blázquez et al. 2006c) for the optical spectra, and with the CaT library (Cenarro et al. 2001) for the near infrared. For each observed star we obtained a flux calibration curve. All of them were averaged to obtain one unique flux curve for each run and instrumental configuration. The deviations of each flux calibration curve from the averaged one were introduced as uncertainties in the error spectra. The typical deviation was of 2% reaching $\sim 7\%$ in the first and last $\sim$150 Å of each setup spectra where the noise is the highest.

6.2.5 Measurement of the kinematic parameters

The stellar kinematics of galaxies (radial velocities and velocity dispersions) were calculated using the routine MOVEL included in R$_{\rm E}$D$^{\rm uc}_{\rm m}$E package (Cardiel 1999). This routine is based on the Fourier quotient method described by Sargent & Turner (1977) and refined with the OPTEMA algorithm (González 1993) that allows us to overcome the typical template mismatch problem. In order to do this, a number of stars of different spectral types and luminosity classes were introduced

in the program to create a model galaxy. These stars were of spectral type B9, A0, A3V, G0, G2III, G5III, G8III, G9III, K0III, K0I, K2III, K3III, M0III and M2III. The model galaxy was created and processed in parallel to the galaxy spectrum. To build the model galaxy all the template spectra were scaled, shifted and broadened according to a first guess of γ (mean line-strength), v (radial velocity) and σ (velocity dispersion). Then the algorithm looked for the linear combination of these template stars that best matched the observed galaxy spectrum. The best linear combination of observed stars was chosen as the one that minimises the residuals between the galaxy spectrum and the broadened optimal template. This provided a first model galaxy with a first kinematic output (γ, v and σ). This model galaxy was then improved using this new guess of kinematic parameters. The process was iterated until it converged. The emission lines, found only for the field dwarf galaxies, and some large sky line residuals, only present in some cases, were masked, so that the program did not use them for the minimisation of the residuals.

To minimize template mismatch effects, it is essential to use as templates a variety of spectral types and luminosity classes which are representative of the stellar population of the observed galaxy; as we will discuss in Section 6.2.5.4, small differences in ages and metallicities could lead to a partial fit of the strongest lines and therefore affect the derived velocity dispersion of the galaxy.

It is also important to check whether the observed stars were filling the slit during the observation. If they were not, the instrumental profile would not affect them in the same way as in the galaxies, and as a consequence, the σ that one would measure for the galaxy would be $\sqrt{\sigma_{inst}^2 + \sigma_{gal}^2}$, where σ_{gal} is the intrinsic velocity dispersion of the galaxy and σ_{inst}, in this case, is the quadratic instrumental difference between the galaxies and the stars.

To correct for this effect the physical slit width[2] is required. We calculated it from the spatial scale and the FWHM (in pixels) of the arc lines, which illuminate homogeneously the slit. To see whether the stars were filling the slit completely we checked that the FWHM of their spatial profile was larger than the physical slit width. If this was not the case, the spatial profile of the star was broadened accordingly. Although this introduced some uncertainties, the data quality improved by making this correction. The value of σ measured and adopted in this work is thus the intrinsic velocity dispersion of the galaxy corrected for possible instrumental effects.

Figure 6.6 shows a typical fit of the observed central spectral of a galaxy and the corresponding optimal template broadened with a gaussian with the derived dynamical parameters. The errors in velocity and σ were computed through Monte-Carlo simulations, repeating the whole process (including the derivation of the optimal template) for 100 simulated galaxy spectra created using the error spectra obtained during the reduction process. The observed and simulated spectra perfectly match.

6.2.5.1 Kinematic parameter profiles

To measure kinematic gradients it is important to determine the minimum S/N needed to measure reliable radial velocities and velocity dispersions. To do that we have designed and carried out a test exercise based on Monte-Carlo simulations that constraints the errors and systematic effects in the measurement of radial velocities and velocity dispersions on fake galaxy spectra with known

[2]During the observation an indicative width of the slit is selected by the user through a web interface.

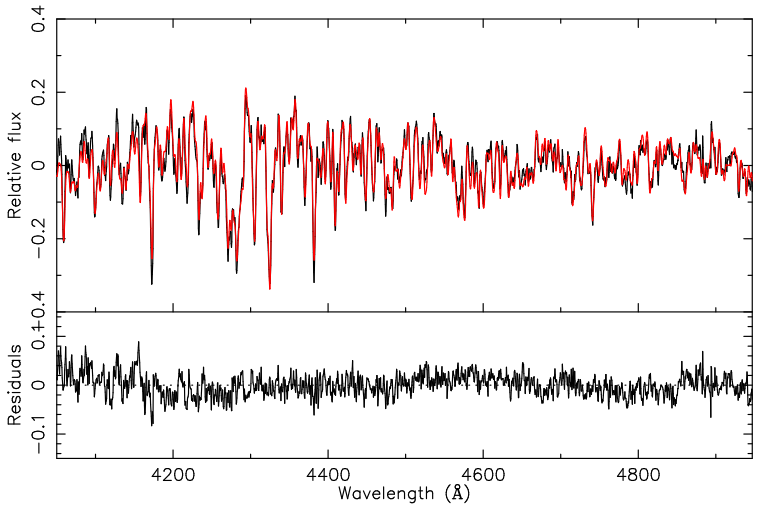

Figure 6.6: Example of the fit computed by MOVEL. Upper panel: in black, the central spectrum of VCC523. The spectrum has been continuum subtracted and normalised. The optimal template that fits the galaxy is shown in red, a linear combination with different weights of the stars observed with the same configuration as the galaxy. Bottom panel: residuals of the galaxy-composite template fit.

input kinematic parameters and different ages, metallicities and S/N ratios. This can be outlined in the following steps: i) from the simple stellar population models from PEGASE.HR (FWHM$\sim$ 0.55 Å; Le Borgne et al. (2003)) we selected a subset of 9 model spectra (3 ages and 3 metallicities) representative of quiescent dwarf galaxies: ages 1 Gyr, 4 Gyr, 10 Gyr; metallicities of $Z = 0.0$, $Z = -0.4$, $Z = -0.7$. The spectral resolution of these models are needed since in our bluer configuration the resolution is $\sim$ 1.6 Å; ii) Taking into account our instrumental resolution, each model was broadened and redshifted to match a set of input velocity dispersions, σ_i, (9 values between 20 km s^{-1} and 60 km s^{-1} in steps of 5 km s^{-1}) and radial velocities, v_i, (800 km s^{-1} and 1500 km s^{-1}, typical values of Virgo cluster members). This amounts a total of 162 model spectra. iii) For each one of the above spectra we added different levels of random noise to match S/N ratios of 10, 15, 20, 25, 30 and 50, hence ending up with 972 model galaxy spectra. iv) For each simulated galaxy spectrum we run exactly the same MOVEL procedure as we did for our dE galaxy sample, using the same template stars and MOVEL parameters. 100 Monte-Carlo simulations for each model galaxy were carried out to get reliable errors of the derived kinematic parameters, σ_o and v_o obtained as the mean value of the 100 Monte-Carlo simulations in each case. Since the input kinematics σ_i and v_i are set by construction, comparisons and reliability analysis are immediate to perform.

The above procedure was carried out for each instrumental configuration in each of the 5 different spectral regions. The results obtained are shown in Figures 6.7, 6.8 and 6.9.

After correcting for any systematic offsets in radial velocity and velocity dispersion due to small intrinsic differences between PEGASE.HR models and our observed stars, we have analysed the simulations looking at the relative differences between the measured values and the parameters introduced in the simulated galaxies ($\Delta v/v = (v_o - v_i)/v_i$ and $\Delta\sigma/\sigma = \sigma_o - \sigma_i)/\sigma_i$). Figures 6.7, 6.8 and 6.9 show these differences as a function of S/N in the wavelength range 4100-4900 Å, a range in common between the WHT and INT observations and where lines as important as the G-band are located. The error bars in these 3 Figures show the relative uncertainties obtained by MOVEL as the RMS scatter resulting from the 100 Monte-Carlo simulations for each model

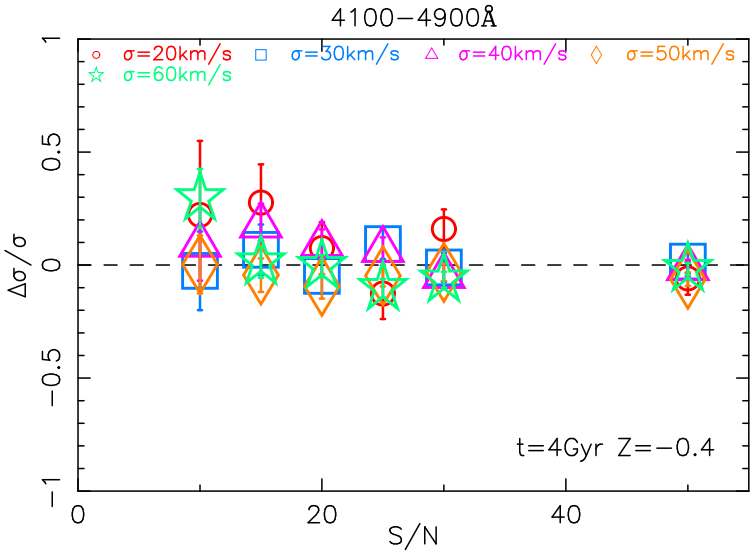

Figure 6.7: Simulations to study the minimum S/N ratio to obtain reliable measurements of the velocity dispersion. It is plotted $\Delta\sigma/\sigma$ (defined as $(\sigma_o - \sigma_i)/\sigma_i$), the relative error introduced when measuring the σ of a galaxy as a function of S/N ratio. Different colours show different σ for the simulated galaxies. Done assuming a stellar population of 4 Gyr and $Z = -0.4$.

galaxy.

In Figure 6.7 we study the influence of the S/N ratio and the instrumental resolution on the measurement of the velocity dispersion of a galaxy. Each point represents a galaxy of similar stellar populations (age 4 Gyr and metallicity -0.4) but different velocity dispersion (from 20 to 60 km s^{-1}). As expected, the errors increase dramatically at the lowest S/N ratios. For low S/N ratios (S/N=10) offsets are found even for galaxies with high σ's, so the velocity dispersions derived at this S/N cannot be trusted. On the contrary, for S/N ratios higher than or equal to 15 we do not find statistically significant offsets, with the exception of measurements below half the instrumental resolution ($\sigma = 20$ km s^{-1}) where special care must be taken. Only for S/N larger than 20 the measured σ can be fully trusted for velocity dispersions as low as half the instrumental resolution.

Figure 6.8 presents the influence of the stellar populations on the measurement of the velocity dispersion of a galaxy. In the upper panel we show the effect of the age on a dwarf galaxy of $\sigma = 40$ km s^{-1} and $Z = -0.4$, while in the lower panel we show the effect of the metallicity for a galaxy with σ =40 km s^{-1} and 4 Gyr old. In this case, although the errors barely depend on metallicity, the age-dependence is crucial, and for populations as young as 1 Gyr the σ measurements are underestimated for a S/N ratio below 15.

In Figure 6.9 we analyse the effect of the stellar populations on the computation of the radial velocity. Neither a change in the velocity dispersion nor in the metallicity have appreciable effects on this variable. Only the age of the stellar population have appreciable influence on the determination of the radial velocity whenever the age is young, around 1 Gyr. The uncertainty induced by age variations, however, is small, $\leq 1\%$, thus rotation velocities can be accurately measured down to S/N$\sim$10.

In Figure 6.10 we plot the expected RMS error (i.e. RMS of the average of all the simulations) as a function of S/N ratio in order to have a statistical estimate of the uncertainty. The

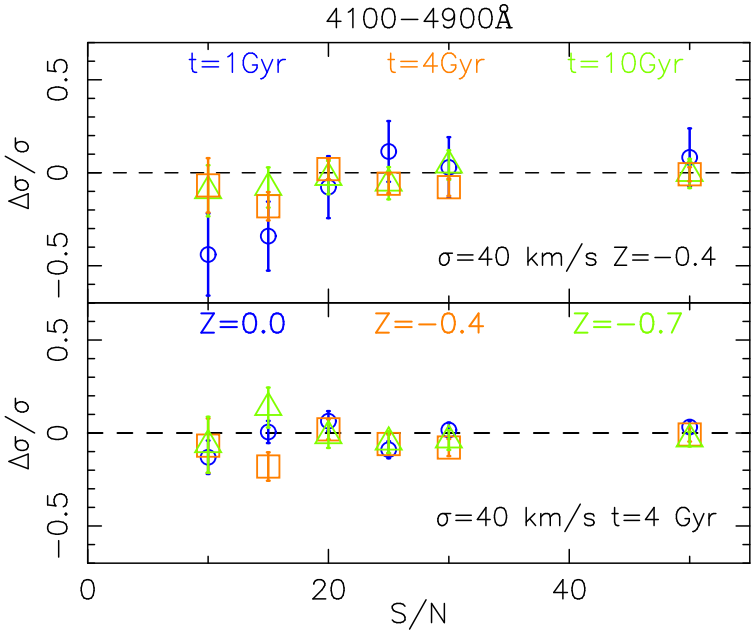

Figure 6.8: Simulations to study the dependence of the stellar population of the galaxy on the measurement of its velocity dispersion. We plot the relative offsets found between the measured σ and the velocity dispersion introduced in the simulated galaxy as a function of the S/N ratio. In both panels a typical σ of 40 km s^{-1} has been considered. In the upper panel we fix the metallicity of the galaxy to -0.4 and study the influence of the age of the stellar population. In the lower panel the parameter fixed is the age to 4 Gyr, and we analyse the influence of the metallicity on σ.

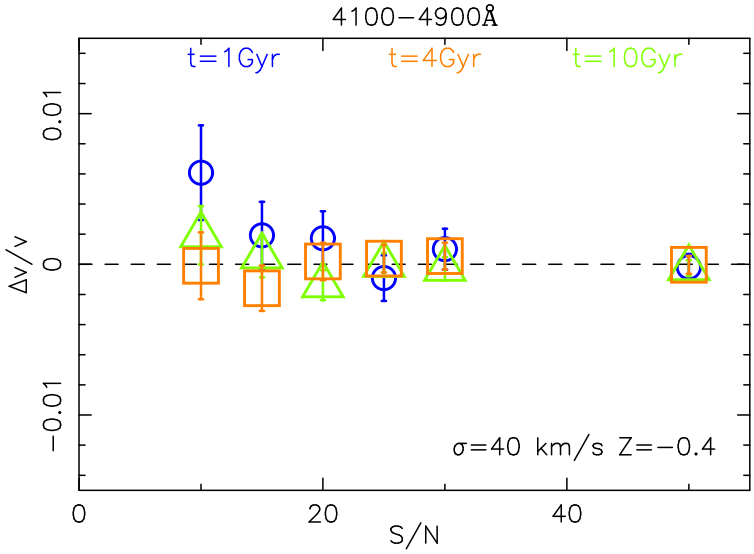

Figure 6.9: Simulations to study the influence of the stellar populations and the S/N ratio on the measurement of the radial velocities. We plot the relative uncertainty when measuring the radial velocities ($\Delta v/v$, defined as $(v_o - v_i)/v_i$) as a function of the S/N ratio. Only the results for the radial velocity v =1500 km s^{-1} are shown because the offsets and errors found are independent of the radial velocity of the galaxy. The results plotted are for a typical dwarf galaxy with velocity dispersion of 40 km s^{-1} and metallicity -0.4. The velocity dispersion does not have any effect on the measurement of radial velocities nor the metallicities. Note the different scale in the y-axis compared to Figures 6.7 and 6.8.

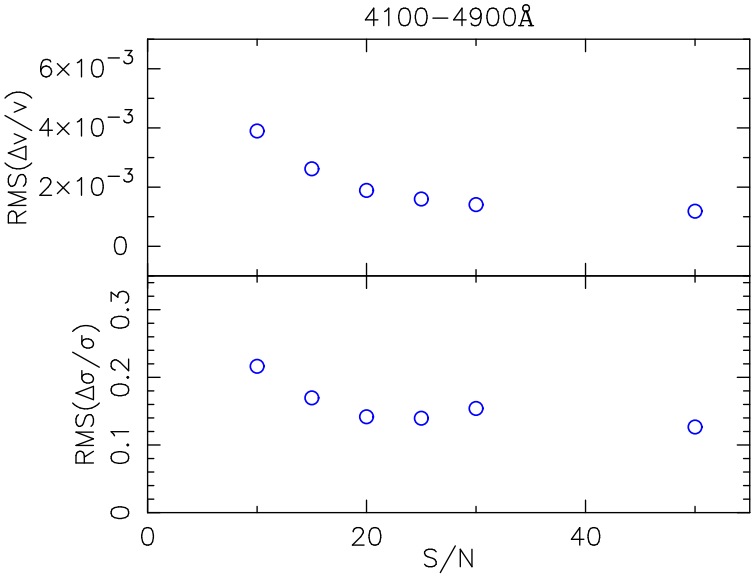

Figure 6.10: Total scatter in the differences found for the 972 simulations computed as a function of the S/N ratio. In this Figure all models for all stellar populations and velocity dispersion parameters have been used.

average of all the simulations (corresponding to different velocity dispersions, ages and metallicities) for each S/N, takes into account that for a target galaxy we do not have a priori information about either its velocity dispersion or the parameters of the stellar population.

Figures 6.7-6.10 clearly show that data with S/N ratios below 15 might induce errors as large as 22% in the determination of σ, in particular for small velocity dispersions (σ ∼20 km s^{-1}), while only 0.4% for radial velocities.

All these tests have been computed for the different wavelength ranges covered by our survey and the results obtained are rather similar. For the red arm of ISIS, where the instrumental resolution is larger, we obtain similar results as those shown in the blue arm (Figures 6.7-6.10) but with slightly larger uncertainties.

These simulations show that radial velocities can be computed with spectra of S/N as low as 10 given that the uncertainty is always below 1%. However, in the study of velocity dispersions, we must discard any measurement with S/N below 15 because σ is, in this case, highly dependent on age and not reliable for σ as low as half the instrumental resolution.

When running the MOVEL algorithm as a function of galaxy radius, we fitted the optimal template at every radius, rather than using the central optimal template, in order to improve the fit. As a result, the optimal templates turn out to be radial dependent. The differences, however, are not very large, because in the linear combination of templates, G-stars always contribute with the highest weight.

Due to the different instrumental configurations used in the observation campaigns (see Table 6.1), more than one kinematic profile per galaxy was obtained. These profiles, consistent within the errors, were averaged to produce a single, high S/N profile per galaxy (see Figure 6.11).

The recessional velocity of each single galaxy, removed for the determination of the rotation curve (Figure 6.11), has been determined by averaging, with a weighted mean, the recessional velocity measured in each single position along the radius. This improved technique for measuring

Table 6.3: Kinematic profiles for VCC990.

R_v ($''$)	v (km s^{-1})	R_σ ($''$)	σ (km s^{-1})
-5.43	1.8 $\pm$ 5.5	-4.98	36.0 $\pm$ 6.2
-3.56	16.8$\pm$ 6.4	-2.36	47.2 $\pm$ 6.0
-2.58	9.8$\pm$ 6.3	-1.38	39.2 $\pm$ 5.4
-2.00	10.5$\pm$ 6.4	-0.80	35.8 $\pm$ 4.6
-1.60	1.7$\pm$ 6.2	-0.40	32.5 $\pm$ 3.5
-1.20	-6.3$\pm$ 4.4	0.00	42.2 $\pm$ 3.1
-0.80	3.9 $\pm$ 2.7	0.40	41.3 $\pm$ 2.8
-0.40	0.1 $\pm$ 2.3	0.80	39.7 $\pm$ 3.6
0.00	6.8 $\pm$ 2.0	1.38	37.7 $\pm$ 3.9
0.40	2.2 $\pm$ 2.4	2.36	36.1 $\pm$ 8.5
0.80	1.0 $\pm$ 3.1	4.97	37.4 $\pm$ 5.6
1.20	-5.2$\pm$ 5.2		
1.60	-11.8$\pm$ 5.6		
2.00	-25.3$\pm$ 6.4		
2.58	-17.1$\pm$ 7.2		
3.56	-29.6$\pm$ 5.7		
5.42	-25.3$\pm$ 6.2		

NOTES: Column 1: radius for the rotation speed profile. Column 2: rotation velocities. Column 3: radius for the velocity dispersion profile. Column 4: velocity dispersions. All the kinematic profiles are electronically available.

recessional velocities (listed on Table 6.4) can be applied since the rotation curves are symmetrical.[3]

Table A.1 gives an example of the tables electronically available with the values of the kinematic profiles.

6.2.5.2 Central velocity dispersion and maximum rotational velocity

To compute the central velocity dispersion (σ) we shifted all the spectra to the same wavelength scale using the rotation curves displayed in Figure 6.11, and we coadded all the individual spectra up to one effective radius. The typical S/N ratio for the spectrum where the central σ is computed is $\sim$60 $^{-1}$. These results are shown in Table 6.4.

The maximum rotational velocity (v_{max}) was calculated as the weighted average of the two highest velocities along the major axis on both sides of the galaxy at the same radius (for non-symmetric profiles at least three values were required). As a consequence values with larger errors weight less than those with smaller errors. For each galaxy these values are presented in Figure 6.11 as purple squares. We show in Appendix 6.2.10 that, given the uncertainty, all galaxies with $v_{max} < 9$ km s^{-1} can be considered non-rotators.

The ratio between these two kinematic measurements, the maximum rotation velocity v_{max} and the velocity dispersion σ, is called anisotropy parameter, v_{max}/σ, and it is used to study the

[3]Note that galaxies as VCC856, those with the poorest quality, have a non-zero central velocity.

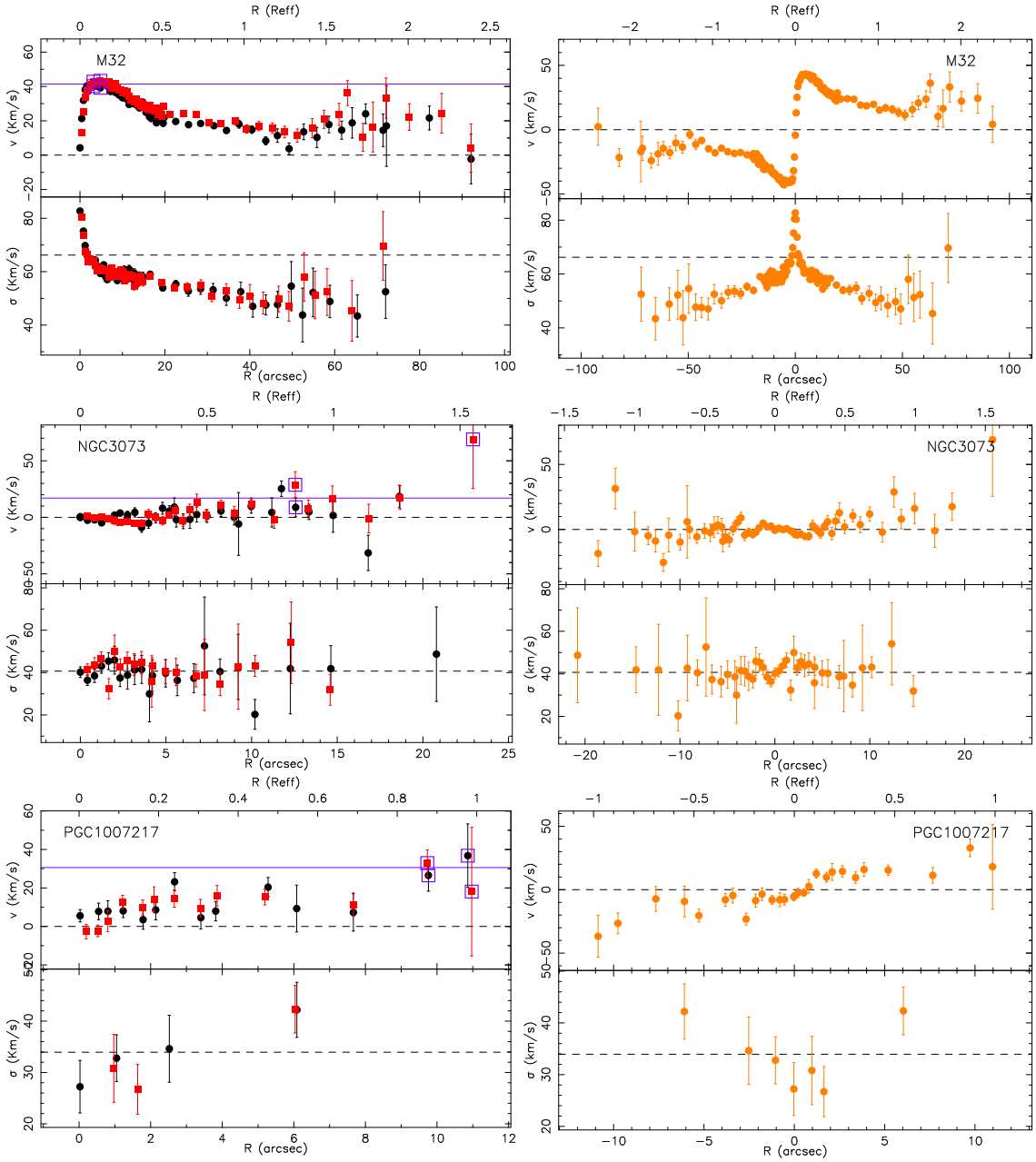

Figure 6.11: Kinematic profiles of the galaxy sample. Each diagram shows in the left upper panel the folded rotation curve of the galaxy and in the left bottom panel the folded velocity dispersion profile. The different sides of the galaxy are indicated with red squares and black dots. On the upper x-axis the radius is given as a fraction of the effective radius (R_{eff}) of each galaxy in the I band (see Section 6.2.6). The purple open squares show the points used to calculate the maximum rotation for each galaxy and the purple line indicates this v_{max}. The dashed line in the velocity dispersion profiles indicate the central σ computed up to the R_{eff} (see Table 6.4). In the right panels the not-folded kinematical profiles are plotted.

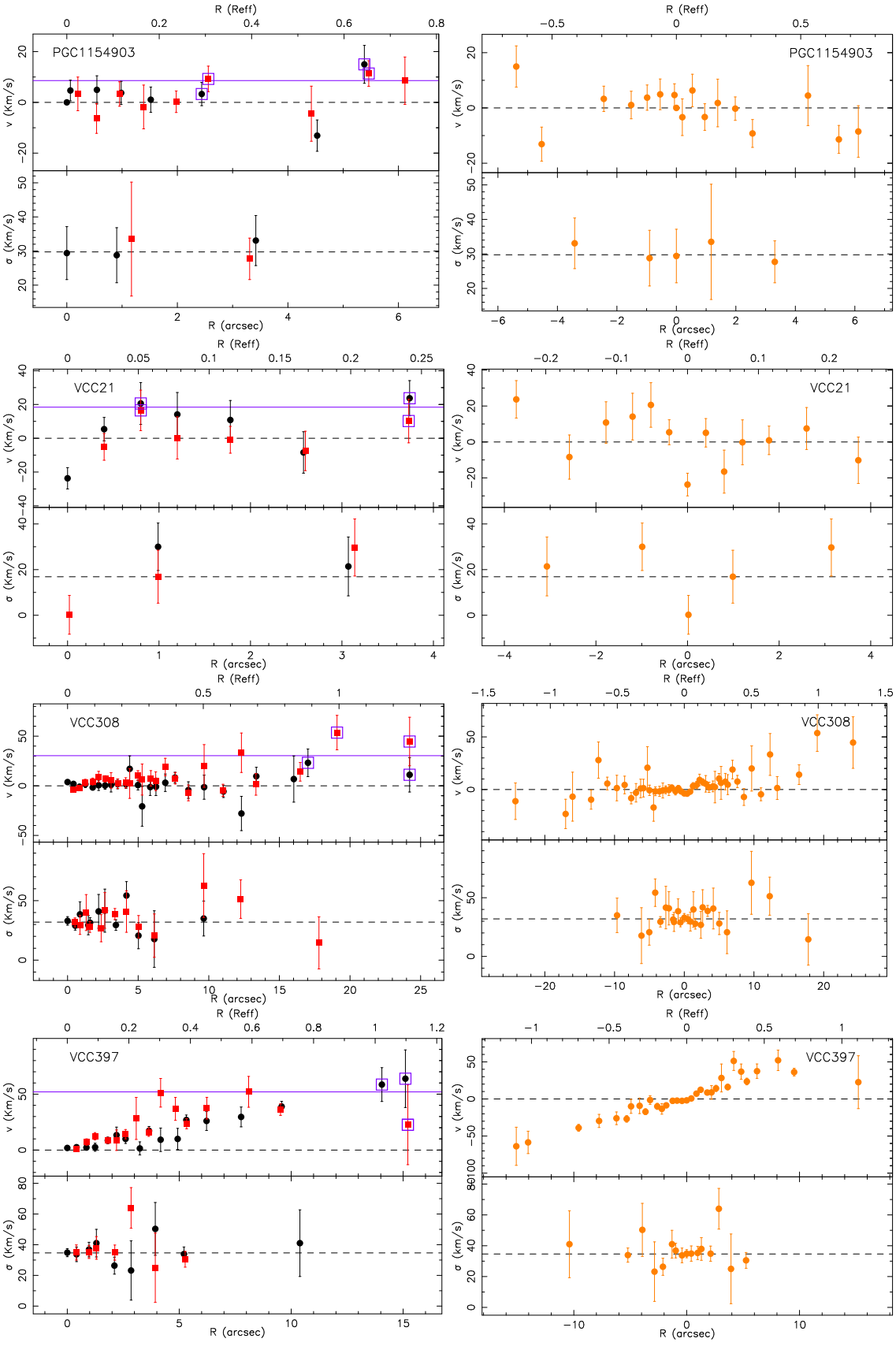

Figure 6.11: Continued

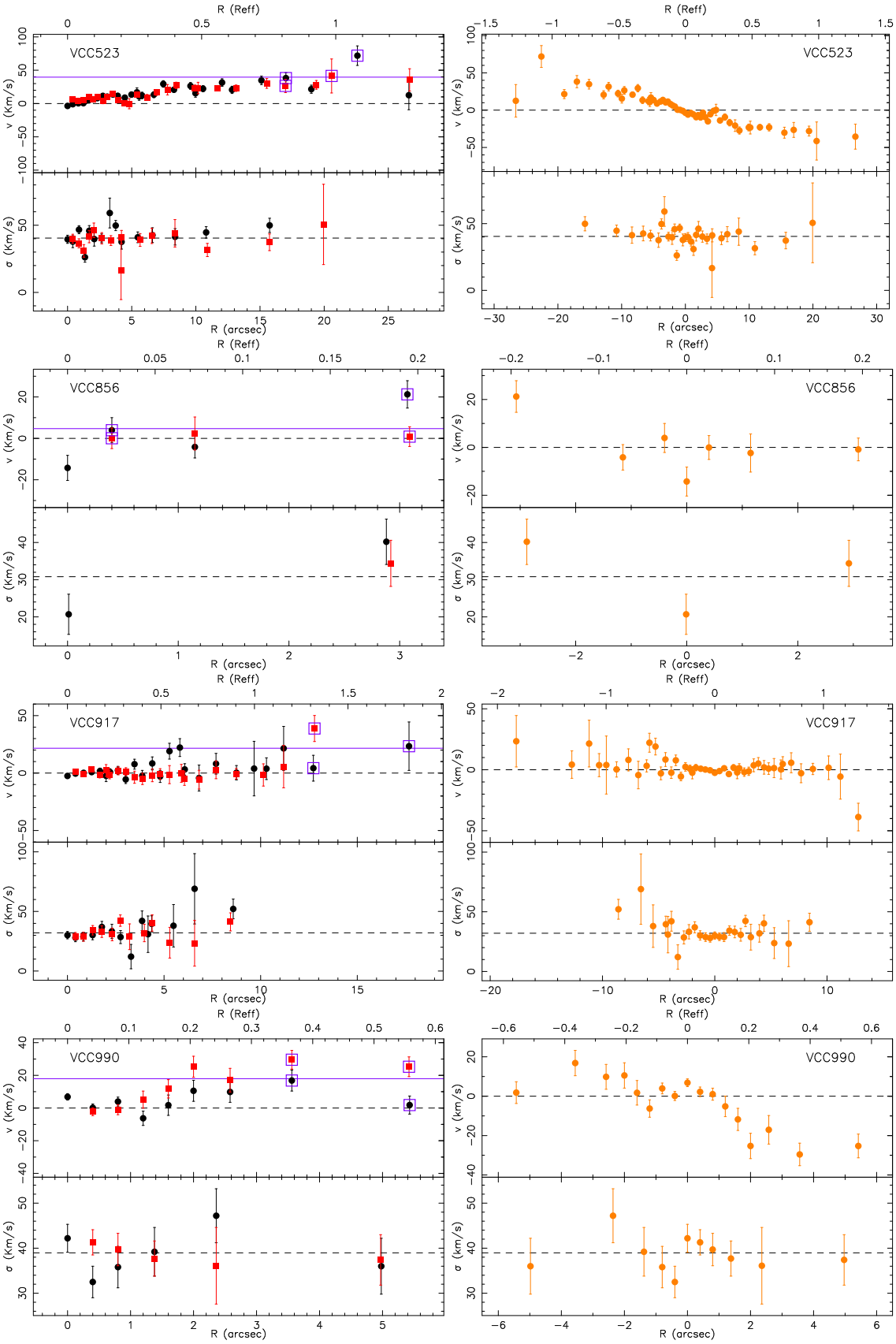

Figure 6.11: Continued

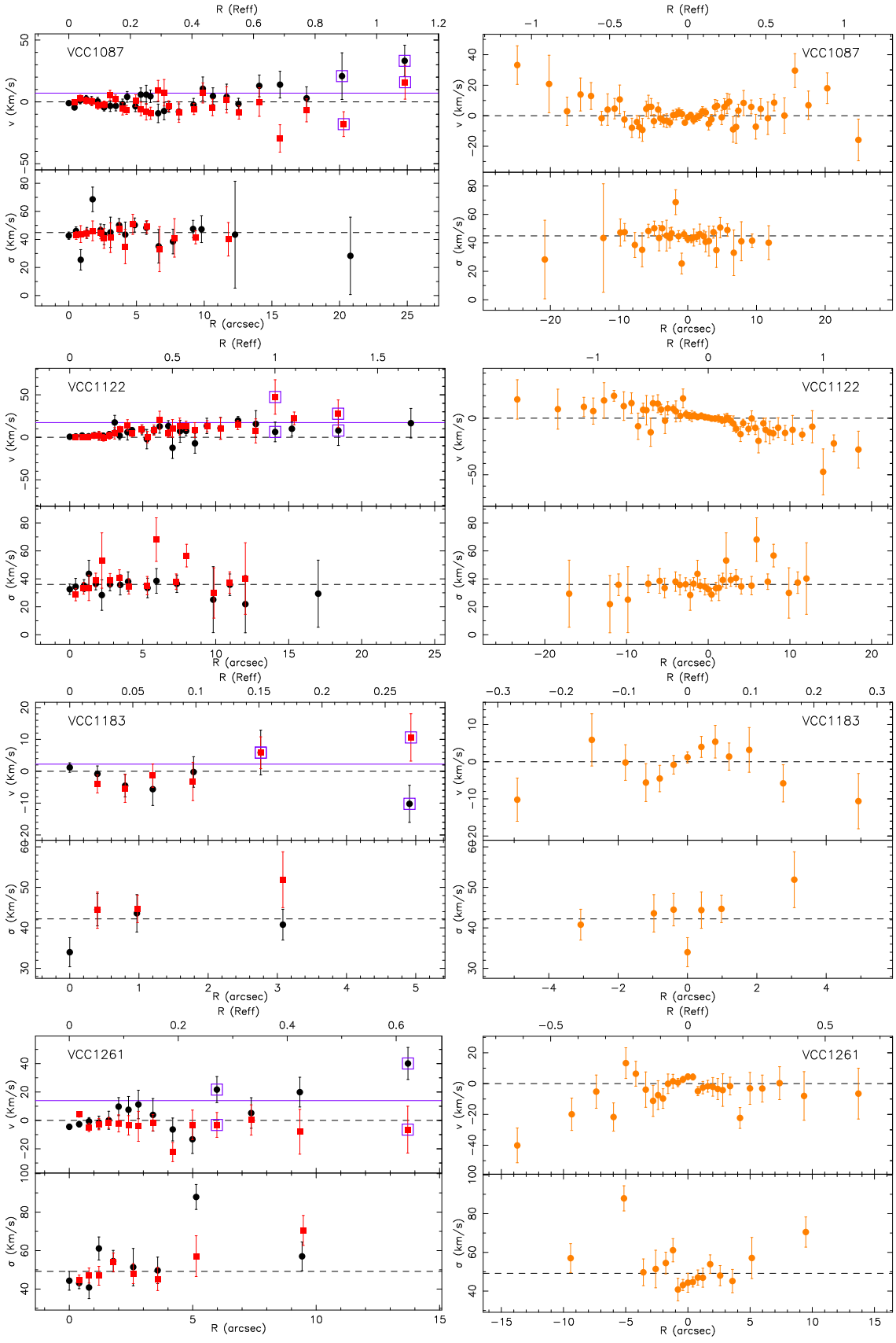

Figure 6.11: Continued

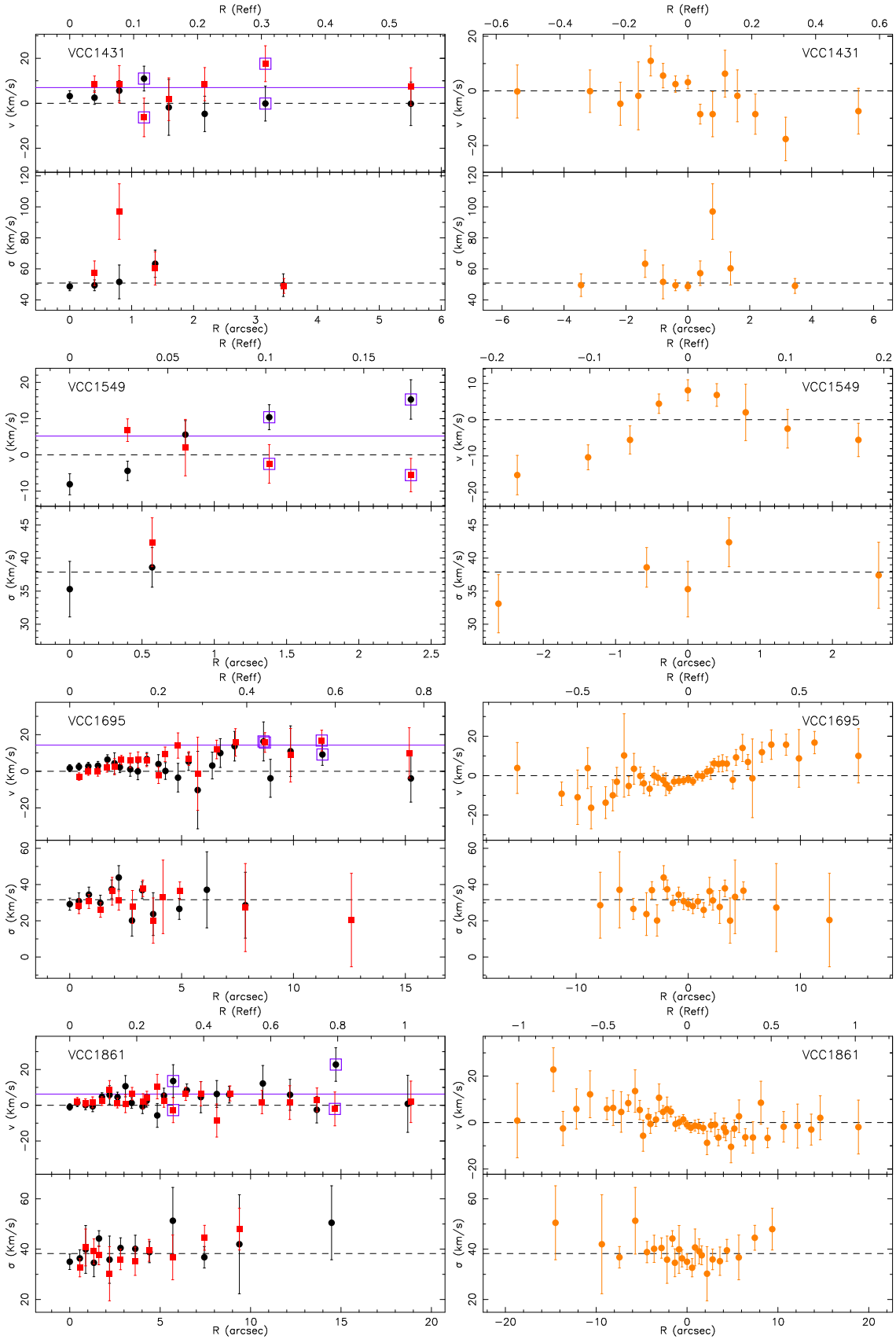

Figure 6.11: Continued

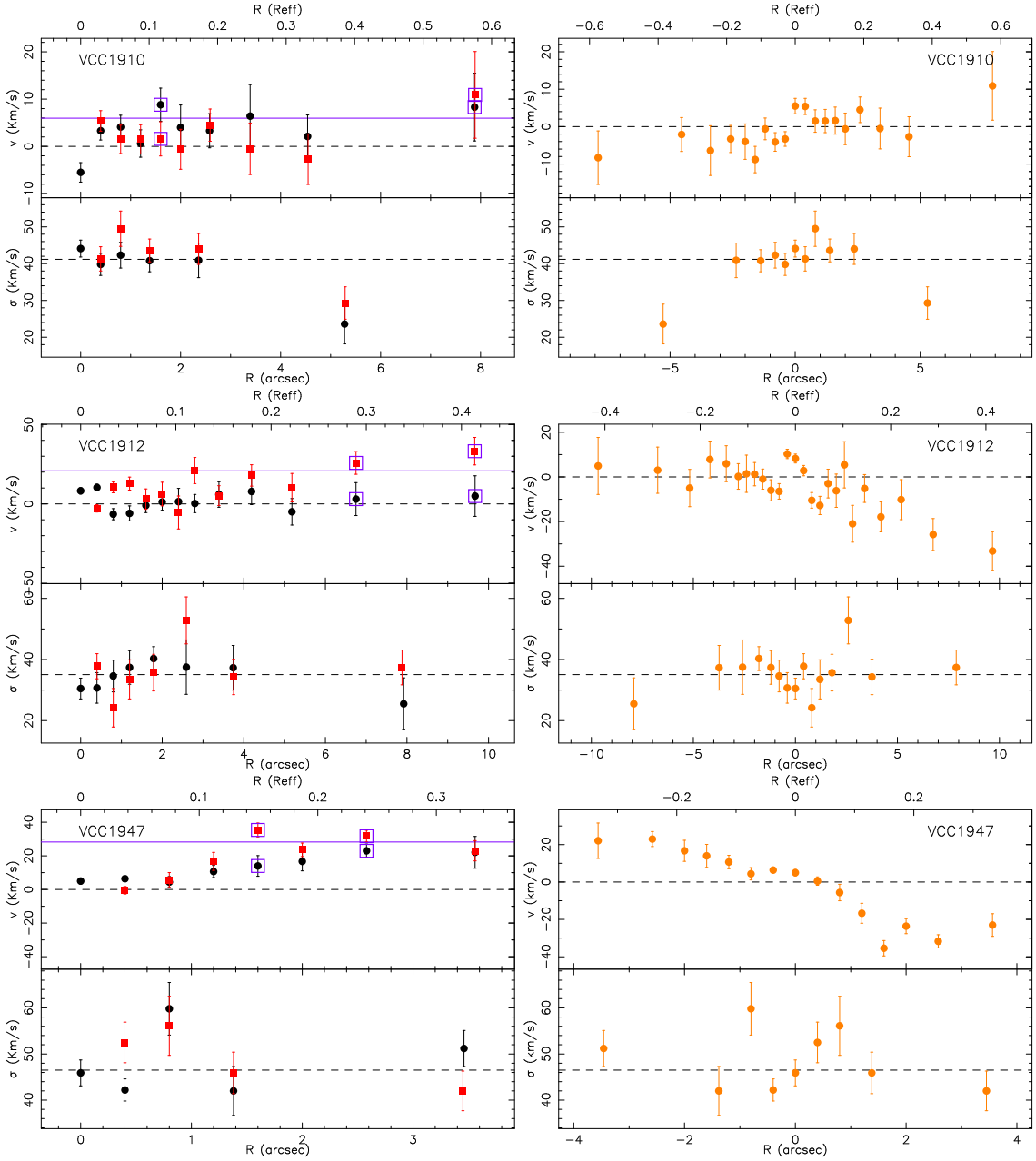

Figure 6.11: Continued

Table 6.4: Kinematic parameters.

Galaxy	σ (km s^{-1})	v_{max} (km s^{-1})	$(v_{max}/\sigma)^*$	v_{rad} (km s^{-1})
PGC1007217	35.2± 0.9	30.6± 5.0	2.3 ± 0.4	1592.3 ± 3.3
PGC1154903	23.1± 4.1	8.6± 2.6	0.5 ± 0.2	1156.3 ± 6.4
NGC3073	39.8± 0.3	17.1± 6.7	1.1 ± 0.4	1168.9 ± 2.5
VCC21	26.1± 4.0	18.4± 5.9	0.9 ± 0.3	463.6 ± 9.2
VCC308	31.7± 1.2	30.4± 8.6	1.0 ± 0.3	1515.3 ± 3.2
VCC397	29.9± 1.1	52.0± 11.6	2.5 ± 0.6	2434.9 ± 2.4
VCC523	45.8± 0.7	39.6± 5.7	1.5 ± 0.2	1515.7 ± 2.6
VCC856	29.6± 2.5	9.7± 1.9	1.0 ± 0.2	980.2 ± 1.9
VCC917	31.4± 1.4	21.6± 7.5	0.8 ± 0.3	1236.2 ± 2.4
VCC990	40.6± 1.0	26.3± 1.6	0.9 ± 0.1	1691.5 ± 2.1
VCC1087	48.3± 0.7	7.1± 6.4	0.2 ± 0.2	644.6 ± 3.2
VCC1122	37.2± 0.8	17.3± 7.7	0.5 ± 0.2	447.8 ± 2.7
VCC1183	41.3± 1.2	10.1± 2.8	0.5 ± 0.1	1290.7 ± 2.3
VCC1261	51.8± 0.9	13.9± 5.2	0.4 ± 0.1	1806.4 ± 2.1
VCC1431	54.1± 1.2	7.0± 3.6	0.1 ± 0.1	1472.8 ± 3.1
VCC1549	38.9± 1.9	5.2± 2.2	0.3 ± 0.1	1377.3 ± 2.9
VCC1695	28.7± 1.1	14.3± 3.1	0.9 ± 0.2	1706.0 ± 3.0
VCC1861	40.4± 0.9	6.3± 4.3	0.2 ± 0.1	617.2 ± 2.6
VCC1910	39.0± 1.1	6.0± 2.3	0.4 ± 0.2	178.6 ± 2.2
VCC1912	37.1± 1.0	20.8± 4.5	0.5 ± 0.1	-110.5 ± 2.0
VCC1947	45.3± 1.1	28.3± 2.1	1.1 ± 0.1	956.3 ± 1.8

NOTES: Column 1: galaxy name. Column 2: central velocity dispersions computed within the R_{eff}. Column 3: maximum rotation velocities. The v_{max} adopted for VCC0856, VCC0990 and VCC1183 have been measured in the rotation curves of Chilingarian (2009) due to their larger extent (see Section 5.3). Column 4: anisotropy parameter corrected from inclination. Column 5: mean radial velocity observed. Values in agreement with those of NED database.

rotational/pressure support of the galaxies. In Table 6.4 we show $(v_{max}/\sigma)^*$, the anisotropy parameter corrected from the inclination. This correction is done following the expression $(v_{max}/\sigma)^* = \frac{v_{max}/\sigma}{\sqrt{\epsilon/(1-\epsilon)}}$, where ϵ is the ellipticity. Note that for those galaxies with ellipticity close to zero, no correction can be done because they are nearly face on. We choose a conservative value of $(v_{max}/\sigma)^* = 0.8$ as the limit between pressure and rotationally supported systems in order to include those objects that, within the errors, are consistent with being flattened by rotation. This assumption is justified by the fact that the measured v_{max} is a lower limit since the rotation curves are still rising.

6.2.5.3 Comparison to the literature

Displaying simultaneously the kinematic profiles measured in this work with those of other authors (Figure 6.12), one sees that the radial extent of the kinematic curves varies from one work to another. In addition, the offsets found in the velocity dispersions are not always consistent within the errors (Figure 6.13). These two differences are important, because different radial extents

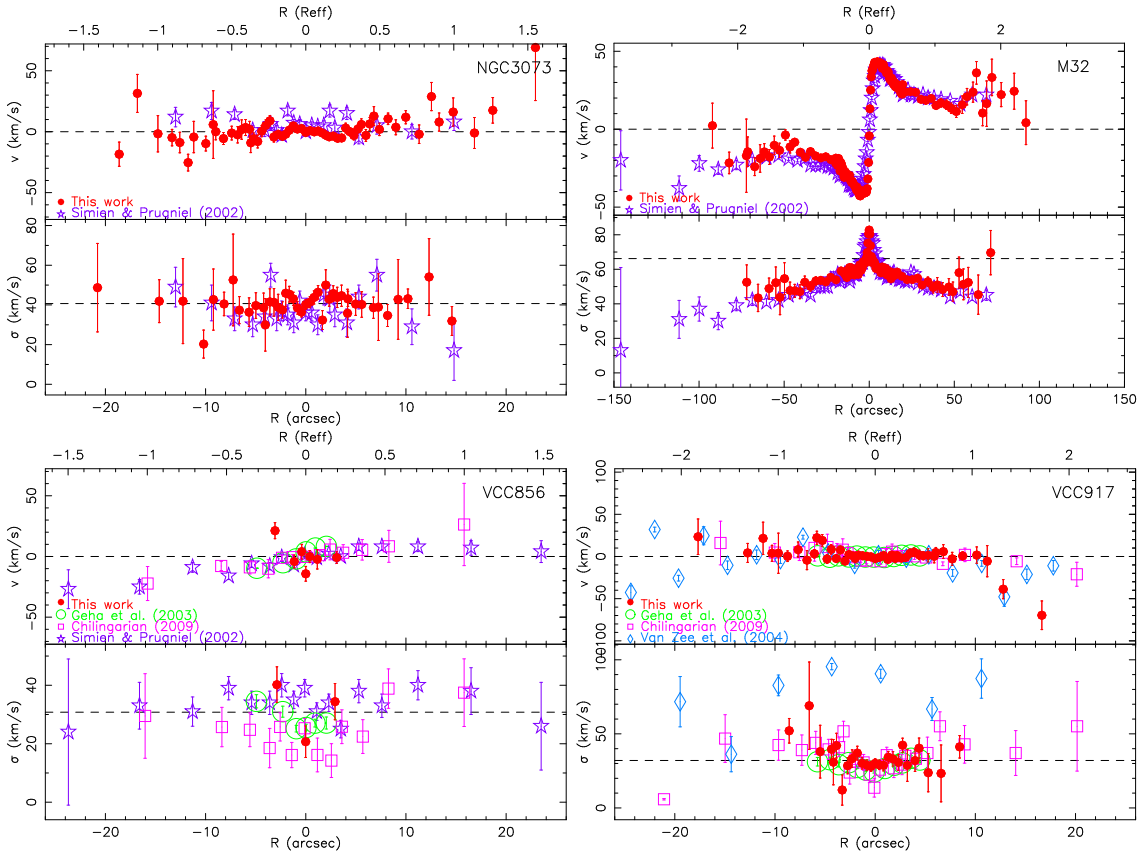

Figure 6.12: Comparison of our kinematic profiles with other works. In each diagram it is shown the rotation curve (upper panel) and the velocity dispersion profile (lower panel). The bottom X-axis is measured in arcseconds and the upper X-axis is measured as a fraction of the effective radius (R_{eff}) of each galaxy in i band (see Section 6). For Van Zee et al. (2004) we only present their velocity profiles for MgbI, more similar in wavelength to our data.

lead to different maximum rotation velocities and offsets in the velocity dispersion profiles lead to different central σ values.

6.2.5.4 *Velocity dispersions*

There are two factors that critically affect the measurements of the velocity dispersion of the galaxies: the not identical instrumental σ for the stars and the galaxies and the spectral types of the stars used to fit the width of the galaxy lines.

Caldwell et al. (2003) made their observations with a $\sigma_{inst} = 100$ km s^{-1}, too high to accurately measure velocity dispersions of typical dwarf galaxies, below 50 km s^{-1}.

Concerning the equality of the instrumental resolution in the templates and in the galaxies Chilingarian (2009) used simple stellar population (SSP) models of PEGASE.HR (Le Borgne et al. 2003), based on ELODIE (Prugniel et al. 2007) ($R = 10000$). In this case, the broadening of the SSP models to σ_{inst} of the galaxies must be cautiously done because σ_{inst} of the models is based on the mean value of the spectral resolution of the library they are based on, therefore small differences after the broadening between the SSP models and the galaxies can arise.

Continuing with the same effect, in the works of Pedraz et al. (2002) and van Zee et al.

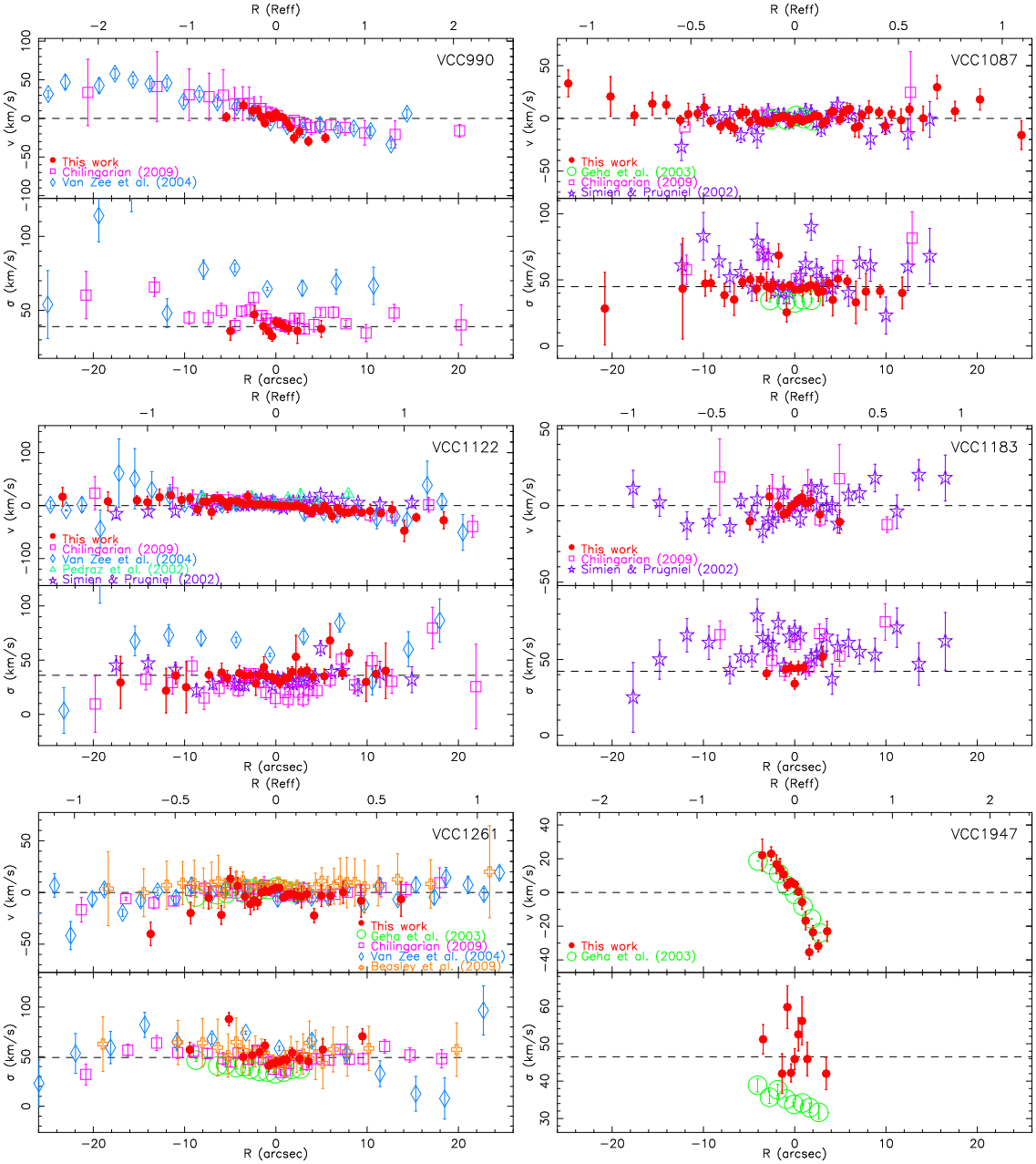

Figure 6.12: Continued

(2004b) the stars observed were not filling the slit because they were not defocused and the seeing was smaller than their slit width. But in the case of Geha et al. (2003) and Beasley et al. (2009), where their slit widths were 0.75" and 1.0" respectively, it is possible that some stars were filling the slit thanks to the seeing. However, in none of these works a correction was made to assure that the instrumental profile in the stars was the same as in the galaxies.

In reference to the templates used to perform σ, some of the authors mentioned above used only one star to fit the galaxy spectrum, and in such a case the fact that the template is not representative of the stellar population of the galaxy might lead to large errors. We have computed Monte-Carlo simulations to see the differences between fitting the galaxy spectrum with only one star and a linear combination of stars of spectral types from B to M, with different luminosity classes. The simulations consisted of a selection of PEGASE.HR models of 3 different ages (1 Gyr, 4 Gyr and 10 Gyr) and 3 different metallicities ($Z = 0.0$, $Z = -0.4$, $Z = -0.7$) with Salpeter IMF (Le Borgne et al. 2003); a total of 9 models. The stars used as templates were from MILES library (Sánchez-Blázquez et al. 2006c). First of all we checked that after broadening the models (originally at FWHM=0.55 Å) to the MILES resolution (FWHM=2.3 Å) we obtained $\sigma = 0$ km s^{-1} when running MOVEL, thereby showing that there was no zero point offset. Secondly, we broadened the models to 40 km s^{-1} to simulate dwarf galaxies of different stellar populations. And finally, we ran MOVEL using 3 different kinds of templates: only one K1III star (as in Geha et al. (2003)), only one G8III star (as in van Zee et al. (2004b)), and a linear combination of B to M stars with different luminosity classes (as in this work). To measure σ we have masked the Balmer lines, especially those bluer than H_δ to avoid possible problems due to emission lines. Our simulations show that a linear combination of different stars is the most accurate method to obtain the velocity dispersion of the galaxies, never finding an error above 25%, independent of the stellar population considered. Note that if a young population dominates the light of the galaxy (for ages of 1 Gyr and below), and a single G or K star is used as a template, an error up to 70% can be done. When a single star is used as template, a dependence on metallicity for young populations (1 or 4 Gyr) is also found, in the sense that decreasing the metallicity increases the uncertainty. This dependence is likely due to offsets introduced by the method employed to compute σ. The results obtained have been summarised in Table 6.5.

6.2.5.5 Rotation curves

Different criteria have been used in the literature to measure the maximum rotation velocity. The main difficulty here is to have an extended rotation curve that reaches a clear plateau where the maximum rotation can be measured. As this is not so easy for dEs, an objective criteria, independent of the shape of the rotation curve in each case, must be adopted. The different criteria used by the various authors have led to maximum rotational velocities that are nevertheless in the majority of the cases nearly consistent within the errors (Figure 6.14). The criterion used by Pedraz et al. (2002) is the same as the one adopted here. Although we achieved a radial extent of 23″ for VCC1122 and Pedraz et al. (2002) only 8″, the latter value was enough to reach the flat part of the rotation curve, and, as a consequence, both measurements of the maximum rotation are identical. The explanation for the differences found with Simien & Prugniel (2002) are mainly based on the fact that only two points were considered to obtain the maximum rotation in that paper. The differences with Geha et al. (2003) are due to the limitation of their data to the core of the galaxies, never reaching radii larger than 6″ (see Figure 6.12). The differences with van Zee et al. (2004b) and Chilingarian (2009) are related to a different radial extent of the rotation curves. Note that

Table 6.5: Uncertainties introduced when different templates are used to calculate the velocity dispersion of a dwarf galaxy with different stellar populations. $\Delta\sigma/\sigma$, defined in Figure 6.7, uses as σ_i 40 km s^{-1}.

	$\frac{\Delta\sigma}{\sigma}$x100		
Age (Gyr)	Z=+0.0	Z=-0.4	Z=-0.7
Linear combination of B to M stars			
1	15%	19%	1%
4	8%	18%	19%
10	7%	14%	23%
G8III			
1	32%	54%	71%
4	15%	18%	20%
10	17%	13%	11%
K1III			
1	29%	47%	59%
4	19%	18%	20%
10	17%	13%	11%

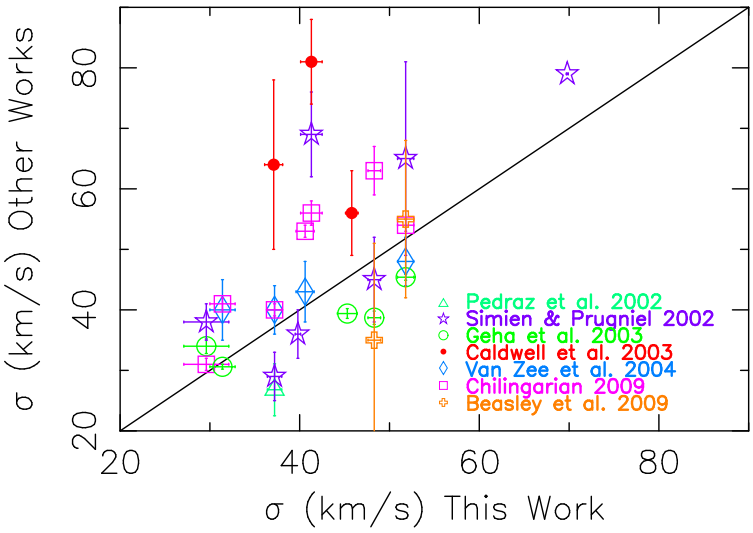

Figure 6.13: Comparison between the velocity dispersions measured in this work versus those of other authors. The colours and symbols are the same as in Figure 6.12. We add a comparison with Caldwell et al. (2003) (solid red points), who only measured central values and no kinematical profiles.

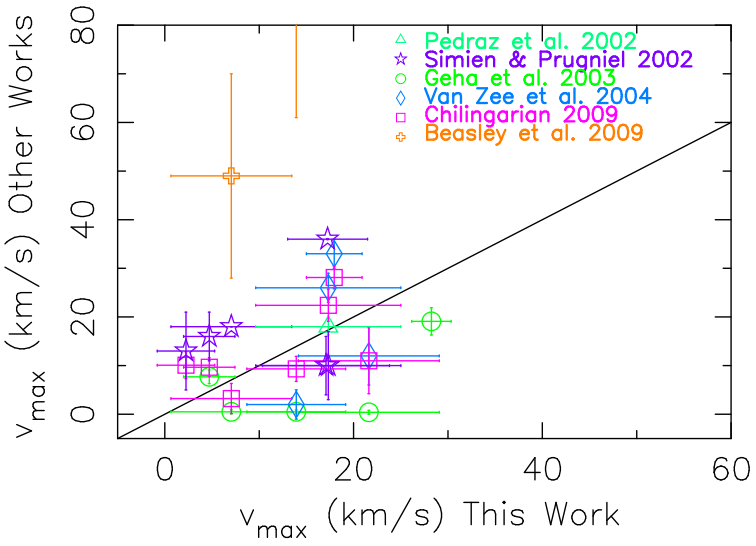

Figure 6.14: Comparison between the maximum rotational velocity measured in this work and those measured by other authors. Symbols and colours are the same as in Figure 6.12. VCC1261 from Beasley et al. (2009) is nearly outside the plot due to its enormous rotation: 105 ± 44 km s^{-1}.

Chilingarian (2009) does not calculate the maximum rotation, but we have applied our criterion to his rotation curves. Finally, the differences found with Beasley et al. (2009) are due to the fact that v_{max} is obtained from the analysis of Globular Clusters located up to $\sim 7R_{eff}$. When their kinematic determined from the stellar component using long slit spectroscopy along the major axis of the galaxy is compared to our data, the agreement is evident (Figure 6.12). The maximum rotation values adopted for the analysis (see Table 6.4) are our own values, except for VCC856, VCC990 and VCC1183, where the data come from Chilingarian (2009) since he obtained larger radii than us. Note that the values from Beasley et al. (2009) can not be adopted here because our work is dedicated to the analysis of the stellar component of dEs.

The comparison with Beasley et al. (2009), who finds rotation speeds much larger at $7R_{eff}$ (100 and 50 km s^{-1} higher for VCC1087 and VCC1261, respectively) than our data at the R_{eff}, indicate that the rotation curves of these galaxies are still rising.

6.2.6 Photometric parameters

In order to make a complete analysis of the kinematics, comparison with some photometric parameters is needed. For our study, we require I-band (Johnson-Cousins) total magnitudes and optical radii (R_{opt}, radius containing 83% of the total I-band luminosity (Catinella et al. 2006)) to study the shape of the rotation curves. Effective radii (R_{eff}, radius containing 50% of the total light) is needed to measure the extent of the radial profiles in physical units of the galaxy. Ellipticities (ϵ) are needed to make the appropriate corrections due to inclination. A parameter to measure the boxyness/diskyness of the isophotes (C_4) is also required to study the possible late-type origin of these dwarf early-type galaxies.

All these parameters have been obtained from i-band Sloan Digital Sky Survey (SDSS, York et al. (2000)) data release 6 (DR6, Adelman-McCarthy et al. (2008)) photometry. They have been

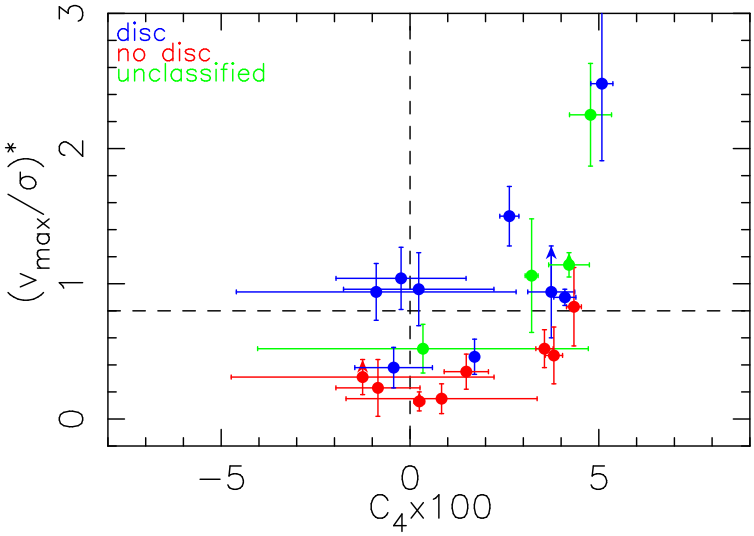

Figure 6.15: Correlation between the anisotropic parameter $(v_{max}/\sigma)^*$ and C_4x100. Colours indicate Lisker et al. (2006b) classification. The galaxies with v_{max} measured inside the central 6" are considered lower limits and are indicated with arrows. The horizontal dashed line at $(v_{max}/\sigma)^* = 0.8$ indicates a rough boundary between pressure and rotationally supported galaxies. The blue points are classified as having a disk in Lisker et al. (2006b), whereas for the red points no disk is found in that paper. See Appendix E.1 for a discussion.

calculated using the IRAF[4] task ELLIPSE as described in Appendix 6.2.11. The transformation from i-band (SDSS) to I-band (Johnson-Cousins) has been done assuming $m_I = m_i - 0.52 \pm 0.01$ mag (Fukugita et al. 1995).

6.2.6.1 C_4: boxyness/diskyness parameter

The boxyness/diskyness (C_4) parameter measures the deviations of the isophotes from a perfect ellipse. If $C_4 > 0$ the isophotes are disky, indicating that some disk substructure is present in the galaxy, and when $C_4 \leq 0$ the isophotes are boxy (Carter 1978; Kormendy & Bender 1996a). This parameter is independent from the surface brightness profile of the galaxy. The C_4 parameter, determined for our galaxies as described in Appendix E.1, is provided in Table 6.6.

Our C_4 classification for disky isophotes agrees in general with the morphological classification of Lisker et al. (2006a) as can be seen in Figure 6.15. Note that Lisker et al. (2006a) classified a galaxy as disky when disk features (spiral arms, edge-on disks, or bars) were detected after subtracting an axisymmetric light distribution from the original image or after unsharp masking. In this Figure we can see that the red dots, those galaxies classified as being without underlying structures in Lisker et al. (2006a), are grouped around $C_4 \leq 0$ (boxy or elliptical isophotes), while the blue dots (galaxies with some disky structure in Lisker et al. (2006a)) are all consistent with $C_4 > 0$ (disky isophotes). This justifies the use of the C_4 parameter to detect the presence of an underlying disk. Three exceptions are found and discussed in Appendix E.1.

In this respect, it is important to underline the correlation between C_4 and the anisotropic parameter evident in Figure 6.15, first found by Bender et al. (1988) for more massive elliptical galaxies.

[4]IRAF is distributed by the National Optical Astronomy Observatory, which is operated by the Association of Universities for Research in Astronomy, Inc., under the cooperative agreement with the National Science Foundation.

Table 6.6: Derived parameters.

Galaxy	d (Mpc)	M_I (mag)	ϵ	R_{eff} (")	C_4x100	Disk classification (L06b)
PGC1007217	20.23 ± 1.40	-17.39 ± 0.15	0.13 ± 0.05	11.11 ± 0.02	$4.8^{(*)} \pm 0.6$	—
PGC1154903	15.00 ± 1.10	-15.91 ± 0.16	0.34 ± 0.02	8.36 ± 0.04	0.3 ± 4.4	—
NGC3073	33.73 ± 14.44	-20.43 ± 0.93	0.14 ± 0.02	14.78 ± 0.03	$3.2^{(*)} \pm 0.2$	—
VCC21	16.74 ± 0.15	-17.78 ± 0.03	0.36 ± 0.03	15.48 ± 0.11	$3.7^{(*)} \pm 0.6$	Disk
VCC308	16.41 ± 0.32	-18.78 ± 0.05	0.04 ± 0.03	19.22 ± 0.04	0.2 ± 2.0	Disk
VCC397	16.41 ± 0.32	-17.62 ± 0.05	0.33 ± 0.03	13.75 ± 0.02	$5.1^{(*)} \pm 0.3$	Disk
VCC523	16.74 ± 0.15	-19.16 ± 0.03	0.25 ± 0.01	20.90 ± 0.03	$2.6^{(*)} \pm 0.3$	Disk
VCC856	16.83 ± 0.46	-18.49 ± 0.06	0.09 ± 0.03	15.82 ± 0.06	-0.2 ± 1.7	Disk
VCC917	16.74 ± 0.15	-17.39 ± 0.03	0.41 ± 0.02	9.68 ± 0.04	$4.3^{(*)} \pm 0.2$	No Disk
VCC990	16.74 ± 0.15	-18.27 ± 0.03	0.34 ± 0.02	9.73 ± 0.02	$4.1^{(*)} \pm 0.3$	Disk
VCC1087	16.67 ± 0.46	-18.94 ± 0.06	0.28 ± 0.03	22.74 ± 0.05	-0.9 ± 1.1	No Disk
VCC1122	16.74 ± 0.15	-17.94 ± 0.03	0.50 ± 0.04	14.06 ± 0.05	$3.8^{(*)} \pm 0.2$	No Disk
VCC1183	16.74 ± 0.15	-18.59 ± 0.03	0.22 ± 0.12	18.23 ± 0.01	$1.7^{(*)} \pm 0.0$	Disk
VCC1261	18.11 ± 0.50	-19.39 ± 0.06	0.37 ± 0.05	22.07 ± 0.03	$1.5^{(*)} \pm 0.6$	No Disk
VCC1431	16.14 ± 0.45	-18.47 ± 0.06	0.03 ± 0.01	10.32 ± 0.01	0.2 ± 0.1	No Disk
VCC1549	16.74 ± 0.15	-18.18 ± 0.03	0.16 ± 0.01	13.56 ± 0.05	-1.3 ± 3.5	No Disk
VCC1695	16.52 ± 0.61	-18.13 ± 0.08	0.22 ± 0.05	19.78 ± 0.10	-0.9 ± 3.7	Disk
VCC1861	16.14 ± 0.45	-18.57 ± 0.06	0.04 ± 0.02	18.52 ± 0.04	0.8 ± 2.5	No Disk
VCC1910	16.07 ± 0.44	-18.63 ± 0.06	0.14 ± 0.04	13.70 ± 0.02	-0.4 ± 1.0	Disk
VCC1912	16.74 ± 0.15	-18.62 ± 0.03	0.54 ± 0.06	23.34 ± 0.02	$3.6^{(*)} \pm 0.2$	No Disk
VCC1947	16.74 ± 0.15	-18.46 ± 0.03	0.23 ± 0.01	10.70 ± 0.02	$4.2^{(*)} \pm 0.5$	—

NOTES: Column 1: galaxy name. Column 2: distances in Mpc from Surface Brightness Fluctuations (SBF) for individual Virgo galaxies from Mei et al. (2007) when available, or the mean A/B Cluster distance from Mei et al. (2007) for the rest of them (note that E, N and S Clouds are East, North and South areas of Cluster A). The distance for NGC3073 from SBF by Tonry et al. (2001) and PGC1007217 and PGC1154903 distances are from NED/IPAC Database derived from redshift with $H_0 = 73 \pm 5$ km s^{-1} Mpc^{-1} (these two distances must be used cautiously). Column 3: Absolute magnitudes in I-band (Johnson-Cousins in AB system) converted from i-band measured in SDSS images using $m_I = m_i - 0.52$ mag. Column 4: ellipticities from i-band (SDSS) images. The quoted errors indicate the RMS scatter in the ellipticity between 3″ and the R_{eff}. Column 5: Effective radius from i-band (SDSS) images. Column 6: Diskyness/Boxyness parameter from i-band (SDSS) images. The asterisks indicate C_4 measured as the maximum in the region 3″- $3R_{eff}$ if prominent disky features are found; in the rest of the cases the quoted values are the average in this same radial range and the errors the RMS scatter (see Appendix E.1). Column 7: Disk/No Disk classification by Lisker et al. (2006b) (L06b) (no values indicate that these galaxies are not included in their analysis).

6.2.7 Analysis

The analysis presented in this work is primarily focused on the rotationally supported systems. Although the majority of the dwarf galaxies (15 out of 21) show some rotation ($v_{max} > 9$ km s^{-1}, Table 6.4), only 11 are rotationally supported ($(v_{max}/\sigma)^* > 0.8$) (Toloba et al. 2009a). Here we try to understand whether the observed kinematic properties of the rotationally supported systems are consistent with those of star forming galaxies of similar luminosity.

6.2.7.1 Shape of the rotation curves

Catinella et al. (2006) made a systematic study of the shape of the rotation curves of late-type spiral galaxies as a function of luminosity based on the method described in Persic et al. (1996). They fitted the rotation curves following the Polyex model (Giovanelli & Haynes 2002) which has the form:

$$V_{PE}(r) = V_0\Big(1 - e^{-r/r_{PE}}\Big)\left(1 + \frac{\alpha r}{r_{PE}}\right) \tag{6.1}$$

This analytical function depends on 3 parameters: V_0, r_{PE} and α, which represent the amplitude, the exponential scale of the inner region and the slope of the outer part of the rotation curve, respectively. The mean fitted rotation curves from Catinella et al. (2006) are normalised to the optical radius (R_{opt}, radius containing 83% of the total I-band luminosity), and the velocities are corrected from inclination. To compare them with our rotationally supported galaxies, we have calculated the inclinations as in Giovanelli et al. (1997a):

$$cos^2 i = \frac{(1-\epsilon)^2 - q_0^2}{1 - q_0^2} \tag{6.2}$$

where i is the inclination, ϵ is the ellipticity and q_0 is a constant value that depends on the thickness of the disk. Here we assume $q_0 = 0.3$, a conservative value for dwarf galaxies shaped as thick disks (Lisker et al. 2007).[5]

The comparison between the mean rotation curves of Catinella et al. (2006) and those of our rotationally supported objects must be done in the same luminosity regime since the derived parameters of the Polyex model are luminosity dependent. As the dwarf galaxies analysed in this work have magnitudes below the minimum magnitude in Catinella et al. (2006) ($M_I = -19.4$), the reference Polyex model of low luminosity star forming systems has been determined extrapolating linearly the three faintest values of the Polyex parameters to $M_I = -18.49$, the mean I-band magnitude of the galaxies here analysed. The parameters used to construct this curve are $V_0 =$ 74.58 km s^{-1}, $r_{PE} = 0.35$" and $\alpha = 0.03$.

In Figure 6.16 we compare the mean fitted rotation curves of Catinella et al. (2006) for late-type spirals (obtained from emission lines, black solid curves) with the rotation curves of our rotationally supported dEs determined from absorption lines (grey symbols). Of the 11 rotationally supported dEs, only 7 have been considered for this analysis because 3 of them, VCC21, VCC917 and NGC3073, have poor quality rotation curves ($\frac{\Delta v_{max}}{v_{max}}$ larger than 25%), and VCC308 has ϵ lower than 0.1, implying that the galaxy is nearly face on. The blue dots in Figure 6.16 show the median

[5]For early-type spirals $q_0 = 0.2$ (Giovanelli et al. 1997a). The most recent measurements of the thickness of dwarf galaxies gives $q_0 = 0.3 - 0.35$ (Sánchez-Janssen et al. 2010). The difference in v_{max} after the correction for inclination between using $q_0 = 0.2$ and $q_0 = 0.35$ is of 4.4%, insignificant.

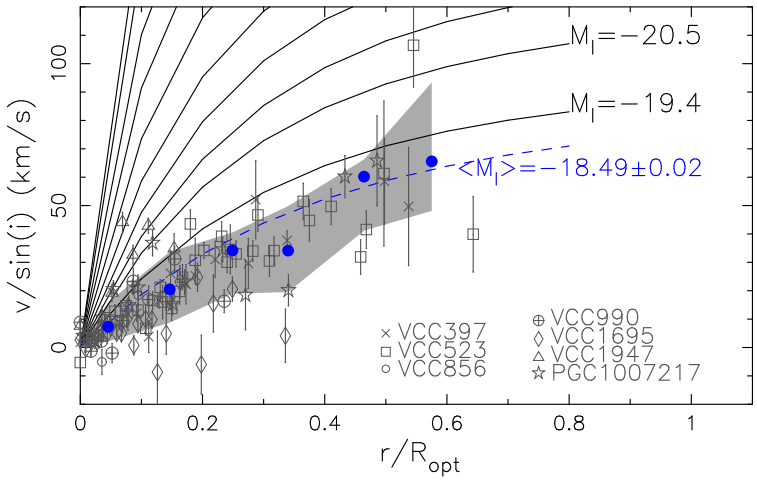

Figure 6.16: The observed rotation curves of rotationally supported dEs (grey symbols) are compared to the mean rotation curves of late-type spiral galaxies (black solid and blue dashed lines) from Catinella et al. (2006). Blue filled dots represent the median observed rotation curve of rotationally supported dE in bins of $r/R_{opt} = 0.1$. The last bin contains all data for $r/R_{opt} \geq 0.5$. The grey area indicates rotation velocities within 1σ from the median.

rotation curve of our dEs in bins of $\frac{r}{R_{opt}} = 0.1$. The grey area contains the 1σ deviation from this median value (68% of the values are inside this area). The blue dashed line is the extrapolated Polyex model for $M_I = -18.49$.

It is evident from Figure 6.16 that our rotationally supported galaxies are characterised by rotation curves that are similar to those of late-type spiral galaxies of equal luminosity. Or, in other words, galaxies with similar rotation curves have similar absolute magnitudes despite their morphological type. We see that rotationally supported dEs dynamically behave like small late-type spiral galaxies.

It is interesting to see that, despite their similar exponential radial light distribution, dEs have two different kinematic behaviour, they can be either pressure or rotationally supported. Furthermore, rotationally supported dEs have rotation curves similar to those late-type spirals despite the fact that these latter objects are gas dominated systems.

6.2.7.2 *Tully-Fisher relation*

Given the similarity in the kinematic properties of rotation supported dEs with those of late-type spirals we expect that these systems follow the Tully-Fisher relation, as firstly proposed by van Zee et al. (2004b). The Tully-Fisher relation is a typical scaling relation valid for star forming, rotating systems, linking the total luminosity to the maximal rotation velocity of the galaxy.

In Figure 6.17 we compare the Tully-Fisher relation for our (dark blue)[6] and van Zee et al. (2004b) (light blue) dEs to that of normal late-type galaxies of Giovanelli et al. (1997b) (grey symbols) and De Rijcke et al. (2007) (red dashed area), respectively. Figure 6.17 clearly shows that these rotationally supported dEs follow the Tully-Fisher relation with a similar scatter as the normal spirals of De Rijcke et al. (2007) and thus kinematically behave as late-type spirals. The v_{max} of dEs plotted in Figure 6.17 is probably a lower limit since it is generally measured where

[6]No asymmetric drift is applied neither to our dEs nor to those of van Zee et al. (2004b). This correction would increase v_{max} by 2.5 ± 0.9 in those rotationally supported systems plotted in Figure 6.17.

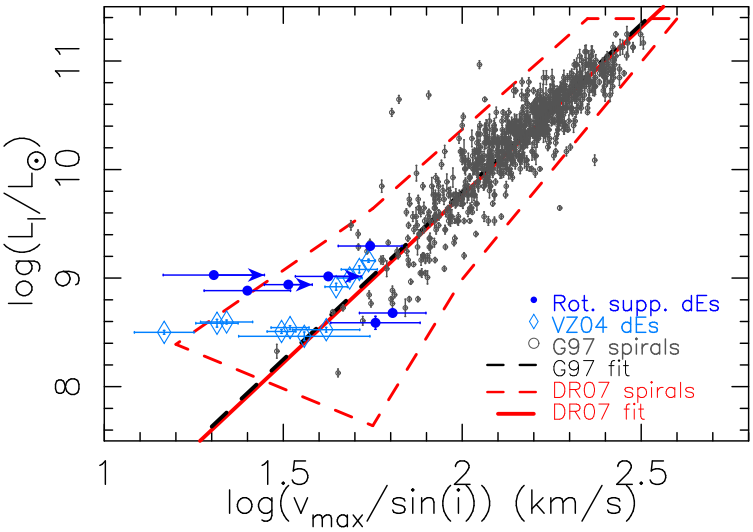

Figure 6.17: Tully-Fisher relation for 7 of our rotationally supported dEs (in dark blue), the dEs from van Zee et al. (2004a,b, VZ04, in light blue), the normal spirals from Giovanelli et al. (1997b, G97, in grey) and De Rijcke et al. (2007, DR07, red limited area). Absolute magnitudes of dEs have been obtained using distances from Mei et al. (2007) (criterion described in Table 6.6). For Giovanelli et al. data we use $H_0 = 73$ km s^{-1} Mpc^{-1} (Mei et al. (2007)). The arrows indicate lower limits of v_{max} (those obtained in the inner 6"). Fits of the Tully-Fisher relation are indicated in black for the normal spirals of Giovanelli et al. (1997b) and in red for De Rijcke et al. (2007, DR07). DR07 fit has been transformed to I band using the colour-morphology relation from Fukugita et al. (1995) and using $H_0 = 73$ km s^{-1} Mpc^{-1} and $M_{I\odot} = 4.08$ and $M_{B\odot} = 5.48$ from Binney & Merrifield (1998).

the rotation curve is still rising, as suggested by the kinematics of the globular clusters. It is thus conceivable that the agreement between the Tully-Fisher relation of rotationally supported dEs and late-type spirals of similar luminosity is even better than that depicted in Figure 6.17.

6.2.7.3 Dark matter content

The shape of the rotation curves gives information about the dark matter content and distribution of late-type galaxies (e.g., Catinella et al. 2006). Similarly, σ can be used to measure the dark matter content of pressure supported systems. Following Beasley et al. (2009) we estimate the total dynamical mass of our sample galaxies using the relation:

$$M_{tot} = M_{press} + M_{rot} \tag{6.3}$$

where M_{press} is the mass inferred from the velocity dispersion after the contribution from rotation has been removed and M_{rot} is the mass deduced by the intrinsic rotation velocity of the galaxies. M_{press} inside the half-light radius is defined as in Cappellari et al. (2006):

$$\begin{aligned} M_{press} &\simeq 2.5 G^{-1} \sigma^2 R_{eff} \\ &\simeq 580 \left(\frac{\sigma^2}{\mathrm{km^2 s^{-2}}}\right)\left(\frac{R_{eff}}{\mathrm{pc}}\right)\mathrm{M}_\odot \end{aligned} \tag{6.4}$$

The rotation curves of rotationally supported systems are characterised by an approximately

Table 6.7: Dynamical and stellar mass-to-light ratios in I-band in solar units.

Galaxy	$(\Upsilon_I)_\odot$	$(\Upsilon^*_I)_\odot$
PGC1007217	4.0 ± 0.8	1.9
PGC1154903	1.8 ± 3.1	1.2
NGC3073	0.6 ± 0.4	0.2
VCC21	1.5 ± 0.4	0.5
VCC308	1.5 ± 0.3	1.1
VCC397	4.8 ± 1.2	0.9
VCC523	2.2 ± 0.2	1.3
VCC856	1.1 ± 0.2	2.0
VCC917	2.5 ± 0.4	2.4
VCC990	1.9 ± 0.1	2.8
VCC1087	2.3 ± 0.1	2.4
VCC1122	2.4 ± 0.1	2.2
VCC1183	1.9 ± 0.1	1.4
VCC1261	2.3 ± 0.1	1.4
VCC1431	2.3 ± 0.1	3.4
VCC1549	2.1 ± 0.2	3.1
VCC1695	1.7 ± 0.3	1.2
VCC1861	1.6 ± 0.1	2.8
VCC1910	1.6 ± 0.1	3.2
VCC1912	2.1 ± 0.1	0.6
VCC1947	1.8 ± 0.1	1.7

NOTES: $(\Upsilon^*_I)_\odot$ is only indicative, the large errors in the stellar populations (Michielsen et al. 2008) make the uncertainties of $(\Upsilon^*_I)_\odot$ of the same order as the values.

constant gradient suggesting solid body rotation up to the R_{eff}. In this case M_{rot} is given by the relation:

$$\begin{aligned} M_{rot} &= \frac{R_{eff} v^2_{max}}{G} \\ &= \left(\frac{R_{eff}}{\mathrm{pc}}\right)\left(\frac{v^2_{max}}{\mathrm{km^2 s^{-2}}}\right)\left(\frac{1}{4.3\times10^{-3}}\right)\mathrm{M}_\odot \end{aligned} \tag{6.5}$$

Dynamical mass-to-light ratios (Υ_I, Table 6.7) are then measured using the I-band luminosities and equation 6.4 for pressure supported systems and the sum of equations 6.4 and 6.5 for rotationally supported objects [7]. Stellar mass-to-light ratios (Υ^*_I, Table 6.7) are computed using the models of single stellar populations (SSP) of Vazdekis et al. (2010) and the ages and metallicities from Michielsen et al. (2008).

Figure 6.18 presents the relation between the dynamical mass-to-light ratio and the absolute I-band magnitude for our galaxies (red and blue dots), the sample of classical elliptical galaxies from Cappellari et al. (2006, Υ_{Jeans} in I-band), the dEs from Geha et al. (2002) and the Milky Way

[7] Note that this method to obtain M_{tot} is equivalent to introducing the asymmetric drift.

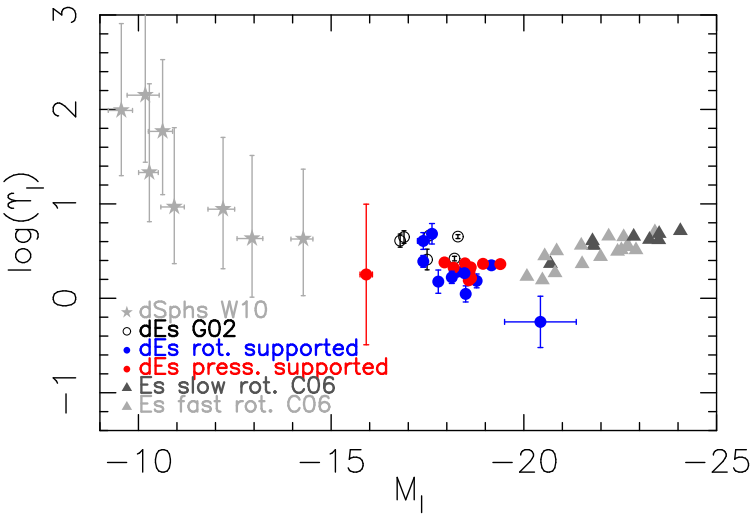

Figure 6.18: Dynamical mass-to-light ratio as a function of the absolute magnitude in I-band. Red and blue dots are our pressure and rotationally supported dEs respectively. For comparison open circles are dEs by Geha et al. (2002, G02), grey asterisks are dSphs from Wolf et al. (2010, W10) and dark and light grey triangles are slow and fast rotators respectively from Cappellari et al. (2006, C06). The transformation to I band has been performed using the colour-morphology relation by Fukugita et al. (1995) for Es. For the dwarf galaxies we have used $V - I = 1.03 \pm 0.04$ as calculated by van Zee et al. (2004a). Note that NGC3073 in not a dE given its high luminosity ($M_I = -20.4$ mag).

dwarf spheroidals (dSphs) from Wolf et al. (2010)[8]. Consistently with Zaritsky et al. (2006) and Wolf et al. (2010), we observe that the total mass-to-light ratio within the R_{eff} of dEs is the lower limit of the decreasing and increasing Υ_I vs. luminosity relations observed in giant ellipticals (Cappellari et al. 2006) and dSphs (Wolf et al. 2010), respectively. Dwarf early-type galaxies have on average $\Upsilon_I = 2.00 \pm 0.04\ \Upsilon_{I\odot}$, with a slightly higher dispersion in rotating systems ($RMS = 0.06\ \Upsilon_{I\odot}$) than in pressure supported systems ($RMS = 0.04\ l\Upsilon_{I\odot}$) .

Our sample of dEs have on average $M_{dyn}/M^* = 1.6 \pm 1.2$ (obtained as the ratio between the dynamical and stellar mass-to-light ratios, Υ_I and Υ_I^*, respectively, Table 6.7), thus they are not dominated by dark matter within the R_{eff}(as previously suggested by Geha et al. (2002); Forbes et al. (2008)), consistently with what is found is massive ellipticals (Cappellari et al. 2006) but contrary to dSphs (Wolf et al. 2010).

6.2.8 Discussion

How does this observational evidence compare with the different scenarios of galaxy formation? In a more general context we recall that in the most recent hierarchical models of galaxy formation only the most massive ellipticals have been formed through major merging events (De Lucia et al. 2006). The strong morphological segregation observed in high density environments (Sandage et al. 1985; Ferguson & Binggeli 1994; Blanton et al. 2005) indicates that the cluster environment plays a major role in the formation of dEs.

In Toloba et al. (2009a) we have shown that rotationally supported dEs, characterised by a disky structure, are preferentially located in the field and in the periphery of the cluster, while pressure supported systems are closer to the center. We also found that rotationally supported dEs

[8]The Υ_I values of Wolf et al. (2010) have been converted to equation 6.4 for consistency.

have, on average, younger stellar populations than pressure supported systems. This evidence suggests that rotationally supported dEs are low luminosity late-type galaxies which recently entered the cluster and lost their gas because of the interaction with the hostile environment, being transformed, on short time scales, into dEs. It seems thus clear that not all dwarf early-type galaxies are the low luminosity extension of massive ellipticals.

The new kinematic data in our hand support this scenario: rotationally supported systems have rotation curves similar to those of late-type galaxies of similar luminosity and follow the Tully-Fisher relation, the most representative scaling relation for late-type systems. Since the angular momentum of these objects is conserved, the most plausible scenario for gas stripping is the ram pressure exerted by the dense and hot IGM on the fragile ISM of the low luminosity star forming galaxies freshly entering the cluster environment (see Boselli et al. (2008a,b) for an extensive discussion).

For these rotationally supported objects gravitational interaction with the cluster potential or with other cluster members (galaxy harassment) can be excluded since they would, on relatively short time scales, reduce the angular momentum of the perturbed galaxies, leading to the formation of pressure supported systems. This process, however, could still be invoked to explain the kinematic and structural properties of the remaining pressure supported dEs populating the core of the cluster (half of our sample), whose statistical analysis of their scaling relations (Fundamental Plane) will be the subject of a future communication.

It is indeed possible that, as for the massive galaxies, gravitational interactions played a major role at early epochs, when the velocity dispersion of the cluster was lower since galaxies were accreted through small groups (preprocesing) than at the present epoch (Boselli & Gavazzi 2006).

6.2.9 Conclusions

We present medium resolution (R$\sim$3800) spectroscopy for 21 dwarf early-type galaxies, 18 located in the Virgo cluster and 3 in the field. These spectra has been obtained with the IDS at the INT(2.5m) and with ISIS at the WHT(4.2m) at El Roque de los Muchachos Observatory (La Palma, Spain). We have used these data to measure the kinematic profiles of these systems and calculate their maximum rotation velocity as well as their central velocity dispersion. In order to guarantee the reliability of the data, we have compared our observations with the data of 972 simulated galaxies in 5 different wavelength ranges corresponding to those used during the observations, and we have run, for each simulated galaxy, 100 Monte-Carlo simulations. The comparison between observed data and simulations shows that the adopted data extraction technique is appropriate for measuring the kinematic parameters of the target galaxies. We have also shown that velocity dispersions can not be measured for S/N ratios below 15, while for radial velocities with S/N$\geq$10 accurate results are obtained.

Our analysis has shown that dEs have on average dynamical M/L ratios within the effective radius smaller than those of massive ellipticals and dSphs (in average $log(\Upsilon_I) = 0.3 \pm 0.0$ $\log(\Upsilon_{\rm I\odot})$). We thus confirm that, within the effective radius, dEs are not dark matter dominated objects.

We have found that rotationally supported dEs have rotation curves similar to those of star

forming systems of similar luminosity and follow the same Tully-Fisher relation. Combined with the evidence that these systems are young objects with disk-like structures generally located in the outskirts of the cluster (Toloba et al. 2009a), these observations are consistent with a picture where these rotationally supported dEs result from the transformation of star forming systems that recently entered the cluster and lost their gas through their interaction with the environment. The observed conservation of the angular momentum in the rotationally supported dEs suggests that a milder ram pressure stripping event as the responsible of the gas removal has to be preferred to more violent gravitational interactions (harassment) which would rapidly heat up the perturbed systems. Therefore, all these evidences suggest that dEs are not the low luminosity end of massive early-types because if that was the case all dEs would be rotating with v_{max}/σ higher than those of Es, but a population of non-rotators has also been found and, in addition, the evidences of being stripped late-type spirals are strong enough as to consider it as a possible origin of dEs in clusters.

Acknowledgements. We thank the MAGPOP EU Marie Curie Training Network for financial support for the collaborating research visits and observations that allowed to make this paper. ET thanks the financial support by the Spanish research project AYA2007-67752-C03-03. We thank Consolider-GTC project for partial financial support. This paper made use of the following public databases: SDSS, NED, HyperLEDA, GOLDMine. We are grateful to the anonymous referee for a critical report that has improved the quality of the paper.

6.2.10 Appendix: Quantification of the bias introduced in v_{max}

Using the technique described in Section 6.2.5.2 to measure the maximal rotation speed, it seems that none of the galaxies have zero rotation (look at the v_{max} presented in Table 6.4). However, rotation curves like PGC1154903 or VCC1087 (Figure 6.11) appear to be statistically consistent with no rotation. The fact that we always find positive maximum velocities is a consequence of the method used to measure it. To quantify the bias introduced by using this technique we have run some simulations. We have taken a zero-rotation object with errors typical of those galaxies that statistically are non-rotators. We have taken a typical rotation curve with 11 bins, at 0, 2″, 4″, 7″, 12″ and 16″, with symmetrical errors of 2, 5, 7, 10, 12 and 15 km s^{-1} respectively. From these errors we have generated 100 simulated rotation curves assigning to each radius a random number with a Gaussian distribution, of which the width is the error associated to that radius. After folding these simulated rotation curves, shown in Figure 6.19, we calculated v_{max} following exactly the same technique as the one we used for the target galaxies. We then obtained a mean value for the 100 values of v_{max} and its scatter, 9 ± 6 km s^{-1}, shown as a thick black line and a grey shaded area in Figure 6.19. As a result, we consider that those galaxies with $v_{max} < 9$ km s^{-1} are not rotating, based on our data. For the other galaxies the rotation is significant (three times above the standard deviation, except for VCC1122 and VCC1261, see Table 6.4, 3rd column), so that the systematic bias described here is much less relevant. For VCC1122 (17.3 ± 7.7 km s^{-1}) and VCC1261 (13.9 ± 5.2 km s^{-1}) the rotation is marginal, as also shown by their low v_{max}/σ.

6.2.11 Appendix: Absolute I band magnitudes, optical and half-light radii and ellipticity

The I-band images for our sample of 21 dwarf galaxies were drawn from Sloan Digital Sky Survey (SDSS, York et al. (2000)) data release 6 (DR6, Adelman-McCarthy et al. (2008)) and converted

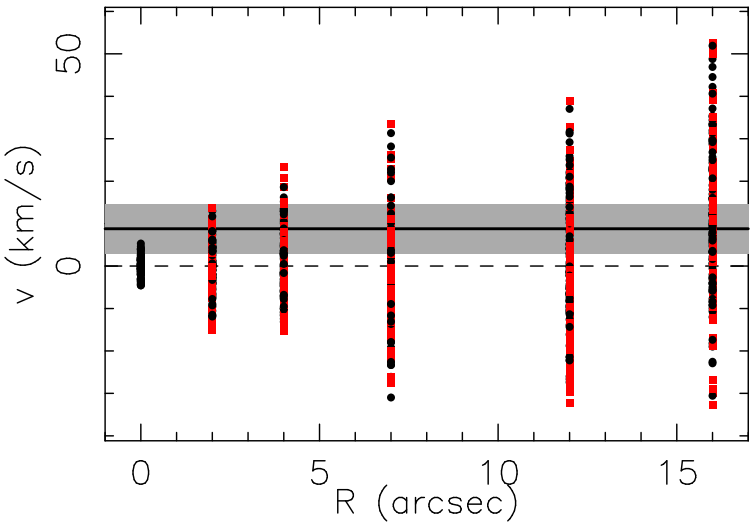

Figure 6.19: Simulations performed to quantify the bias that can be introduced in the measurement of v_{max}. Plotted are the 100 folded rotation curves computed with random numbers distributed as a Gaussian with width the typical errors of the target galaxies for that radius. Red squares and black dots are the left and right arms of the unfolded rotation curves respectively. The thick black line is the mean v_{max} for all the simulations. The grey shaded area is the scatter for this mean.

to Johnson-Cousins systems following Appendix 6.2.12. The photometric parameters were calculated using the IRAF task ELLIPSE.

To remove the stars from the images we used the IRAF task FIXPIX. This task allows us to remove the stars interpolating the surrounding galaxy area. To improve the final outcome, we averaged the results of interpolating along the horizontal and vertical directions for each star. For those galaxies that were on the edge of the FITS images or had a very bright nearby star, a more careful procedure was implemented. Taking advantage of the fact that the galaxies are ellipticals, so that they have smooth and axisymmetric surface brightness profiles, the BMODEL task of IRAF can be used to replace the affected areas of the galaxy by the azimuthal average of the unaffected ones. The output from BMODEL was used only to replace a small fraction of pixels, so this procedure was not affected by the possible presence of more subtle features, such as bars or spiral arms, which could not be reproduced by the model provided by the BMODEL task. Once extremely bright nearby stars had been removed the same procedure as above was followed with ELLIPSE and FIXPIX.

The procedure followed to run ELLIPSE is dependent on the parameters we want to measure. First of all we run ELLIPSE fixing only the center of the galaxy assuming a step between isophotes of 1 pixel, the rest of the parameters were left free. We also made the masks for the stars to be removed as described above. With the aim of measuring the absolute magnitude, R_{opt} and R_{eff} we run ELLIPSE again fixing, the center of the galaxy, the ellipticity and the position angle (PA) to avoid overlap between consecutive isophotes. The adopted ϵ and PA in this case are the typical values in the outer parts of the galaxy (beyond 1.5-2R_{eff}, region where these two parameters stabilise). To measure ϵ and C_4 we run again ELLIPSE after removing the stars leaving fixed only the center of the galaxy.

Asymptotic magnitudes and the radii were derived as in Gil de Paz et al. (2007). We first computed the accumulated flux and the gradient in the accumulated flux (i.e., the slope of the growth curve) at each radius, considering as radius the major-axis value provided by ELLIPSE.

After choosing an appropriate radial range, we performed a linear fit to the accumulated flux as a function of the slope of the growth curve. The asymptotic magnitude of the galaxy was the Y-intercept, or, equivalenly, the extrapolation of the growth curve to infinity. Once the asymptotic magnitude was known, the optical and effective radii of each galaxy were obtained as the major-axis of an elliptical isophote containing 83% and 50% of the total flux respectively. For the asymptotic magnitudes different sources of error have been considered (see Appendix 6.2.12). The resulting uncertainty is ∼0.02 mag.

The ellipticities (ϵ) were measured as the mean value between 3" and the R_{eff}, the galaxy region covered by our spectroscopic observations.

6.2.12 Appendix: Errors in magnitudes

The zero points (ZP) and the errors in the i-band magnitudes have been computed as described in SDSS documentation. The ZP have been obtained from F_0, the flux a source produces in counts per second in the image, calculated as a function of three parameters (aa, kk and $airmass$) defined as:

$$F_0 = \frac{t_{exp}}{10^{0.4(aa+kk\times airmass)}} \tag{6.6}$$

where the exposure time (t_{exp}) is the same for all the SDSS images (53.91 seconds). The uncertainties in the i-band magnitudes are affected by different sources of error: firstly, the errors in the flux, that can be calculated following the equation:

$$\Delta F = \sqrt{\frac{F + sky}{gain} + N_{pix}(dark\ variance + \Delta sky)} \tag{6.7}$$

where F is the total flux in counts, the sky and Δsky are the background sky and its error (in counts), the $gain$ and the $dark\ variance$ are given in the header and N_{pix} is the number of pixels in the largest aperture where the flux is measured. This error was typically 10^{-3}mag. Other error sources are the error introduced in the fit to the growth curve (between 10^{-3}mag and 6×10^{-3}mag), and the error due to photometric zero point differences between the different scans of SDSS, which might lead to an error of 0.01 mag. SDSS i-band magnitudes are not exactly in the AB system, so an error of 0.01 mag might also be introduced (see SDSS documentation about the photometric flux calibration). And finally, we have transformed our data from the SDSS i-band to the Johnson-Cousins I-band assuming $m_I = m_i - 0.52 \pm 0.01$ mag Fukugita et al. (1995) given that their $r - i$ colour ranges from 0.23 mag to 0.57 mag.

Adding quadratically all these sources of error, the final estimated error is 0.02 mag for the apparent I-band magnitudes.

6.2.13 Appendix: The C_4 Boxyness/Diskyness parameter

The boxyness/diskyness parameter is defined as the fourth moment in the Fourier series as follows

$$I(\Phi) = I_0 + \sum_k [S_k sin(k\Phi) + C_k cos(k\Phi)] \tag{6.8}$$

$I(\Phi)$ is the intensity measured in each isophote. The first two moments in this series describe completely an ellipse. Higher order moments ($k \geq 3$) define deviations of the isophotes from

ellipses. The third order moments (S_3 and C_3) represent isophotes with three fold deviations from ellipses (e.g. egg-shaped or heart-shaped), while the fourth order moments (S_4 and C_4) represent four fold deviations. Rhomboidal or diamond shaped isophotes have nonzero S_4. For galaxies that are not distorted by interactions, C_4 is the most meaningful moment indicating the disky/boxy shapes of the isophotes (see Figure 1 from Peletier et al. (1990) for an example of these different shapes).

C_4 is measured in i-band SDSS images using ELLIPSE that performs equation 6.8 along the radius of the galaxy fixing only the center of the galaxy and leaving the rest of ELLIPSE parameters free, as described in Section 6.2.6.1. Figure 6.20 shows C_4 as a function of radius for 3 dEs. Due to the large changes of C_4 with radii taking an averaged value is therefore not the best way to detect disks in these galaxies, especially if they cover only a limited range in radius. We have thus adopted the following procedure:

If at least one prominent bump is detected, which has a width larger than $\sim$6" inside three effective radii (above this radius the scatter of C_4 and its error becomes too large as to be reliable), we consider the galaxy to be disky, and assign the maximum C_4 between 3" and $3R_{eff}$ to the global C_4. The error in this measurement has been estimated by dividing the photometric error of the maximum of C_4 by the square root of the number of points that describe the disky structure in order to quantify the reliability of the bump considered. If the bump is described by a large number of points it is highly likely that the bump is truly there and as a consequence the error will be small, but if the number of points is small but the photometry is of high quality then the error will be small again. In any other case the error will be large and the result must be used cautiously.

Otherwise, if the values oscillate around $C_4 \sim 0$ (lower panel of Figure 6.20), are always negative or if there is a bump with a small radial coverage (see middle panel Figure 6.20), we assign a mean value and its scatter between 3" and $3R_{eff}$ to the global C_4. In this case, the RMS quantifies simultaneously the quality of the photometry and the possible presence of small bumps (as it is the case of VCC308, middle panel of Figure 6.20).

The results obtained for this parameter are listed in Table 6.6 and plotted vs. the anisotropic parameter, $(v_{max}/\sigma)^*$, in Figure 6.15. The agreement between the C_4 classification in disky/boxy galaxies and the morphological classification from Lisker et al. (2006b) is evident but apart from three red dots. These filled circles correspond to VCC917, a rotationally supported galaxy (above the horizontal dashed line) with strong disky isophotes but no structure found by Lisker et al. (2006a)); VCC1122, a not rotationally supported dE but with an appreciable rotation in Figure 6.11 and very important disky structures in the inner R_{eff} not detected by Lisker et al. (2006a)); and VCC1912, inside half the effective radius a moderate rotation is found in this system with a clear disky feature that peaks at $1.5R_{eff}$. For this galaxy, however, no underlying structure was found by Lisker et al. (2006a). More importantly VCC308 and VCC856, two rotationally supported galaxies with boxy C_4, present prominent spiral arms in Lisker et al. (2006a). In Ferrarese et al. (2006), based on ACS-HST images, VCC856 also shows spiral arms but their analysis of the isophotes' shapes shows that they are boxy too. Looking at Table 6.6 we see that both galaxies are nearly face-on, which means that the isophotes are boxy since face-on disks are round and not disky. As a consequence we emphasise the fact that boxy isophotes could miss disk features (mainly if the galaxies are face-on), but not the other way round (see VCC917).

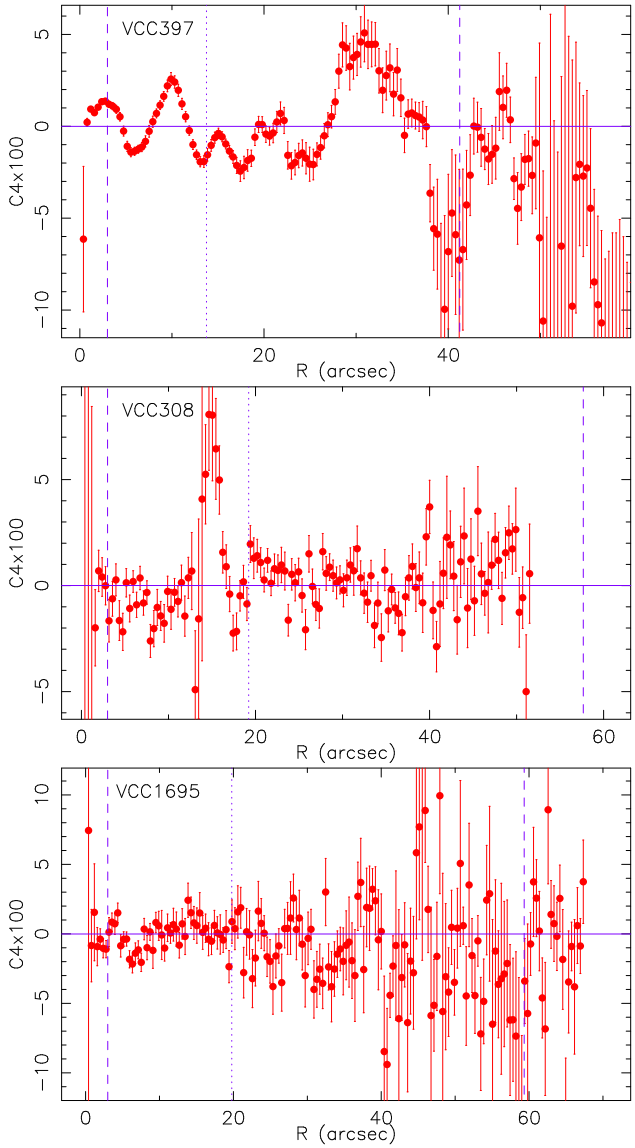

Figure 6.20: Examples of C_4 vs. radius for three galaxies: VCC397, VCC308 and VCC1695. The dashed purple lines indicate the region between 3" and the $3R_{eff}$. The dotted purple line shows the R_{eff}. In the upper panel one can see that if an average value is used between the dashed lines, C_4 will be compatible with zero and as a consequence, the prominent disky structure will be smeared out by the adjacent regions. In contrast, in the middle panel a galaxy with no clear disky structures is shown. In this latter case the errors are larger. The bump in C_4 only covers $\sim$ 3", while the rest of the galaxy is boxy. In this situation a mean value of the C_4 and its scatter is more representative. In the lower panel VCC1695 is an example of a typical boxy shaped galaxy.

6.3 Toloba et al. (2009) ApJ, 707, L17

Kinematic Properties as Probes of the Evolution of Dwarf Galaxies in the Virgo Cluster

E. Toloba[a], A. Boselli[b], J. Gorgas[a], R. F. Peletier[c], A. J. Cenarro[de], D. A. Gadotti[f], A. Gil de Paz[a], S. Pedraz[g], U. Yildiz[ch]

[a]Universidad Complutense de Madrid, 28040, Madrid, Spain
[b]Laboratoire d'Astrophysique de Marseille, UMR 6110 CNRS, 38 rue F. Joliot-Curie, 13388 Marseille, France
[c]Kapteyn Astronomical Institute, Postbus 800, 9700 AV Groningen, the Netherlands
[d]Instituto de Astrofísica de Canarias, E-38200, La Laguna, Tenerife, Spain
[e]Centro de Estudios de Física del Cosmos de Aragón, E-44001, Teruel, Spain
[f]Max-Planck-Institut für Astrophysik, Karl-Schwarzschild-Str. 1, D-85748 Garching bei München, Germany
[g]Centro Astronómico Hispano Alemán, Calar Alto (CSIC-MPG), Almería, Spain
[h]Leiden Observatory, Leiden University, P.O. Box 9513, 2300 RA, Leiden, The Netherlands

Abstract—We present new observational results on the kinematical, morphological, and stellar population properties of a sample of 21 dEs located both in the Virgo cluster and in the field, which show that 52% of the dEs i) are rotationally supported, ii) exhibit structural signs of typical rotating systems such as discs, bars or spiral arms, iii) are younger (~ 3 Gyr) than non-rotating dEs, and iv) are preferentially located either in the outskirts of Virgo or in the field. This evidence is consistent with the idea that rotationally supported dwarfs are late type spirals or irregulars that recently entered the cluster and lost their gas through a ram pressure stripping event, quenching their star formation and becoming dEs through passive evolution. We also find that all, but one, galaxies without photometric hints for hosting discs are pressure supported and are all situated in the inner regions of the cluster. This suggests a different evolution from the rotationally supported systems. Three different scenarios for these non-rotating galaxies are discussed (in situ formation, harassment and ram pressure stripping).

6.3.1 Introduction

Dwarf galaxies ($M_B > -18$) are the most numerous objects in the nearby Universe. They have gained importance since hierarchical models proposed dwarfs as the building blocks of massive galaxies (e.g., White & Rees 1978; White & Frenk 1991). These systems can be divided in star forming (Im, BCD, Sd,...) and quiescent (dE, dS0) dwarfs, the latter being the dominant population in clusters, the former the most common in the field (Sandage et al. 1985; Ferguson & Binggeli 1994; Blanton et al. 2005; Croton et al. 2005). The study of the population of low-mass galaxies and of the mechanisms leading to the strong morphology segregation between the different types of dwarfs is fundamental to understand the assembly and evolution of the overall population of galaxies.

In the case of dEs, various scenarios have been suggested to explain their formation. Whether they are the low luminosity extension of the giant ellipticals (Es) or they are the result of different formation and evolution processes is still an open question (Ferguson & Binggeli 1994). It has been proposed that dEs were late-type systems where the interstellar medium (ISM) was swept

away by the kinetic pressure due to supernova explosions (Yoshii & Arimoto (1987); see however Silich & Tenorio-Tagle (2001)). Other theories suggested that late-type spirals stopped their star formation once their ISM was removed during their interaction with the environment and evolved into quiescent dwarfs. The existence of a morphological segregation effect on the dwarf galaxy population (Ferguson & Binggeli 1994) favors this second scenario. Different processes could be at the origin of gas removal in clusters: interaction with the intergalactic medium (IGM) (e.g., van Zee et al. 2004b), as ram-pressure stripping, galaxy-galaxy interactions (e.g., Byrd & Valtonen 1990) and harassment (e.g., Moore et al. 1998; Mastropietro et al. 2005). These mechanisms are able to reproduce some of the observed properties of local dEs in clusters. Structural parameters, such as surface brightness, and spectrophotometric properties, such as stellar populations, are easily reproduced after a ram pressure event (Boselli et al. 2008a,b). The detailed study of (Lisker et al. 2006a,b, 2007) shows that there exists a population of galaxies that have properties in between those of dEs and star forming dwarfs. In these objects, which are classified as dEs, some remains of spiral discs, such as spiral arms or irregular features, are still visible. If dEs are formed from star forming galaxies through ram pressure stripping, we expect that the angular momentum of the parent galaxies should be conserved, while in the case of multiple dynamical perturbations the system is rapidly heated and the rotation is lost. Measuring the kinematics of dEs is therefore an important test to understand their origin.

In the last decade considerable efforts have been made to measure the kinematic properties of dE in Virgo, the closest rich cluster (e.g., Pedraz et al. 2002; Geha et al. 2002, 2003; van Zee et al. 2004b). These works have shown the existence of both rotating and pressure supported systems. This fact, together with the varieties of morphologies found by Lisker et al. (2006a) makes it clear that the formation of dEs might rather be complex. Would every different population of dEs have a separate formation process? To answer this question we started a kinematical survey of dE in the Virgo cluster.This is the first of a series of papers devoted to the study of the kinematics and stellar populations of dEs in the Virgo cluster.

6.3.2 The Data

6.3.2.1 Observations and Data Reduction

The data were obtained as part of the MAGPOP-ITP collaboration (Multiwavelength Analysis of Galaxy Populations-International Time Program), a Marie Curie Research Training Network. The observed sample, selected from the Sloan Digital Sky Survey (SDSS) as described in Michielsen et al. (2008), contains 18 Virgo and 3 field dEs. The Virgo galaxies were chosen to have $m_B > 15$ and dE or dS0 classification in the Virgo Cluster Catalog Binggeli et al. (VCC, 1985), with available GALEX data (Boselli et al. 2005). The field sample was required to be in the SDSS velocity range 375km s^{-1}< v_{hel} <1875km s^{-1} and $-18.5 < M'_r < -15$ mag. Quiescent galaxies were selected to have FUV-NUV>0.9 or $u - g$ >1.2 when there were no UV detections.

We obtained medium resolution ($R \simeq 3800$) long-slit spectroscopy along the major axis of 21 dEs during three different runs at Roque de los Muchachos Observatory, Canary Islands: two at the WHT (4.2m), using the spectrograph ISIS ($3445 - 8950$Å), and one at the INT (2.5m) with the IDS ($4600 - 5960$Å). With a slit width of 2"and exposure times of 1 hour/configuration, the gratings used in each campaign were R1200B for IDS and R1200B and R600R for ISIS. ISIS has the possibility to observe with a dichroic and split the light into two beams to cover a larger

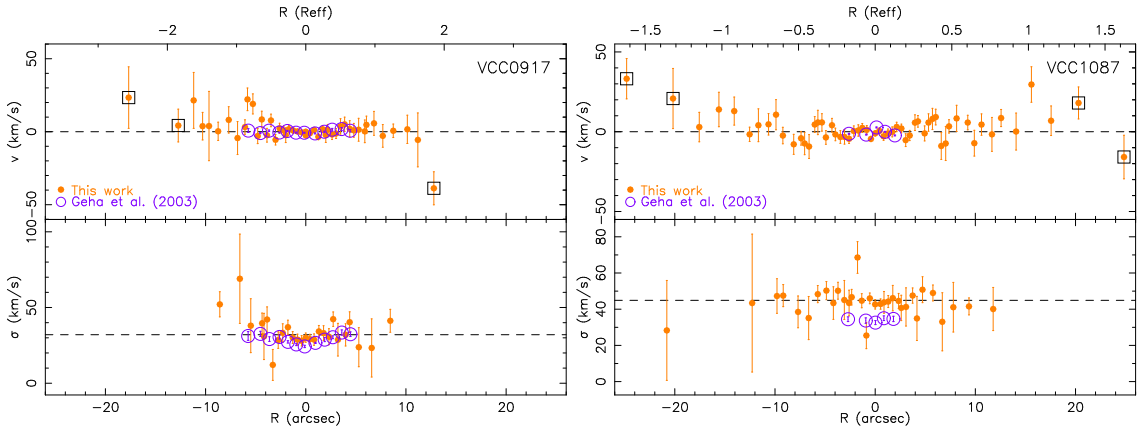

Figure 6.21: Example of the kinematical profiles obtained. The open squares show the values used to calculate v_{max} and the dashed line the lower pannel, the central σ.

wavelength range. Only in the first run we also used the mirror to cover the range $4800 - 5600$Å. The spectral resolution obtained was 1.6Å(FWHM) (49km s^{-1}) and 3.2Å(FWHM) (58km s^{-1}) in the blue and red arms of ISIS respectively, and 1.8Å(FWHM) (45km s^{-1}) with IDS.

The reduction was done using standard procedures for long-slit spectra in the optical range, using REDUCE(Cardiel 1999), a package specially focused on the parallel treatment of errors. The flux calibration was done using the stars observed from the MILES and CaT libraries (Sánchez-Blázquez et al. 2006c; Cenarro et al. 2001, respectively). More details of the observations will be presented in Toloba et al. in preparation (Paper I).

6.3.2.2 Kinematic and photometric parameters

To calculate the stellar kinematics we used MOVEL, available in REDUCE. MOVEL is an algorithm based on the Fourier quotient method described by Sargent & Turner (1977) and improved with OPTEMA (González 1993), that allows us to overcome the typical template mismatch problem. MOVEL uses an iterative procedure to determine the radial velocity and the stellar broadening of the galaxy, by fitting a galaxy model, created as a linear combination of the stars introduced as templates, to the data.

To make sure that the stars used as templates have the same instrumental profile as the target galaxies, they were defocused to fill the slit in the same way as the galaxies. In Paper I more details are given about how this was exactly done.

The maximum rotational velocity (v_{max}) was calculated as the weighted-average of the 2 highest velocities along the major axis on both sides of the galaxy at the same radius (for non-symmetric profiles at least 3 values are required), typically located at around 10" from the center (Figure 6.21). After de-redshifting the spectra using the rotation curves, the central velocity dispersion (σ) has been computed coadding all the individual spectra up to 1 effective radius. The typical S/N for the central σ is $\sim$60/Å, while $S/N \geq$10 for v_{max} at 10".

The photometric parameters: the effective radius (R_{eff}), the ellipticity (ϵ) at R_{eff} and the boxyness/diskyness parameter (A_4/A), measured in a radius range from 5" to $4R_{eff}$, were calculated using the IRAF task ELLIPSE over the H and K band photometry observed within the MAGPOP collaboration (Peletier et al. in preparation).

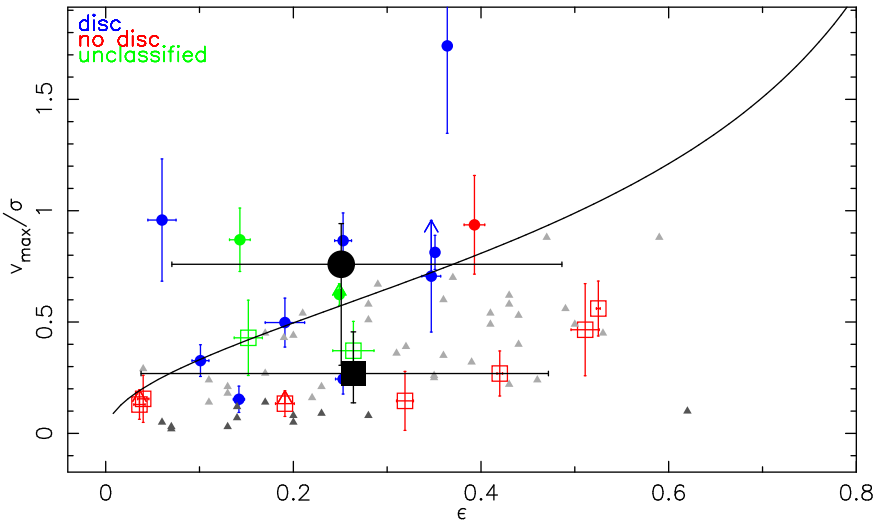

Figure 6.22: Anisotropy diagram. The solid line is the model for an isotropic oblate system flattened by rotation (Binney 1978). Triangles are giant ellipticals (from Emsellem et al. (2007)), with slow rotators ($v_{max}/\sigma < 0.1$) in dark grey, and fast rotators ($v_{max}/\sigma > 0.1$) in light grey. Blue, red and green symbols show our sample of dEs as classified by Lisker et al. (2006a). The filled dots and the open squares indicate galaxies with and without discs on the basis of A_4/A. Lower limits on v_{max} are indicated with arrows. The black symbols represent the median for dEs with (black dot)/without disc (black square) based on A_4/A classification, their error bars contain 34.1% ($\sim 1\sigma$) of the values at both sides of the median.

6.3.3 Results

Given the radial decrease of the galaxy surface brightness, the S/N in the outer parts of some of the galaxies was not enough to reach a plateau of the rotation curves. To be cautious, for those galaxies where the v_{max} is measured at a radius $< 6''$, the value is considered as a lower limit.

Figure 6.22 shows the anisotropy diagram. v_{max}/σ is the ratio between the maximum rotational velocity and the central velocity dispersion of the galaxies. The colour code corresponds to the classification of Lisker et al. (2006a). In blue are all the dEs that have signs indicating a possible spiral origin, those classified as certain, probable and possible discs (spiral arms, edge-on discs or bars) and also those classified as "other" (mainly irregular central features). In red are indicated those that do not show any underlying structure and in green the galaxies that were not in the sample of Lisker et al. (2006a); those are the 3 field dEs and VCC1947. We do not distinguish between galaxies with and without blue centers (Lisker et al. 2006b) and between nucleated and non-nucleated dwarfs (Binggeli et al. 1985) due to the lack of statistics, with only 3 galaxies with a blue nucleus and 3 non−nucleated objects.

The average A_4/A parameter, which measures how different the isophotes are from a perfect ellipse ($A_4/A > 0$ means disky isophotes, $A_4/A < 0$ boxy isophotes (Kormendy & Bender 1996b)), shows that all disky galaxies (except two) have been classified by Lisker et al. (2006a) as discs. The two exceptions are (see Table 6.8): VCC0917 where Lisker et al. (2006a) did not see the disc revealed by the disky isophotes, and VCC0308 where the low ellipticity suggests that the galaxy is face-on, so A_4/A can not accurately determine the underlying features (the unsharp masking technique of Lisker et al. (2006a) is here more useful). Regarding the four galaxies not included in the sample of Lisker et al. (2006a) (Table 6.8) A_4/A suggests that the two with higher v_{max}/σ contain discs (PGC1007217 and VCC1947), while the two with lower v_{max}/σ do not

Table 6.8: A_4/A Alternative classification.

Galaxy	v_{max}/σ	ϵ	100xA_4/A	A_4/A Classification
PGC1007217	0.87±0.14	0.14±0.01	0.48±0.11	disc
PGC1154903[9]	0.37±0.13	0.26±0.02	0.02±0.35	no disc
NGC3073	0.43±0.17	0.15±0.02	-0.35±0.03	no disc
VCC0308	0.96±0.27	0.06±0.02	-0.09±0.07	no disc
VCC0917	0.94±0.22	0.39±0.01	6.32±1.63	disc
VCC1947	0.62±0.05	0.25±0.01	0.35±0.05	disc

Note: Galaxies without morphological classification in Lisker et al. (2006a) and VCC0308 & VCC0917 whose classification by A_4/A disagrees with Lisker et al. (2006a).

(NGC3073 and PGC1154903).

The anisotropy diagram (Figure 6.22) separates rotationally supported galaxies (above the solid line) from pressure dominated (below the solid line). Figure 6.22 shows that: 1) as ellipticals, dEs can be separated into slow (v_{max}/σ <0.1) and fast (v_{max}/σ >0.1) rotators (Emsellem et al. 2007); 2) a large fraction (52%) of the dEs are rotationally supported and 3) all of the rotationally supported galaxies have morphological and/or photometric signs of a spiral origin.

The apparent discordance with Geha et al. (2003), who found that the majority of the dEs were not rotating, is due to the fact that their data are limited to the core of the galaxies, never reaching radii larger than 6″ (Figure 6.21), where the increase of the rotational velocity is generally observed (Paper I). A maximum offset of 10km s^{-1} in σ with respect to Geha et al. (2003) is found; however, it does not affect this result, since it makes v_{max}/σ larger. This discrepancy could be due to the use of a K-type star template in the case of Geha et al. (2003), whereas a linear combination of different spectral types (from B to M in our case) is more appropriate for dEs. Also a wider slit (2" compared to 0.5" in Geha et al. (2003)) could increase the σ measured if there were some ordered motion along the minor axis.

Figure 6.23 shows $(v_{max}/\sigma)^* = \frac{v_{max}/\sigma}{\sqrt{\epsilon/(1-\epsilon)}}$ as a function of the projected angular distance from the cluster center (we assume Virgo to be at 17Mpc, Gavazzi et al. (1999b)). $(v_{max}/\sigma)^*$ is v_{max}/σ divided by the isotropic oblate model, which means that for values of $(v_{max}/\sigma)^* > 0.8$ the galaxies are rotationally supported. To improve statistics we have included the dEs of van Zee et al. (2004b) (open triangles), whose data are consistent with ours (see Paper I).

Rotationally supported systems are generally located in the cluster outskirts or in the field, while the σ-dominated dwarfs are found only in the central regions of the cluster. This idea had been suggested before (Geha et al. 2003; van Zee et al. 2004b), but no clear confirmation was found. van Zee et al. (2004b) studied the inner 6 degrees (radius) of Virgo, and found a hint that very slow rotators or non-rotating dEs were located in the core or in the highest density clumps. Our observations reach distances further away from M87, and the evidence of a trend is clearer. The non-parametric Spearman statistical test finds a correlation (r =0.54) with a confidence of 98.9%. Indeed a significant difference in the two dwarf galaxy populations can be seen also in their median values, with dE with signs of a spiral origin having systematically higher velocity rotations and being situated at the periphery of the cluster ($(v_{max}/\sigma)^* = 0.96^{+0.30}_{-0.51}$, $D = 0.99^{+0.64}_{-0.53}$

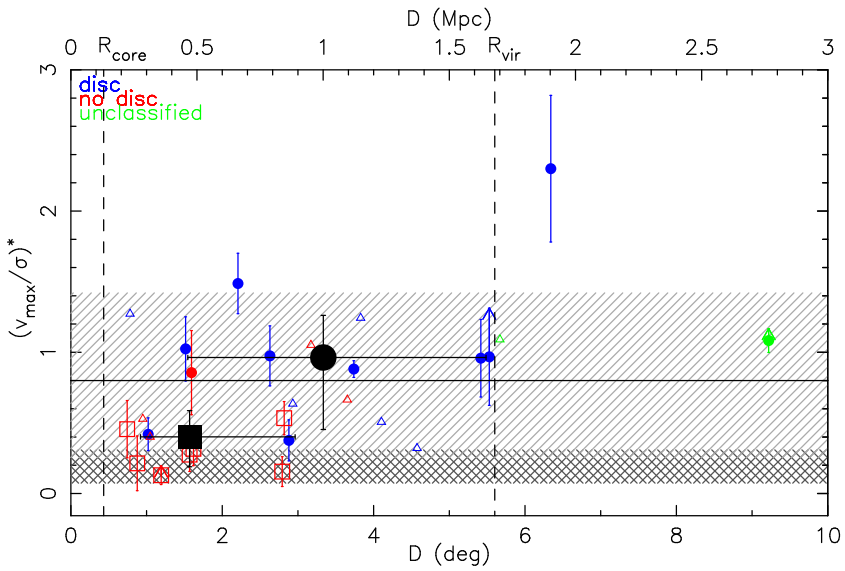

Figure 6.23: Anisotropy parameter versus the angular distance to M87 (centre of Virgo). The symbols are as in Figure 6.22. The light dark grey rectangles limit the $(v_{max}/\sigma)^*$ regions for fast and slow rotating Es as defined by Emsellem et al. (2007). The open triangles are van Zee et al. (2004b), included in the median values. The dashed lines show the Virgo core radius (130 kpc) and virial radius (1.68Mpc) (Boselli & Gavazzi 2006). The solid line divides the diagram into rotationally ($(v_{max}/\sigma)^* > 0.8$) and pressure supported galaxies ($(v_{max}/\sigma)^* < 0.8$).

Mpc) with respect to non-disc dE ($(v_{max}/\sigma)^* = 0.40^{+0.19}_{-0.21}$, $D = 0.47^{+0.41}_{-0.19}$ Mpc). We emphasize that any relation with the cluster-centric distance is smeared out by projection effects.

Figure 6.24 shows the anisotropy parameter as a function of the age of the galaxies from Michielsen et al. (2008). The Spearman non-parametric test finds a correlation ($r = -0.64$) with a 99.9% of confidence. Indeed the median values for the two populations are significantly different; the dEs with discs are ∼3Gyr younger than the others. Figure 6.24 also shows that while dEs with no signs of a spiral origin might be of all ages but on average old (5/8 of the squares are older than 7 Gyr), disc galaxies are preferentially young (9/12 of the dots are younger than 7 Gyr), suggesting that the 2 populations might have a different origin.

To conclude, our results suggest that the rotationally supported dEs are preferentially located in the field or in the outskirts of the cluster and are on average younger than those that are pressure supported, with no signs of spiral features, generally situated in the core of the cluster.

6.3.4 Discussion

It is believed that the difference between fast and slow rotators in Es is due to a different formation origin, with slow rotators, the most massive objects, principally located in dense environments and resulting from major mergers, while fast rotators, being less massive and more gas−rich (Emsellem et al. 2007), have a star formation history that is more extended in time. For dwarf galaxies this segregation in mass is difficult to be appreciated because of their small dynamical range (8.8< $L_H/L_{H\odot}$ <9.7 in our sample). Moreover, models indicate that the probability that dEs have undergone a major merging event is almost null (De Lucia et al. 2006). This is consistent with the fact that dEs are on average much younger than Es (Michielsen et al. 2008), whose formation happened probably at z >2 (Renzini 2006). If their star formation activity was quenched in recent

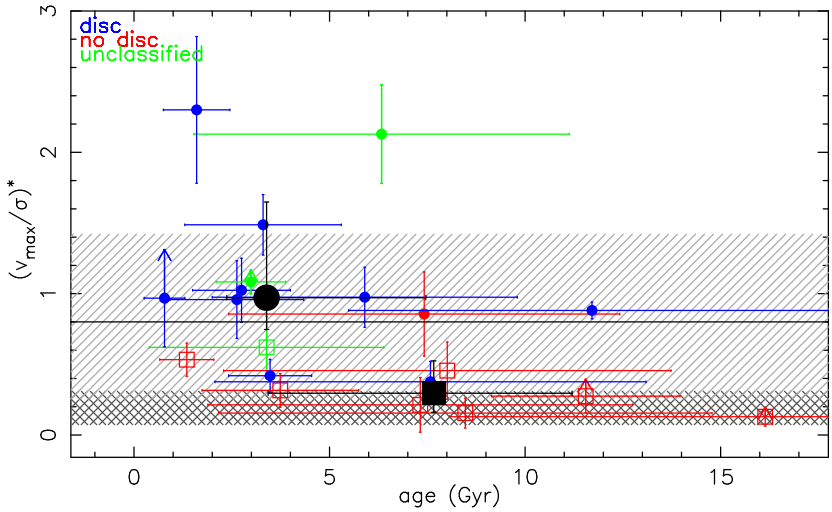

Figure 6.24: Anisotropy parameter versus the luminosity-weighted age from Michielsen et al. (2008). Symbols and shaded areas are as in Figures 6.22 and 6.23.

epochs, this would hardly be due to major merging events since the high σ of clusters already formed prevented strong dynamical interactions (Boselli & Gavazzi 2006).

Dwarf elliptical systems might have a different origin according to their structural, spectrophotometric and kinematical properties. Although harassment would be able to explain the origin of the pressure supported dwarfs, it is not likely to explain all the properties of rotationally supported systems ($(v_{max}/\sigma)^* > 0.8$). Harassment has long time scales since it needs multiple encounters to be efficient in removing gas and stars and quenching the star formation (Boselli & Gavazzi 2006), a scenario inconsistent with the observations which indicate that the star formation was active down to recent epochs, as the luminosity-weighted ages derived by Michielsen et al. (2008) suggest (see Figure 6.24). Furthermore, dynamical interactions heat the system removing rotation and enhancing velocity dispersion. In the simulations of Mastropietro et al. (2005) those galaxies that keep rotation after the harassment still retain an important spiral structure, yet they can not be classified as ellipticals. Moreover harassment is more efficient in the core of the clusters (in the inner 100kpc), while our result indicates that these rotationally supported systems are located mostly in the outskirts. All these evidences are however consistent with a recent ram pressure stripping event as proposed by Boselli et al. (2008a,b). Indeed, ram pressure would easily remove the total gas content of the infalling low luminosity, late-type galaxies, quenching their star formation, but conserving, at least on short time scales, their angular momentum and therefore their rotation. The spectrophotometric and structural properties of dE in Virgo are consistent with a recent ($\leq$2 Gyr) interaction with the cluster hot IGM (Boselli et al. 2008a,b). Consistent with observations (Crowl & Kenney 2008), hydrodynamical simulations indicate that ram pressure stripping can be efficient up to the virial radius, or even more outside in dwarf systems with shallow potential wells as those analysed here (Roediger & Brüggen 2008).

Pressure supported galaxies ($(v_{max}/\sigma)^* < 0.8$) might have a different origin: 1) they might be galaxies formed in situ through the isotropic collapse of the gas at early epochs, thus not transformed by the environment, and be the extension of Es, with the exception that they probably did not undergo major merging events (De Lucia et al. 2006). Indeed they have old stellar populations,

they do not present spiral structures (Lisker et al. 2006a) and they are virialised within the cluster, thus are members since early epochs (Conselice et al. 2001). 2) They can be star forming systems that entered into the cluster in the early epochs, maybe through the accretion of groups where pre-processing was active, and later modified by galaxy harassment or 3) they are star forming systems that entered into the cluster several Gyr ago, where ram pressure, although less efficient than today, because of the lower density of the IGM and of the smaller velocity dispersion of the cluster still in formation, had the time through multiple cluster crossing to remove the gas and stop the star formation activity. The lack of supply of new generations of stars on the plane of the disc increases σ on long time scales, while a decrease of the rotation would in any case require dynamical interactions. The 2 σ-dominated disc dwarfs (VCC1183, VCC1910) could be galaxies in the last stages of their transformation into dEs.

The analysis done so far, although crucial for understanding the origin of the rotationally supported systems, is still insufficient to explain the origin of the σ supported galaxies. It is probable that harassment and ram pressure were acting together with a relative weight that might have changed with time. Observations of high redshift clusters, mainly populated by massive, red sequence galaxies at late epochs (De Lucia et al. 2006) consistently suggest that harassment and ram pressure are the most probable effects. It is however clear that a complete study of the kinematical, structural and spectrophotometric properties of early and late type galaxies in clusters combined with model predictions, is a powerful way to study the role of the environment on their evolution, a work we plan to do in the near future.

In summary, we report the first clear evidence of a correlation between the presence of rotationally supported dEs and the distance to the center of the Virgo cluster. We have seen that the further away a dwarf galaxy is from M87, the larger its rotation is and the younger it appears. In the outer parts many of them show spiral features beside their elliptical appearance. These kinematical data are consistent with the idea of ram pressure stripping transforming dwarf star forming galaxies into dEs. Dwarf ellipticals that are pressure supported and show no sign of spiral features are likely to be late-type systems that entered in the cluster at early epochs and were later transformed by a combined effect of multiple encounters with nearby companions and the interaction with the hot and dense IGM. They might also be originally formed in clusters from an isotropic collapse of the primordial gas cloud.

Acknowledgments. We thank the MAGPOP EU Marie Curie Training and Research Network for financial support and the anonymous referee for useful comments. ET and AGdP thank the Spanish research projects AYA2007-67752-C03-03 and AYA2006-02358 respectively. A.J.C. is Juan de la Cierva Fellow of the Spanish Ministry of Science and Innovation. This paper made use of the following public databases: SDSS, NED, HyperLEDA (Paturel et al. 2003), GOLDMine (Gavazzi et al. 2003b).

6.4 Toloba et al. (2011) A&A, in prep.

Formation and evolution of dwarf early-type galaxies in the Virgo cluster II. The Scaling Relations

E. Toloba[a], A. Boselli[b], R. F. Peletier[c], J. Gorgas[a]

[a]Departamento de Astrofísica y CC. de la Atmósfera, Universidad Complutense de Madrid, 28040, Madrid, Spain
[b]Laboratoire d'Astrophysique de Marseille, UMR 6110 CNRS, 38 rue F. Joliot-Curie, F-13388 Marseille, France
[c]Kapteyn Astronomical Institute, Rijksuniversiteit Groningen, Postbus 800, 9700 AV Groningen, the Netherlands

Abstract—We present the spectrophotometric analysis of a sample of 18 dwarf early-type galaxies (dEs) in the Virgo cluster presented in the first paper of this series. We analyse the Kormendy relation, the surface brightness-luminosity and the size-luminosity diagrams, the Faber-Jackson relation and the Fundamental Plane both in the B and K-bands. Contrary to previous findings, we show that dEs follow the same Faber-Jackson relation and Fundamental Plane as massive early-type galaxies (Es) but differ on their structural scaling relations (the Kormendy relation, the surface brightness-luminosity and the size-luminosity diagrams). The spectrophotometric properties analysed in this work agree with the scenario of formation where dEs are low-luminosity late-type galaxies that entered the Virgo cluster and were transformed via their interaction with the harsh cluster environment.

6.4.1 Introduction

The origin of dwarf early-type galaxies (dEs) is yet unknown. Whether they are the small extension of the massive ellipticals (Es) or they are a different population of galaxies is still in active debate. Some observational evidences seem to suggest that these low-luminosity systems are a very heterogeneous population: they present a great variety of underlying structures, like discs, spiral arms, irregular features, some of them are also nucleated. Their luminosity profiles are exponential (Lisker et al. 2006a,b; Ferrarese et al. 2006; Lisker et al. 2007) and they are not composed of a simple, old and metal poor stellar population, but they rather contain stars of different ages spanning luminosity-weighted ages from 1 Gyr old to as old as the oldest objects in the universe (14 Gyr) (Michielsen et al. 2008; Koleva et al. 2009b). Although in appearance dEs bear a resemblance to Es, the wide range in physical properties that they exhibit is in contrast with the more homogeneous population of Es.

The morphology segregation is present also for dwarfs, with dEs the most common population in dense environments like clusters whereas low-luminosity late-type galaxies dominate the number of objects in the field (Sandage et al. 1985; Ferguson & Binggeli 1994; Blanton et al. 2005; Croton et al. 2005). This evidence suggests that the environment played a key role in shaping their evolution. To explain this evidence two mechanisms have been proposed to generate dEs transforming late-type galaxies: galaxy harassment (Moore et al. 1998; Mastropietro et al. 2005) and ram pressure stripping (Boselli et al. 2008a,b). In the former process close encounters are required to disrupt the late-type galaxies and transform them into dEs. However, in clusters like Virgo the density of objects needed to experience a complete transformation into a dE is only achieved in the center and after relatively long time scales (Boselli & Gavazzi 2006). As a consequence, those

late-type galaxies in the outskirts of Virgo that are harassed will still have the appearance of a late-type galaxy (Smith et al. 2010). On the other hand, in a ram pressure stripping event late-type galaxies infalling in the cluster are swept away from their gas content just through their interaction with the intergalactic medium (IGM) provoking the abrupt stop of their star formation and being reddened in short time scales (Boselli et al. 2008a).

One important method to check if low-luminosity late-type galaxies could be the progenitors of dEs is to analyse the resemblance of their kinematic properties. In the case of dEs being small Es they should behave similarly. The correlation of mass-rotation found in Emsellem et al. (2007) for the SAURON sample of Es indicates that rotation increases with decreasing mass. If dEs are low-luminosity spirals transformed via harassment, then they should be pressure supported because the system is heated rapidly by multiple encounters favoring the random motions against the ordered ones. However, ram-pressure stripping acting on the gaseous component, should not affect, on relatively short time scales, the kinematics of the galaxy that should thus retain its angular momentum. In the last decade many efforts have been done to study the kinematic properties of dEs. These works have shown that some dEs present important rotation while others do not (Pedraz et al. 2002; Geha et al. 2002, 2003; van Zee et al. 2004b; Chilingarian 2009; Toloba et al. 2011).

In Toloba et al. (2009a) we presented a probe of the evolution of dEs inside the Virgo cluster. We found that the kinematic properties of dEs are directly related to the virgocentric distance: rotationally supported dEs tend to be in the outer parts of the cluster while pressure supported dEs are preferentially in the center. Moreover, those dEs in the outer parts are younger than those in the center and present disky underlying structures in contrast to those located in the cluster core. In Toloba et al. (2011, hereafter Paper I) we found that those dEs rotationally supported have rotation curves with the same shape as late-type galaxies of the same luminosity. All these evidences suggest an scenario where low-luminosity late-type galaxies, the major population in the field, enter into the Virgo cluster and are transformed into dEs. Those dwarf early-types currently in the outer parts of the Virgo cluster are likely to be ram-pressure stripped late-type galaxies, whereas those in the center, could have suffered more than one transforming mechanism (for a complete discussion see Toloba et al. 2009a).

Another method to explore the origin of these systems is to analyse the scaling relations, such as the Kormendy diagram, the Faber-Jackson or the Fundamental Plane. These diagrams, widely used to determine distances, are a useful tool to study the structural and kinematic properties of early-type galaxies. The tightness of the scaling relations has been classically interpreted as early-type galaxies constituting an homogeneous population since shaped by the same formation process (Jorgensen et al. 1996; Pahre et al. 1998b). Therefore, the location of dwarf galaxies in these relations is a key aspect to interpret their formation as an extension of massive Es or a result of other physical mechanisms. In contrast, Navarro et al. (1997) suggested that this tightness could be due to the uniformity of the dark matter halos of the galaxies rather than to a common formation mechanism.

Some works have addressed these scaling relations for dwarf galaxies in the past (Bender et al. 1992; Graham & Guzmán 2003b; Geha et al. 2003; de Rijcke et al. 2005; Matković & Guzmán 2007; Kormendy et al. 2009), but whether dEs follow the same trends as Es is still unclear. For instance, in the case of the Faber-Jackson relation, expressed as $L \propto \sigma^n$, where n is $\sim$4 for massive galaxies (Faber & Jackson 1976b; Sargent & Turner 1977; Schechter & Gunn 1979; Schechter 1980; Terlevich et al. 1981; Tonry & Davis 1981), several authors have reported lower

values of n for dwarf galaxies, such us $n \sim 3$ by Tonry & Davis (1981), $n = 2.4$ for galaxies fainter than $M_B = -20$ by Davies et al. (1983), $n = 2.5$ by Held et al. (1992), or more recently $n = 2.01$ and $n = 1.57$ by Matković & Guzmán (2005) and de Rijcke et al. (2005), respectively. In summary, some authors have found that dEs display a continuous sequence with Es in the scaling relations (e.g., Graham & Guzmán 2003b), while others suggest that dEs show a change of slope (e.g., de Rijcke et al. 2005; Matković & Guzmán 2007), finding that the sequences of Es and dEs are even perpendicular Bender et al. (1992); Kormendy et al. (2009) or that dEs populate an area in the Fundamental Plane disconnected from Es (Geha et al. 2003).

In this paper we revisit the scaling relations in Johnson B-band comparing our sample of dEs in the Virgo cluster with several samples of Es (Bender et al. 1992; Pahre 1999; Jorgensen et al. 1996; Gavazzi et al. 2003a), bulges (Bender et al. 1992; Falcón-Barroso et al. 2002) and dEs (Bender et al. 1992; Geha et al. 2003; van Zee et al. 2004b; de Rijcke et al. 2005; Gavazzi et al. 2003a) in different environments. We use for these samples state-of-the-art distances and velocity dispersion measurements. For the first time for dwarf galaxies we analyse these scaling relations in the near-infrared (NIR) K-band. This band, tracing the bulk of the stellar mass, is insensitive to recent episodes of star formation and is the most indicated for such a study.

The main aim of this paper is to study the formation mechanisms of dwarf galaxies. In Toloba et al. (2009a, 2011) we found that there are considerable differences between rotationally supported and pressure-supported dEs, which might indicate strong differences in the physical processes involved in their formation. In this work we analyse if these differences also show up in the scaling relations.

This paper is structured as follows: Sections 6.4.2 and 6.4.3 present the sample used in this work and briefly describe the the observations. Section 6.4.4 reports the photometric parameters. Section 6.4.5 analyse the scaling relations of early-type galaxies. In Sections 6.4.6 and 6.4.7 we discuss and summarise the conclusions about the possible origin of dEs in a context of various models of galaxy formation and evolution. Finally, Appendix 6.4.8 describes the comparing samples of dEs, bulges and more massive Es and Appendix 6.4.9 gives a detailed description of the state-of-the-art distances used.

6.4.2 The sample

The sample analysed in this work was described in detail in Toloba et al. (2011, hereafter Paper I). In summary, the sample consists of galaxies with $M_r > -16$ classified as dE or dS0 in the Virgo Cluster Catalog (VCC) by Binggeli et al. (1985) and galaxies in low density regions with magnitudes between -18.5$< M_r <$-14.5 and distances similar to Virgo (5-25 Mpc).

All galaxies have been selected to have SDSS imaging and to be within the GALEX MIS fields (Boselli et al. 2005). They are required to have FUV-NUV$>$0.9 or $u - g >$1.2 when UV detections are not available to assure they are quiescent objects. The observed sample consists of 18 Virgo.

6.4.3 Observations and data reduction

The observing time used for this work was part of the International Time Program (ITP 2005-2007) at El Roque de los Muchachos Observatory (La Palma, Spain).

6.4.3.1 Long-slit optical spectroscopy

The medium resolution ($R \simeq 3800$) long-slit spectroscopic observations were carried out in three different observing runs at La Palma telescopes. Two out of the three runs were conducted at 4.2m WHT with the ISIS double-arm spectrograph and one run at 2.5m INT with the IDS spectrograph. The wavelength range coverage is from 3500 Å to 8950 Å at the WHT, with a gap between 5000-5600 Å in one of the observing campaigns, and 4600-5960 Å at the INT. The resolution obtained is 1.6 Å (FWHM) (40 km s^{-1}) and 3.2 Å (FWHM) (58 km s^{-1}) in the blue and red arms of ISIS respectively and 1.8 Å (FWHM) (46 km s^{-1}) with IDS.

The reduction has been performed through standard procedures for long-slit spectroscopy in the optical range using REDUCE (Cardiel 1999), a package specially focused on the parallel treatment of errors. An accurate description of the data acquisition and reduction is given in Paper I.

6.4.3.2 Near-infrared photometry

The photometric data were observed in the H (1.65μm) and K (2.2μm) bands in 6 different observing campaigns at El Roque de los Muchachos Observatory. Two out of the 6 runs were carried out at 3.6m TNG telescope with the NICS NIR camera, three at the 4.2m WHT with LIRIS NIR imager and one at the 2.5m NOT using the NOTCam NIR instrument. All the instruments used provided a resolution of 0.25"/pixel. The observations were carried out applying a dithering technique over 4, 8 or 9 positions on the square grid of the CCD in order to construct sky frames. Since the instruments have $4.2' \times 4.2'$ field of view and the surface brightness of the galaxies fell dramatically beyond 30" in radius, every frame of observation have sufficient space in order to extract sky information.

The exposure timing varied from 10 seconds to 30 seconds for individual shots in order to prevent saturation. Total integration times varied from 10 minutes up to over an hour depending on the faintness of the galaxies. All the images have been reduced using the package SNAP (*Speedy Near-Infrared data Automatic Pipeline,* `http://www.arcetri.astro.it/~filippo/snap/` by Mannucci). This software was explicitly written for the TNG telescope's NICS instrument, but, since many important characteristics of the NICS, LIRIS and NOTCam are similar, we modified SNAP with certain scripts to successfully reduce LIRIS and NOTCam data. The photometric calibration of the data was performed using 2MASS (2 Micron All Sky Survey Skrutskie et al. 2006)[10] and UKIDSS (UKIRT Infrared Deep Sky Survey Lawrence et al. 2007).

6.4.4 Photometric parameters

Photometric parameters, such as the total magnitude, effective surface brightness (μ_{eff}) and effective radius (R_{eff}), have been determined in the K and B bands. All the data are given in Vega system.

As specified in Table 6.9, 13 out of the 21 dEs in our sample were observed in H and/or

[10]This publication makes use of data products from the Two Micron All Sky Survey, which is a joint project of the University of Massachusetts and the Infrared Processing and Analysis Center/California Institute of Technology, funded by the National Aeronautics and Space Administration and the National Science Foundation.

K-bands. For the 8 dEs left we took their H-band images from GOLDMine. All galaxies were transformed to K-band assuming $H - K = 0.21$ (Peletier et al. 1999).

In order to compare with scaling relations already published in the optical range we have obtained the B-band (Johnson) photometry for our galaxies from g and r bands using Sloan Digital Sky Survey (SDSS, York et al. 2000) Data Release 7 (DR6 Abazajian et al. 2009). The transformation has been done following Blanton & Roweis (2007):

$$B = g + 0.2354 + 0.3915[(g - r) - 0.6102] \tag{6.9}$$

where g and r asymptotic magnitudes have been measured as described in Section 6.4.4.1. To transform the AB system of SDSS photometry into Vega system we used $m_{B,Vega} = m_{B,AB} + 0.09$ mag (Blanton & Roweis 2007).

6.4.4.1 Methodology

The parameters used in the scaling relations are asymptotic magnitudes, effective radii (R_{eff}, radius along the major-axis containing 50% of the total light), effective surface brightness ($< \mu_{eff} >$, the mean surface brightness within the R_{eff}) and the ellipticity ϵ.

All these parameters, that are presented in Table 6.9, have been calculated using the IRAF[11] task ELLIPSE and following the same procedure described in Paper I.

Stars present in the g-band images have been removed using the masks we obtained for i-band SDSS images in Paper I. We matched the coordinates of both g and i-bands using the IRAF task WREGISTER. The mask of stars for the H/K-band was calculated running ELLIPSE fixing just the center of the galaxy and leaving the rest of the parameters free. To remove the stars from the images we used the IRAF task FIXPIX. This task allows us to remove the stars interpolating the surrounding galaxy area. To improve the final outcome, we averaged the results of interpolating along the horizontal and vertical directions for each star. For those galaxies that were on the edge of the FITS images or had a very bright nearby star, a more careful procedure was implemented. Taking advantage of the fact that the galaxies are ellipticals, so that they have smooth and axisymmetric surface brightness profiles, the BMODEL task of IRAF can be used to replace the affected areas of the galaxy by the azimuthal average of the unaffected ones. The output from BMODEL was used only to replace a small fraction of pixels, so this procedure was not affected by the possible presence of more subtle features, such as bars or spiral arms, which could not be reproduced by the model provided by the BMODEL task. Once extremely bright nearby stars have been removed the same procedure as above was followed with ELLIPSE and FIXPIX.

To obtain the asymptotic magnitude and the effective radius we run ELLIPSE fixing the center of the galaxy, the ellipticity and the position angle (PA) to avoid overlap between consecutive isophotes. The step between isophotes was assumed of 1 pixel. In the g-band we adopted ϵ and PA obtained in i-band (see Paper I) and, for the NIR, we used the typical values of ϵ and PA in the outer parts of the galaxy (beyond 1.5-2R_{eff}, region where these parameters stabilise).

The methodology followed to obtain the asymptotic magnitude and the effective radius was performed as in Gil de Paz et al. (2007). We first computed the accumulated flux and the gradient

[11]IRAF is distributed by the National Optical Astronomy Observatory, which is operated by the Association of Universities for Research in Astronomy, Inc., under the cooperative agreement with the National Science Foundation.

in the accumulated flux (i.e., the slope of the growth curve) at each radius, considering as radius the major-axis value provided by ELLIPSE. Secondly we chose a radial range where this gradient had a linear regime. Finally we performed a linear fit to the accumulated flux as a function of the slope of the growth curve. The asymptotic magnitude of the galaxy was the Y-intercept, or, equivalenly, the extrapolation of the growth curve to infinity. Once the asymptotic magnitude was known, the effective radii of each galaxy was obtained as the major-axis of an elliptical isophote containing 50% of the total flux.

The ellipticities were measured running again ELLIPSE over the images cleaned of stars and fixing only the center of the galaxy. The ϵ value considered was the mean value between 3" and the R_{eff}, the galaxy region covered by our spectroscopic observations.

To obtain the mean effective surface brightness within the effective radius we measured half the total flux inside the area of an ellipse with semi-major axis equal to the effective radius. Such area is given by $\pi R_{eff}^2(1-\epsilon)$, therefore, being m the asymptotic magnitude, $< \mu_{eff} >$ is obtained as follows:

$$< \mu_{eff} >= m + 2.5log(2) + 2.5log(\pi R_{eff}^2(1-\epsilon)) \tag{6.10}$$

6.4.5 Scaling Relations

The aim of the present paper is that of studying whether dEs follow the same B and K-band scaling relations as giant ellipticals, bulges and dwarf spheroidals.

6.4.5.1 Kormendy Relation

Figure 6.25 presents the Kormendy relation for massive early-type galaxies including bulges and dwarf early-types in the B and K-bands, upper and lower panel respectively. Whereas bulges are the continuation of massive Es at smaller radii, dwarf galaxies form a cloud right below the trend followed by Es. When dSphs are included in the diagram (upper panel) it is more clear that all the dwarf systems describe a perpendicular trend to the one followed by Es. This means that, whereas for early-type galaxies smaller galaxies have larger surface brightness, for dwarfs, smaller galaxies have fainter effective surface brightness.

Although in the B-band young and old dEs form a uniform cloud, in the K-band the oldest dEs show a brighter effective surface brightness.

6.4.5.2 Surface Brightness - Luminosity Relation

Figure 6.26 shows the relation between the surface brightness within the R_{eff} in the B (upper panel) and K (lower panel) bands as a function of the absolute magnitudes. In both bands dEs follow a trend that is perpendicular to the one of massive early-type galaxies. This is consistent with the results found by Graham & Guzmán (2003b), for dEs and Es, and de Rijcke et al. (2005) and Kormendy et al. (2009) including dSphs.

Table 6.9: Photometric parameters of our sample of dEs in the Virgo cluster.

Galaxy	RA(J2000) (h:m:s)	Dec.(J2000) (°:':")	M_B (mag)	$R_{eff,B}$ (arcsec)	$< \mu_{eff,B} >$ (mag arcsec^{-2})	M_K (mag)	$R_{eff,K}$ (arcsec)	$< \mu_{eff,K} >$ (mag arcsec^{-2})	Ref.
VCC 21	12:10:23.14	+10:11:18.9	-16.16±0.03	13.86±0.09	22.18±0.07	-18.82±0.05	10.80±0.19	18.81±0.05	2
VCC 308	12:18:50.77	+07:51:41.3	-16.99±0.05	19.16±0.04	22.45±0.04	-20.00±0.07	16.70±0.03	18.83±0.03	2
VCC 397	12:20:12.25	+06:37:23.6	-15.80±0.05	13.56±0.07	22.50±0.05	-19.13±0.07	12.57±0.03	18.73±0.07	1
VCC 523	12:22:04.13	+12:47:15.1	-17.56±0.03	26.73±0.23	22.38±0.02	-20.62±0.05	17.17±0.18	18.34±0.04	1
VCC 856	12:25:57.93	+10:03:13.8	-16.62±0.06	16.21±0.09	22.45±0.04	-19.90±0.08	14.15±0.11	18.68±0.06	2
VCC 917	12:26:32.40	+13:34:43.8	-15.60±0.03	9.68±0.03	21.88±0.05	-18.59±0.05	8.61±0.04	18.49±0.12	2
VCC 990	12:27:16.91	+16:01:28.4	-16.43±0.03	9.88±0.03	21.21±0.03	-19.30±0.05	9.92±0.08	18.10±0.07	1
VCC 1087	12:28:17.88	+11:47:23.7	-17.15±0.06	27.02±0.15	22.75±0.10	-20.40±0.08	17.09±0.35	18.45±0.08	1
VCC 1122	12:28:41.74	+12:54:57.3	-16.15±0.03	14.26±0.07	21.98±0.09	-19.11±0.05	11.81±0.09	18.27±0.19	2
VCC 1183	12:29:22.49	+11:26:01.8	-16.86±0.03	21.85±0.14	22.68±0.17	-19.88±0.05	13.92±0.04	18.24±0.14	2
VCC 1261	12:30:10.35	+10:46:46.3	-17.59±0.06	23.76±0.10	22.08±0.11	-20.78±0.08	20.54±0.03	18.29±0.11	1
VCC 1431	12:32:23.39	+11:15:47.4	-16.41±0.06	10.31±0.02	21.66±0.01	-20.19±0.08	9.22±0.02	17.65±0.02	1
VCC 1549	12:34:14.85	+11:04:18.1	-16.15±0.03	13.09±0.04	22.36±0.02	-19.55±0.05	11.83±0.04	18.36±0.02	2
VCC 1695	12:36:54.79	+12:31:12.3	-16.68±0.08	27.61±0.37	23.34±0.08	-19.23±0.09	15.15±0.48	19.24±0.11	2
VCC 1861	12:40:58.60	+11:11:04.1	-16.79±0.06	21.57±0.14	22.88±0.02	-20.05±0.08	12.01±0.02	18.16±0.01	1
VCC 1910	12:42:08.68	+11:45:15.9	-16.66±0.06	14.14±0.06	22.10±0.05	-20.29±0.08	14.43±0.05	18.12±0.02	1
VCC 1912	12:42:09.12	+12:35:48.8	-16.91±0.03	23.53±0.09	22.22±0.15	-20.06±0.05	19.71±0.06	18.35±0.21	1
VCC 1947	12:42:56.36	+03:40:35.6	-16.54±0.03	11.26±0.04	21.55±0.02	-20.20±0.05	8.56±0.02	17.29±0.02	1

NOTES: Columns 4, 5 and 6 present the absolute magnitude, the effective radius and the effective surface brightness within the effective radius in B band (Johnson), respectively. Columns 7, 8 and 9 show the same parameters in K band. All the magnitudes used throughout this work use the Vega system. Column 10 specifies the reference of the infrared image: 1 means this work, 2 means that the image was gathered from GOLDMine database (Gavazzi et al. 2003a). The distances assumed for each galaxy are calculated from their surface brightness fluctuations by Mei et al. (2007), see Appendix 6.4.9.

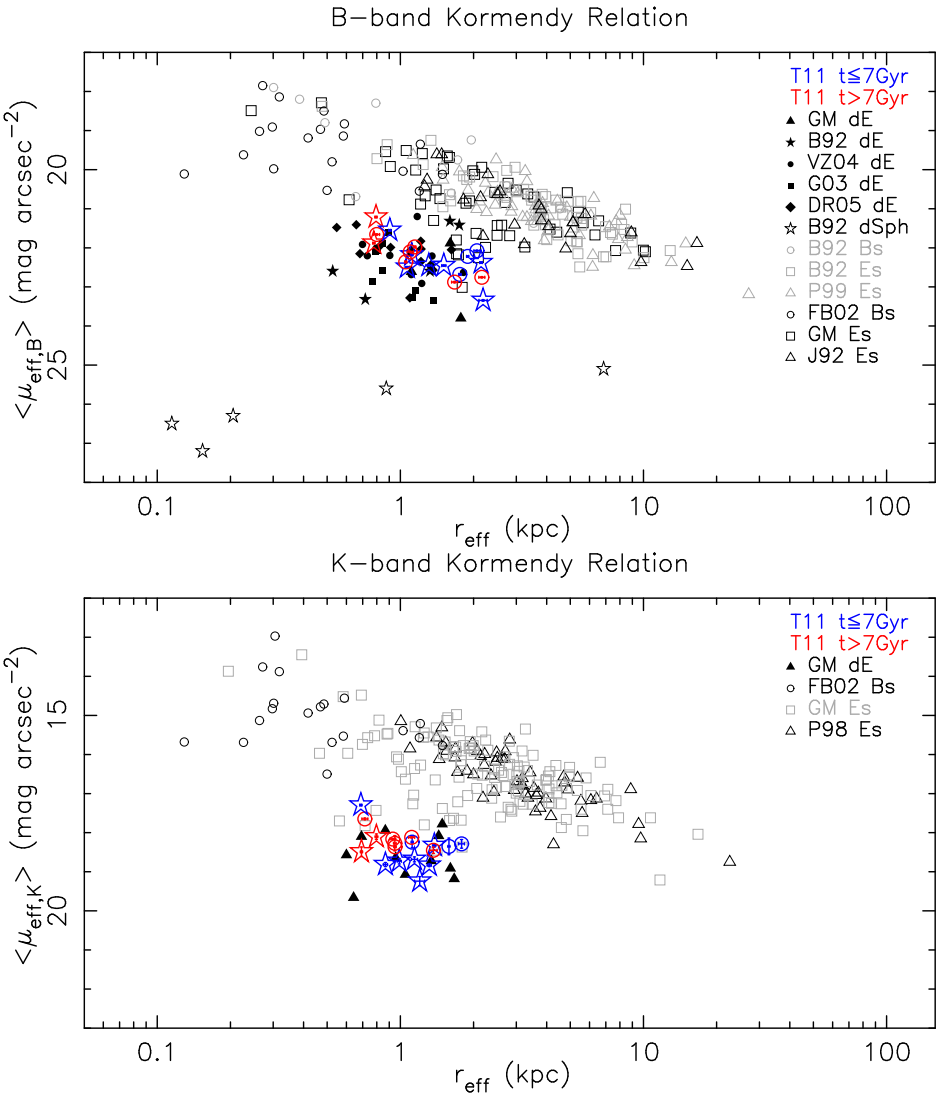

Figure 6.25: Kormendy relation in B-band, upper panel, and K-band, lower panel. For the B-band diagram the dE sample consist of red (older than 7 Gyr) and blue (younger than 7 Gyr) symbols from our sample, stars mean rotationally supported while circles mean pressure supported, Gavazzi et al. (2003a, GM, filled triangles), Bender et al. (1992, B92, filled stars), van Zee et al. (2004b, VZ04, filled circles), Geha et al. (2003, G03, filled squares) and de Rijcke et al. (2005, DR05, filled diamonds). The sample of dSphs is from Bender et al. (1992, open black stars). The sample of massive early-type galaxies is the compilation of Bender et al. (1992, B92, open grey squares), Pahre (1999, P99, open grey triangles), Gavazzi et al. (2003a, GM, open black squares) and Jorgensen et al. (1992, J92, open black triangles). The sample of bulges comes from Bender et al. (1992, B92, open grey circles) and Falcón-Barroso et al. (2002, FB02, open black circles). For the K-band relation the dE sample consists of the red and blue symbols from our sample with the same symbols and colours as in the left panel and the sample from GM in filled black triangles. The sample of bulges here consists only on FB02 sample (black open circles). And the sample of Es has data from GM (grey open squares) and from Pahre et al. (1998b, P98, black open triangles).

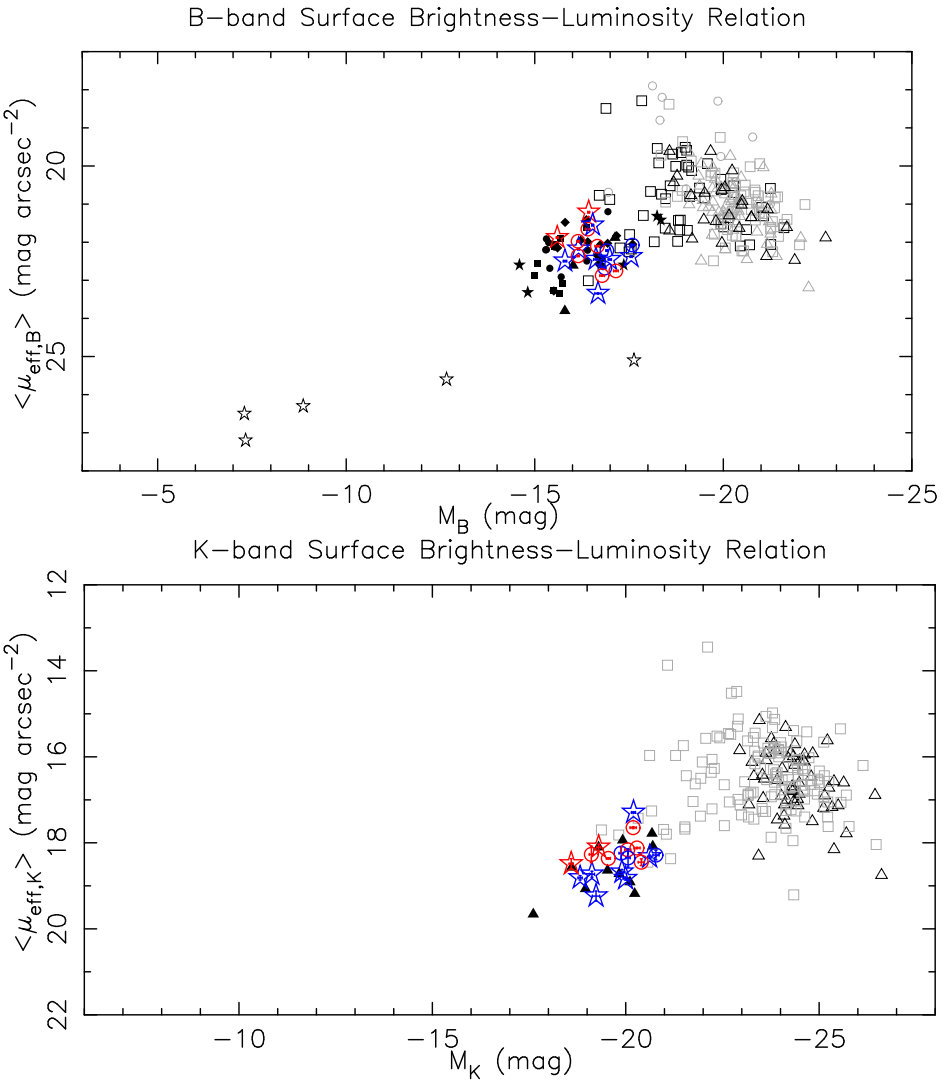

Figure 6.26: Surface brightness within the effective radius as a function of the absolute magnitudes, in B-band in the upper panel and in K-band in the lower panel. Symbols are as in the Kormendy relations (Figure 6.25) with the absence of Falcón-Barroso et al. (2002) bulges.

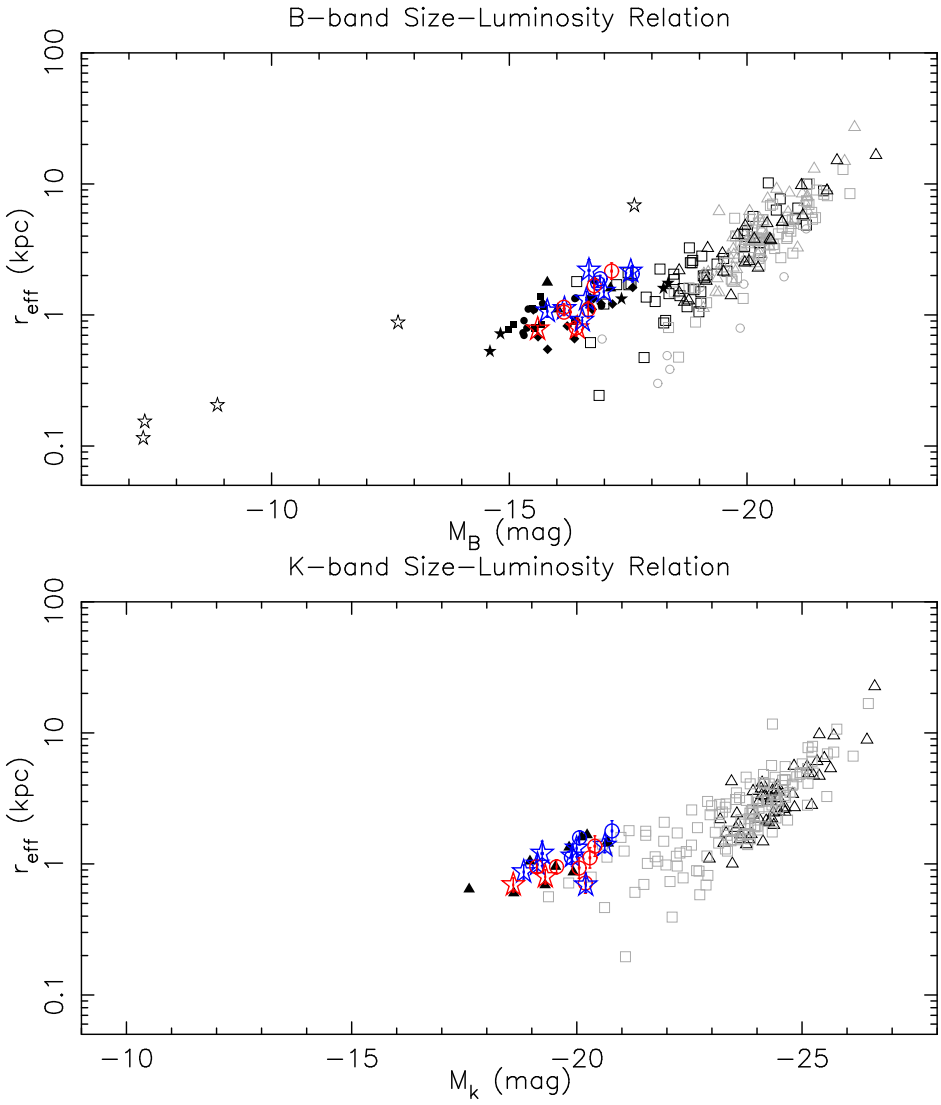

Figure 6.27: Absolute magnitude in B-band, upper panel, and in K-band, lower panel vs. the half-light radius in logarithmic scale. Symbols are as in Figure 6.25 but for Falcón-Barroso et al. (2002) bulges for which the absolute magnitudes were not available.

The separation found for different stellar populations of dEs, is more evident in the K-band than in the B-band, as in the Kormendy relation. Whereas in the B-band old and young dEs form a cloud of objects, in the K-band young dEs are fainter than the old ones.

6.4.5.3 Size - Luminosity Relation

The correlations found in Figures 6.25 and 6.26 imply a relation between the size and luminosity of the galaxies.

Figure 6.27 shows the relation between the size and luminosity of early-type galaxies. Giant ellipticals and bulges follow a different relation than that of dEs. Massive systems present steeper slopes, which results in dwarf galaxies presenting fainter luminosities than massive galaxies of the same size, or the other way round, for a fixed magnitude, dwarf galaxies appear larger than Es and bulges. A difference in the location of dwarf galaxies depending on their stellar population, or

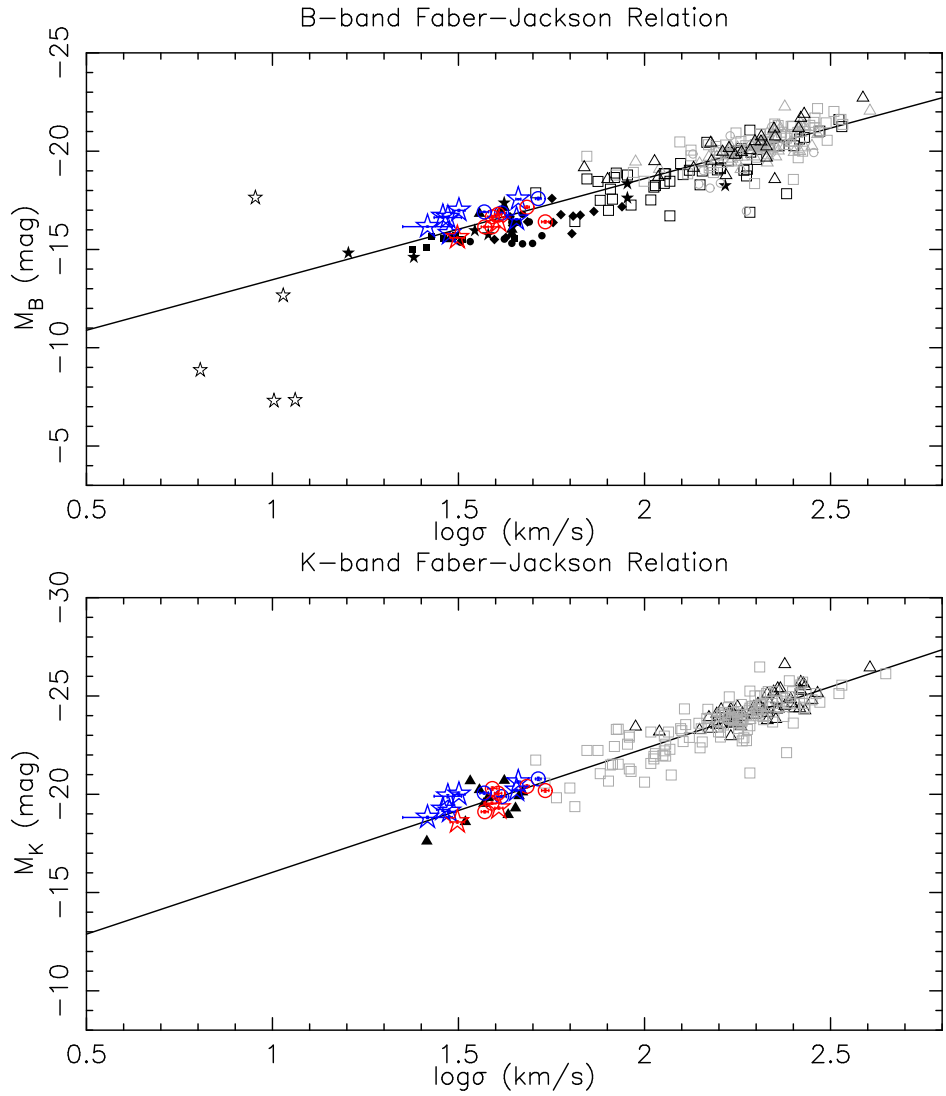

Figure 6.28: Faber-Jackson relation in B and K-bands. The symbols are the same as in Figure 6.25.

equivalently on their kinematic support, is present in this Figure as well as in the scaling relations discussed above (Figures 6.25 and 6.26). In these three Figures older galaxies (in red) are brighter in surface brightness and smaller in half-light radius than those younger (in blue). Whereas this dichotomy between the two populations is clearly evident in the K-band, in the B-band the larger scatter makes this separation less clear.

6.4.5.4 Faber-Jackson relation

Figure 6.28 shows the Faber-Jackson relation in the B-band, in the upper panel, and in the K-band, in the lower panel. The linear fit shown in both panels has been determined by considering only the giant galaxies. The slopes found for Es are $n = 4.25 \pm 0.01$ and $n = 3.83 \pm 0.01$ in the B and K bands respectively. When the fit is made only including the dwarf galaxies the slopes found are $n = 3.74 \pm 0.03$ (independently from the inclusion or not of dSphs) and $n = 3.48 \pm 0.48$ again for the B and the K bands. This similarity in the slopes found for Es and dEs is clearly shown in Figure 6.28. This result is completely contrary to the previous analysis of the Faber-Jackson relation including dwarf galaxies that obtained slopes for the dEs of $\sim$2 (Davies et al. 1983; Held

et al. 1992; Matković & Guzmán 2005; de Rijcke et al. 2005).

In Figure 6.28 it is also seen that for a fixed σ older dEs appear fainter both in the B and K bands.

6.4.5.5 Fundamental Plane

The scaling relations discussed above, such as the Kormendy relation and Faber-Jackson diagram, are in two-dimensions. In this Section we study the three-dimension space defined by the effective surface brightness, the velocity dispersion and the effective radius of the galaxies (the Fundamental Plane, FP Djorgovski & Davis 1987; Dressler et al. 1987). The edge-on view of the FP is widely expressed as:

$$logR_{eff} = \alpha \log\sigma + \beta \log < \mu_{eff} > +\gamma \tag{6.11}$$

where α, β and γ are the coefficients that minimise the scatter of the FP.

Figure 6.29 presents this edge-on view of the FP in the B and K bands, and it shows that dwarf galaxies populate the region in between those of massive galaxies and the bulges of spirals in both wavelengths. But, whereas dEs in the B-band follow the FP of massive Es or lie above it (preferentially those dEs from the literature), in the K-band nearly all dEs stay over the fit defined by Es.

6.4.5.6 Fundamental Plane in the κ-space

The κ-space was defined by Bender et al. (1992) in an attempt to have an almost perfect edge-on projection of the FP and to give a physical meaning to each coordinate. In this new space the coordinates are approximately measuring the mass (κ_1), the effective surface brightness (κ_2) and the mass-to-light ratio (κ_3). Although the interpretation given to this projection of the FP is the same as the original definition based on σ, $< \mu_{eff} >$ and R_{eff}, we include it here for completeness.

Figure 6.30 shows the edge-on and face-on projections of the FP in the κ-space in the B and K-bands, left and right panels respectively. Contrary to previous results (e.g., Geha et al. 2003), dEs do not lie in an area distinctly different from other stellar systems, but in between bulges and dSphs (in the B band) and are the low mass end in the K band where data for dSphs are not available. Therefore, the absence of stellar systems in between galaxy populations previously found was just an observational bias in the data sets plotted.

In particular, the face-on view of the FP shows in both, the B and K bands, that the most massive early-type galaxies are those with the highest surface brightness, whereas for dwarf galaxies those with the highest surface brightness have low masses. The edge-on view relates the mass-to-light ratio (M/L), measured from dynamical parameters such as σ, with the mass of the galaxy. Massive galaxies present lower M/L for lower masses, but in the case of dEs all galaxies have similar M/L independently of the masses of the galaxies, that is also a small range. The trend for dSphs is to increase the M/L for decreasing mass. This relation is more appreciable in B-band but also seen in K-band (notice the very different ranges in the M/L-axis). The U-shape observed here was also found in the Paper I when we analysed the M/L ratio, calculated with an independent method, versus the magnitude in the I-band.

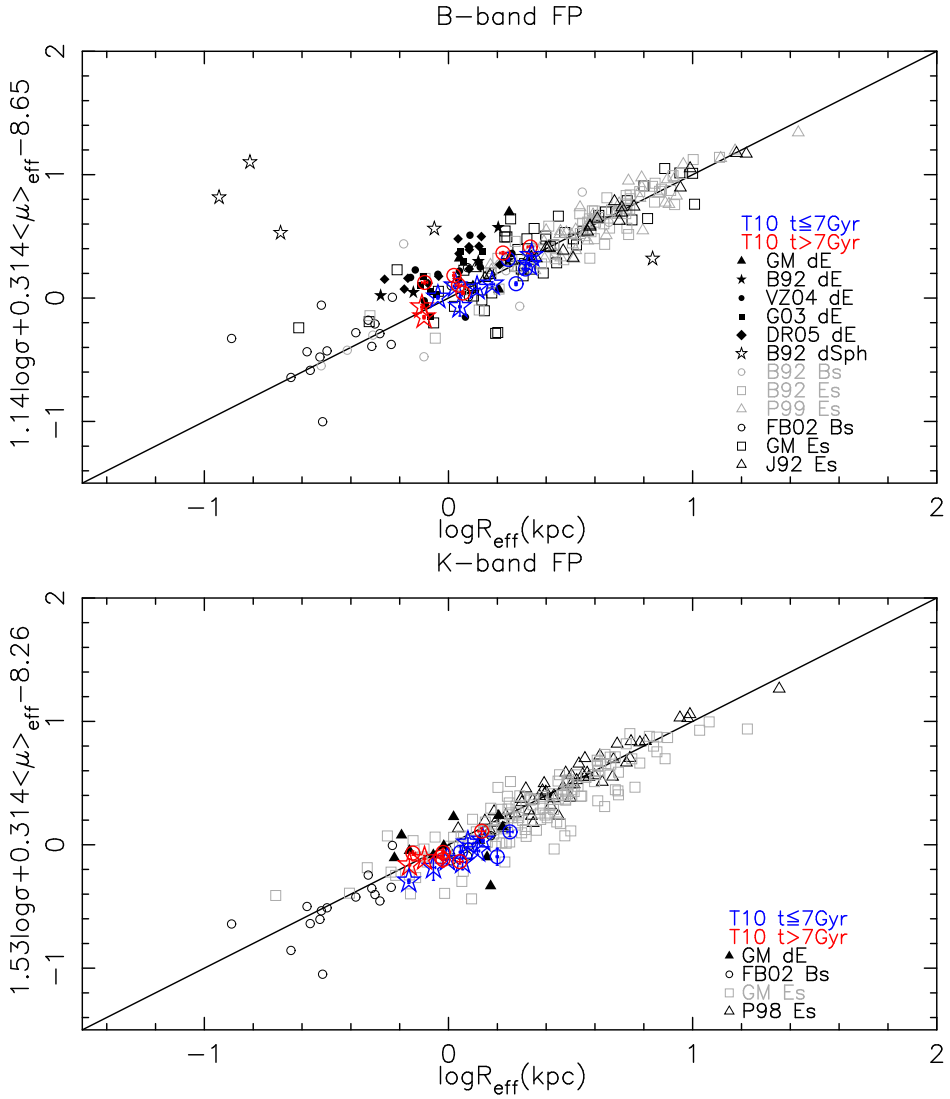

Figure 6.29: Fundamental plane in B-band. Filled black symbols are dwarf early-type galaxies (dEs) from different works. Black and grey open symbols are normal early-type galaxies (Es), bulges (Bs) and dwarf spheroidal galaxies (dSph) from different sources. Blue symbols are our sampled dEs younger than 7 Gyr and the red symbols are those older than 7 Gyr, in the coloured symbols stars mean rotationally supported and circles are pressure supported (from Toloba et al. (2009a) and Paper I). The continuum line shows the fit by de Rijcke et al. (2005). Fundamental plane in K-band. Filled black triangles are dwarf early-type galaxies (dEs) from GOLDMine Database (see section 5.1). Black and grey open symbols are normal early-type galaxies (Es) and bulges (Bs) from different references. Coloured symbols are our sample of dEs as described in Figure **??**. The continuum line shows the fit by Pahre et al. (1998b).

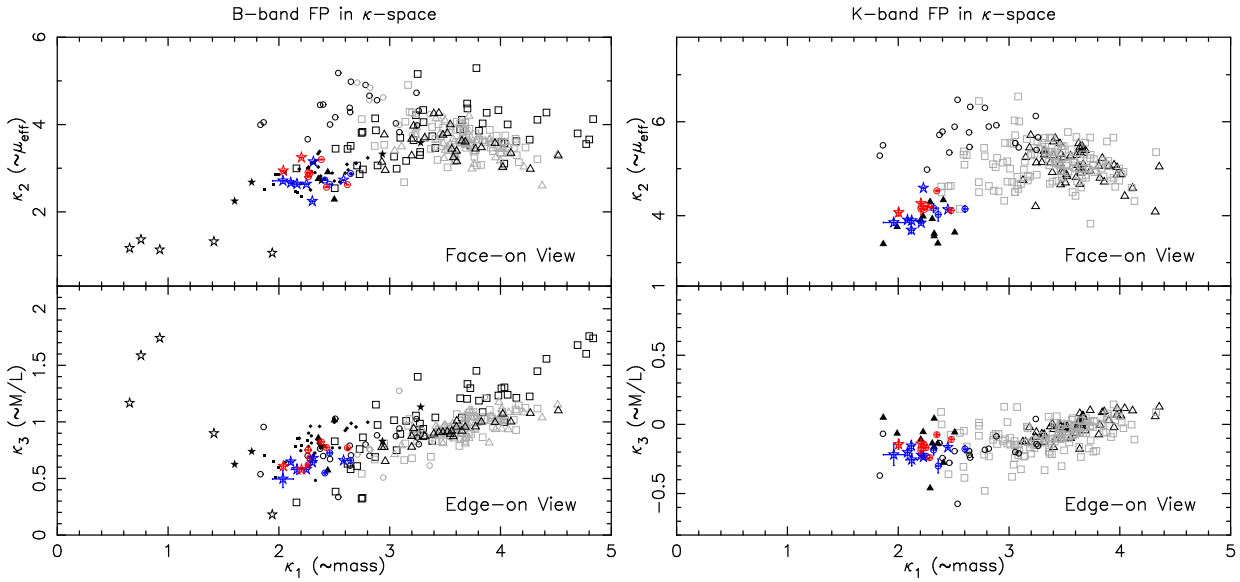

Figure 6.30: Face-on (upper panels) and edge-on (lower panels) view of the Fundamental Plane in the κ-space. Symbols are as in Figure 6.29.

In the four panels of Figure 6.30 dEs older than 7 Gyr and usually pressure supported, lie above the younger dEs that are rotationally supported, thus they present brighter surface brightnesses and larger M/L, in accordance to Figures 6.25 and 6.26 and the analysis made about the dynamical M/L in Paper I.

6.4.6 Discussion

The tightness of the scaling relations of massive early-type galaxies has been interpreted as an evidence of a similar formation and evolution mechanisms for all of them (Jorgensen et al. 1996; Pahre et al. 1998b). Thus finding whether dEs follow these same relations has been considered an important topic of study in order to prove if dEs are the low luminosity counterpart of Es and, as a consequence, they both had the same origin and have suffered analogous evolutionary processes.

Previous works based on the analysis of the scaling relations of dwarf galaxies have shown that Es and dEs exhibit different slopes in all of them, e.g., for the Kormendy relation Kormendy (1985); Capaccioli et al. (1992); Kormendy et al. (2009); for the size-luminosity relation Kormendy (1977); Guzmán et al. (1993); Binggeli & Cameron (1991); Caon et al. (1993); Boselli et al. (2008b); Kormendy et al. (2009); Janz & Lisker (2008), for the Faber-Jackson relation Matković & Guzmán (2005); de Rijcke et al. (2005) or Guzmán et al. (2003); de Rijcke et al. (2005); Geha et al. (2003) in the Fundamental Plane. However, although the results are similar, their interpretation is very different. Whereas some authors indicate that these changes of the slopes are the prove of Es and dEs being different families of objects (e.g., Kormendy 1977; Bender et al. 1992; Geha et al. 2003; Boselli et al. 2008b; Janz & Lisker 2008; Kormendy et al. 2009), other authors find several explanations to justify that dEs are the low-luminosity counterparts of Es although these two populations show different trends in these relations. For instance, Graham & Guzmán (2003b) explain the different trend as the consequence of the steepening of the central radial profile with luminosity, going from $n = 1$ (Sersic index for an exponential surface brightness profile) for dwarf galaxies to $n = 4$ ($R^{1/4}$ profile) for the brightest ellipticals; or de Rijcke et al. (2005) that, compar-

ing their data with models of evolution of dwarf and intermediate-luminosity early-type galaxies (Yoshii & Arimoto 1987), suggest that the position of dEs in these fundamental relations could be due to supernova-driven mass-loss.

In this paper we have analysed all these scaling relations for a sample of dEs in the Virgo cluster as a function of their ages and their dynamical properties in comparison with samples of Es, dEs and dSphs from the literature. We have proved that when state-of-the-art distances and velocity dispersions are used, the big deviations of dEs and dSphs found in relations such as the Faber-Jackson relation and the FP presented in previous works (e.g., Davies et al. 1983; Bender et al. 1992; de Rijcke et al. 2005; Matković & Guzmán 2005) become smaller. Therefore, the importance of having accurate distance and kinematic measurements is evident.

Comparing the scaling relations in the B and K-bands we have noticed that in all of them the scatter is larger in the bluest wavelength than in the reddest one. Due to the fact that the B-band is more sensitive to young stellar populations and the K-band to old ones, that are the bulk of stars in early-type galaxies, this larger scatter found in the optical versus the infrared suggests that the deviations found in the scaling relations are not only a consequence of structural differences between Es and dEs. If that is the case, then the deviations found should be independent of the wavelength studied.

The kinematic properties of dEs are correlated with their location in the scaling relations. This fact is more clearly seen in the K-band where the dispersion due to the influence of the stellar populations is removed. This result is contrary to what was previously found by Geha et al. (2003) analysing the FP in the κ space. They found that rotationally and pressure supported dEs populate the same region of the FP, this is highly likely to be the consequence of the poor radial coverage of their rotation curves (~ 6", see Paper I for an extended discussion on their kinematic data).

Graves & Faber (2010a,b) found that the position of galaxies across the FP is determined by their structural properties, and that the movement of galaxies along its thickness is only possible if they experience significant changes in their internal structure. The scaling relations analysed in this work are in agreement with this view due to the fact that we have found that pressure and rotationally supported dEs lie in distinct regions.

We can distinguish between two families of scaling relations: those based on the virial theorem, such as the Faber-Jackson relation and the FP, and those based on structural properties, such as Kormendy, the surface brightness-luminosity and the size-luminosity relations. The behaviour of dEs changes depending on the family of diagrams under study. In the particular case of the virial relations, Es and dEs do not show a change of slope because both populations are virialised in the sense that they are relaxed systems, so their position will essentially depend on the strength of their potential wells. When we analyse the diagrams that are based on structural characteristics we find that Es and dEs exhibit a change of slope that can be as dramatic as resulting in perpendicular trends for Es and dEs, as in the Kormendy relation. These evidences suggest that dEs are not the low-luminosity counterpart of massive ellipticals, because their structural characteristics, which are the result of their formation and evolution, are different.

6.4.7 Conclusions

In this work we analyse a sample of 18 dwarf early-type galaxies from the Virgo cluster. The spectroscopic data was observed at the WHT (La Palma, Spain). The near-infrared photometric images in the K-band were observed for 10 out of the 18 dEs at the WHT, TNG and NOT telescopes (La Palma, Spain), for the 8 remaining the data was drawn from GOLDMine database (Gavazzi et al. 2003a). The optical photometry used for this sample of dEs has been obtained from SDSS (York et al. 2000).

The scaling relations studied in this work are Kormendy, Faber-Jackson, surface-brightness and size-luminosity relations and the Fundamental Plane. We have found that, in all of them, the kinematics drives the location of dwarf galaxies in these diagrams. Rotationally and pressure supported dEs form two different groups of dwarf galaxies in these plots.

A change of slope between Es and dEs has been found only in those scaling relations that analyse the structural properties of galaxies, indicating that the processes that shape their formation and/or evolution are not the same for both populations of objects. However, when scaling relations linked to the virial theorem are analysed, such as the FP or the Faber-Jackson relation, then dwarf and giant galaxies follow the same trends. The structural differences between Es and dEs in these last two diagrams should be looked into their thickness.

All the results found for the scaling relations analysed here suggest that dEs and Es are two different populations. This is in agreement with the picture we presented in Paper I where dwarf early-type galaxies are the result of the transformation of low-luminosity late-type galaxies that entered the Virgo cluster. The transformation was achieved via ram-pressure stripping for those currently located in the outer parts of the cluster, due to the fact that these dEs conserve the same angular momentum as their progenitors and present stellar populations younger than those located in the core of the cluster. However, those dEs currently located in the center of Virgo probably, apart from the ram-pressure stripping experienced when they entered the cluster, also suffered harassment when they arrived at the regions with higher density of objects. The combination of these two transforming mechanisms is enough as to fade them until reaching the red colours observed today with the consequent older ages and the full transformation removing nearly all the hints from their previously late-type appearance.

Acknowledgments. We thank the MAGPOP EU Marie Curie Training Network for financial support for the collaborating research visits and observations that allowed to make this paper. ET thanks the financial support by the Spanish research project AYA2007-67752-C03-03. This paper made use of the following public databases: SDSS, NED, HyperLEDA, GOLDMine.

6.4.8 Appendix: Samples for comparison

In this work we present the fundamental scaling relations in Johnson B and K (λ_{eff} =2.2μm, FWHM= $0.34\mu m$) bands in the Vega system for dwarf early-type galaxies. These two bands have been chosen because they are the most studied in the literature so they allow us to make comparisons with different samples of normal early-types. For completion also bulges (Bs) and dwarf spheroidal galaxies from the Local Group (dSph) have been taken into account.

In this appendix we describe relevant aspects of each one of the works considered:

- Bender et al. (1992, B92): data available only in the B band. After checking the velocity dispersion (σ) for the galaxies and bulges in common with Sánchez-Blázquez et al. (2006b) and Falcón-Barroso et al. (2002) respectively and finding that the values are consistent within the errors, we have used B92 values for Es and Bs. In the case of the bright dEs, their σ have been updated using Pedraz et al. (2002); Geha et al. (2003); van Zee et al. (2004b); Sánchez-Blázquez et al. (2006b); Geha et al. (2006, 2010) but for NGC4515 and IC3393 that no updates have been found and IC767 and VCC351 whose σ in B92 are consistent with McElroy (1995). The velocity dispersion of the dSphs of B92 have also been improved using the recent measurements obtained by Wolf et al. (2010).

- Pahre et al. (1998b, P98): reference fit of the FP in K-band. As the fits they perform depend on the cluster considered, we are only taking Coma as reference because Coma was their largest sample. Also their compilation of Coma galaxies have been used for our study in the B-band. The parameters needed for this study are published in V-band (Johnson) in Pahre (1999, P99), we have transformed them into B-band calculating $B-V$ colour for each galaxy using the continuum photometry of GOLDMine Database. The effective radii are considered invariants between B and V bands.

- Jorgensen et al. (1992, J92): photometric parameters of their sample of Coma galaxies in the B-band.

- Falcón-Barroso et al. (2002, FB02): reference sample of bulges in both B and K bands.

- Geha et al. (2003, G03): sample of Virgo dEs, we only use those galaxies not in common with ours or van Zee et al. (2004b) (described below). G03 provides V band photometry that has been transformed into B band using a $B-V$ colour calculated for each galaxy using the continuum photometry of GOLDMine Database, for three galaxies this colour was not available and a fixed $B-V=0.8$ was assumed, the typical value obtained for the dEs considered. The surface brightness presented in this work is not within the effective radius, therefore $<\mu>_{eff}$ has been calculated using the apparent magnitude, the ellipticity and R_{eff} they provide through Equation 6.10.

- van Zee et al. (2004b, VZ04): the photometric optical properties of their sample of dEs in the Virgo cluster have been gathered from van Zee et al. (2004a) and the spectroscopically measured σ from Chilingarian (2009), where the full-fitting technique was applied to the spectra of van Zee et al. (2004b), a more accurate procedure that uses simple stellar populations as kinematic templates rather than only one star as in van Zee et al. (2004b). The surface brightness within the effective radius has been calculated using Equation 6.10, as in G03.

- de Rijcke et al. (2005, DR05): sample of dEs in the Fornax cluster in the B-band. The fit they performed in the B-band for giant early-type galaxies has been used as reference fit in the B-band FP.

- Gavazzi et al. (2003a, GM): GM data have been collected from the GOLDMine Database. The photometry both in B and H-bands of the Virgo Es and dEs was measured by Gavazzi et al. (2000, 2005) and converted into K-band assuming a constant colour of $H-K=0.21$. The Virgo dEs used in the B-band are those not included in G03, VZ04 nor in our sample. The velocity dispersions used for Es are a compilation of McElroy (1995); Gavazzi et al.

(1999a) and Caldwell et al. (2003), for dEs are from Pedraz et al. (2002); Simien & Prugniel (2002); Geha et al. (2003); van Zee et al. (2004b); Thomas et al. (2006) and Thomas et al. (2006).

6.4.9 Appendix: Distances

In order to compare simultaneously samples of galaxies located in different environments, we have to use absolute magnitudes and half-light radii measured in kpc, thus the distances to the galaxies are required. To make this study homogeneous, the distances employed in the works described above have been updated with the most recent measurements obtained using the surface brightness fluctuations technique (SBF). For the Virgo cluster galaxies we have considered the distances calculated in Mei et al. (2007, HST/ACS survey) for individual galaxies when available, or the mean distance to A or B clusters also from Mei et al. (2007). To know in which Virgo area galaxies reside in we have used the Virgo Cluster Catalog (Binggeli et al. 1985, VCC). For Coma and Fornax cluster galaxies we have used the mean SBF distance to the cluster by Thomsen et al. (1997, HST/ACS survey) and Blakeslee et al. (2009, HST/ACS survey) respectively. The rest of the distances for individual galaxies or for small groups as NGC5044 or NGC3258 have been compiled from one of the following works: Jensen et al. (1998); Tonry et al. (2001); Blakeslee et al. (2001); Ciardullo et al. (2002); Jensen et al. (2003); Jerjen et al. (2004). Local Group dSph have their distances computed using different techniques: Fornax and Draco through RR Lyrae (Mackey & Gilmore 2003; Bonanos et al. 2004, respectively), Sculptor through SBF (Jerjen et al. 1998), Carina through Cepheids (Mateo et al. 1998) and Ursa Minor through the colour-magnitude diagram (Carrera et al. 2002) . As a consequence, those galaxies that do not have their distances measured in one of these works have not been considered in our study. The exception are the bulges of Falcón-Barroso et al. (2002), which distances have been derived from optical recession velocities given in RC3 (de Vaucouleurs et al. 1991), corrected to the centroid of the Local Group (Karachentsev & Makarov 1996), and assuming a Hubble constant of $H_0 = 73$ km s^{-1} Mpc^{-1}, value measured from the SBF of Virgo galaxies by Mei et al. (2007). The field dEs from our sample have been excluded from the analysis of the scaling relations because the distances available show errors above 1 Mpc (using NED), achieving 14 Mpc in the case of NGC3073 (Tonry et al. 2001), while for the rest of the objects the errors are below 0.5 Mpc.

6.5 Conclusions

In this Chapter we have analysed a sample of 21 dEs, 18 out of the total are located in the Virgo cluster and the 3 remaining are from the field. The spectroscopic data we have used to perform this study was gathered within the MAGPOP-ITP collaboration that was granted with a total of 53 nights in the largest telescopes of El Roque de los Muchachos Observatory (La Palma, Spain). 67% of the near-infrared (H and/or K band) was also gathered using the allocated time for this project and the 33% remaining was drawn from GOLDMine database (Gavazzi et al. 2003a). The optical photometry in i, g and r bands have been obtained from SDSS (York et al. 2000), data releases 6 and 7 (Adelman-McCarthy et al. 2008; Abazajian et al. 2009).

From the spectroscopic analysis of the kinematic properties of this sample we have found that the rotationally supported population is more frequent than originally thought (e.g., Geha et al. 2002, 2003)) and that the kinematic behaviour of dwarf galaxies is linked to: their position within the cluster, their internal structures, and the ages of their stellar populations. Those dwarfs rotationally supported show underlying disky structures, are younger, on average, and are located in the outer parts of the cluster, while those pressure supported do not show any internal structures and tend to be older and more concentrated around M87, the central galaxy of the cluster.

The study of the shapes of the rotation curves for those dEs rotationally supported has shown that they are similar to those late-type galaxies of the same luminosity. Also, these dEs follow the Tully-Fisher relation for spiral galaxies. Regarding the dark matter content of these galaxies, we have shown that the dynamical mass-to-light ratio of dEs present lower values than both dSphs and Es, and its comparison with the stellar mass-to-light values obtained from their ages and metallicities using the SSP models of Vazdekis et al. (2010) reveals that dEs are not dark matter dominated objects, at least at radius below $R_{\rm eff}$.

From the analysis of the scaling relations we have found that the previous gaps found between Es and dEs were an observational bias. Introducing all the available data in the photometric bands studied (B and K) there are no gaps in any of the relations. We have also focused our study in the location of dEs that have different kinematic behaviour and we have deduced that rotationally supported dEs appear in all the scaling relations, parallel to those dEs that are pressure supported. The changes of slope (that could also be interpreted as an offset) found in the Kormendy relation, and in the surface brightness-luminosity and size-luminosity diagrams, suggest that Es and dEs are structurally different, being these results also independent from the wavelength under study. This suggests a different origin for dEs with respect to Es. This structural change is in contrast to the agreement between Es and dEs in the Faber-Jackson relation and in the Fundamental Plane, but this is a result of the fact that these two diagrams represent the virial theorem, thus relaxed populations, such as Es and dEs, must follow the same trends.

All these results are consistent with a picture where most dEs are low-luminosity late-type galaxies that have entered the Virgo cluster and have lost their gas content through a ram-pressure stripping event without modifying the kinematics of their progenitors. Once they fall to the center of the cluster, where the density of neighbours and intergalactic medium is much higher than in the outskirts, other processes such as harassment can also contribute to the complete transformation into old, relaxed (structurally and kinematically) systems.

7

Conclusiones

En este trabajo hemos estudiado el papel que desempeña el entorno en la formación y evolución de galaxias masivas y enanas de primeros tipos. Nos hemos acercado a este problema, analizando por separado una muestra de galaxias masivas situadas en diferentes entornos y una muestra de galaxias enanas que se encuentran principalmente en el cúmulo de Virgo. El análisis de las muestras realizadas en esta tesis nos ha permitido estudiar el escenario jerárquico de formación de galaxias y profundizar en la posibilidad de que las galaxias enanas de primeros tipos sean o no la contrapartida a baja luminosidad de las galaxias elípticas masivas.

7.1 Galaxias masivas de primeros tipos en los cúmulos de Coma y Virgo y en el campo

La historia de formación estelar de galaxias de los primeros tipos la hemos estudiado mediante el análisis de los índices de intesidad de línea en una muestra de 35 galaxias elípticas masivas situadas en los cúmulos de Coma y de Virgo, y el campo. En este trabajo hemos considerado el cúmulo de Coma como una región de alta densidad y el cúmulo de Virgo y el campo como entornos de baja densidad. En particular, y por primera vez, hemos utilizado el índice NH3360 definido por Davidge & Clark (1994), como indicador de las abundancias de N en las galaxias (Bessell & Norris 1982; Tomkin & Lambert 1984), y los índices CNO3862, CNO4175 y CO4685, definidos por Serven et al. (2005), que miden simultáneamente las abundancias de C, N y O. La combinación de estos cuatro índices es una técnica innovadora para separar el C y el N, que por lo general se estudian mezclados en las bandas de CN. La importancia del C y N en el estudio de las galaxias de primeros tipos se basa en que los elementos actúan como relojes cosmológicos ya que sus escalas de tiempo de formación son diferentes.

En este análisis, el primero realizado utilizando un índice puramente de N, hemos encontrado los siguientes resultados:

- La relación entre el índice de NH y la dispersión de velocidades para galaxias de primeros tipos es plana, en contra de resultados anteriores basados en índices de CN. Esta relación plana indica que el N es un elemento primordial, lo que significa que se produjo en la primera generación de estrellas que se formaron en la galaxia, ya que las abundancias de los elementos secundarios aumentan con la masa de las galaxias (Kelson et al. 2006; Schiavon 2007).

- Las abundancias de N son independientes del entorno, a diferencia del C, que es más abundante en Virgo y en el campo que en Coma.

Estos resultados sugieren que la historia de formación estelar de las galaxias de primeros tipos depende del entorno donde estén situadas, y además nos indica que la escala de tiempo para producir C y N es diferente.

En el caso del N, el hecho de que no haya diferencias sistemáticas entre galaxias que habitan regiones de densidad distinta y que no dependa de la velocidad de dispersión de las galaxias sólo puede explicarse si el N se produce tanto en estrellas masivas ($M > 8M_{\odot}$) como de masa intermedia ($4 < M < 8M_{\odot}$). En este contexto las estrellas masivas son responsables de que el N no dependa del entorno, de la misma manera que sucede con el magnesio que, debido a su rápida producción en las supernovas de tipo II, su abundancia es independiente del entorno pero además está fuertemente correlacionada con la masa de las galaxias. Las estrellas de masa intermedia son, por lo tanto, las responsables de que no haya correlación del N con la masa de las galaxias. Esto se debe a que las galaxias menos masivas, que son las que presentan una formación estelar más extendida en el tiempo debido al *downsizing* (ver por ejemplo Cowie et al. 1996), tienen más tiempo para incorporar más N, lo que se traduce en un aumento de N con respecto a las galaxias masivas y el consecuente aplanamiento de la pendiente en la relación NH3360$-\sigma$.

En el caso del C aún está en discusión si las estrellas que lo producen son masivas o de baja masa ($1 - 4M_{\odot}$). Los resultados encontrados en nuestro análisis nos han llevado a proponer que el C se produce, en proporciones comparables, en los dos tipos de estrellas. La fuerte pendiente del diagrama C$-\sigma$ es la consecuencia del C producido en las estrellas masivas, mientras que las diferencias sistemáticas encontradas entre regiones de alta y baja densidad provienen de la producción de C en estrellas de baja masa. Debido al hecho de que la historia de formación estelar de galaxias situadas en regiones de baja densidad es más larga en el tiempo que las de las situadas en áreas de alta densidad (ver por ejemplo Sánchez-Blázquez 2004; Nelan et al. 2005; Thomas et al. 2005; Sánchez-Blázquez et al. 2006b), el C liberado por las estrellas masivas incrementa la cantidad de C disponible en Virgo y en el campo para las siguientes generaciones de estrellas haciendo que las galaxias situadas en estos entornos presenten mayores abundancias de C que aquellas ubicadas en el cúmulo de Coma.

En un estudio posterior en colaboración con el Dr. G. Worthey y su estudiante de doctorado J. Serven, hemos analizado las abundancias de C y N en comparación con un nuevo conjunto de modelos desarrollados por J. Serven. En este estudio hemos visto que el índice de NH3360 está contaminado por Mg. Esto nos ha llevado a la definición de dos nuevos índices, NH3375, libre de toda contribución de Mg, y Mg3334, donde hemos aislado esta contaminación. Al analizar el nuevo índice de NH en nuestra muestra de galaxias masivas de primeros tipos encontramos que NH3375 presenta una ligera dependencia con la masa. En este trabajo se han analizado el N y el Mg en función de la metalicidad. Los índices de N, NH3360 y NH3375, presentan un comportamiento similar en función de la metalicidad que indica que ambos están midiendo las mismas abundancias de N. Sin embargo, en el caso del Mg, este elemento contribuye de manera muy diferente a los índices Mgb y Mg3334. Hemos estudiado este resultado con los nuevos modelos de J. Serven. Para ello hemos medido estos índices de Mg y N para una población vieja de metalicidad solar a la que hemos añadido una subpoblación de estrellas viejas y pobres en metales. Aunque esta subpoblación no reproduce completamente la anticorrelación de los índices de NH con la metalicidad, sí que explica el comportamiento diferente observado en Mg3334 con respecto a Mgb.

Hemos interpretado este resultado como una evidencia de la existencia de una subpoblación vieja y pobre en metales en las galaxias elípticas.

7.2 Galaxias enanas de primeros tipos en el cúmulo de Virgo

La muestra de galaxias enanas de primeros tipos analizada en este trabajo consta de 18 dEs en el cúmulo de Virgo y 3 dEs en el campo. Todas ellas se observaron en espectroscopía de resolución intermedia ($40-46$ km s^{-1}), haciendo así posible realizar un estudio detallado de los perfiles cinemáticos. Combinando estos datos con los datos fotométricos obtenidos en el infrarrojo cercano, o disponibles en la literatura (base de datos de GOLDMine y SDSS, Gavazzi et al. 2003a; York et al. 2000), hemos conseguido reunir unos datos únicos para hacer un estudio completo tanto de la cinemática como de las propiedades estructurales de estas galaxias en diferentes longitudes de onda. Los principales resultados y conclusiones de este análisis son los siguientes:

- Hemos analizado el cociente entre la velocidad de rotación máxima y dispersión de velocidades de las galaxias en función de la elipticidad de las galaxias, y hemos encontrado que existen dos poblaciones de dEs: aquellas que están soportadas por rotación y las que están dominadas dinámicamente por los movimientos aleatorios de las estrellas.

- Este soporte rotacional está además relacionado con la ubicación de las dEs dentro del cúmulo de Virgo: aquellas situadas en las partes más externas del cúmulo están soportadas por rotación, mientras que las situadas cerca del centro están preferentemente sportadas por presión.

- Las galaxias soportadas por rotación presentan edades más jóvenes que las que están soportadas por presión.

- La forma de las curvas de rotación de las dEs soportadas rotacionalmente es similar a las de galaxias de los últimos tipos con la misma luminosidad.

- Las galaxias enanas soportadas por rotación siguen la relación de Tully-Fisher típica de las galaxias espirales.

- A través de las propiedades cinemáticas de esta muestra de galaxias enanas hemos podido analizar la relación dinámica de masa-luminosidad ($M_{\rm dyn}/L$) dentro de un radio efectivo. Hemos confirmado que la relación $M_{\rm dyn}/L$ de las galaxias enanas es inferior que la que presentan las galaxias elípticas masivas y las galaxias esferoidales. Al comparar la relación masa-luminosidad dinámica con la estelar, calculada a partir de las edades de Michielsen et al. (2008) y los modelos de Vazdekis et al. (2010), hemos confirmado que las galaxias enanas de primeros tipos no están dominadas por materia oscura, al menos dentro del radio efectivo.

- Todas las relaciones de escala estudiadas en este trabajo muestran que las galaxias soportadas por rotación y por presión aparecen bien diferenciadas en todas ellas. Ésto es más fácil de apreciar en la banda infraroja que en la óptica, a que esta última está altamente influenciada por las poblaciones jóvenes que puedan estar presentes en las galaxias.

- En cuanto a la relación Faber-Jackson tanto las galaxias enanas como las masivas presentan la misma pendiente, en contra de los estudios previos sobre esta relación de escala.

- Al analizar el Plano Fundamental en las bandas B y K hemos encontrado que las galaxias enanas siguen el mismo plano que las gigantes. La dispersión que presentan las galaxias es mayor en la banda B que en la banda K, muy posiblemente por que esta banda óptica está muy influenciada por las poblaciones estelares jóvenes.

Estos resultados apoyan un escenario en el que las galaxias enanas no son las contrapartidas a baja luminosidad de las galaxias elípticas masivas, sino una población muy diferente de objetos. Cuando se estudian las propiedades generales de las galaxias que no están específicamente relacionados con sus características estructurales, tales como su masa o luminosidad total, las galaxias enanas siguen las mismas relaciones de escala que las galaxias elípticas masivas, pero, cuando las propiedades estructurales y/o cinemáticas son las que se analizan, estando éstas más vinculadas a sus procesos de formación y evolución, las diferencias son evidentes. Este es el caso de la relación tamaño-luminosidad, la forma de las curvas de rotación o el soporte cinemático. En estos casos, nuestros resultados indican que las galaxias enanas tienen más características en común con las galaxias de los últimos tipos que con las elípticas masivas.

Todas estas evidencias son consistentes con un escenario en el que las galaxias enanas de los primeros tipos son galaxias de los últimos tipos de baja luminosidad que han sido transformadas. Estas galaxias de tipo tardío entraron en el cúmulo y perdieron el gas por un proceso de *ram-pressure stripping* (ver por ejemplo Boselli et al. 2008a), como consecuencia la formación estelar se apagó pero las galaxias conservaron el momento angular de sus progenitores. Éste sería el proceso que ha transformado a las galaxias que actualmente se observan en las partes exteriores del cúmulo, ya que las poblaciones estelares que presentan son más jóvenes y están soportadas por rotación. Las galaxias que están situadas cerca de las regiones centrales del cúmulo probablemente cayeron antes que las observadas en las partes externas, por lo que además del *ram-pressure stripping* se vieron afectadas por *harassment* al acercarse al núcleo del cúmulo (ver por ejemplo Moore et al. 1999) provocando una transformación completa en galaxias de primeros tipos eliminando cualquier rastro del momento angular o las estructuras de disco de las galaxias progenitoras.

7.3 Consideraciones finales

Este trabajo ha demostrado que el entorno juega un papel importante en la formación y evolución de galaxias. En el caso de las galaxias elípticas masivas, hemos visto que los elementos formados en estrellas de baja masa, como el carbono, presentan abundancias diferentes en función de la densidad del entorno, siendo mayor para las galaxias en entornos de baja densidad. Esto evidencia que las galaxias de Virgo y las que están en el campo tienen una historia de formación estelar más extendida en el tiempo que las que habitan el cúmulo de Coma, donde la formación estelar se ha detenido de forma abrupta. En el caso de las galaxias enanas de primeros tipos, hemos visto que las galaxias a diferentes distancias del centro del cúmulo pueden ser interpretadas como fotos de la misma galaxia en las diferentes etapas de su evolución.

En nuestro estudio hemos encontrado lo que predice el modelo jerárquico de formación de galaxias, que la historia de formación estelar de las galaxias depende del entorno. Sin embargo,

la idea de que las galaxias enanas de primeros tipos son la contrapartida a baja luminosidad de las galaxias masivas se ha puesto en entredicho a la luz de los resultados obtenidos en el Capítulo 6, donde hemos encontrado que todas las propiedades analizadas en dEs se asemejan a las que presentarían galaxias de tipos tardíos de baja luminosidad después de su interacción con el medio intergaláctico del cúmulo. Por otra parte, si las dEs fuesen elípticas de baja luminosidad entonces su mecanismo de formación debería ser similar al de las masivas, pero De Lucia et al. (2006) han encontrado que la probabilidad de que las galaxias enanas se formasen como resultado de la fusión de otras galaxias es nula.

8

Conclusions

In this work we have studied the role of the environment in the formation and evolution of massive and dwarf early-type galaxies. We have approached this problem analysing separately a sample of massive galaxies located in different environments and a sample of dwarf early-type galaxies mainly located in the Virgo cluster. The analysis of the samples performed in this thesis has allowed us to test the hierarchical scenario and dig into the possibility of dwarf early-type galaxies being the low-luminosity counterparts of the massive ellipticals.

8.1 Massive early-type galaxies in the Coma and Virgo clusters and in the field

The star formation history of early-type galaxies has been studied by analysing the line-strength indices in a sample of 35 massive ellipticals located in the Coma and the Virgo clusters, and the field as examples of different density regions (for this work the Coma cluster is considered a high density region whereas Virgo and the field are used as low density environments). In particular, and for the first time, we have used the index NH3360, defined by Davidge & Clark (1994), which is a powerful tool tracer of the N abundances in galaxies (Bessell & Norris 1982; Tomkin & Lambert 1984), and the indices CNO3862, CNO4175 and CO4685, defined by Serven et al. (2005), that measure together abundances of C, N and O. The combination of these four indices is an innovative technique to separate C and N contributions, usually studied together through the cyanogen bands. The importance of C and N in the study of early-type galaxies resides in the fact that they are cosmological clocks with formation time scales that are different, although not yet clear, with respect to Mg (rapidly ejected to the interstellar medium through type II supernovae) and Fe (ejected in very long time scales by type Ia supernovae).

This analysis, the first done using an index that depends only on N, has shown that:

- The relation between the NH3360 index of early-type galaxies and their velocity dispersions is flat, contrary to what was previously claimed by other authors that used CN-absorption features. This flat trend indicates that N is a primary element, which means that it was produced in the first generation of stars, because the abundances of secondary elements increase with the mass of the galaxies (Kelson et al. 2006; Schiavon 2007).

- N is independent of the local environment, contrary to C which is stronger in Virgo and in the field with respect to the Coma cluster.

These results suggest that the star formation history of early-type galaxies depends on the environment, and that the time scales of the production of C and N in these galaxies are different.

In the particular case of N, its lack of systematic differences between galaxies inhabiting regions of distinct density and its independence of the velocity dispersion of the galaxies can only be explained if N is produced by both massive ($M > 8M_{\odot}$) and intermediate-mass ($4 < M < 8M_{\odot}$) stars. In this scenario the massive stars are responsible for the equal abundances measured in high and low density regions, in the same way as Mg that, due to its rapid production by type II supernovae, shows the same abundance independently of the environment and it is tightly correlated to the mass of the galaxies. The intermediate-mass stars are thus responsible of the flat relation with the mass of the galaxies because low-mass galaxies, which star-formation is more extended in time due to a downsizing effect (e.g., Cowie et al. 1996), have a longer time to incorporate more N, which results in an increase of N with respect to massive galaxies, flattening the slope in the NH3360$-\sigma$ diagram.

In the case of C it is still under debate whether the stars that produce it are massive or lower-mass stars ($1 - 4M_{\odot}$). We propose that C is produced in comparable proportions by the two types of stars. The significant slope of the C$-\sigma$ relations would be the consequence of C being produced in massive stars, whereas the systematic differences found as a function of the environment would come from the C production of low-mass stars. Due to the fact that the star formation history of galaxies located in lower density regions is longer than those in high density areas (e.g., Sánchez-Blázquez 2004; Nelan et al. 2005; Thomas et al. 2005; Sánchez-Blázquez et al. 2006b), the C released by massive stars would increase the budget of C in Virgo and in the field generating an offset in the C abundance when compared to the Coma cluster.

In a later study in collaboration with Dr. G. Worthey and his Ph.D student J. Serven, we have analysed C and N abundances in comparison to a new set of models developed by them. In this study we have shown that the index NH3360 is contaminated by Mg. This led to the definition of two new indices, NH3375 free of any Mg contribution, and Mg3334 where Mg is isolated. When the new NH index was analysed for our sample of early-type galaxies, we found that it presented a slight dependence as a function of σ, in contrast to NH3360. In this work we have analysed N and Mg as a function of the metallicity. The N indices, NH3360 and NH3375 present a similar behaviour as a function of the metallicity indicating that both are measuring the same contribution of N, but Mg in Mgb and Mg3334 contributes differently. We have studied this evidence with the models developed for this study measuring these Mg and N indices in an SSP of an old and solar metallicity population with different contributions of an old, metal-poor subpopulation of stars. Although this subpopulation cannot completely reproduce the anticorrelation of NH indices with metallicity, it explains the different behaviour observed for Mg3334 with respect to Mgb. We have interpreted this evidence as the existence of an old, metal-poor subpopulation of stars in elliptical galaxies.

8.2 Dwarf early-type galaxies in the Virgo cluster

The sample of dwarf early-type galaxies analysed in this work consists of 18 dEs located in the Virgo cluster and 3 dEs in the field. All of them were observed in medium-resolution spectroscopy (40$-$46 km s^{-1}), making possible a detailed study of their radial kinematic profiles. Combining these data with photometric data obtained in the near-infrared, or available in the literature (GOLD-

Mine database and SDSS, Gavazzi et al. 2003a; York et al. 2000), we have gathered a unique set of data to make a complete study of the kinematic and the structural properties of these galaxies in different wavelengths. The main results and conclusions of this analysis are the following:

- Quantifying the maximum rotation measured in our rotation curves over the velocity dispersion of the galaxies as a function of the ellipticity of the galaxies we have shown that there are two populations of dEs: those that are rotationally supported and those that are pressure-supported or dominated by random motions.
- The dynamic support is related to the location of the dEs within the Virgo cluster: those located in the outer parts of the cluster or in the field are rotationally supported whereas those located near the center are preferentially pressure-supported.
- Rotationally supported galaxies have younger luminosity-weighted ages than those dominated by random motions.
- By comparing the shape of the rotation curves, we have shown that rotationally supported dEs have rotation curves similar to those of normal late-type galaxies of similar luminosity.
- Rotationally supported dEs follow the same Tully-Fisher scaling relation of late-type galaxies.
- The kinematic properties of these dwarf galaxies have made possible the analysis of the dynamical mass-to-light ($M_{\rm dyn}/L$) ratios within the effective radius. We have confirmed that their dynamical $M_{\rm dyn}/L$ is smaller than those of massive ellipticals and dSphs. The comparison of the dynamical $M_{\rm dyn}/L$ with the stellar M_*/L obtained from their stellar populations (Michielsen et al. 2008) have led us to confirm that dEs are not dark matter dominated objects, at least within their half-light radius.
- All scaling relations show a systematic difference between the location of rotationally supported dEs (the young ones) and the pressure supported ones (the old dEs). This evidence is always more clear in the K-band where the influence of young stellar populations in the photometric parameters is removed.
- In the study of the Faber-Jackson relation we have shown that massive and dwarf galaxies have the same slope.
- In the analysis of the Fundamental Plane of early-type galaxies in the B and the K bands we have found that dEs follow the same FP of more massive stellar objects. In addition, the scatter observed in the B-band is larger than in the K-band, possibly due to the influence of young stellar populations.

These results support an scenario in which dwarf galaxies are not the low-luminosity counterparts of massive ellipticals, but a very different population of objects. When general properties of the galaxies that are not specifically related to their structural characteristics, such as their masses or total luminosities, are studied dwarf galaxies follow the same trends as normal elliptical galaxies, but, when structural properties and/or kinematics are analysed, properties more linked to their formation and evolution processes, striking differences are found. This is the case of the size-luminosity relation, the shapes of the rotation curves or the dynamical support. In these

cases our results indicate that dwarf early-type galaxies have more characteristics in common to low-luminosity late-type galaxies than to bright early-type ones.

All these evidences are consistent with a scenario in which dwarf early-type galaxies are transformed low-luminosity late-type galaxies. These low-luminosity late-types entered the cluster and lost their gas content through a ram-pressure stripping event (e.g., Boselli et al. 2008a), fading but conserving the angular momentum of the progenitors. These are the galaxies currently observed in the outer parts of the Virgo cluster that have younger populations and are rotationally supported. Those that are currently located near the central regions of the cluster are more likely to have fall before the ones observed in the outer parts, thus apart from the ram-pressure stripping experienced when they entered the cluster, they suffered harassment (e.g., Moore et al. 1999) when achieving the core of the cluster which provoked the complete transformation into early-types removing completely the angular momentum of their progenitors and their disky structures.

8.3 Final remarks

This work has demonstrated that the environment plays a major role in the formation and evolution of galaxies. In the case of massive galaxies, we have seen that those elements formed in low-mass stars, such as carbon, present different abundances as a function of the density of the region where the galaxies are located, being higher for those galaxies in low density environments. This evidences that galaxies in Virgo and in the field have more extended star formation histories than those in the Coma cluster, where the star formation stopped more abruptly. In the case of dwarf galaxies, we have seen that galaxies at different clustercentric distances can be studied as snapshots of the same galaxy in the different stages of its evolution.

This environmental dependence of bright ellipticals is predicted by the hierarchical merging scenario of galaxy formation, thus our study is consistent with it. However, the usual thought of dEs being the low-luminosity counterparts of massive early-types has been highly questioned by the results obtained in Chapter 6, where we have found that all the properties analysed in dEs resemble those of late-type galaxies of similar luminosity after their interaction with the hot intergalactic medium of the cluster. Moreover, if dEs were low-luminosity ellipticals implies that their formation mechanism should be similar, but De Lucia et al. (2006) have found that the probability a dE being formed as a result of a merger is null.

9

Future work

The analysis done so far has shown the power and efficiency in using combined kinematic and spectrophotometric data in the study of the evolution of early-type galaxies, from low surface brightness dwarfs to giant ellipticals. Once again this analysis has confirmed the importance of mass and environment in shaping galaxy evolution. At the same time, this work has opened new directions of research that deserve further attention, such as the radial variations even outside the effective radius and a multiwavelength analysis.

9.1 Kinematic and stellar population gradients

The measurement of kinematics and stellar populations along the galactic radius provides information of utmost importance about the formation of galaxies. In particular, gradients in dEs can reveal clues of great value about their similarities/differences with giant ellipticals.

The study of the gradients in massive ellipticals (see Sánchez-Blázquez et al. 2006a, and references therein) has shown that the environment plays an important role in the star formation histories of galaxies. Sánchez-Blázquez et al. (2006a) found that the positive age gradient (the age of the galaxy increasing along the radius) is more pronounced in galaxies inhabiting low density regions than those populating rich clusters like Coma. In terms of the metallicity, the gradients are usually negative, thus the metallicity increases towards their center. In this case, galaxies in the Coma cluster exhibit a steeper gradient in comparison with galaxies in the field and the Virgo cluster. This study, made through the analysis of Lick/IDS indices, also concluded that the strength of the gradients are highly dependent on the specific index analysed. For example, if the metallicity gradient is obtained using CN_2 and Mgb, then it correlates with the central age of the galaxies. On the contrary, if Fe4383 or Ca4227 is used, the metallicity gradient correlates with the velocity dispersion gradient (the σ variation with the radius of the galaxy).

However, not much work has been done for dEs in getting kinematic profiles and stellar population gradients (Gorgas et al. 1997; Pedraz et al. 2002; Simien & Prugniel 2002; Geha et al. 2002, 2003; van Zee et al. 2004b; Chilingarian 2009; Koleva et al. 2009a; Toloba et al. 2009a, 2011), because such a study is very difficult in dwarfs due to their low surface brightness at large radii. Two methods have recently proved to be highly efficient in this kind of study. On the one hand, the study of globular clusters inside dwarf galaxies (Beasley et al. 2006, 2009) has the advantage of reaching radii on the order of $6-8R_{eff}$ at the distance of Virgo, but they do not provide information about the stellar content of the galaxy. On the other hand, the study of resolved stellar populations of dwarf galaxies in the Local Group (e.g., Geha et al. 2006, 2010) has

the advantage of also reaching radii of around $8R_{eff}$, simultaneously providing all the ingredients needed to study in astonishing detail the star formation history of these galaxies. However, it can not be performed for galaxies beyond the Local Group.

Koleva et al. (2009a), for the Fornax cluster and some small groups, and Chilingarian (2009), for the Virgo cluster, have performed some analysis about the age and metallicity gradients of dEs using integrated spectroscopy at around the R_{eff}. In both of these studies the full-spectrum fitting technique was used to derive radial profiles of the SSP-equivalent ages and metallicities. They both have found metallicity gradients, being the nuclear regions more metal-rich than the outer parts of the galaxy, and nearly constant ages along the radius. Only in some cases, the central parts of the galaxies show younger ages. These results are therefore consistent with those found for more massive early-type galaxies (see however Boselli et al. 2008a).

These first results on dEs can still be explored in much more detail. Up to now, dEs gradients have been analysed fitting the full optical SED (Spectral Energy Distribution) of the galaxy with SSP (Simple Stellar Population) models. Thus it will be useful to make a comparison reproducing the same analysis but using line-strength indices, as done for massive ellipticals, to check that the results are consistent. Moreover, a similar analysis as the one made in Sánchez-Blázquez et al. (2006a) studying the gradients of specific chemical species such as Fe, Mg, C and N, is an important method to compare the star formation histories of dwarf galaxies with those of Es. This analysis, taking also into account the clustercentric distance of the galaxies and their kinematic properties, can give major insight on the processes that gave birth the local objects. In this direction, I will perform a detailed analysis of the stellar population gradients for the sample of dEs studied in this work.

9.2 Multi-wavelength surveys at different redshifts

In a longer term perspective, the study of dwarf galaxies should be extended to other wavelengths to obtain the complete information of all the components of the galaxies, and to higher redshifts in order to see the different stages of the formation of dwarf galaxies.

In recent years a great effort has been made in this direction in the Virgo cluster. Photometric surveys that have targeted this cluster are ACSVCS survey (Ferrarese et al. 2006), that studied the 100 brightest ellipticals with ACS-HST, and the study of Virgo using SDSS of Lisker and collaborators (Lisker et al. 2006a,b, 2007, 2008, 2009). These studies have already been finished while others are currently being carried out: NGVS (optical, PI: Ferrarese), HeVICS (Herschel, far-IR, Davies et al. 2010), ALFALFA+AGES (HI, Giovanelli et al. 2005), and GUVics (Galex, UV, Boselli et al. 2011).

Dwarf early-type galaxies that we observe today in the Virgo cluster have red colours and elliptical shapes. If they experienced a transformation from low-luminosity late-type galaxies, in higher redshift clusters we should progressively see, with increasing distance, that low-luminosity star-forming galaxies are more abundant than they are today, being dEs less numerous (in agreement with what was found by Babul & Ferguson 1996). In fact, the number of low-luminosity star-forming galaxies in the field is expected to be much larger at high redshift than today because, in a transformation scenario, a high fraction of them would have been converted into dEs in local clusters.

Observing such galaxies in clusters at different redshifts we will be in the unique position to analyse the evolution of dwarf galaxies throughout the cosmic time. Nowadays this high redshift study is biased towards dwarfs with extremely strong star-formation bursts, due to the fact that it is the only way to observe such a low surface-brightness objects at large distances. However, with the future giant telescopes, like the European-Extremely Large Telescope (E-ELT), it will be possible to observe dwarf galaxies at high redshifts with wide ranges in their properties, allowing us to make the connection with the dwarfs in the local Universe.

9.3 SMAKCED: Stellar populations, MAsses and Kinematics of Cluster Early-type Dwarf galaxies

To fulfill this work in the two aspects described above, reaching larger radii and covering other wavelength ranges, we have started the SMAKCED collaboration. It is constituted by groups in Madrid, Heidelberg, Groningen, Marseille, Canarias, Oulu and Vienna. It aims to understand the physical processes involved in the formation and evolution of dwarf early-type galaxies. Virgo is the cluster chosen for this study because it contains a large number of dEs and it is close enough to resolve their structure in detail.

The main goal of this collaboration is to make an observational survey gathering high-resolution spectra and near-infrared images for a complete magnitude-limited sample of all Virgo cluster early-type galaxies in the magnitude range $-16 \geq M_r \geq -19$ (approximately $-15 \geq M_B \geq -18$). The sample is statistically significant and contains a wide range of properties covering all dE subclasses (with disks, without disks, other structures, blue nuclei, etc.)

The first purpose of SMAKCED is to gather spectroscopic and NIR imaging to study dEs in the Virgo cluster with a radial coverage of up to $2R_{\rm eff}$. With these data we will study the rotational support of early-type dwarfs as a function of galaxy mass, environment and stellar populations (see Section 6.3), as well as their radial stellar population gradients. By combining the spectroscopy with NIR data we will construct the NIR fundamental plane down to low luminosities and compare the structural properties of dEs with giant early-types and S0s, in order to understand whether they have a common origin, extending in this way the analysis done in Section 6.4. We will also study the star formation history of the target galaxies by combining their UV to NIR SED with high-resolution spectral indices. To study the amount and distribution of the dark matter in these objects we will obtain accurate stellar mass-to-light ratios and we will compare them with the dynamical values obtained from the spectra. In addition, we will compare the luminosity and mass function with state-of-the-art cosmological semi-analytical models. This complete study will help us to check whether all the previously mentioned relations are modulated by the environment, i.e. looking for any dependence with galaxy number density or clustercentric distance. The ultimate aim of this collaboration is to combine the data acquired within it with the available coverage of Virgo dwarf galaxies at other wavelength regimes in order to build a unique multifrequency database for them.

This survey, that began its observations on February 2010, in combination with model predictions (cosmological simulations, harassment and ram-pressure stripping) will be a strong tool to study the formation and evolution processes of dEs inhabiting rich clusters.

A

Tables of line-strength indices in massive ellipticals

In this appendix I present a summary of the reduction procedure performed for the spectral range 3140-4040Å, and some tables that include the observational sample and the line-strength indices used in the analysis performed in Chapter 5 as well as the rest of indices defined in Serven et al. (2005) and in the Lick/IDS system that can be measured in the wavelength range $3140-5250$ Å.

The sample used in Chapter 5 was selected from the galaxies in Sánchez-Blázquez et al. (2006b) to have objects located in low and high density environments with available spectroscopy in the optical range and to cover a wide range in velocity dispersions. The reduction followed is the standard procedure for long-slit spectroscopy using R$_{\rm E}$D$^{\rm uc}_{\rm m}$E. The steps taken consists on bias and dark current subtraction, flat-fielding (using observations of tungsten lamps and twilight sky to correct for high and low frequency variations respectively), cosmic ray cleaning, C-distortion correction, wavelength calibration, S-distortion correction, sky subtraction, atmospheric and interstellar extinction correction and flux calibration. A more detailed explanation of the procedure can be seen in Section 6.2.

Galaxy spectra have been extracted within a central equivalent aperture of 4" at the distance of NGC 6703, which corresponds to a physical aperture of 0.76 kpc. All the indices have been measured at a velocity dispersion of $\sigma = 200$ km s^{-1} and have been corrected for the effects of σ using a combination of synthetic spectra from Bruzual & Charlot (2003) and Vazdekis et al. (2010). The technique used to perform such a correction is explained in Appendix C.

Name	Morph. type	M_B	Env.	PA (deg)	SA (deg)	σ (km s^{-1})
IC 832	E	−19.96	Coma	168.0	168.0	175.3
IC 3957	E	−19.26	Coma		9.3	171.2
IC 3959	E	−20.03	Coma		9.3	226.1
IC 3963	SA0	−19.25	Coma	840.0	296.4	130.3
IC 3973	S0/a	−18.85	Coma	142.0	48.5	256.3
MGC+5−31−063	E6	−19.68	Coma		70.0	155.1
NGC 4842A	E/SA0	−19.89	Coma		172.4	232.2
NGC 4842B	SA0	−18.80	Coma		172.4	180.7
NGC 4864	E2	−20.55	Coma		128.7	220.6
NGC 4865	E	−19.91	Coma		70.0	307.9
NGC 4867	E3	−19.01	Coma		128.7	246.9
NGC 4874	cD	−22.53	Coma	39.7	79.0	313.0
NGC 4875	SAB0	−19.72	Coma		48.5	189.6
NGC 4908	E5	−21.01	Coma		163.0	201.5
NGC 1453	E2−3	−21.52	Field		0.0	336.6
NGC 1600	E3	−22.31	Field		0.0	308.1
NGC 1700	E4	−21.80	Field		0.0	252.7
NGC 221	cE2	−17.58	NGC 221 group	170.0	170.0	82.5
NGC 2329	S0−	−21.73	Abell 569	175.0	175.0	228.3
NGC 2693	E3	−21.67	Field	160.0	0.0	322.1
NGC 2694	E1	−19.15	Field		0.0	142.7
NGC 2778	E	−19.06	Pair	40.0	220.0	167.4
NGC 2832	E+2	−22.38	Abell 779	160	160.0	322.1
NGC 3377	E5−6	−19.16	Leo Group	35.0	0.0	142.0
NGC 3379	E1	−20.57	Leo Group	71.0	0.0	228.1
NGC 3608	E2	−19.62	Field	75.0	0.0	203.2
NGC 3641	E pec	−17.91	Field	3.0	240.0	163.4
NGC 4365	E3	−20.90	Virgo	40.0	220.0	257.8
NGC 4374	E1	−20.87	Virgo	135.0	0.0	300.7
NGC 4472	E2/S0(2)	−21.47	Virgo	155.0	155.0	309.7
NGC 5638	E1	−19.78	Pair	150.0	150.0	159.4
NGC 5831	E3	−19.72	Field	55.0	55.0	163.1
NGC 584	E4	−20.63	NGC 854 Group	120.0	0.0	224.4
NGC 6411	E	−21.07	Field	70.0	70.0	183.7
NGC 6702	E:	−21.42	Field	65.0	65.0	167.5
NGC 6703	SA0−	−20.83	Field		60.0	190.7

Table A.1: Sample of massive early-type galaxies analysed in Chapter 5.

NOTES: the table is divided into high (above the line) and low (below the line) density environment. Column 2: Morphological type. Column 3: Absolute magnitude in B band. Column 4: Environment. Column 5: Position angle (measured north−east). Column 6: Slit position angle from Sánchez-Blázquez (2004). Column 7: Velocity dispersion from Sánchez-Blázquez et al. (2006b), the error considered is of 10 km s^{-1}. Data in columns from 2−5 are from HyperLeda Database (Paturel et al. 2003).

Galaxy	Mg3334		NH3360		NH3375		CNO3862		CNO4175		CO4685		Mgb	
IC 0832	0.7476	0.3568	3.3849	0.4290	3.9635	0.5085	-4.2258	0.6631	1.2809	0.2604	3.0645	0.2534	4.0264	0.1218
IC 3957	1.0478	0.5735	5.5670	0.7315	6.1339	0.8727	7.2193	0.5643	5.8261	0.2824	3.3400	0.2380	4.5625	0.1208
IC 3959	1.3532	0.8841	4.8930	0.4469	5.5814	0.5247	1.4636	0.6148	6.3852	0.1957	4.1300	0.1841	4.9892	0.1015
IC 3963	0.6046	0.4465	4.1279	0.7589	4.2258	0.9298	-0.4293	0.6825	3.4929	0.2959	3.1297	0.2884	4.0733	0.1233
IC 3973	1.0396	1.1187	4.5719	0.7311	5.1341	0.8770	9.7588	0.5153	6.1591	0.2080	5.3355	0.2110	4.5850	0.1097
MGC+5−31−063	1.0165	0.8473	4.5139	1.3589	4.4109	1.6815	-5.5305	0.9485	1.4575	0.3604	-0.1055	0.3621	4.0907	0.1546
NGC 4842A	1.0851	0.8728	4.0374	0.6624	4.4177	0.8036	-2.0601	0.6945	4.9507	0.2618	4.1369	0.2480	5.0011	0.1272
NGC 4842B	1.0132	0.8409	3.5608	1.1910	3.6515	1.4577	-3.4602	0.8418	3.3381	0.3360	3.9839	0.3131	4.5725	0.1458
NGC 4864	1.2384	0.8316	4.9180	0.6055	5.5470	0.7177	3.0848	0.6190	4.2644	0.3493	3.7662	0.3427	4.4042	0.1641
NGC 4865	1.5019	2.5874	4.4246	0.4544	4.7231	0.5407	9.7580	0.5177	5.2420	0.1856	5.8214	0.2184	4.7715	0.0990
NGC 4867	0.7931	0.7910	4.6051	0.5907	4.7054	0.7175	8.6711	0.5169	4.8707	0.3223	5.5174	0.3220	4.7455	0.1540
NGC 4874	2.0802	4.0719	4.6903	1.2928	5.0955	1.5955	1.9959	0.8462	6.9258	0.3106	4.6280	0.3237	4.7444	0.1589
NGC 4875	0.3105	0.6415	4.6376	0.9097	4.1296	1.1414	-7.6316	0.8182	3.5347	0.2940	2.9106	0.2632	4.6107	0.1323
NGC 4908	0.8107	0.6498	5.8436	0.7477	5.9809	0.9027	13.9999	0.4653	3.2006	0.2454	3.0251	0.2383	4.4383	0.1152
NGC 1453	2.4545	6.1946	4.7970	0.2683	5.5430	0.2684	12.5246	0.3010	8.9072	0.3581	6.9756	0.3738	5.4095	0.1693
NGC 1600	1.7296	2.9465	4.8700	0.3370	5.5552	0.3683	11.6462	0.2778	8.1913	0.6449	7.1537	0.5775	4.7677	0.2748
NGC 1700	1.3030	1.0922	3.7966	0.1937	4.6117	0.1696	12.2478	0.1826	6.8631	0.2558	7.3757	0.2479	4.2235	0.1140
NGC 221	0.5507	0.0712	2.668	9 0.1551	3.1660	0.1178	8.2491	0.0539	1.8766	0.0656	2.3115	0.0428	2.9810	0.0300
NGC 2329	0.8459	0.5453	3.3595	0.2462	3.8499	0.2532	5.2901	0.2374	5.2726	0.5243	4.8578	0.5591	6.4239	0.1220
NGC 2693	1.0918	2.2712	4.7371	0.3294	5.0314	0.3789	11.4209	0.5081	8.5540	0.3705	6.6803	0.3767	5.0906	0.1832
NGC 2694	0.6968	0.3727	4.0420	0.5920	4.2364	0.7159	9.9749	0.4848	4.8179	0.4889	5.1260	0.4142	4.4787	0.1879
NGC 2778	0.9049	0.2999	4.6331	0.2461	5.1209	0.2589	12.5106	0.1190	6.9116	0.2033	7.3148	0.1997	4.4178	0.0752
NGC 2832	0.8988	1.8711	5.1273	0.3190	5.4044	0.3413	4.6299	0.3771	8.3170	0.2638	5.7017	0.3181	6.6507	0.4739
NGC 3377	1.0203	0.2398	4.2221	0.1595	4.9100	0.1621	10.5496	0.4380	4.6373	0.2035	5.2611	0.1660	3.9341	0.0724
NGC 3379	1.2702	0.7898	5.1090	0.1667	5.9373	0.1261	13.9110	0.1503	8.5014	0.2301	6.4624	0.2103	4.7665	0.0981
NGC 3379	1.2702	0.7898	5.1090	0.1667	5.9373	0.1261	13.9110	0.1503	7.9164	0.1339	7.1140	0.1387	4.2531	0.0765
NGC 3608	0.8959	0.4427	5.2646	0.2466	5.7982	0.2739	13.9569	0.4103	8.0213	0.2860	6.4813	0.2439	4.6621	0.1130
NGC 3641	0.9002	0.3629	5.2978	0.4157	5.8235	0.4911	11.9819	0.4340	5.7709	0.2847	4.7708	0.2775	4.0259	0.1007
NGC 4365	1.1713	1.1383	4.6917	0.5146	5.7822	0.6100	14.0021	0.2205	8.7757	0.1496	7.7699	0.1929	5.1620	0.1065
NGC 4374	1.5633	2.4816	4.9625	0.5767	6.1207	0.6787	13.7099	0.3002	7.9339	0.2041	6.1051	0.2178	4.8768	0.0985
NGC 4472	2.0383	3.6271	4.8734	0.7127	6.1793	0.8502	14.1771	0.3043	9.5301	0.2237	8.5517	0.3121	4.5962	0.1245
NGC 5638	0.9556	0.3326	4.6896	0.3457	5.1883	0.4055	12.3352	0.4251	6.3813	0.1951	6.5909	0.1788	4.0082	0.0696
NGC 5831	0.6137	0.3285	4.0073	0.4572	4.5934	0.5451	11.2068	0.4456	6.1797	0.1797	7.2249	0.1810	3.8430	0.0702
NGC 584	0.5973	0.3741	4.213	0 0.2187	4.2888	0.2174	11.8654	0.1492	6.1594	0.3220	7.0925	0.2885	4.1525	0.1336
NGC 6411	1.1393	1.5254	5.5111	2.2053	5.1760	2.7402	11.6253	0.7483	7.0080	0.0843	5.1854	0.0517	4.1956	0.0325
NGC 6702	0.6756	0.3259	3.6004	0.4243	3.9983	0.5034	10.8427	0.4545	3.9027	0.2483	6.7202	0.2504	5.2514	0.0800
NGC 6703	0.8534	0.3873	4.0377	0.2946	4.5198	0.3446	11.8809	0.4354	5.9358	0.1773	7.7586	0.1778	3.4281	0.0664

Table A.2: Line-strength indices used in Chapter 5.

NOTES: the table is divided into high (above the line) and low (below the line) density environment. Each index covers two columns, the first one is the value of the index and the second one is its error. The first and third index have been defined by Serven et al. (2010). The second by Davidge & Clark (1994) and the remaining by Serven et al. (2005).

Galaxy	Sc3613		Cr3594		Ni3667		Co3701		Ni3780		D4000		B4000	
IC 0832	2.0712	0.1334	0.9481	0.1634	−2.5126	0.1756	−0.1749	0.0940	−2.2545	0.1928	2.0960	0.0054	1.8040	0.0045
IC 3957	2.7459	0.2040	1.0368	0.2516	−3.8182	0.2654	−0.2497	0.1434	−3.5051	0.2795	2.4150	0.0076	2.0780	0.0063
IC 3959	2.3883	0.1328	0.9204	0.1797	−3.0734	0.1701	−0.3442	0.0861	−2.9747	0.1960	2.5920	0.0058	2.2310	0.0045
IC 3963	2.6331	0.2103	0.7658	0.2565	−3.4273	0.2895	−0.2182	0.1639	−3.1010	0.2937	2.5320	0.0076	2.1780	0.0063
IC 3973	2.5946	0.2029	1.0443	0.2287	−3.0376	0.2535	−0.4013	0.1264	−2.7241	0.2626	2.6160	0.0054	2.2520	0.0045
MGC+5−31−063	2.5965	0.3565	0.7024	0.3989	−2.8831	0.4704	−0.3273	0.2600	−2.5764	0.4580	2.3500	0.0082	2.0210	0.0073
NGC 4842A	2.4713	0.1966	0.9751	0.2212	−3.1217	0.2465	−0.3369	0.1289	−3.1835	0.2670	2.4780	0.0063	2.1330	0.0054
NGC 4842B	3.0355	0.3216	0.9528	0.3539	−3.0702	0.4106	−0.3681	0.2272	−3.3351	0.4184	2.4940	0.0082	2.1450	0.0073
NGC 4864	2.2268	0.1793	0.8208	0.2145	−3.1534	0.2281	−0.2941	0.1169	−3.1736	0.2523	2.3460	0.0082	2.0180	0.0073
NGC 4865	2.7433	0.1322	0.8147	0.1724	−3.1900	0.1825	−0.2765	0.0768	−2.8515	0.2280	2.4800	0.0045	2.1340	0.0045
NGC 4867	2.4227	0.1773	0.7537	0.2070	−2.7105	0.2248	−0.3327	0.1134	−2.3253	0.2256	2.4040	0.0073	2.0690	0.0063
NGC 4874	2.4634	0.3942	0.5709	0.3869	−3.5266	0.4579	−0.3321	0.2136	−3.4115	0.4874	2.5500	0.0082	2.1950	0.0073
NGC 4875	2.1479	0.2498	0.6532	0.2821	−3.0427	0.3132	−0.3514	0.1690	−2.8684	0.3158	2.2860	0.0063	1.9670	0.0054
NGC 4908	2.2726	0.2143	1.5105	0.2554	−3.3997	0.2676	−0.5005	0.1454	−3.3138	0.2931	2.6410	0.0067	2.2720	0.0054
NGC 1453	2.4729	0.0852	1.2917	0.1405	−3.2003	0.1458	0.4901	0.1413	−3.3585	0.2447	2.3360	0.0110	2.0100	0.0100
NGC 1600	2.2089	0.1080	1.1534	0.1489	−3.0564	0.1488	−0.4645	0.0756	−3.2854	0.2221	2.4830	0.0240	2.1350	0.0200
NGC 1700	2.6687	0.0612	1.0955	0.1290	−3.0066	0.0932	−0.3730	0.0414	−2.9202	0.1363	2.4610	0.0081	2.1170	0.0071
NGC 221	2.9629	0.0352	0.9384	0.0965	−2.5375	0.0500	−0.2751	0.0235	−2.2058	0.0635	2.5050	0.0042	2.1560	0.0028
NGC 2329	1.8483	0.0770	0.7414	0.1150	−2.4835	0.1069	−0.1193	0.0534	−2.6156	0.1282	2.4180	0.0122	2.0810	0.0102
NGC 2693	2.4066	0.0922	1.2880	0.1432	−3.1387	0.1444	−0.3615	0.0626	−3.2601	0.2281	2.3860	0.0110	2.0530	0.0100
NGC 2694	2.7735	0.1683	0.8680	0.2187	−3.1487	0.2240	−0.4698	0.1296	−3.4358	0.2352	2.3310	0.0161	2.0030	0.0141
NGC 2778	2.7151	0.0731	1.0700	0.1441	−3.2023	0.0944	0.0393	0.0737	−3.4232	0.1200	2.6530	0.0050	2.2830	0.0045
NGC 2832	2.2793	0.1056	1.2820	0.1504	−3.4767	0.1556	−0.4041	0.0717	−3.6554	0.2578	2.6510	0.0063	2.2830	0.0054
NGC 3377	2.5830	0.0464	0.9467	0.1294	−2.7867	0.0648	−0.1856	0.0287	−2.6726	0.1010	2.3900	0.0063	2.0570	0.0054
NGC 3379	2.6311	0.0546	1.1887	0.1375	−3.2571	0.0737	−0.4059	0.0352	−3.3911	0.1300	2.6190	0.0082	2.2560	0.0073
NGC 3608	2.6265	0.0766	1.1064	0.1522	−3.2517	0.1028	−0.4125	0.0513	−3.4500	0.1471	2.5000	0.0104	2.1530	0.0082
NGC 3641	2.4621	0.1135	0.9005	0.1701	−2.9853	0.1482	−0.3698	0.0814	−2.8433	0.1654	2.3990	0.0073	2.0640	0.0063
NGC 4365	2.6908	0.1447	1.1892	0.1865	−3.1926	0.1864	−0.5018	0.0959	−3.3422	0.2226	2.4330	0.0036	2.0940	0.0036
NGC 4374	2.5429	0.1861	1.4107	0.2214	−3.0900	0.2471	−0.2231	0.1127	−3.4729	0.3050	2.4360	0.0063	2.0980	0.0051
NGC 4472	2.6628	0.2009	1.1780	0.2236	−3.5017	0.2497	−0.3621	0.1142	−3.5637	0.3066	2.8180	0.0063	2.4270	0.0054
NGC 5638	2.6702	0.0941	1.0468	0.1552	−3.1443	0.1250	−0.4580	0.0693	−3.3523	0.1510	2.6670	0.0050	2.2960	0.0042
NGC 5831	2.8753	0.1210	1.0878	0.1735	−3.0658	0.1584	−0.3954	0.0862	−3.1589	0.1760	2.5560	0.0050	2.1990	0.0036
NGC 584	2.8212	0.0620	1.0787	0.1308	−3.1173	0.0864	−0.2397	0.0344	−3.0087	0.1225	2.5650	0.0112	2.2070	0.0102
NGC 6411	3.0195	0.5782	1.5573	0.6221	−2.6550	0.7308	−0.6401	0.4121	−3.6968	0.7541	2.5250	0.1580	2.1120	0.1240
NGC 6702	2.6953	0.1192	0.8729	0.1722	−2.9005	0.1627	−0.2010	0.0846	−2.8663	0.1771	2.5140	0.0063	2.1630	0.0054
NGC 6703	2.5853	0.0878	0.9879	0.1481	−3.2145	0.1164	−0.1784	0.0580	−3.0838	0.1450	2.4780	0.0036	2.1320	0.0036

Table A.3: Lick/IDS and Serven et al. (2005) line-strength indices measured in the wavelength range 3140−5250 Åin an equivalent aperture of 4″ at the distance of NGC 6703. All the indices have been measured at $\sigma = 200$ km s^{-1} and have been corrected for velocity dispersion effects following the explanations in Appendix C.

NOTES: the table is divided into high (above the line) and low (below the line) density environment. Each index covers two columns, the first one is the value of the index and the second one is its error. There are all the indices that can be measure in the wavelength range 3140−5250 Å from the LicK/IDS and Serven et al. (2005). They are listed in wavelength order of the blue passband.

Galaxy	Mg3835		Mn3794		Co3840		CaHK		Co3876		Al3953		Eu3970	
IC 0832	4.9883	0.1737	−2.1759	0.2184	3.2280	0.1712	15.6806	0.4807	0.7836	3.2380	−1.5244	0.3501	5.6127	0.1224
IC 3957	5.0262	0.2237	−3.9813	0.3205	2.7871	0.2324	19.5944	0.5351	−0.3033	1.2321	−1.8658	0.3500	6.0885	0.1370
IC 3959	5.4517	0.1729	−3.6407	0.2345	2.8597	0.1994	20.1205	0.4730	0.0984	0.6737	−1.4193	0.3199	5.9236	0.1327
IC 3963	5.6124	0.2106	−3.4565	0.3228	3.0911	0.2344	21.2262	0.5299	0.0840	0.3157	−2.4653	0.3546	6.0414	0.1315
IC 3973	5.2290	0.1929	−3.2979	0.2967	3.1812	0.2433	20.6437	0.4493	0.4866	4.1435	−1.0575	0.3711	6.0938	0.1295
MGC+5−31−063	5.1291	0.2715	−3.7463	0.4801	2.7164	0.3571	21.2698	0.5954	−0.4456	1.5538	−3.0064	0.4850	6.3016	0.1570
NGC 4842A	5.0890	0.2078	−3.3782	0.2991	2.8187	0.2309	19.0293	0.5075	−0.4713	3.2520	−1.0614	0.3706	5.8227	0.1446
NGC 4842B	5.0923	0.2503	−3.8543	0.4449	2.5893	0.3244	20.0914	0.5798	−0.3192	1.4125	−1.4755	0.4017	5.9300	0.1599
NGC 4864	5.3488	0.2792	−3.4035	0.2888	2.8769	0.2218	19.2809	0.6310	0.1451	0.9532	−1.6237	0.5113	6.1835	0.1665
NGC 4865	5.1540	0.2211	−3.3405	0.2330	3.0882	0.2575	20.6535	0.4585	0.1793	2.4208	−2.3104	0.9207	6.1222	0.1464
NGC 4867	5.1533	0.2559	−2.8010	0.2607	2.9074	0.2243	19.9149	0.5469	0.6007	4.7119	−1.7079	0.5426	5.9992	0.1578
NGC 4874	4.5787	0.3032	−3.4358	0.5127	2.8954	0.4085	19.9640	0.5777	−0.7427	10.4690	0.5269	0.6390	6.1985	0.2046
NGC 4875	5.4024	0.2227	−3.5345	0.3438	2.5731	0.2653	19.3144	0.5308	0.1692	0.8302	−1.6753	0.3787	5.9879	0.1355
NGC 4908	5.0377	0.1970	−4.1437	0.3405	3.0768	0.2457	20.5339	0.5231	−0.1611	0.8699	−1.4887	0.3489	5.9979	0.1327
NGC 1453	4.8442	0.4364	−3.8700	0.2180	2.6838	0.2668	21.7126	0.7009	−1.1459	20.0876	2.6907	1.6480	5.9240	0.2319
NGC 1600	4.8325	0.8258	−3.6851	0.2135	2.6470	0.2418	24.1189	1.1278	−0.1135	1.8385	2.3712	1.7320	5.9072	0.3802
NGC 1700	5.0498	0.2866	−3.5760	0.1802	2.8028	0.1739	23.0619	0.5596	0.1759	1.4865	0.6707	0.4260	6.2919	0.1484
NGC 221	5.1850	0.1099	−2.4645	0.1550	2.7511	0.1055	20.8661	0.2635	0.2073	0.3534	−3.6385	0.1635	5.7492	0.0572
NGC 2329	4.1956	0.3886	−2.8897	0.1722	1.8548	0.1568	17.3505	0.7925	−0.4105	2.7641	−0.8459	0.6491	4.9026	0.2297
NGC 2693	4.8748	0.4305	−3.7211	0.2060	2.8362	0.2541	21.8467	0.7156	−0.3409	5.2462	2.0507	1.2071	6.1205	0.2253
NGC 2694	5.0605	0.5597	−3.8538	0.2999	2.9686	0.1958	23.5754	0.8853	−0.1549	0.7452	−1.1938	0.6831	5.7127	0.2326
NGC 2778	5.1869	0.1397	−3.8790	0.2196	2.7667	0.1315	20.0357	0.4471	−0.5004	1.9286	−1.5146	0.2314	5.9216	0.0998
NGC 2832	5.5686	0.2734	−4.0893	0.2233	2.8392	0.2599	18.3704	0.5356	0.0572	0.9389	0.1109	0.4426	5.9910	0.1724
NGC 3377	5.0495	0.2079	−3.3398	0.1828	3.0284	0.1178	23.5256	0.3835	−0.2546	0.7966	−3.7011	0.3527	5.9231	0.0994
NGC 3379	5.0272	0.2857	−4.0153	0.1922	2.7900	0.1561	21.9076	0.4705	0.3096	2.0797	−2.0537	0.4944	6.0126	0.1335
NGC 3608	4.7601	0.3330	−4.1963	0.2114	2.7126	0.1512	23.7563	0.5438	−0.1573	0.9166	−2.3566	0.5202	6.0755	0.1508
NGC 3641	5.0910	0.2198	−4.0422	0.2275	2.9045	0.1577	20.3401	0.5137	−0.3508	1.3209	−1.5324	0.3381	6.1405	0.1277
NGC 4365	5.1003	0.1612	−3.7858	0.2368	2.7762	0.2147	18.5009	0.4521	0.1982	1.7212	−0.4533	0.2157	6.0501	0.1143
NGC 4374	5.0898	0.2692	−4.3286	0.3021	2.7767	0.2797	22.7725	0.4374	−0.1173	1.5121	−1.5675	0.6752	5.9139	0.1507
NGC 4472	5.0867	0.2307	−3.4605	0.2896	2.5531	0.2841	19.2137	0.5018	−0.1030	1.4390	0.2517	0.3684	6.1032	0.1534
NGC 5638	5.2558	0.1327	−4.0528	0.2279	2.7823	0.1440	20.8994	0.4294	0.0487	0.2414	−1.4842	0.2197	6.1532	0.0985
NGC 5831	5.1470	0.1359	−3.6757	0.2368	2.9499	0.1600	19.8115	0.4439	−0.0557	0.2608	−1.7255	0.2358	5.9450	0.0925
NGC 584	4.7847	0.3768	−3.7298	0.1845	2.7679	0.1581	24.2358	0.6126	−0.1272	0.9144	−1.9708	0.6026	6.0830	0.1737
NGC 6411	6.3049	0.0944	−4.8287	0.7921	2.3875	0.5622	58.6259	0.4026	−2.0603	9.1869	3.6622	0.4925	7.3235	0.0822
NGC 6702	5.2368	0.1750	−3.3899	0.2279	2.7746	0.1617	19.3981	0.4896	0.4319	1.6706	−2.0399	0.3076	5.9463	0.1078
NGC 6703	5.1118	0.1300	−3.6184	0.2127	2.6607	0.1459	19.5420	0.4489	−0.2222	1.0703	−2.0283	0.2703	5.8420	0.0936

Table A.3: Continued.

Galaxy	Mn4018		K4042		$H_{\delta A}$		V4112		$H_{\delta F}$		Fe4058		Sr4076	
IC 0832	−13.8319	0.3133	−0.0093	0.0739	0.4783	0.1732	0.4731	0.2249	1.3968	0.1010	1.2283	0.1650	0.2942	0.0917
IC 3957	−16.1200	0.3572	0.2146	0.0807	−2.5790	0.1937	−3.0224	0.2912	0.3092	0.1170	2.6617	0.1778	0.4480	0.1111
IC 3959	−15.6283	0.3453	0.0981	0.0544	−2.0910	0.1862	−3.3395	0.2100	0.4985	0.0881	2.3768	0.1238	0.3090	0.0930
IC 3963	−13.1672	0.3311	0.1393	0.0890	−1.7367	0.1919	−2.4501	0.2928	0.7416	0.1186	2.7834	0.1886	0.3442	0.1095
IC 3973	−15.0846	0.3992	−0.0200	0.0618	−1.6950	0.2228	−2.3130	0.2320	0.5722	0.0986	1.8065	0.1396	0.1412	0.1081
MGC+5−31−063	−13.9365	0.4156	−0.0247	0.1081	−0.8786	0.2283	−1.4051	0.3340	0.9024	0.1523	1.9095	0.2426	0.5395	0.1292
NGC 4842A	−15.7260	0.4048	0.2113	0.0780	−1.9634	0.2217	−2.5893	0.2794	0.4907	0.1136	2.4230	0.1744	0.3435	0.1208
NGC 4842B	−15.6040	0.4104	0.0868	0.0984	−1.5857	0.2265	−2.1892	0.3247	0.6599	0.1397	2.6382	0.2166	0.2336	0.1361
NGC 4864	−15.9143	0.4838	0.2825	0.1067	−1.4789	0.2588	−2.3073	0.3617	0.9047	0.1521	2.3007	0.2424	0.1236	0.1514
NGC 4865	−14.5978	0.4816	0.0862	0.0556	−1.7978	0.2815	−2.3176	0.2087	0.4656	0.0918	2.4174	0.1279	0.3570	0.1288
NGC 4867	−14.7917	0.4628	0.0063	0.0959	−1.6901	0.2625	−1.6700	0.3427	0.6457	0.1358	2.0349	0.2180	0.0393	0.1490
NGC 4874	−16.4302	0.6269	0.0778	0.1006	−2.1456	0.3315	−2.9419	0.3505	0.4125	0.1492	1.7344	0.2331	0.0394	0.1839
NGC 4875	−15.9207	0.3819	−0.0342	0.0851	−0.9617	0.2035	−1.6009	0.2824	1.0025	0.1262	1.6289	0.1919	0.2746	0.1204
NGC 4908	−14.2316	0.3360	0.0747	0.0759	−2.3755	0.1940	−3.4294	0.2712	0.3737	0.1090	3.3098	0.1669	0.4239	0.1186
NGC 1453	−18.2254	0.8065	0.3422	0.1306	−3.1536	0.3934	−4.2306	0.4439	−0.3277	0.1783	2.4059	0.2975	0.1429	0.2391
NGC 1600	−19.8155	1.1038	0.2414	0.2365	−2.3992	0.5120	−3.2111	0.7562	0.1598	0.3045	2.2405	0.5393	0.1129	0.3900
NGC 1700	−17.9571	0.5124	0.1663	0.0869	−2.2461	0.2436	−3.5315	0.2875	0.4851	0.1240	2.9483	0.1928	0.2897	0.1342
NGC 221	−8.4459	0.1193	−0.1209	0.0333	−1.2259	0.0747	−1.9129	0.1194	0.9060	0.0587	1.1489	0.0863	0.4132	0.0440
NGC 2329	−13.4450	0.6117	0.2340	0.1676	−1.9261	0.3578	−2.7784	0.5398	0.4646	0.2196	2.1772	0.3713	0.0040	0.2306
NGC 2693	−18.3804	0.7760	0.1325	0.1311	−2.7211	0.3750	−3.4950	0.4392	−0.0045	0.1790	2.2759	0.2991	0.2507	0.2363
NGC 2694	−17.7224	0.6977	0.1027	0.1687	−2.2921	0.3303	−3.3718	0.5059	0.2014	0.2201	3.2665	0.3519	0.5352	0.1956
NGC 2778	−14.4513	0.2543	0.1598	0.0550	−3.1069	0.1491	−4.2337	0.2317	−0.0062	0.0940	2.6762	0.1193	0.3708	0.0843
NGC 2832	−15.6261	0.5847	0.1195	0.0834	−3.0201	0.3279	−3.8284	0.3162	−0.1695	0.1247	2.4662	0.1910	0.2648	0.1718
NGC 3377	−11.7842	0.2618	−0.2648	0.0725	−1.6281	0.1437	−2.3954	0.2034	0.5471	0.0955	0.8898	0.1650	0.4414	0.0807
NGC 3379	−12.8734	0.3696	−0.0940	0.0816	−2.9877	0.2149	−4.2267	0.2709	0.0515	0.1120	1.1174	0.1845	0.3882	0.1173
NGC 3608	−13.7827	0.4133	−0.0799	0.0990	−2.7175	0.2264	−3.8239	0.3268	0.0465	0.1334	1.6045	0.2198	0.2361	0.1309
NGC 3641	−14.7271	0.3502	−0.0999	0.0879	−2.3305	0.1965	−3.2134	0.2923	0.2863	0.1257	2.0405	0.1924	0.5557	0.1092
NGC 4365	−15.6437	0.3798	0.1434	0.0415	−2.9959	0.2057	−4.6711	0.1806	0.1051	0.0817	2.9373	0.0984	0.4342	0.1014
NGC 4374	−13.2798	0.4574	−0.0548	0.0699	−2.9639	0.2809	−3.8282	0.2555	0.0183	0.1054	1.1947	0.1625	0.2057	0.1287
NGC 4472	−15.4436	0.5292	0.1726	0.0715	−3.3383	0.2983	−5.0829	0.2786	−0.1110	0.1149	2.8908	0.1625	0.5048	0.1609
NGC 5638	−14.7903	0.2341	0.0741	0.0488	−2.7232	0.1352	−3.7165	0.2071	0.1269	0.0879	2.5825	0.1067	0.4337	0.0795
NGC 5831	−14.1367	0.2374	0.1525	0.0498	−2.5120	0.1383	−3.7248	0.1916	0.2912	0.0836	3.1398	0.1097	0.4669	0.0836
NGC 584	−14.5406	0.4884	−0.0637	0.1159	−2.4529	0.2595	−3.6230	0.3646	0.3717	0.1471	2.3715	0.2532	0.3542	0.1591
NGC 6411	−8.6695	0.1173	0.0869	0.0115	−2.5177	0.1102	−3.6807	0.1163	0.2871	0.0436	2.5694	0.0237	0.4760	0.0482
NGC 6702	−14.4539	0.3060	0.0516	0.0745	−1.2430	0.1725	−2.3319	0.2474	0.9018	0.1025	2.8188	0.1598	0.3122	0.1025
NGC 6703	−14.3288	0.2535	0.1108	0.0460	−2.6536	0.1498	−3.6016	0.2010	0.1520	0.0797	2.7446	0.1017	0.3269	0.0834

Table A.3: Continued.

Galaxy	CN1		CN2		Si4101		Ca4227		Ni4292		Cr4264		G4300	
IC 0832	0.0290	0.0040	0.0721	0.0070	2.4336	8.9789	1.0178	0.0956	2.3502	0.2063	0.4981	0.2052	4.2224	0.1538
IC 3957	0.0980	0.0040	0.1488	0.0065	1.0248	3.5244	1.4684	0.0950	2.9436	0.2570	0.9382	0.2627	5.7433	0.1638
IC 3959	0.1130	0.0030	0.1650	0.0060	1.9256	21.0811	1.4290	0.0989	3.0361	0.2343	0.5222	0.2348	5.6327	0.1638
IC 3963	0.0580	0.0050	0.0934	0.0075	1.1802	2.1158	1.3231	0.1057	3.3228	0.2637	1.0489	0.2438	5.7269	0.1898
IC 3973	0.0970	0.0030	0.1532	0.0072	5.2497	195.7282	1.3323	0.1186	2.8571	0.2134	−0.8798	0.2690	5.3351	0.1812
MGC+5−31−063	0.0310	0.0060	0.0724	0.0080	1.4362	3.7813	1.2160	0.1223	2.7712	0.2988	1.5484	0.2700	5.8441	0.2080
NGC 4842A	0.0870	0.0040	0.1377	0.0073	2.3044	30.1926	1.6930	0.1251	3.2084	0.2341	1.7177	0.3192	5.8784	0.1927
NGC 4842B	0.0630	0.0050	0.1076	0.0078	1.2994	5.2816	1.6941	0.1276	3.0562	0.2561	1.4416	0.3013	5.8041	0.1979
NGC 4864	0.0780	0.0060	0.1315	0.0086	2.7801	26.2610	1.5184	0.1416	3.1767	0.2501	0.9490	0.3349	5.7866	0.2331
NGC 4865	0.0800	0.0030	0.1336	0.0081	−2.1017	52.3921	1.4605	0.1551	2.6837	0.2110	−0.2418	0.2638	5.3226	0.2251
NGC 4867	0.0880	0.0051	0.1402	0.0087	3.9539	89.0270	1.4858	0.1470	2.8198	0.2324	0.1386	0.3107	4.9990	0.2220
NGC 4874	0.1160	0.0050	0.1751	0.0098	−1.4091	31.5991	1.4256	0.1900	3.3952	0.2571	0.1527	0.3836	6.3749	0.3062
NGC 4875	0.0690	0.0050	0.1225	0.0066	1.9097	9.1507	1.4316	0.1098	3.0547	0.2366	1.1317	0.2789	5.5180	0.1860
NGC 4908	0.0610	0.0041	0.1056	0.0068	1.0398	6.3204	1.5170	0.1107	2.8576	0.2453	1.9927	0.2735	5.6409	0.1673
NGC 1453	0.1480	0.0060	0.2065	0.0111	0.8463	13.7344	1.6575	0.2498	2.7262	0.2645	0.0181	0.4388	5.9987	0.3387
NGC 1600	0.1380	0.0120	0.2006	0.0158	−0.4526	11.2935	1.1480	0.3061	2.8336	0.3675	0.4021	0.6180	5.8817	0.4281
NGC 1700	0.1110	0.0041	0.1678	0.0072	4.2752	128.3118	1.2541	0.1207	2.6213	0.2488	−0.0681	0.3022	5.7115	0.2016
NGC 221	0.0320	0.0022	0.0733	0.0031	1.2272	1.0950	1.2305	0.0361	2.4715	0.2244	1.0420	0.1671	5.1009	0.1029
NGC 2329	0.0900	0.0090	0.1363	0.0111	1.6148	18.8331	1.3036	0.2027	2.7134	0.3122	0.7136	0.4460	5.1048	0.3274
NGC 2693	0.1410	0.0060	0.2020	0.0114	−0.1132	2.2330	1.7404	0.2384	2.7073	0.2460	−0.4217	0.4430	5.5793	0.3091
NGC 2694	0.0820	0.0080	0.1274	0.0104	0.5849	1.2909	1.6059	0.1551	2.5714	0.3077	0.8211	0.3587	5.6266	0.2608
NGC 2778	0.1190	0.0030	0.1664	0.0052	0.4171	1.3482	1.4991	0.0789	3.0199	0.2353	1.1273	0.2491	5.7964	0.1427
NGC 2832	0.1370	0.0041	0.1920	0.0095	0.3053	5.8954	1.4702	0.1958	2.8247	0.2288	1.2507	0.4338	5.5696	0.2772
NGC 3377	0.0740	0.0032	0.1203	0.0050	1.0780	2.3082	1.2509	0.0690	2.4533	0.2224	0.7109	0.2198	5.1974	0.1296
NGC 3379	0.1390	0.0040	0.1912	0.0069	0.8467	9.8164	1.4034	0.1080	2.6044	0.2434	0.7690	0.2893	5.7588	0.1737
NGC 3608	0.1310	0.0050	0.1798	0.0070	0.6288	3.9682	1.3308	0.1142	2.7084	0.2517	0.7848	0.2898	5.6456	0.1800
NGC 3641	0.0960	0.0050	0.1451	0.0060	0.8916	2.6902	1.3383	0.1039	3.0971	0.2419	0.5923	0.2586	5.6610	0.1861
NGC 4365	0.1430	0.0020	0.1983	0.0063	2.1356	88.2548	1.5957	0.1132	3.4518	0.2114	−0.0523	0.2474	6.1367	0.1903
NGC 4374	0.1250	0.0030	0.1788	0.0082	−0.5383	16.2052	1.4438	0.1496	2.7767	0.2234	0.7423	0.3133	5.7914	0.2363
NGC 4472	0.1570	0.0040	0.2137	0.0085	0.1565	3.7665	1.7565	0.1879	2.8595	0.2342	0.1794	0.3346	5.8894	0.2579
NGC 5638	0.1090	0.0030	0.1577	0.0049	0.6168	1.7419	1.4631	0.0714	3.0793	0.2196	1.2402	0.2419	5.7048	0.1392
NGC 5831	0.0990	0.0032	0.1451	0.0044	0.8623	2.5860	1.5763	0.0793	3.2162	0.2362	0.7545	0.2264	6.0542	0.1331
NGC 584	0.0960	0.0060	0.1469	0.0084	1.6558	17.3005	1.3812	0.1324	2.6000	0.2630	0.3457	0.3005	5.5779	0.2110
NGC 6411	0.1120	0.0000	0.1529	0.0032	1.0467	4.4897	1.5199	0.0563	2.4763	0.2299	1.0022	0.2533	5.8640	0.0975
NGC 6702	0.0640	0.0040	0.1074	0.0064	1.5695	5.0648	1.2706	0.0905	3.0660	0.2265	0.7563	0.2311	5.3360	0.1687
NGC 6703	0.1020	0.0020	0.1496	0.0048	0.7138	3.4945	1.3360	0.0761	2.6506	0.2324	1.1520	0.2357	5.5443	0.1263

Table A.3: Continued.

Galaxy	$H_{\gamma A}$		$H_{\gamma F}$		Ti4296		Sc4312		Fe4383		Ca4455		Si4513	
IC 0832	−3.7650	0.1435	−0.6312	0.1135	3.5795	0.1228	0.4423	0.2034	4.3219	0.2239	1.0881	0.1749	−0.7326	0.1123
IC 3957	−6.5030	0.1531	−1.9659	0.1168	4.8710	0.1410	0.8715	0.2596	5.4166	0.2176	1.2492	0.1890	−0.5861	0.1153
IC 3959	−5.7440	0.1051	−1.6601	0.1278	4.7287	0.1090	0.8811	0.2381	5.1185	0.1964	1.4983	0.1898	−0.4598	0.0863
IC 3963	−5.7140	0.1813	−1.3797	0.1197	4.8641	0.1463	0.5939	0.2745	5.3779	0.2641	1.3028	0.1943	−0.8160	0.1457
IC 3973	−4.9220	0.1189	−1.1498	0.1549	4.5191	0.1111	0.8710	0.2104	5.4950	0.1979	1.4208	0.1774	−0.4177	0.0888
MGC+5−31−063	−5.7760	0.2228	−1.6787	0.1478	4.6313	0.1813	0.9470	0.2828	4.3608	0.3092	0.9480	0.2233	−0.9401	0.1676
NGC 4842A	−6.9650	0.1495	−2.0956	0.1464	5.0912	0.1250	0.7764	0.2517	5.5584	0.2419	1.4919	0.2272	−0.5725	0.1113
NGC 4842B	−6.5710	0.1964	−1.9429	0.1409	4.9890	0.1524	0.8817	0.2575	5.6160	0.2668	1.3309	0.2043	−0.7418	0.1432
NGC 4864	−6.4760	0.2157	−2.0547	0.1674	4.9692	0.1619	0.8461	0.2635	5.2168	0.3121	1.6214	0.2379	−0.7208	0.1565
NGC 4865	−5.1100	0.1022	−1.3442	0.2042	4.4068	0.1054	0.9318	0.2098	5.0363	0.2030	1.4861	0.1901	−0.7496	0.0950
NGC 4867	−4.9830	0.1907	−1.2649	0.1746	4.4155	0.1438	0.9042	0.2446	4.8277	0.2889	1.2984	0.2407	−0.2401	0.1328
NGC 4874	−7.1550	0.1883	−2.2762	0.2306	5.3781	0.1450	1.0136	0.2586	5.8193	0.3190	1.6729	0.2484	−1.0022	0.1437
NGC 4875	−5.9150	0.1631	−1.6777	0.1283	4.7605	0.1424	0.7240	0.2465	4.8505	0.2541	1.5262	0.2019	−1.1542	0.1264
NGC 4908	−5.7800	0.1457	−1.5933	0.1275	4.6404	0.1343	0.7176	0.2450	4.9687	0.2223	1.1567	0.1823	−0.7899	0.1202
NGC 1453	−7.3550	0.2144	−2.5567	0.2645	4.9993	0.1653	1.4438	0.2441	5.9289	0.3587	1.6949	0.2587	−0.4756	0.1464
NGC 1600	−6.6930	0.3910	−2.0962	0.3028	4.9158	0.2659	1.1750	0.2959	5.2986	0.5434	1.4024	0.3815	−0.4153	0.2467
NGC 1700	−5.9270	0.1451	−1.4951	0.1609	4.5194	0.1332	1.1777	0.2360	5.5192	0.2282	1.6915	0.1817	−0.7499	0.1164
NGC 221	−4.4430	0.0563	−0.6747	0.0444	3.9027	0.1123	0.8079	0.2552	4.9388	0.1056	1.2988	0.1202	−1.1003	0.0612
NGC 2329	−5.6840	0.3411	−1.5576	0.2365	4.3805	0.2231	0.8960	0.2750	5.3240	0.4605	1.3711	0.3245	−0.6722	0.2515
NGC 2693	−6.4830	0.2181	−1.9439	0.2496	4.6585	0.1571	1.1655	0.2255	5.7191	0.3470	1.7343	0.2674	−0.5365	0.1535
NGC 2694	−6.0650	0.2853	−1.8527	0.1806	4.5823	0.2150	1.1786	0.2924	5.1884	0.3465	1.8223	0.2231	−0.6846	0.2079
NGC 2778	−6.5490	0.1184	−2.1457	0.0981	4.9488	0.1308	1.0355	0.2667	5.3685	0.1822	1.5777	0.1639	−0.8959	0.1076
NGC 2832	−7.0270	0.1621	−2.3409	0.2336	4.7843	0.1274	0.9208	0.2278	5.8540	0.2956	1.6342	0.2392	−0.4218	0.1244
NGC 3377	−4.9980	0.1102	−0.9705	0.0866	4.1074	0.1204	0.9904	0.2460	5.0304	0.1683	1.4059	0.1349	−0.9682	0.0950
NGC 3379	−6.3350	0.1312	−1.9076	0.1381	4.6576	0.1267	1.2070	0.2419	5.4578	0.1999	1.6906	0.1726	−0.6687	0.1049
NGC 3608	−6.1900	0.1631	−1.7868	0.1364	4.6352	0.1462	1.1651	0.2543	5.3025	0.2360	1.6113	0.1866	−0.7671	0.1232
NGC 3641	−5.5660	0.1733	−1.3954	0.1234	4.6971	0.1386	0.7081	0.2555	4.7214	0.2474	1.3706	0.1820	−0.7433	0.1385
NGC 4365	−6.2940	0.0802	−1.5171	0.1471	5.1638	0.0943	0.6743	0.2434	5.4807	0.1702	1.4896	0.1694	−0.6826	0.0808
NGC 4374	−6.6080	0.1112	−2.0090	0.1981	4.7502	0.1102	1.1582	0.2217	5.5279	0.2092	1.6523	0.1726	−0.7793	0.0991
NGC 4472	−6.8680	0.1362	−2.0752	0.2131	4.8994	0.1202	1.1170	0.2319	5.9503	0.2534	1.9129	0.2241	−0.5590	0.1114
NGC 5638	−6.3310	0.1045	−1.8791	0.0892	4.8648	0.1186	0.8716	0.2611	5.2513	0.1738	1.5226	0.1631	−0.8409	0.0946
NGC 5831	−6.0650	0.1025	−1.6033	0.0919	4.9925	0.1248	0.7567	0.2716	5.3997	0.1725	1.4828	0.1727	−0.7809	0.0926
NGC 584	−5.7110	0.1932	−1.4526	0.1620	4.4647	0.1582	1.2266	0.2480	5.4908	0.2596	1.7561	0.1998	−0.8779	0.1398
NGC 6411	−5.7760	0.0090	−1.5509	0.0825	4.5673	0.1102	1.4249	0.2299	5.8754	0.0855	1.6935	0.1100	−0.5496	0.0675
NGC 6702	−5.3060	0.1486	−1.1647	0.1133	4.4575	0.1279	0.5269	0.2507	5.5899	0.2111	1.5006	0.1806	−0.7217	0.1247
NGC 6703	−6.6410	0.0946	−1.9550	0.1028	4.6239	0.1259	1.1263	0.2400	5.6799	0.1611	1.5866	0.1691	−0.9151	0.0936

Table A.3: Continued.

Galaxy	Ti4533		Fe4531		Eu4592		C4668		S4693		Ba4552		Zn4720	
IC 0832	0.9576	0.0703	2.8857	0.1607	0.0797	0.0663	6.0491	0.2376	0.6156	0.0835	0.0477	0.1460	−0.5363	0.0911
IC 3957	1.3166	0.0676	3.3073	0.1833	−0.0313	0.0555	6.4738	0.2330	0.5505	0.0802	−0.0386	0.1268	−0.6108	0.0882
IC 3959	1.4838	0.0535	3.4697	0.1393	−0.0120	0.0351	7.5865	0.1896	0.7214	0.0603	−0.1280	0.5202	−0.5001	0.0807
IC 3963	1.2808	0.0784	3.4841	0.1921	−0.1404	0.0819	6.1327	0.2829	0.6915	0.1012	−0.0065	0.0824	−0.3174	0.1011
IC 3973	1.2926	0.0579	3.4507	0.1365	−0.1063	0.0880	8.4602	0.2342	0.9059	0.0669	−0.0304	0.1653	−0.5796	0.0873
MGC+5−31−063	0.8815	0.1009	3.1034	0.2243	0.1132	0.0937	4.2982	0.3308	0.2805	0.1238	0.0766	0.1932	−0.4156	0.1281
NGC 4842A	1.3826	0.0698	3.5050	0.1731	−0.0288	0.0535	7.7288	0.2521	0.8013	0.0844	−0.1730	0.7334	−0.5886	0.1022
NGC 4842B	1.2441	0.0877	3.0350	0.1999	−0.0018	0.0713	7.2889	0.2949	0.6416	0.1078	−0.1649	0.4720	−0.7964	0.1218
NGC 4864	1.2134	0.1008	3.3298	0.2312	0.0474	0.0774	6.2831	0.3290	0.5078	0.1210	−0.0219	0.1204	−0.5864	0.1314
NGC 4865	1.1964	0.0568	3.6802	0.1249	−0.1647	0.1591	7.7594	0.2378	0.6351	0.0646	0.0363	0.2724	−0.2145	0.0789
NGC 4867	1.2328	0.0922	3.1187	0.2110	−0.0958	0.0924	8.0024	0.3159	0.8942	0.1118	−0.1010	0.4827	−0.3727	0.1254
NGC 4874	1.3081	0.0927	3.4086	0.2101	−0.1016	0.1115	7.7287	0.3433	0.6236	0.1088	−0.1105	0.8496	−0.6309	0.1409
NGC 4875	1.0658	0.0760	3.0868	0.1794	−0.0784	0.0715	6.1593	0.2589	0.5667	0.0907	0.0229	0.1036	−0.4076	0.0981
NGC 4908	1.1744	0.0721	3.5480	0.1596	−0.0035	0.0529	6.0955	0.2465	0.6808	0.0843	0.0512	0.1830	−0.5112	0.0927
NGC 1453	1.4828	0.1071	3.9007	0.2335	−0.1715	0.1888	9.0490	0.3883	1.0578	0.1227	−0.0218	0.2177	−0.0537	0.1486
NGC 1600	1.4786	0.1855	3.7242	0.3962	−0.2237	0.2364	8.6283	0.5624	0.7785	0.2119	0.0296	0.2629	−0.1213	0.2409
NGC 1700	1.2608	0.0735	3.7912	0.1549	−0.0441	0.0562	9.0979	0.2444	0.8666	0.0826	0.1049	0.5204	0.0954	0.0913
NGC 221	0.9688	0.0258	3.2317	0.0885	0.0745	0.0292	6.2265	0.0981	0.5224	0.0310	0.1043	0.1269	−0.2238	0.0303
NGC 2329	1.2058	0.1684	3.6943	0.3609	−0.0690	0.1279	7.6986	0.5243	0.6866	0.2035	0.0247	0.1651	−0.2433	0.2139
NGC 2693	1.3144	0.1130	3.7511	0.2393	−0.1354	0.1479	8.9953	0.3868	0.8837	0.1279	0.1107	0.9103	−0.0981	0.1554
NGC 2694	1.2663	0.1209	3.3779	0.2717	0.0095	0.1004	8.2997	0.3783	0.8384	0.1453	−0.0306	0.1235	−0.3180	0.1517
NGC 2778	1.3528	0.0594	3.6392	0.1445	−0.1257	0.0703	8.2804	0.1934	0.8899	0.0696	−0.0138	0.0782	−0.0698	0.0752
NGC 2832	1.4971	0.0908	3.7736	0.1999	−0.1283	0.1375	9.1762	0.3525	0.9341	0.1065	−0.1292	1.0598	−0.4982	0.1383
NGC 3377	1.0322	0.0508	3.2739	0.1216	−0.0312	0.0410	6.4729	0.1639	0.4995	0.0585	0.0909	0.1920	−0.1021	0.0613
NGC 3379	1.2865	0.0635	3.5514	0.1398	−0.0401	0.0488	7.6200	0.2053	0.8417	0.0705	−0.0018	0.0619	−0.1850	0.0820
NGC 3608	1.2421	0.0790	3.5896	0.1680	−0.1486	0.0978	7.8672	0.2340	0.7914	0.0858	0.0987	0.3412	0.0089	0.0903
NGC 3641	1.2084	0.0820	3.4315	0.1874	−0.1067	0.0789	6.6256	0.2616	0.4428	0.0990	0.0092	0.0836	−0.2440	0.1051
NGC 4365	1.3372	0.0501	3.6822	0.1096	−0.1198	0.0951	8.8237	0.1968	0.8237	0.0543	−0.0240	0.1357	−0.2015	0.0679
NGC 4374	1.2561	0.0610	3.4619	0.1249	−0.1059	0.1024	7.4789	0.2274	0.7283	0.0642	−0.0047	0.0649	−0.2019	0.0799
NGC 4472	1.4096	0.0797	3.7285	0.1681	−0.1219	0.1239	9.5192	0.3117	1.0135	0.0927	−0.0345	0.2675	−0.1178	0.1115
NGC 5638	1.2701	0.0525	3.5016	0.1333	−0.0866	0.0539	7.7169	0.1715	0.7486	0.0617	−0.0203	0.0816	−0.0896	0.0687
NGC 5831	1.1637	0.0533	3.4456	0.1321	−0.0919	0.0561	8.1495	0.1775	0.7868	0.0627	0.0552	0.1495	−0.1872	0.0683
NGC 584	1.3040	0.0868	3.4928	0.1920	−0.0412	0.0659	8.0341	0.2767	0.8654	0.1015	−0.0695	0.2870	−0.0387	0.1097
NGC 6411	1.2787	0.0315	3.7496	0.0595	−0.1270	0.0637	7.6584	0.0743	0.7926	0.0206	0.1218	0.3544	−0.0272	0.0294
NGC 6702	1.2072	0.0740	3.5425	0.1707	−0.0702	0.0672	8.7547	0.2364	0.8813	0.0883	0.0616	0.1722	−0.2180	0.0953
NGC 6703	1.3105	0.0507	3.6495	0.1255	−0.1295	0.0751	8.7420	0.1759	0.8768	0.0589	0.0128	0.0752	−0.0581	0.0648

Table A.3: Continued.

Galaxy	Mn4757		Mg4780		H_β		H_{β_P}		Ni4910		Fe4930		Ti5000	
IC 0832	0.1260	0.1049	0.4106	0.1369	1.7302	0.0930	1.8800	0.0614	−0.4178	0.1311	1.7493	0.1498	1.8625	0.1393
IC 3957	0.0747	0.1008	0.5930	0.1308	1.6359	0.0877	1.9160	0.0587	−0.4301	0.1289	1.9530	0.1882	2.4691	0.1361
IC 3959	0.0282	0.0758	0.8750	0.1178	1.7601	0.0763	1.9120	0.0440	−0.5504	0.1041	1.8364	0.1369	2.3018	0.1030
IC 3963	−0.0832	0.1227	0.6463	0.1483	1.9096	0.1091	2.0570	0.0750	−0.4534	0.1482	1.9537	0.1644	1.9620	0.1645
IC 3973	0.0358	0.0849	0.3799	0.1294	2.0042	0.0801	2.1150	0.0462	−0.5953	0.1190	1.8415	0.1656	2.4496	0.1029
MGC+5−31−063	0.1360	0.1522	0.3985	0.1885	1.6133	0.1358	1.8390	0.0969	−0.5470	0.1660	1.8912	0.2046	1.6380	0.1943
NGC 4842A	0.1269	0.1109	1.0134	0.1617	1.3255	0.0927	1.6520	0.0628	−0.7913	0.1292	1.9094	0.1598	2.1849	0.1356
NGC 4842B	0.4406	0.1379	0.9594	0.1819	1.6178	0.1177	1.8830	0.0784	−0.3837	0.1539	2.0403	0.1991	2.0942	0.1711
NGC 4864	0.0348	0.1539	0.8211	0.1938	1.6999	0.1310	1.9050	0.0859	−0.6049	0.1668	2.4309	0.2346	2.0667	0.1802
NGC 4865	−0.0060	0.0771	0.2538	0.1188	1.8123	0.0885	1.9900	0.0461	−0.7421	0.1195	1.9574	0.1583	2.1010	0.0985
NGC 4867	−0.1398	0.1420	0.6515	0.1874	1.8807	0.1283	2.0740	0.0821	−0.8449	0.1694	1.7342	0.2194	1.7742	0.1682
NGC 4874	−0.0927	0.1422	1.2423	0.2457	1.6426	0.1259	1.8040	0.0724	−0.4422	0.1618	1.6093	0.2596	2.2809	0.1556
NGC 4875	−0.0384	0.1160	0.8974	0.1457	1.7084	0.0976	2.0240	0.0631	−0.4320	0.1331	1.6216	0.1790	2.1233	0.1425
NGC 4908	0.2303	0.1056	0.8089	0.1457	1.6239	0.0937	1.8880	0.0636	−0.4824	0.1278	1.8536	0.1626	1.9568	0.1345
NGC 1453	0.1675	0.1542	0.7145	0.2348	0.7136	0.1276	0.8930	0.0819	−0.6299	0.1706	2.2094	0.2791	1.8133	0.1643
NGC 1600	−0.2807	0.2673	1.1980	0.3590	1.4936	0.2138	1.6080	0.1365	−0.8224	0.2732	1.8765	0.4262	2.4470	0.2758
NGC 1700	−0.1727	0.0998	0.4550	0.1352	1.9120	0.0905	2.0870	0.0573	−0.6945	0.1256	2.0271	0.1604	2.5935	0.1232
NGC 221	0.3015	0.0350	0.4618	0.0714	2.2667	0.0344	2.5350	0.0374	−0.5961	0.1018	1.9331	0.0722	1.7472	0.0705
NGC 2329	−0.2170	0.2514	0.6392	0.2995	1.1554	0.2121	1.5300	0.1396	−0.8081	0.2423	1.6403	0.3537	2.0074	0.2862
NGC 2693	−0.1550	0.1628	1.0216	0.2505	1.2517	0.1344	1.3910	0.0837	−0.9072	0.1775	1.9630	0.2825	2.4605	0.1762
NGC 2694	−0.1062	0.1812	0.9394	0.2097	1.6382	0.1570	1.9500	0.1094	−0.7048	0.1835	1.9289	0.2270	2.4119	0.2234
NGC 2778	−0.0076	0.0848	0.7701	0.1141	1.3014	0.0766	1.5530	0.0575	−0.4403	0.1113	2.0473	0.1207	1.3001	0.1179
NGC 2832	0.0727	0.1332	0.9299	0.2216	1.4828	0.1178	1.6470	0.0689	−0.8001	0.1562	1.6684	0.2384	2.8181	0.1490
NGC 3377	0.1253	0.0711	0.6647	0.1007	1.9020	0.0663	2.1320	0.0494	−0.6957	0.1077	1.8406	0.0976	1.6788	0.1024
NGC 3379	0.2599	0.0887	0.9077	0.1309	1.4453	0.0810	1.6760	0.0532	−0.7543	0.1124	1.7442	0.1317	2.1540	0.1113
NGC 3608	0.0144	0.1062	0.8071	0.1410	1.5183	0.0964	1.8060	0.0636	−0.7752	0.1286	1.9313	0.1529	2.1098	0.1300
NGC 3641	0.0819	0.1212	0.9871	0.1481	1.5541	0.1070	1.7690	0.0737	−0.6023	0.1313	1.7247	0.1664	1.7029	0.1522
NGC 4365	0.3421	0.0681	0.7568	0.1223	1.6380	0.0684	1.8360	0.0422	−0.7924	0.1047	1.9418	0.1183	2.4902	0.0873
NGC 4374	0.1706	0.0826	1.0664	0.1692	1.2420	0.0766	1.4220	0.0447	−0.7394	0.1049	1.7431	0.1435	1.9206	0.1028
NGC 4472	0.3482	0.1152	0.7639	0.1860	1.5017	0.1012	1.6700	0.0620	−0.7417	0.1336	1.9784	0.2029	2.4558	0.1304
NGC 5638	0.1160	0.0760	0.7871	0.1065	1.6516	0.0708	1.8850	0.0530	−0.5789	0.1130	1.9975	0.1170	1.9096	0.1012
NGC 5831	0.2466	0.0757	0.5362	0.1108	1.8095	0.0700	2.0550	0.0524	−0.5748	0.1124	2.0681	0.1133	2.0993	0.1015
NGC 584	0.1296	0.1241	0.5641	0.1631	1.7288	0.1072	1.9870	0.0709	−0.6934	0.1424	2.0594	0.1835	2.5388	0.1572
NGC 6411	0.0874	0.0111	0.7149	0.0619	1.8441	0.0289	2.0230	0.0340	−0.7300	0.0705	1.9362	0.0481	2.2886	0.0462
NGC 6702	−0.0681	0.1070	0.3284	0.1365	2.1352	0.0939	2.3420	0.0654	−0.4788	0.1285	2.0761	0.1484	2.2122	0.1466
NGC 6703	0.0373	0.0696	0.5444	0.1067	1.6995	0.0674	1.9290	0.0480	−0.5106	0.1098	2.1475	0.1112	1.9208	0.0973

Table A.3: Continued.

Galaxy	Mg_1		Mg_2	
IC 0832	0.1200	0.0020	0.2530	0.0032
IC 3957	0.1250	0.0020	0.2770	0.0022
IC 3959	0.1470	0.0010	0.3030	0.0022
IC 3963	0.1100	0.0030	0.2470	0.0032
IC 3973	0.1320	0.0020	0.2800	0.0022
MGC+5−31−063	0.0890	0.0030	0.2230	0.0040
NGC 4842A	0.1430	0.0020	0.3020	0.0030
NGC 4842B	0.1310	0.0030	0.2860	0.0032
NGC 4864	0.1360	0.0030	0.2750	0.0040
NGC 4865	0.1290	0.0010	0.2760	0.0020
NGC 4867	0.1290	0.0030	0.2780	0.0032
NGC 4874	0.1440	0.0030	0.2980	0.0032
NGC 4875	0.1200	0.0020	0.2730	0.0032
NGC 4908	0.1270	0.0020	0.2790	0.0032
NGC 1453	0.1280	0.0030	0.2760	0.0032
NGC 1600	0.1300	0.0050	0.2980	0.0060
NGC 1700	0.1020	0.0020	0.2370	0.0020
NGC 221	0.0690	0.0010	0.1770	0.0010
NGC 2329	−0.6160	0.0050	−1.0500	0.0071
NGC 2693	0.1190	0.0030	0.2820	0.0040
NGC 2694	0.0870	0.0040	0.2390	0.0050
NGC 2778	−0.4150	0.0045	−0.5990	0.0082
NGC 2832	−0.5890	0.0020	−1.2260	0.0112
NGC 3377	0.1040	0.0010	0.2250	0.0022
NGC 3379	0.1390	0.0020	0.2780	0.0022
NGC 3608	0.1330	0.0020	0.2700	0.0032
NGC 3641	−0.1330	0.0063	−0.1750	0.0092
NGC 4365	−0.0090	0.0110	0.0420	0.0180
NGC 4374	0.1340	0.0010	0.2730	0.0022
NGC 4472	−0.2410	0.0073	−0.2980	0.0141
NGC 5638	−0.2490	0.0045	−0.3150	0.0063
NGC 5831	−0.3040	0.0045	−0.3920	0.0073
NGC 584	0.1160	0.0020	0.2420	0.0032
NGC 6411	0.1180	0.0000	0.2550	0.0000
NGC 6702	−0.6190	0.0020	−0.9500	0.0028
NGC 6703	0.1320	0.0020	0.2730	0.0022

Table A.3: Continued.

B

Comparison of line-strength indices in low and intermediate resolution for a sample of dwarf early-type galaxies

This Appendix show the comparison of the Lick/IDS indices measured in Michielsen et al. (2008) with those measured in the intermediate resolution data presented in Chapter 6. The sample at both resolutions is the same one. A total of 21 dwarf early-type galaxies located mainly in the Virgo cluster.

The indices measured in this Appendix were obtained extracting the central 4" of the spectra of each galaxy and transforming them to the Lick/IDS system, which means that each index must be measured at a specific resolution indicated in Table B.1.

To quantify whether the differences observed between the two resolutions are significant we have looked for systematic deviations (see Table B.2), measured as:

$$\Delta I = \frac{\sum_{j=1}^{N} \frac{y_j - x_j}{\sigma y_j^2 + \sigma x_j^2}}{\sum_{j=1}^{N} \frac{1}{\sigma y_j^2 + \sigma x_j^2}} \tag{B.1}$$

where y_j and x_j is the same index measured at low and medium resolution, σy_j and σx_j^2 the errors for that indices respectively and N is the number of galaxies in common at both resolutions.

Figure B.1 shows the indices measured at low (M08) and medium resolution (This work). The solid line is the relation $1:1$. To analyse the differences found between both studies we calculated the typical deviation as:

$$\sigma = \sqrt{\frac{N \sum \frac{(y_j - x_j)^2}{\sigma y_j^2 + \sigma x_j^2}}{(N-1) \sum \frac{1}{\sigma y_j^2 + \sigma x_j^2}}} \tag{B.2}$$

And we made a t-student statistical test to check if we could refuse the null hypothesis of $\Delta I = 0$ with a significance level of $\alpha < 0.01$. This would happen if the t parameter follows

$$t = \frac{\Delta I}{\sigma / \sqrt{N}} \geq t_{\alpha/2.N-1} \tag{B.3}$$

index	σ km s^{-1}	index	σ km s^{-1}
CN_1	325	Fe4668	250
CN_2	325	Hβ	225
Hδ_A	325	Fe5015	200
Hδ_F	325	Mg_1	200
Ca4227	300	Mg_2	200
G4300	300	Mgb	200
Hγ_A	275	Fe5270	200
Hγ_F	275	Fe5335	200
Fe4383	250	Fe5406	200
Ca4455	250	Fe5709	200
Fe4531	250	Fe5782	200

Table B.1: Lick/IDS system to measure indices.

which means that for $N = 10$ then $t_{0.010,9} \geq 2.82$, for $N = 13$ then $t_{0.010,12} \geq 2.68$, and for $N = 20$ then $t_{0.010,19} \geq 2.54$. As it can be seen in Table B.2 where all these parameters are listed for the indices under comparison, for all the cases the null hypothesis can not be refused, which means that the differences are not statistically significant.

Index	N	ΔI	σ	t
CN1	10.000	0.011	0.017	2.163
CN2	10.000	0.008	0.017	1.530
HdA	10.000	-0.687	0.897	2.422
HdF	10.000	-0.216	0.497	1.375
Ca4227	10.000	0.049	0.198	0.787
G4300	10.000	0.023	0.653	0.110
HgA	10.000	-0.688	1.037	2.098
HgF	10.000	-0.390	0.624	1.979
Fe4383	10.000	0.005	0.607	0.024
Ca4455	10.000	-0.048	0.278	0.548
Fe4531	20.000	0.275	0.675	1.825
Fe4668	20.000	0.450	0.824	2.446
Hbeta	13.000	-0.085	0.360	0.852
Fe5015	13.000	0.138	0.581	0.859
Mg1	13.000	-0.001	0.011	0.302
Mg2	13.000	-0.009	0.019	1.732
Mgb	13.000	-0.174	0.411	1.528
Fe5270	13.000	-0.120	0.305	1.415
Fe5335	13.000	-0.061	0.289	0.761
Fe5406	13.000	-0.058	0.242	0.864
Fe5709	20.000	-0.121	0.336	1.616
Fe5782	20.000	-0.014	0.237	0.267

Table B.2: Comparison between the indices measured at low and medium resolution. N is the number of galaxies for each index; ΔI the systematic deviation; σ the typical deviation and t is the statistical parameter of the t-student test.

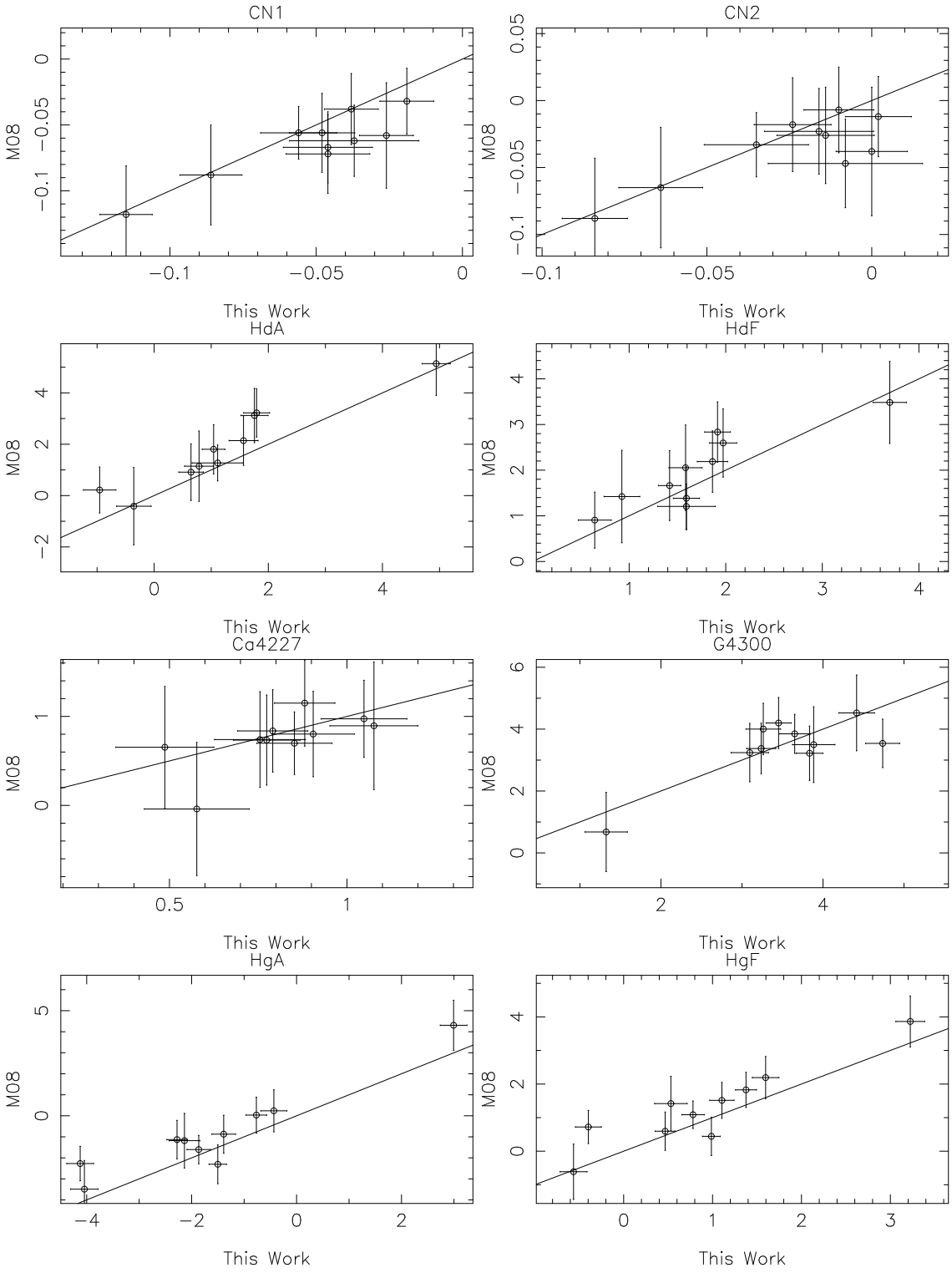

Figure B.1: Comparison between the Lick/IDS indices measured at low-resolution by Michielsen et al. (2008, M08) and at medium-resolution (This work). The solid line plotted is the $y = x$ line.

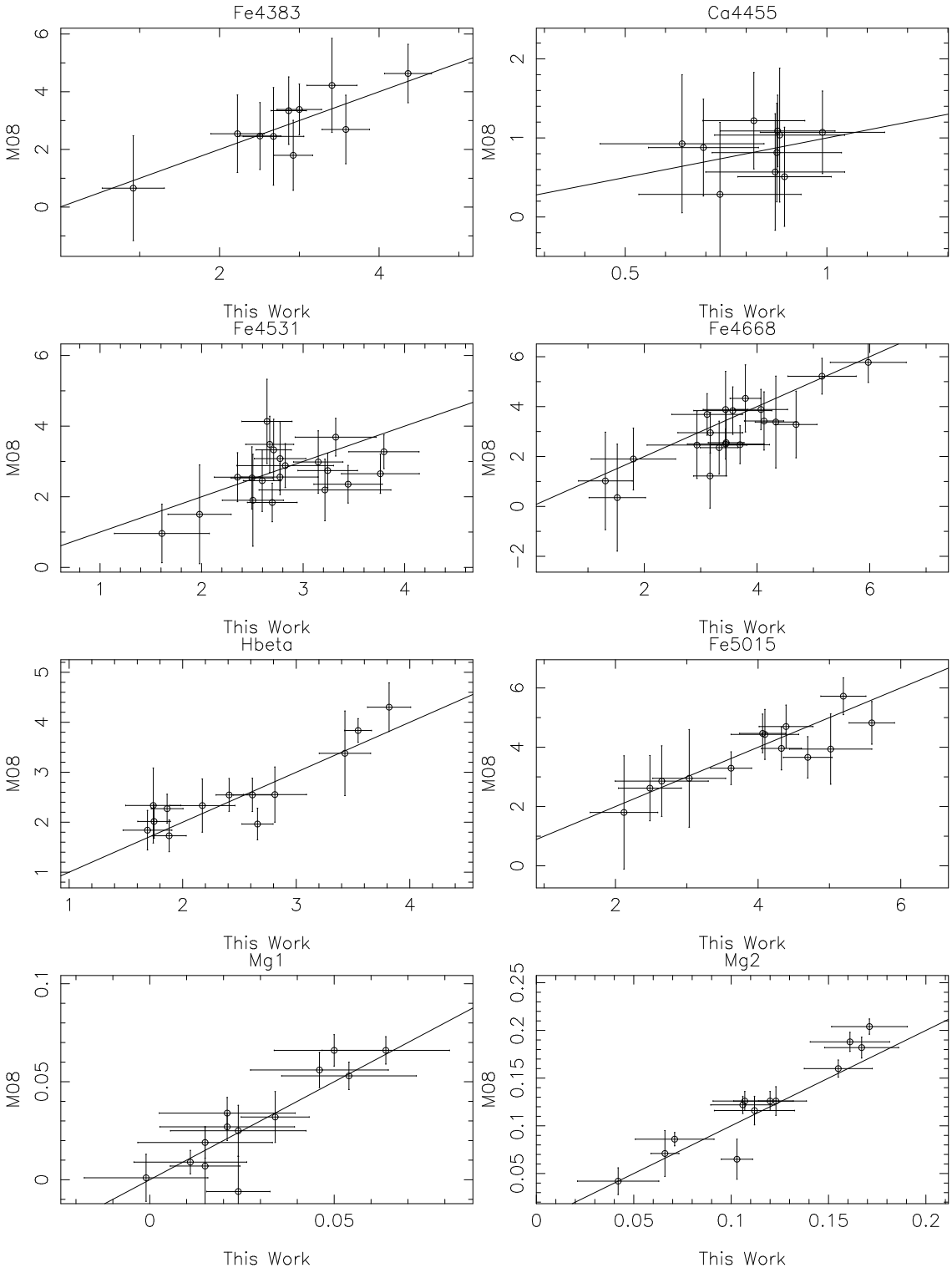

Figure B.1: Continued.

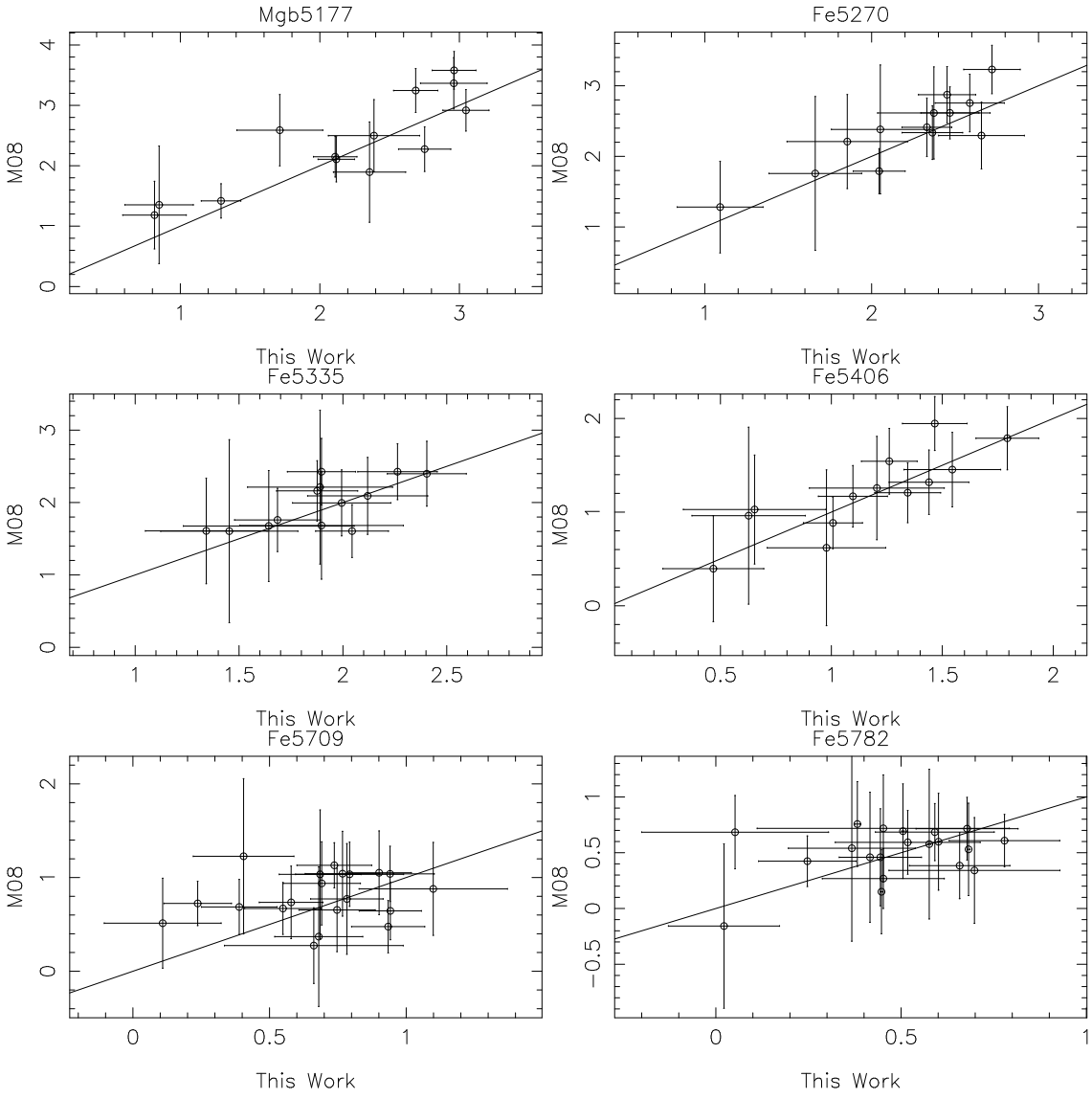

Figure B.1: Continued.

C

Method to correct line-strength indices for the velocity dispersion of the galaxies

The line-strength indices in galaxies must be measured at the same velocity dispersion, including quadratically the instrumental resolution and the σ of the galaxy. For the work presented in Chapter 5 we decided to measure the indices at the resolution they were defined, 200 km s^{-1}, and correct them for the velocity dispersion of each galaxy.

To obtain the correcting factor for each velocity dispersion, we convert the SSP models of Bruzual & Charlot (2003), used for indices at $\lambda < 3600$ (see discussion at, Toloba et al. 2009b), and of Vazdekis et al. (2010) for the remaining, to a resolution of 200 km s^{-1}, and broad them in steps of 10 km s^{-1} until 400 km s^{-1}. We measure all the indices under study in all of these broadenings (the variation of the indices for these σ's are shown in the right panels of Figure C.1). Being $I(\sigma)$ the index measured at the different broadenings and $I(0)$ the index measured at the resolution 200 km s^{-1}, we fit a third degree polynomial to the curves $I(\sigma)/I(0) - \sigma$. Therefore, we apply the factor indicated by this polynomial to each index measured in the observed galaxies.

Figure C.1 shows in the right panels the index-σ diagrams for the sample of galaxies from Chapter 5 using this technique to correct from the velocity dispersion of the galaxies.

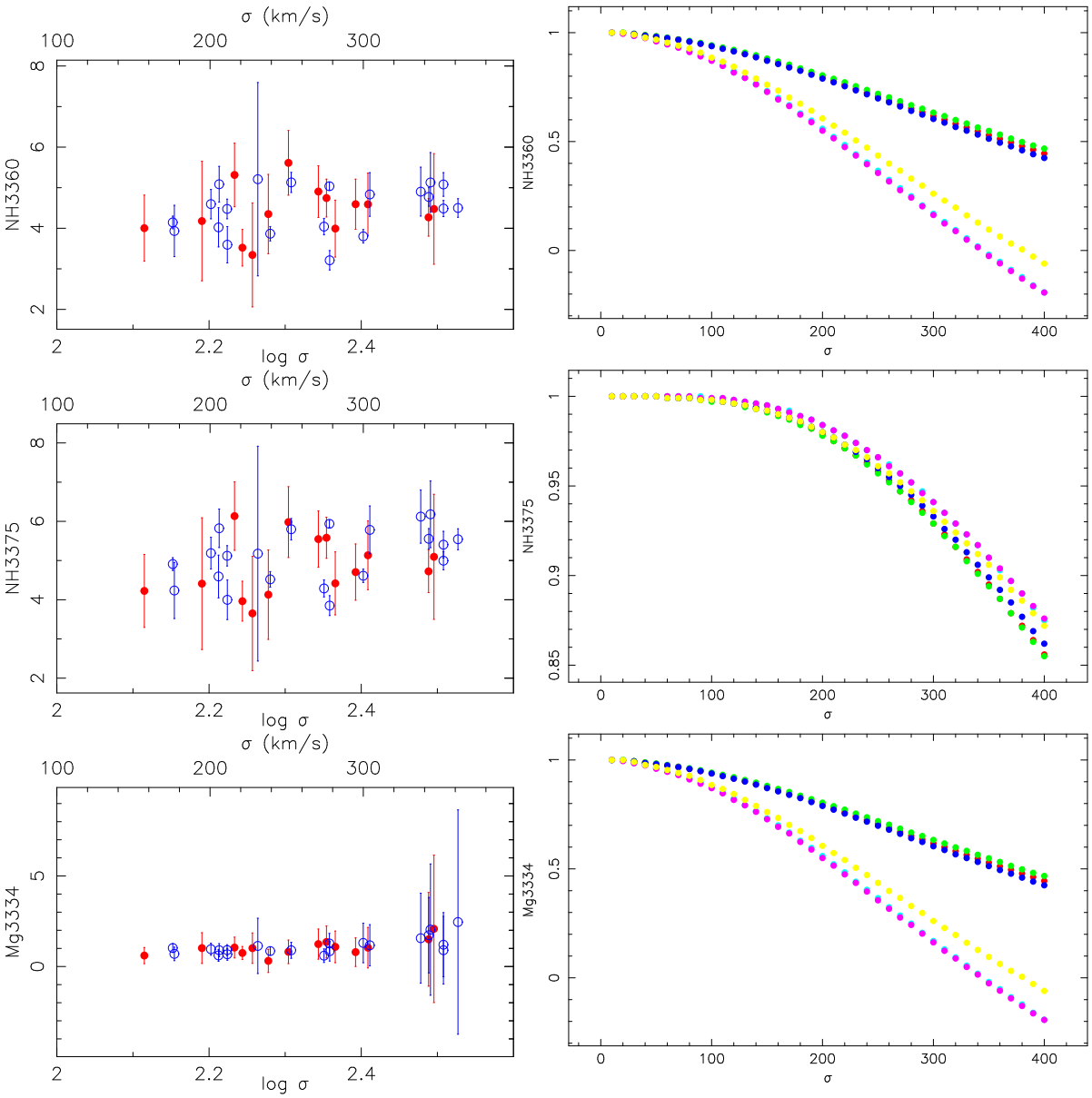

Figure C.1: Right panels: index-σ diagrams for the Lick/IDS indices, NH3360 from Davidge & Clark (1994), and the indices defined by Serven et al. (2005) and Serven et al. (2010). These indices have been measured at 200 km s^{-1} and have been corrected for the velocity dispersion of the galaxies. Blue dots are for galaxies located in low density environments (Virgo and the field), and red dots for galaxies in the Coma cluster. **Left panels:** Dependence of the indices on the velocity dispersion measured in the models of Bruzual & Charlot (2003) and Vazdekis et al. (2010). Red dots are for a SSP of 8 Gyr and Z=0.0, green 10 Gyr and Z=0.0, blue 16 Gyr and Z=0.0, cyan 8 Gyr and Z=0.2 (or 0.4 if measured in Bruzual & Charlot 2003), magenta 10 Gyr and Z=0.2 (or 0.4 if measured in Bruzual & Charlot 2003), and yellow 16 Gyr and Z=0.2 (or 0.4 if measured in Bruzual & Charlot 2003).

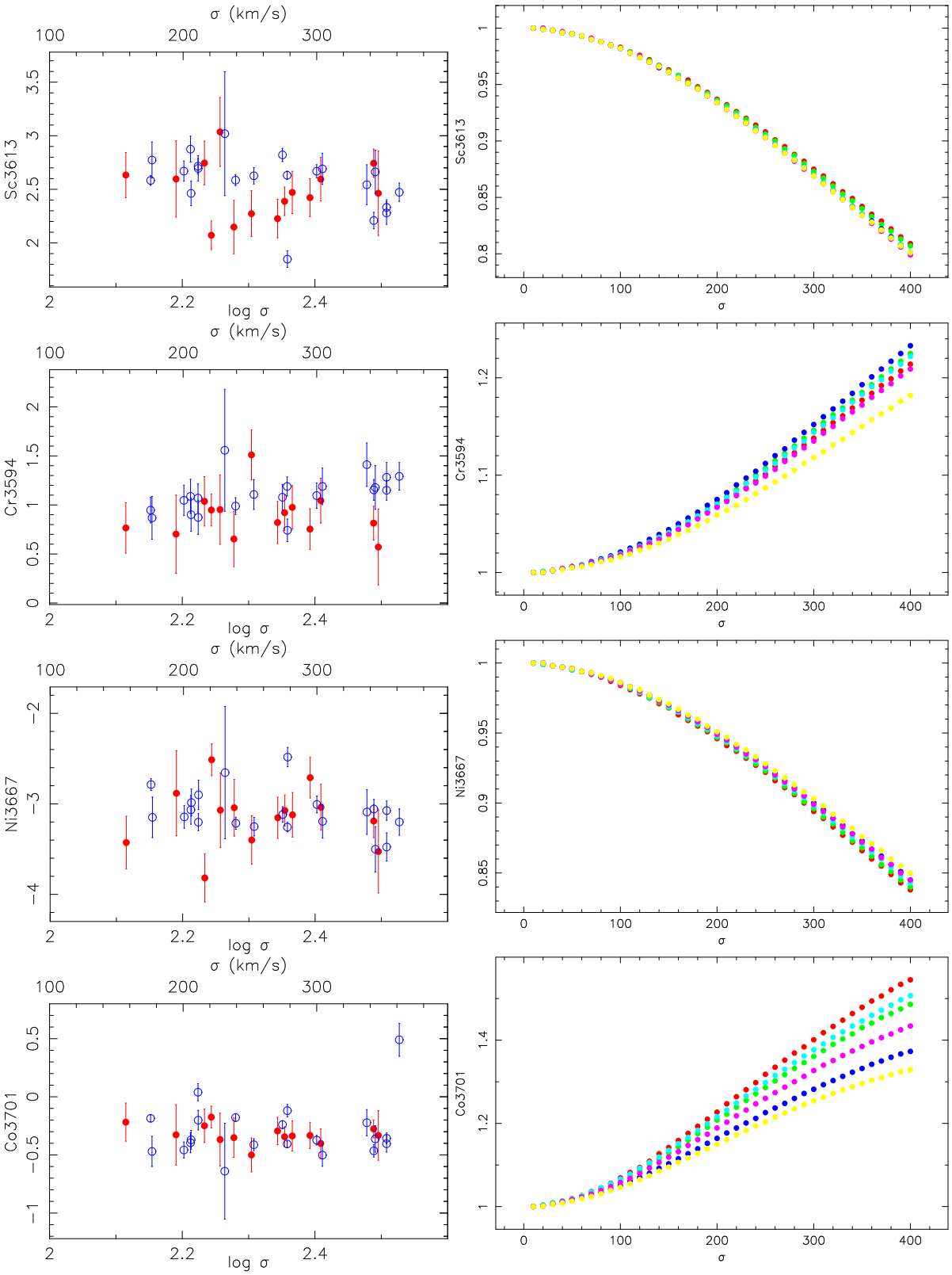

Figure C.1: Continued

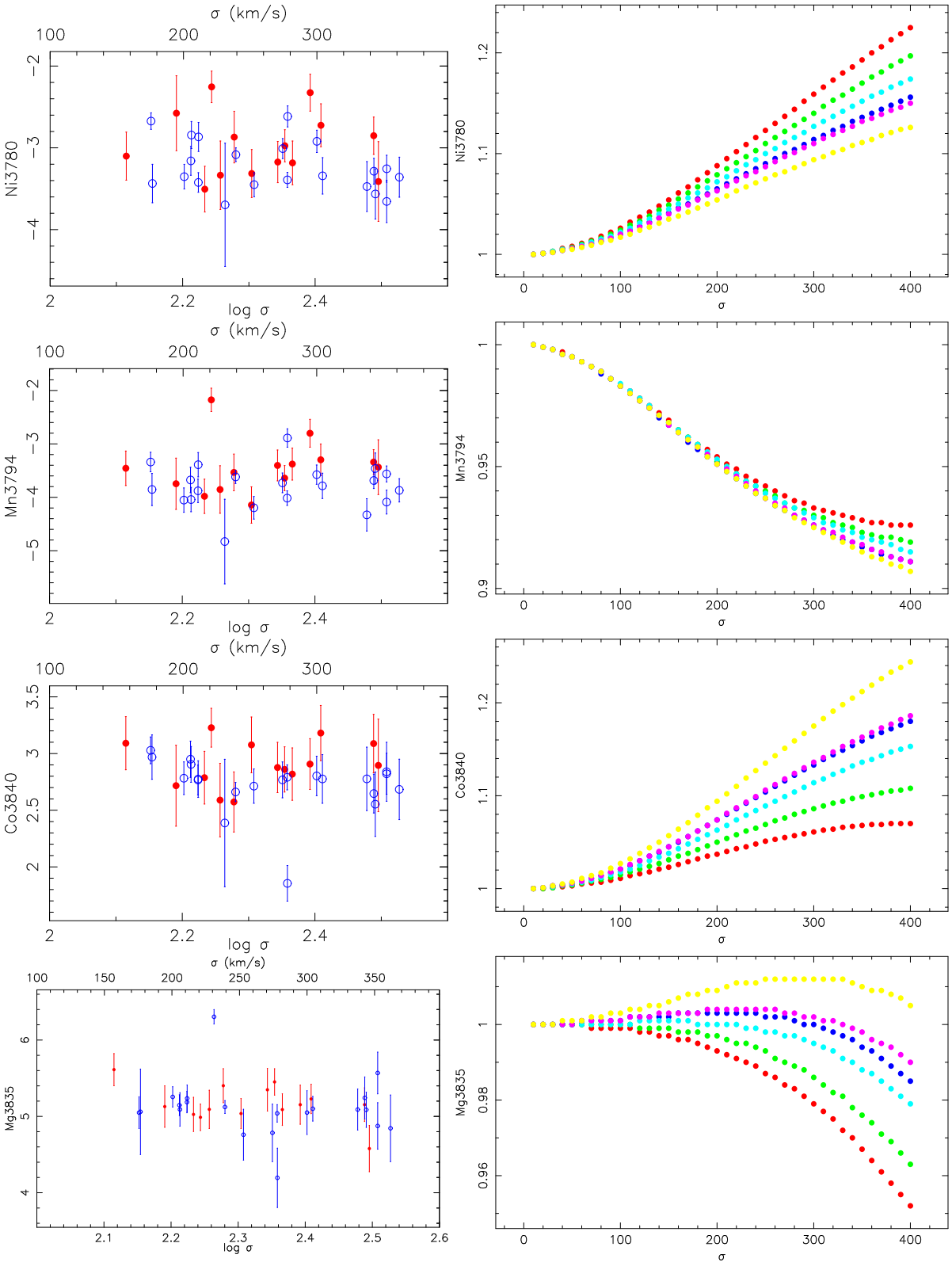

Figure C.1: Continued

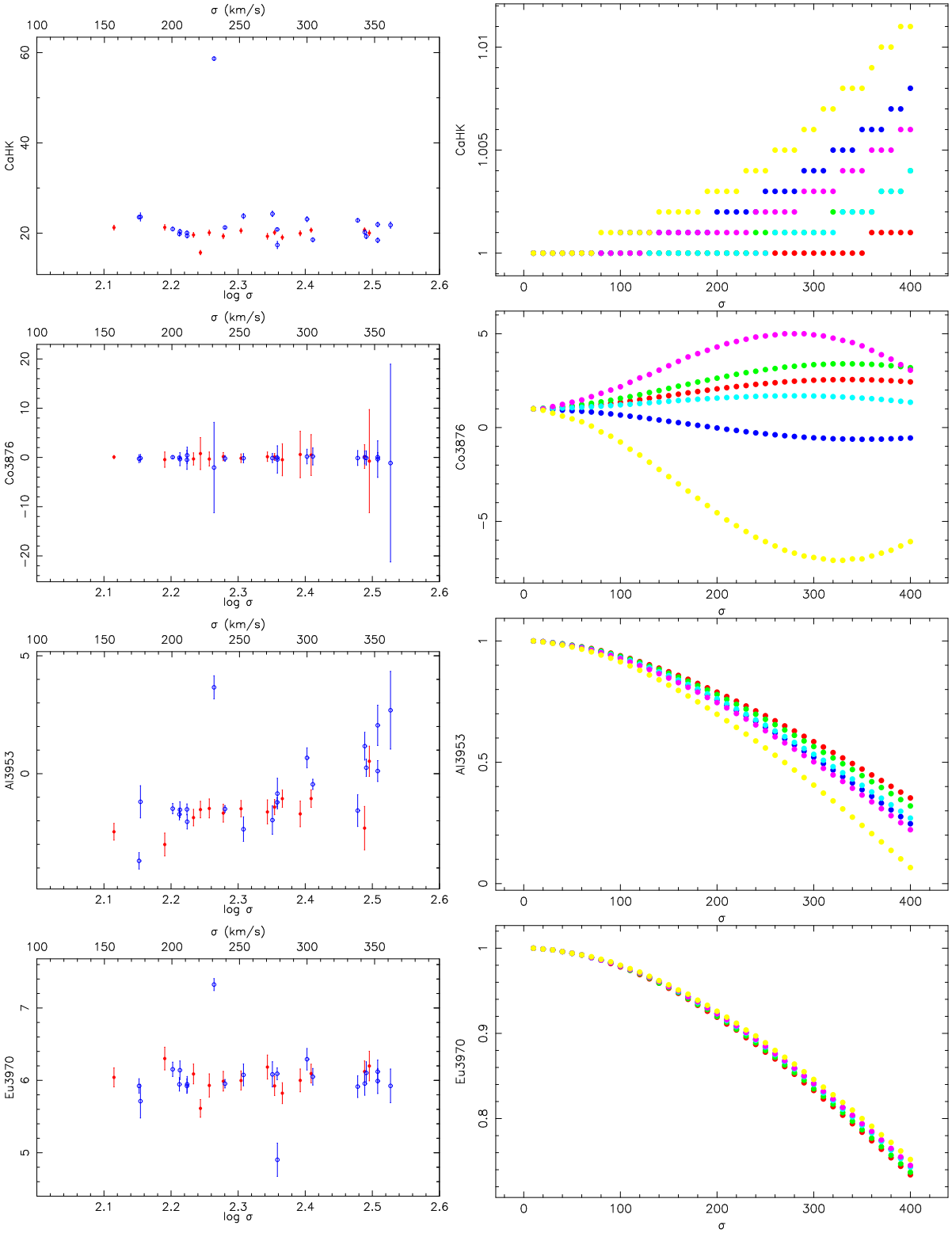

Figure C.1: Continued

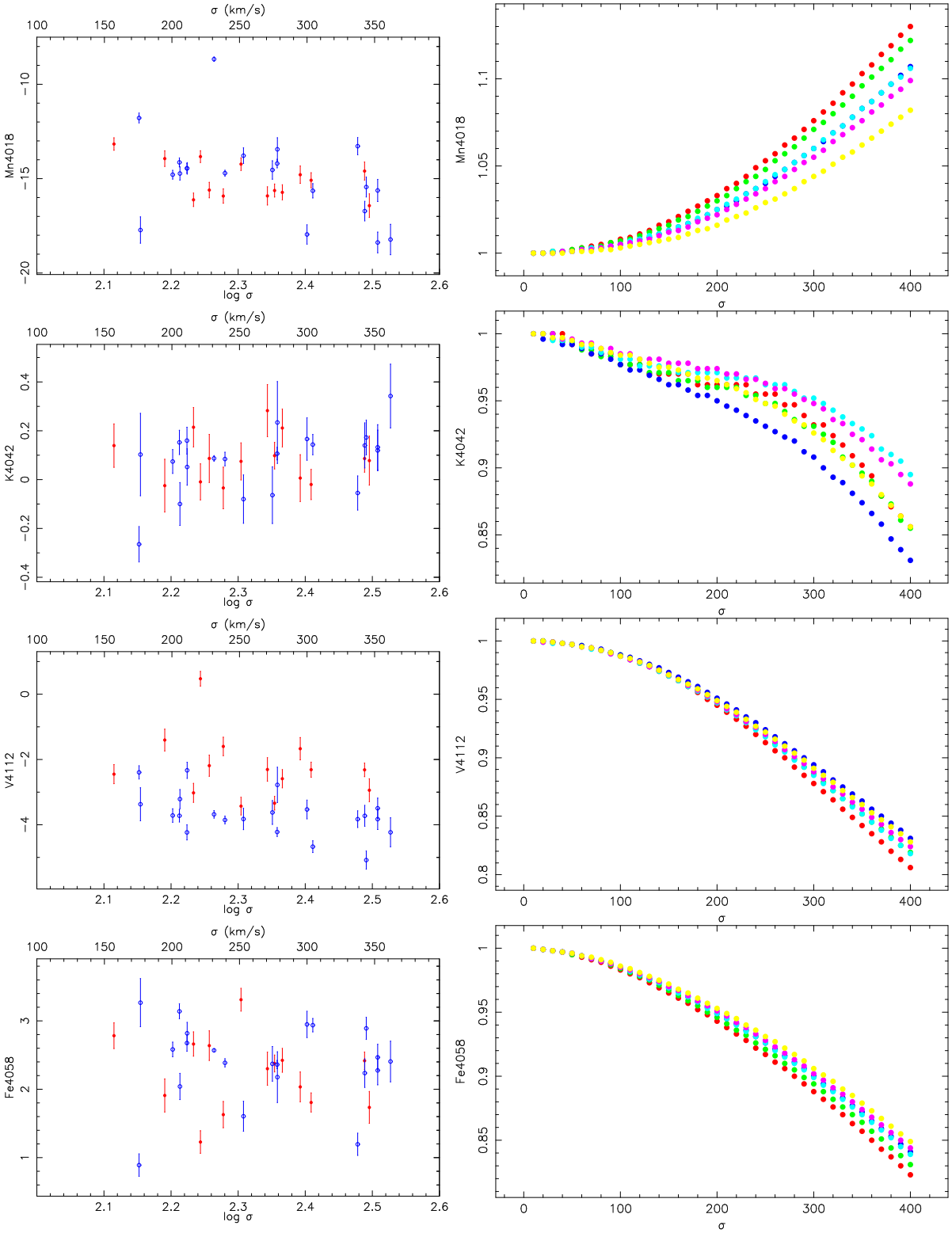

Figure C.1: Continued

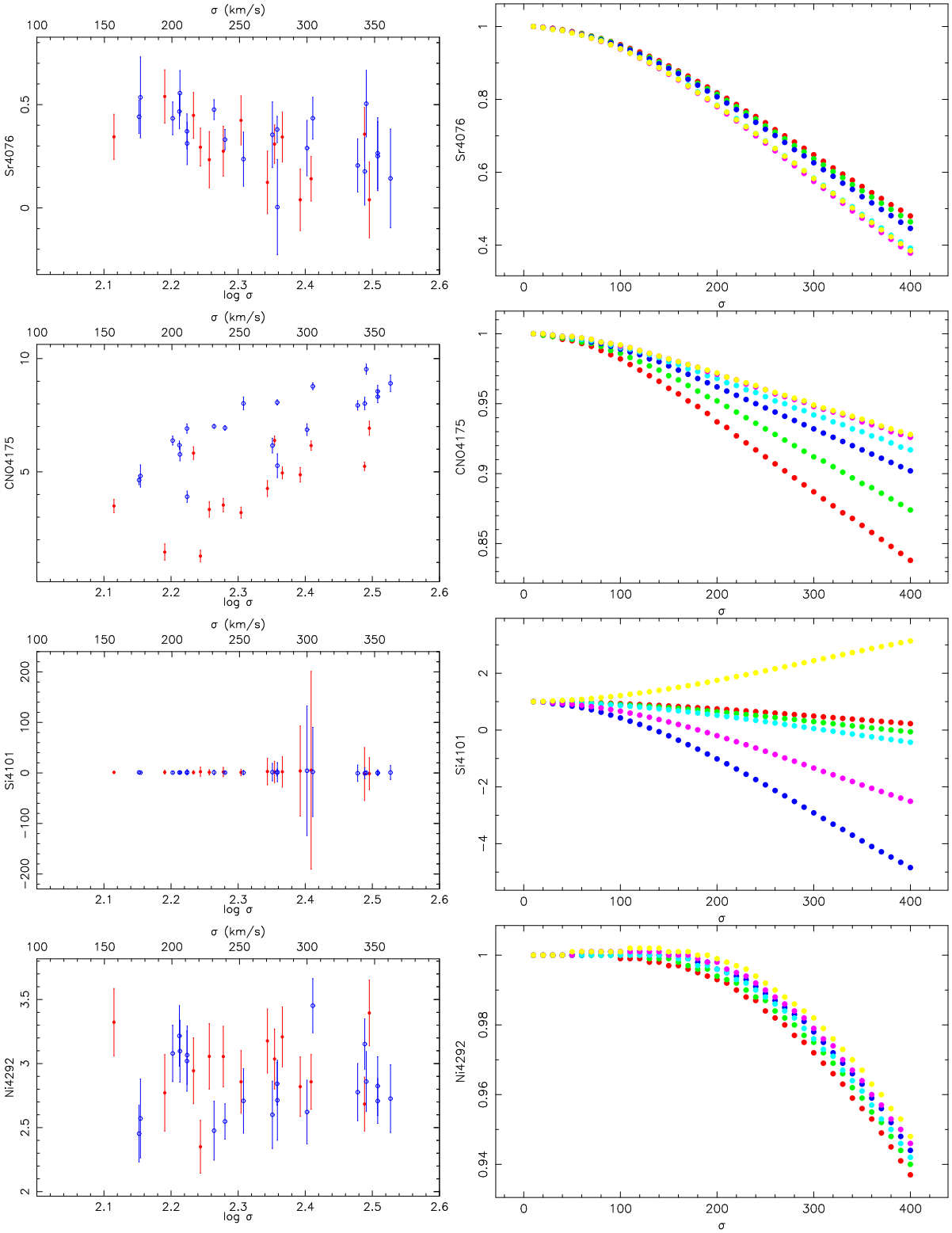

Figure C.1: Continued

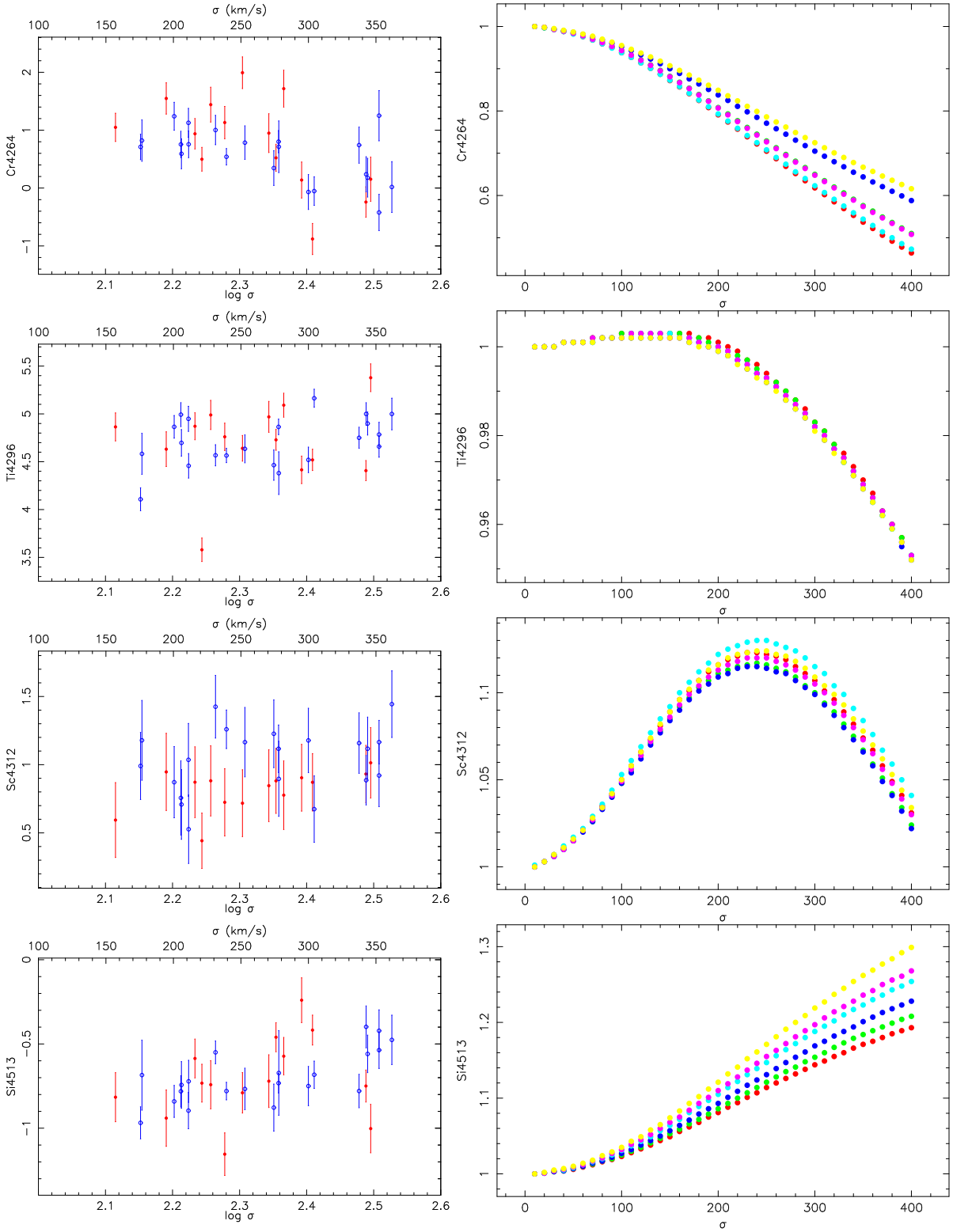

Figure C.1: Continued

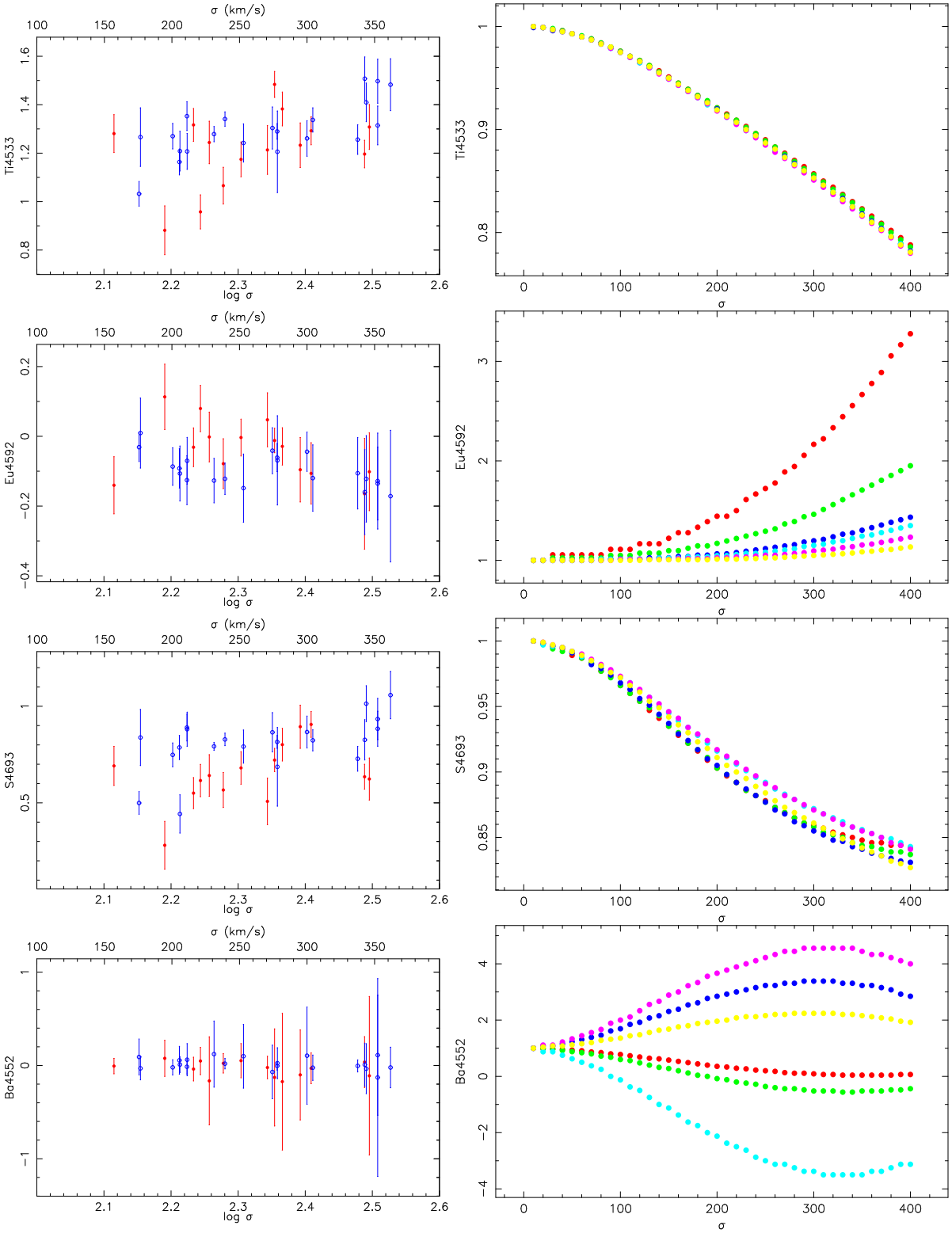

Figure C.1: Continued

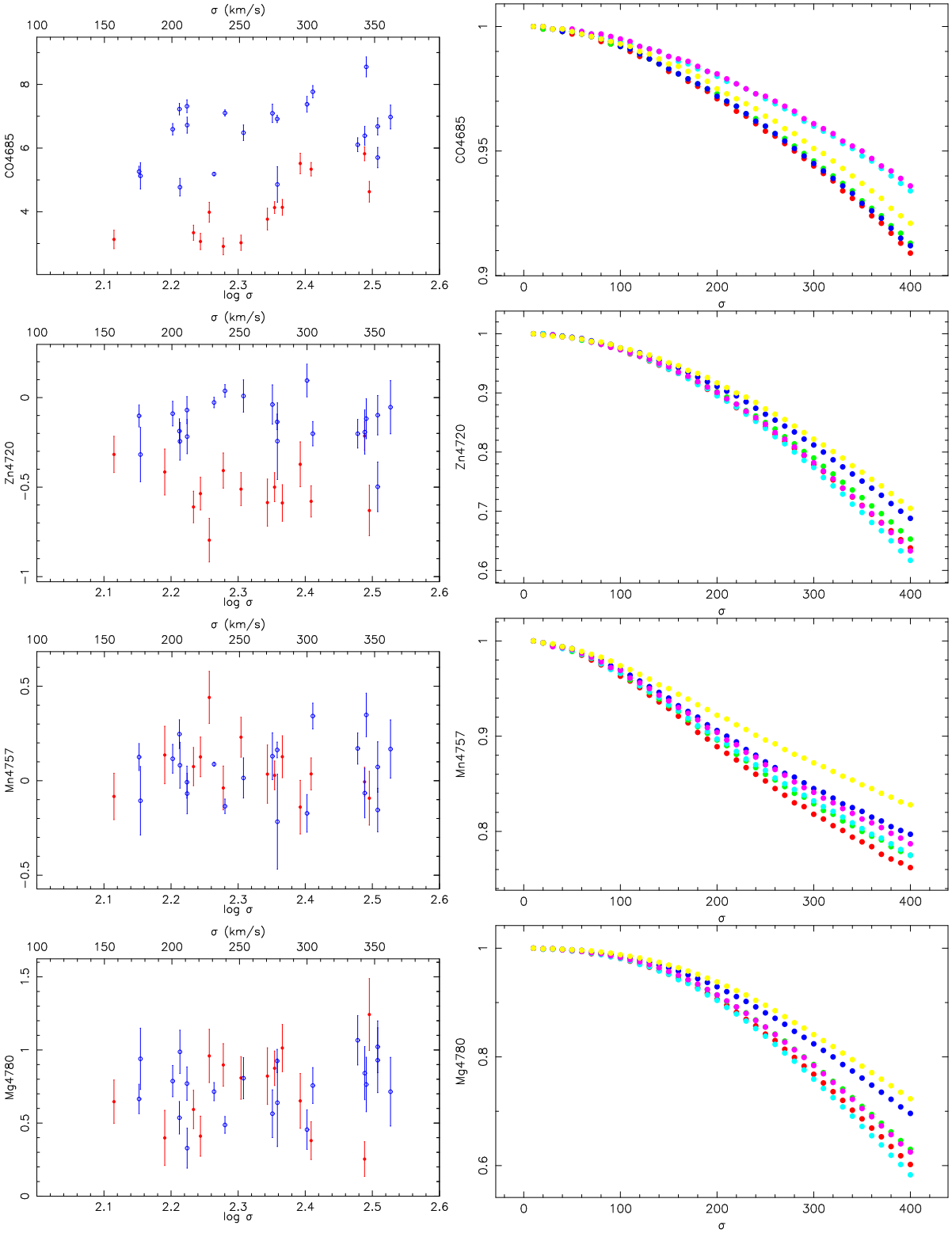

Figure C.1: Continued

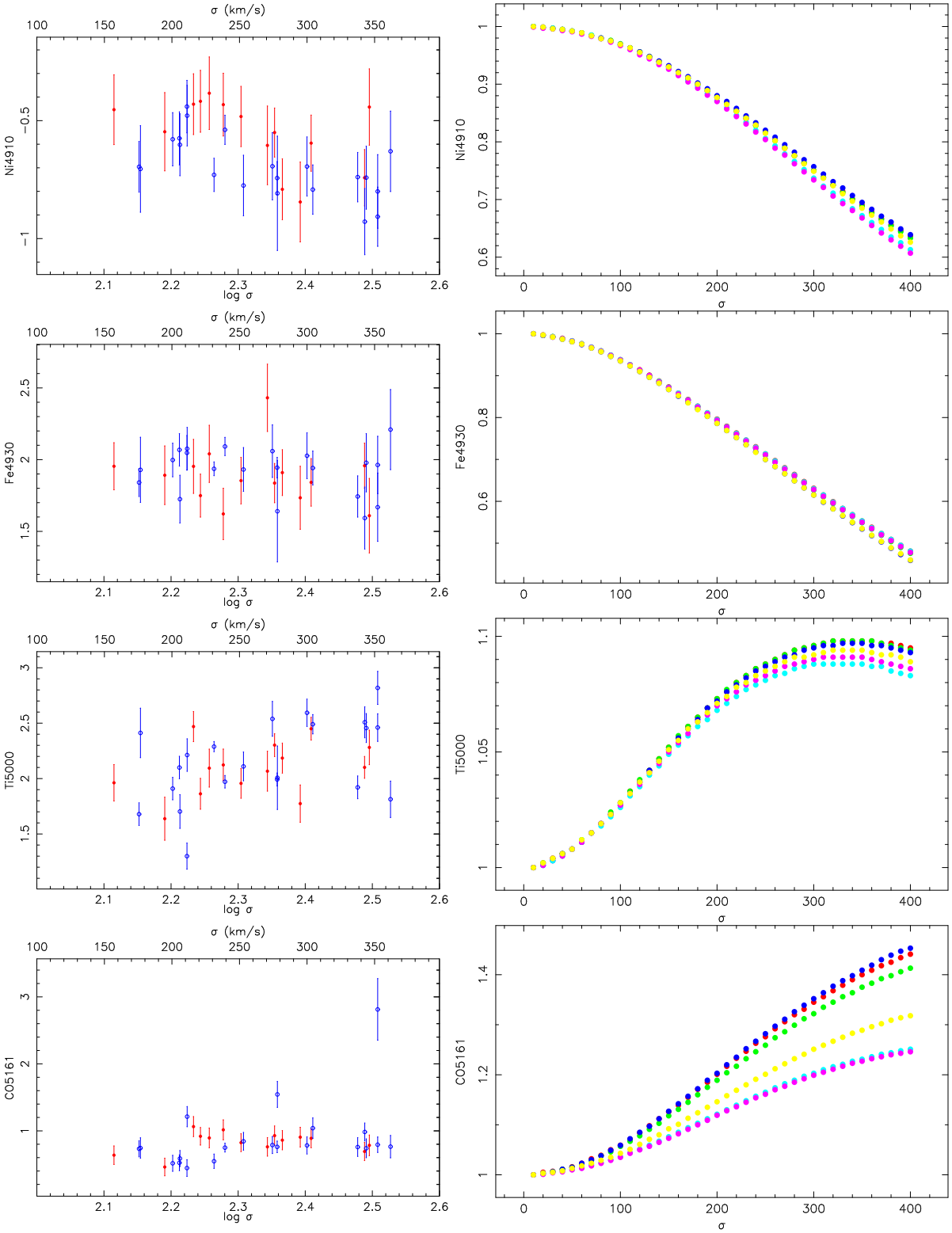

Figure C.1: Continued

D

Tables of the kinematic profiles of dwarf early-type galaxies

The Tables of the kinematic profiles published in Toloba et al. (2011) and presented in Chapter 6 are electronically available `http://vizier.cfa.harvard.edu/viz-bin/VizieR?-source$=$J/A$+$A/526/A114`. For completeness we include them in this Appendix.

R_v ($''$)	v (km s^{-1})	v_e (km s^{-1})	R_σ ($''$)	σ (km s^{-1})	σ_e (km s^{-1})
−92.11	2.3	14.4	−71.98	52.5	10.0
−82.30	−21.6	6.9	−65.33	43.4	7.9
−72.18	−17.0	23.5	−58.85	48.8	6.0
−71.39	−14.5	9.5	−54.88	52.2	9.1
−67.28	−24.1	5.7	−52.42	43.7	10.0
−64.11	−18.8	8.8	−49.77	54.5	9.1
−61.63	−14.6	5.3	−46.52	47.7	4.8
−58.64	−17.8	4.8	−43.78	47.5	3.7
−55.81	−10.3	5.9	−40.70	47.0	4.0
−52.69	−13.6	4.6	−37.86	52.5	3.5
−49.25	−3.7	3.3	−34.46	50.0	2.6
−46.50	−11.4	3.9	−31.35	53.2	2.3
−43.76	−8.3	2.3	−28.42	53.5	2.0
−40.49	−14.8	2.2	−25.52	52.7	1.9
−37.46	−18.0	2.3	−22.57	55.3	1.3
−34.50	−14.4	1.7	−19.49	53.9	1.2
−31.55	−17.2	1.5	−16.52	59.0	0.9
−28.41	−18.5	1.2	−14.82	58.1	1.6
−25.57	−17.8	1.0	−14.41	57.3	1.5
−22.55	−19.6	0.8	−14.01	58.1	1.7
−19.80	−21.8	3.5	−13.60	56.4	1.5
−19.60	−18.6	1.8	−13.20	55.1	1.5
−19.24	−20.6	1.6	−12.79	59.4	1.6
−18.83	−23.1	1.6	−12.38	57.3	1.5
−18.42	−22.5	1.4	−11.98	58.1	1.4
−18.01	−18.8	1.6	−11.57	60.9	1.4
−17.60	−24.0	1.5	−11.16	59.9	1.4
−17.19	−26.8	1.5	−10.80	56.8	1.2
−16.78	−21.3	1.4	−10.42	60.8	1.2
−16.37	−22.3	1.5	−10.01	58.9	1.1
−15.96	−25.5	1.4	−9.61	58.3	1.1
−15.55	−24.9	1.3	−9.20	59.1	1.1
−15.20	−28.6	1.4	−8.80	56.6	0.9
−14.83	−30.8	1.2	−8.39	59.7	0.9
−14.42	−30.9	1.2	−7.99	59.8	0.9
−14.02	−27.5	1.1	−7.58	59.7	0.9
−13.61	−28.6	1.1	−7.19	59.8	0.8
−13.20	−29.8	1.1	−6.80	58.6	0.9
−12.79	−29.8	1.1	−6.41	57.0	0.7
−12.38	−30.8	1.0	−6.01	58.1	0.8
−11.97	−30.7	1.0	−5.61	62.5	0.7
−11.56	−29.5	1.0	−5.20	61.4	0.8
−11.16	−32.6	0.9	−4.80	59.3	0.8
−10.80	−33.0	1.1	−4.40	61.8	0.7
−10.43	−34.2	1.0	−3.99	60.9	0.6
−10.02	−33.4	0.9	−3.59	64.3	0.6
−9.62	−34.6	0.8	−3.19	64.4	0.6
−9.21	−35.1	0.8	−2.78	64.0	0.5
−8.80	−36.2	0.7	−2.38	63.6	0.5
−8.39	−36.5	0.7	−2.00	64.2	0.4

Table D.1: Kinematic profiles for M32. NOTES: Column 1: radius for the rotation speed profile. Column 2: rotation velocities. Column 3: rotation velocity errors. Column 4: radius for the velocity dispersion profile. Column 6: velocity dispersions. Column 7: velocity dispersion errors.

R_v ($''$)	v (km s^{-1})	v_e (km s^{-1})	R_σ ($''$)	σ (km s^{-1})	σ_e (km s^{-1})
−7.99	−37.6	0.7	−1.60	66.8	0.4
−7.57	−39.0	0.7	−1.21	69.7	0.4
−7.17	−37.1	0.7	−0.80	75.2	0.3
−6.80	−39.6	0.7	−0.40	80.4	0.3
−6.44	−40.3	0.7	0.00	82.7	0.3
−6.03	−41.4	0.6	0.40	80.3	0.3
−5.62	−42.6	0.6	0.80	73.6	0.3
−5.21	−42.8	0.5	1.20	67.5	0.4
−4.81	−39.2	0.5	1.61	66.5	0.4
−4.40	−39.9	0.5	2.00	63.7	0.4
−4.00	−40.2	0.5	2.38	64.7	0.5
−3.58	−40.7	0.4	2.78	64.0	0.4
−3.18	−40.2	0.4	3.18	64.0	0.5
−2.76	−41.0	0.4	3.59	62.3	0.5
−2.37	−40.8	0.4	3.99	60.4	0.6
−2.00	−39.5	0.4	4.40	60.3	0.7
−1.63	−40.3	0.3	4.80	61.3	0.7
−1.22	−38.1	0.3	5.21	60.9	0.7
−0.81	−31.9	0.2	5.61	60.3	0.7
−0.41	−21.3	0.2	6.01	60.6	0.7
0.00	−4.3	0.2	6.42	60.3	0.8
0.41	13.1	0.2	6.80	58.0	0.9
0.81	25.1	0.3	7.18	58.0	0.9
1.22	33.6	0.3	7.57	61.3	0.9
1.63	37.5	0.3	7.98	60.0	0.9
2.00	38.1	0.3	8.39	59.0	1.0
2.36	39.7	0.3	8.80	58.2	1.0
2.77	41.2	0.4	9.20	58.4	1.0
3.18	42.8	0.4	9.60	60.6	1.1
3.59	42.7	0.4	10.01	59.8	1.0
3.99	42.4	0.5	10.41	56.6	1.2
4.40	42.3	0.5	10.83	57.3	1.3
4.81	43.3	0.5	11.20	58.6	1.5
5.22	42.3	0.5	11.57	57.9	1.2
5.63	42.8	0.5	11.98	58.7	1.4
6.03	42.5	0.6	12.39	58.3	1.3
6.44	41.4	0.6	12.79	54.4	1.3
6.80	42.5	0.7	13.20	57.6	1.6
7.17	41.7	0.6	13.60	57.6	1.6
7.57	39.1	0.7	14.01	56.3	1.5
7.98	39.6	0.8	14.42	57.9	1.6
8.39	41.5	0.7	14.82	56.3	1.7
8.80	39.3	0.8	16.41	58.3	0.9
9.21	38.2	0.8	19.22	55.9	1.0
9.62	37.8	0.9	22.25	54.0	1.3
10.02	36.1	0.9	25.28	54.0	1.7
10.44	37.6	0.9	28.45	54.8	2.0
10.84	35.9	1.0	31.06	50.8	2.0
11.20	36.8	1.1	34.47	52.8	2.7
11.57	34.4	0.9	37.57	49.4	3.1
11.97	32.2	1.0	40.02	50.9	4.2

Table D.1: Continued.

R_v ($''$)	v (km s^{-1})	v_e (km s^{-1})	R_σ ($''$)	σ (km s^{-1})	σ_e (km s^{-1})
12.38	32.3	1.1	43.16	48.2	4.0
12.79	31.1	1.0	46.81	49.7	4.8
13.20	32.8	1.1	49.20	47.0	5.5
13.61	30.3	1.2	52.80	58.0	9.0
14.02	30.9	1.3	55.37	51.2	8.9
14.43	28.7	1.2	58.19	52.3	8.7
14.84	30.0	1.2	64.06	45.3	11.3
15.20	27.9	1.4	71.38	69.6	12.8
15.55	27.2	1.3			
15.95	27.0	1.4			
16.37	28.8	1.5			
16.78	26.3	1.5			
17.19	26.5	1.5			
17.60	25.8	1.4			
18.01	27.4	1.4			
18.42	23.5	1.5			
18.84	25.9	1.7			
19.24	22.4	1.7			
19.65	28.6	1.5			
21.29	23.9	0.7			
24.31	24.1	1.0			
27.33	23.6	1.1			
30.45	19.2	1.2			
33.28	18.5	1.6			
36.52	19.7	2.0			
39.27	15.2	2.4			
42.15	16.9	2.7			
45.31	15.7	3.0			
48.20	13.4	3.4			
51.18	11.4	3.9			
54.69	15.7	5.6			
57.47	20.9	5.3			
61.01	23.8	6.4			
63.02	36.2	7.2			
66.65	10.4	8.1			
68.99	16.4	14.6			
72.09	33.2	11.7			
77.57	22.2	7.7			
85.18	24.4	11.5			
92.12	4.2	14.1			

Table D.1: Continued.

R_v ($''$)	v (km s^{-1})	v_e (km s^{-1})	R_σ ($''$)	σ (km s^{-1})	σ_e (km s^{-1})
−18.62	−18.4	9.9	−20.79	48.7	22.3
−16.81	31.4	15.5	−14.62	41.8	10.8
−14.75	−1.6	14.8	−12.26	41.9	21.4
−13.35	−4.8	6.7	−10.19	20.2	7.0
−12.57	−8.8	8.4	−9.22	42.7	15.4
−11.74	−25.3	6.8	−8.15	40.4	5.9
−11.18	−4.3	12.8	−7.25	52.6	23.1
−9.97	−9.7	6.0	−6.62	37.3	6.8
−9.24	5.8	27.7	−5.66	36.3	7.2
−8.98	0.0	6.6	−4.97	39.6	6.4
−8.21	−5.6	4.8	−4.20	38.5	7.4
−7.39	−1.1	5.6	−3.58	41.5	6.5
−6.80	−2.5	6.6	−2.75	38.7	6.5
−6.40	1.7	7.9	−2.32	37.4	4.0
−6.00	3.4	6.5	−2.00	45.9	6.6
−5.60	2.0	6.4	−1.64	45.4	3.9
−5.49	−9.0	8.0	−1.23	43.0	3.3
−5.20	−5.6	4.5	−0.82	38.4	3.1
−4.80	−8.0	5.2	−0.41	36.3	2.4
−4.40	0.3	4.5	0.00	40.2	2.5
−3.98	5.1 4	.5	0.41	41.3	2.7
−3.57	8.9	4.2	0.82	43.7	3.2
−3.18	−4.3	4.0	1.22	46.3	3.3
−2.75	−2.1	3.1	1.66	32.3	4.7
−2.32	−3.8	2.6	2.00	50.0	7.7
−2.00	−2.0	2.6	2.33	42.8	3.5
−1.66	1.1	2.2	2.74	45.7	3.9
−1.24	4.8	2.1	3.14	43.8	5.1
−0.83	2.2	1.3	3.57	44.6	5.3
−0.42	2.5	1.4	4.17	35.8	12.1
0.00	−0.6	1.3	4.20	43.0	3.8
0.42	0.9	1.6	4.97	40.4	5.6
0.84	−0.0	1.6	5.58	40.2	6.4
1.23	0.5	1.8	6.75	38.6	5.3
1.65	−1.0	2.1	7.25	38.9	16.8
2.00	−2.7	3.4	8.16	34.6	5.5
2.33	−4.1	2.5	9.22	42.8	20.1
2.74	−3.5	2.6	10.19	43.1	4.9
3.18	−5.3	1.8	12.31	54.1	19.3
3.58	−5.1	2.9	14.59	31.9	7.2
3.98	2.9	4.0			
4.40	0.0	3.3			
4.80	−3.0	3.6			
5.20	2.1	2.9			
5.55	5.9	4.6			
6.00	−3.0	4.8			
6.38	6.3	5.2			
6.80	12.8	7.7			
7.35	1.9	5.0			
8.21	10.5	4.7			
8.99	3.6	6.1			
9.98	11.8	5.3			
11.31	−2.0	7.5			
12.55	28.8	11.5			
13.31	7.9	7.4			
14.72	16.1	11.5			
16.84	−1.0	12.6			
18.67	17.5	10.4			
22.93	69.0	43.4			

Table D.2: Kinematic profiles for NGC3073.

R_v ($''$)	v (km s^{-1})	v_e (km s^{-1})	R_σ ($''$)	σ (km s^{-1})	σ_e (km s^{-1})
−10.86	−36.7	16.4	−6.08	42.1	5.3
−9.76	−26.5	8.1	−2.52	34.6	6.5
−7.66	−7.2	9.7	−1.04	32.7	4.5
−6.08	−9.3	12.1	−0.02	27.2	5.1
−5.28	−20.4	4.9	0.97	30.8	6.6
−3.81	−7.9	5.0	1.63	26.7	4.8
−3.40	−4.5	5.8	6.03	42.3	4.6
−2.66	−23.1	4.7			
−2.14	−8.5	5.1			
−1.78	−3.5	4.9			
−1.23	−8.0	3.4			
−0.80	−7.9	5.4			
−0.54	−7.7	4.3			
−0.02	−5.5	3.2			
0.20	−2.7	3.7			
0.52	−2.2	3.0			
0.80	2.6	5.4			
1.21	12.7	3.4			
1.77	9.8	3.8			
2.09	13.9	6.5			
2.66	14.4	4.4			
3.39	9.5	4.4			
3.85	15.9	5.3			
5.19	15.3	4.1			
7.66	11.2	6.1			
9.72	32.9	6.8			
10.97	18.0	33.4			

Table D.3: Kinematic profiles for PGC1007217.

R_v ($''$)	v (km s^{-1})	v_e (km s^{-1})	R_σ ($''$)	σ (km s^{-1})	σ_e (km s^{-1})
−5.38	14.9	7.4	−3.41	33.0	7.3
−4.53	−13.1	6.1	−0.90	28.7	8.0
−2.44	3.2	4.5	0.00	29.3	7.7
−1.51	1.0	4.9	1.17	33.5	16.7
−0.98	3.7	4.5	3.30	27.7	6.0
−0.54	4.9	5.5			
−0.06	4.6	4.0			
0.20	−3.3	6.6			
0.53	6.3	5.8			
0.95	−3.2	4.8			
1.39	1.8	8.6			
1.97	−0.2	4.2			
2.56	−9.2	5.0			
4.42	4.4	10.8			
5.46	−11.3	5.0			
6.11	−8.5	9.3			

Table D.4: Kinematic profiles for PGC1154903.

R_v ($''$)	v (km s^{-1})	v_e (km s^{-1})	R_σ ($''$)	σ (km s^{-1})	σ_e (km s^{-1})
-3.74	23.6	10.4	-3.07	21.4	12.9
-2.58	-8.4	12.2	-0.99	30.0	10.4
-1.78	10.7	11.5	0.02	0.2	8.5
-1.20	14.0	12.9	0.99	16.9	11.6
-0.80	20.5	12.3	3.14	29.7	12.5
-0.40	5.3	6.9			
0.00	-23.7	6.3			
0.40	5.0	7.9			
0.80	-16.5	11.9			
1.20	-0.2	12.4			
1.78	0.8	7.9			
2.60	7.4	11.6			
3.73	-10.2	12.8			

Table D.5: Kinematic profiles for VCC21.

R_v ($''$)	v (km s^{-1})	v_e (km s^{-1})	R_σ ($''$)	σ (km s^{-1})	σ_e (km s^{-1})
−24.22	−11.1	17.3	−9.64	35.0	14.7
−17.02	−23.1	13.9	−6.14	17.7	23.8
−16.02	−6.8	23.2	−5.02	20.6	11.0
−13.36	−9.6	9.0	−4.17	54.3	11.7
−12.31	27.9	17.2	−3.42	29.5	4.4
−11.04	5.6	6.0	−2.64	41.6	18.1
−9.67	1.4	12.1	−2.20	41.0	14.2
−8.55	4.3	8.3	−1.59	31.4	4.1
−7.60	−8.2	5.3	−1.46	29.3	8.0
−6.92	−3.0	8.7	−0.88	38.5	10.5
−6.25	1.0	8.8	−0.54	29.0	3.7
−5.85	1.3	8.4	0.00	32.9	3.5
−5.28	20.7	19.9	0.52	31.7	3.7
−4.98	−0.7	4.9	0.88	29.7	8.0
−4.40	−17.1	13.0	1.32	40.0	15.1
−4.13	−1.6	4.2	1.58	27.8	4.5
−3.54	−1.7	4.7	2.38	26.8	11.4
−3.08	−0.9	7.1	2.64	41.8	15.0
−2.65	−0.2	3.7	3.35	38.7	4.6
−2.20	−0.4	5.1	4.17	40.8	17.4
−1.78	1.7	2.6	5.02	28.0	9.4
−1.26	−1.6	3.5	6.14	20.6	18.2
−0.84	1.1	2.8	9.64	62.7	26.8
−0.42	−1.8	1.8	12.26	51.3	16.2
0.00	−3.7	1.7	17.80	14.5	21.9
0.41	−3.9	1.8			
0.84	−2.0	2.2			
1.25	3.2	3.2			
1.77	4.3	3.4			
2.20	9.1	5.4			
2.66	6.9	3.1			
3.08	5.4	7.8			
3.55	2.1	4.8			
4.11	2.9	5.1			
4.40	2.3	14.9			
4.98	10.3	4.8			
5.28	6.3	15.6			
5.89	7.4	7.7			
6.24	4.6	9.4			
6.92	18.9	8.8			
7.62	7.5	5.8			
8.55	−7.1	7.9			
9.67	20.0	21.4			
11.00	−4.5	6.1			
12.31	33.3	19.8			
13.33	1.4	10.8			
16.47	14.1	9.3			
19.08	53.6	17.3			
24.22	44.6	24.4			

Table D.6: Kinematic profiles for VCC308.

R_v ($''$)	v (km s^{-1})	v_e (km s^{-1})	R_σ ($''$)	σ (km s^{-1})	σ_e (km s^{-1})
−15.106	−63.8	25.7	−10.39	41.0	21.7
−14.05	−58.5	15.1	−5.21	33.9	4.5
−9.57	−38.9	4.6	−3.93	50.3	17.2
−7.76	−29.6	8.8	−2.85	23.2	19.3
−6.22	−26.0	8.5	−2.10	26.3	5.5
−5.31	−26.9	4.4	−1.30	41.0	9.0
−4.92	−9.9	9.4	−0.96	36.8	4.7
−4.17	−9.2	10.4	−0.41	33.7	4.7
−3.65	−17.1	3.8	0.00	34.8	2.6
−3.24	−1.4	5.8	0.40	34.9	4.9
−2.60	−10.0	4.0	0.97	35.3	4.2
−2.20	−13.3	7.1	1.30	37.9	7.3
−1.80	−8.5	3.0	2.12	34.8	4.9
−1.24	−2.5	3.5	2.85	64.0	13.2
−0.85	−2.2	2.3	3.93	25.0	22.6
−0.41	−2.5	1.8	5.26	30.4	5.1
0.00	−1.8	1.5			
0.40	0.6	1.8			
0.86	7.1	2.8			
1.23	12.3	3.2			
1.82	8.6	2.7			
2.20	8.8	9.1			
2.60	14.2	4.1			
3.08	28.2	18.8			
3.63	16.0	3.7			
4.17	51.2	12.7			
4.82	36.8	10.2			
5.33	23.5	4.5			
6.23	37.4	9.7			
8.10	52.0	13.7			
9.52	36.1	5.1			
15.21	22.5	35.6			

Table D.7: Kinematic profiles for VCC397.

R_v ($''$)	v (km s^{-1})	v_e (km s^{-1})	R_σ ($''$)	σ (km s^{-1})	σ_e (km s^{-1})
−26.60	12.5	21.7	−15.75	49.9	5.3
−22.59	71.8	14.6	−10.80	44.6	4.2
−19.00	21.5	6.0	−8.38	41.3	6.1
−17.01	38.2	8.1	−6.61	42.6	5.5
−15.11	34.7	6.4	−5.47	41.0	3.9
−12.82	20.5	5.4	−4.21	37.5	5.3
−12.04	31.5	5.6	−3.75	49.7	3.7
−10.56	22.2	4.5	−3.29	59.1	11.1
−9.97	15.4	5.9	−2.65	40.2	3.2
−9.58	26.4	5.1	−2.07	39.7	5.2
−8.29	20.7	3.5	−1.68	45.8	3.8
−7.46	29.4	4.9	−1.35	26.1	3.6
−6.72	13.3	4.4	−0.89	46.6	2.9
−5.80	12.1	4.8	−0.40	37.7	4.4
−5.58	10.8	5.9	0.00	39.5	3.0
−5.40	16.8	6.7	0.40	39.9	3.3
−4.98	13.4	3.3	0.88	36.5	3.3
−4.46	8.8	3.4	1.27	30.9	4.6
−3.90	11.6	3.2	1.68	41.5	4.5
−3.53	13.6	3.6	2.05	46.1	5.4
−3.09	10.3	2.4	2.66	40.2	4.2
−2.75	11.4	2.9	3.38	38.5	3.6
−2.32	8.0	2.8	4.17	16.7	22.0
−1.99	6.3	2.9	4.20	41.2	4.9
−1.64	4.7	2.5	5.65	39.0	4.7
−1.23	0.5	1.9	6.57	42.1	5.7
−0.84	0.3	2.2	8.37	44.0	10.2
−0.40	−0.9	1.8	10.89	31.5	4.9
0.00	−3.5	1.7	15.74	37.3	6.2
0.40	−5.9	2.0	19.95	50.6	29.9
0.83	−3.6	2.0			
1.23	−5.5	2.1			
1.69	−9.4	2.6			
2.00	−6.8	3.4			
2.37	−9.6	3.9			
2.74	−3.5	3.8			
3.10	−9.4	2.7			
3.52	−15.0	3.2			
3.91	−5.4	3.6			
4.42	−0.9	3.1			
4.80	0.2	7.5			
5.43	−13.8	3.0			
6.19	−9.3	4.2			
6.93	−16.7	4.4			
7.79	−20.7	7.7			
8.46	−27.2	4.7			
9.93	−23.2	4.5			
10.17	−23.3	8.5			
11.68	−22.9	3.6			
13.13	−23.0	4.8			
15.52	−30.2	7.3			
16.98	−26.4	10.0			
19.39	−28.0	6.5			
20.58	−41.3	25.5			
26.66	−35.4	16.7			

Table D.8: Kinematic profiles for VCC523.

R_v ($''$)	v (km s^{-1})	v_e (km s^{-1})	R_σ ($''$)	σ (km s^{-1})	σ_e (km s^{-1})
-3.07	21.2	6.5	-2.88	40.2	6.1
-1.15	-4.1	5.3	-0.01	20.7	5.4
-0.40	3.9	6.0	2.92	34.4	6.2
0.00	-14.2	6.0			
0.40	-0.0	4.9			
1.15	-2.3	7.9			
3.09	-0.8	4.7			

Table D.9: Kinematic profiles for VCC856.

R_v ($''$)	v (km s^{-1})	v_e (km s^{-1})	R_σ ($''$)	σ (km s^{-1})	σ_e (km s^{-1})
−17.68	23.3	21.0	−8.58	52.1	8.3
−12.72	4.2	11.2	−6.58	69.0	29.5
−11.19	21.4	19.1	−5.49	38.0	17.8
−10.30	3.8	9.4	−4.35	39.5	6.7
−9.66	3.8	23.7	−4.17	30.9	15.3
−8.74	0.2	6.2	−3.86	42.0	8.3
−7.69	8.0	9.0	−3.29	12.1	10.2
−6.81	−4.3	11.2	−2.74	28.5	5.4
−6.06	3.1	4.9	−2.30	33.2	5.9
−5.81	22.1	7.7	−1.78	36.9	4.6
−5.28	19.0	6.8	−1.30	30.1	3.9
−4.79	−2.9	5.2	−0.82	28.8	3.6
−4.39	8.3	5.6	−0.41	28.0	3.4
−3.87	−2.4	4.7	0.00	30.0	3.0
−3.47	7.7	4.3	0.41	29.1	3.2
−3.01	−5.5	3.5	0.82	28.7	3.7
−2.61	2.3	3.4	1.30	34.2	3.9
−2.20	0.7	2.9	1.77	33.0	4.8
−2.00	−2.4	5.0	2.31	30.7	5.3
−1.68	1.7	2.6	2.73	42.3	4.7
−1.25	0.8	1.9	3.21	28.7	10.7
−0.83	0.1	1.5	3.97	31.9	7.3
−0.41	−0.4	1.3	4.38	40.3	6.8
0.00	−2.5	1.5	5.29	23.7	12.8
0.41	−1.0	1.2	6.58	23.3	19.2
0.83	1.2	1.6	8.43	41.2	7.5
1.25	−3.4	2.0			
1.67	1.7	2.4			
2.00	−2.2	5.1			
2.17	1.2	3.7			
2.62	−1.9	3.4			
3.02	−1.2	3.4			
3.47	3.6	5.2			
3.88	5.0	4.9			
4.39	1.9	5.5			
4.79	0.9	4.7			
5.28	1.3	7.8			
5.89	0.2	7.7			
6.05	4.6	5.9			
6.81	5.7	8.1			
7.69	−2.8	7.7			
8.73	0.6	4.6			
10.14	1.6	9.6			
11.19	−5.6	18.4			
12.78	−38.7	11.3			
16.64	−69.7	16.9			

Table D.10: Kinematic profiles for VCC917.

R_v ($''$)	v (km s^{-1})	v_e (km s^{-1})	R_σ ($''$)	σ (km s^{-1})	σ_e (km s^{-1})
-5.43	1.8	5.5	-4.98	36.0	6.2
-3.56	16.8	6.4	-2.36	47.2	6.0
-2.58	9.8	6.3	-1.38	39.2	5.4
-2.00	10.5	6.4	-0.80	35.8	4.6
-1.60	1.7	6.2	-0.40	32.5	3.5
-1.20	-6.2	4.3	0.00	42.2	3.1
-0.80	3.9	2.7	0.40	41.3	2.8
-0.40	0.1	2.3	0.80	39.7	3.6
0.00	6.8	1.9	1.38	37.7	3.9
0.40	2.2	2.4	2.36	36.1	8.5
0.80	1.0	3.0	4.97	37.4	5.6
1.20	-5.1	5.2			
1.60	-11.7	5.6			
2.00	-25.2	6.4			
2.58	-17.0	7.2			
3.56	-29.5	5.7			
5.42	-25.2	6.0			

Table D.11: Kinematic profiles for VCC990.

R_v ($''$)	v (km s^{-1})	v_e (km s^{-1})	R_σ ($''$)	σ (km s^{-1})	σ_e (km s^{-1})
−24.81	33.1	12.6	−20.80	28.3	27.6
−20.18	20.7	18.8	−12.28	43.4	38.1
−17.56	2.9	9.2	−9.80	47.2	9.5
−15.60	13.9	10.7	−9.18	47.5	6.1
−14.07	12.9	8.7	−7.69	38.5	8.7
−12.53	−1.6	4.5	−6.63	35.1	11.9
−11.65	4.0	10.3	−5.72	48.3	4.7
−10.64	4.6	6.7	−4.86	50.2	5.0
−9.89	10.6	9.4	−4.17	43.4	9.0
−9.21	−2.4	5.1	−3.71	50.2	4.6
−8.13	−7.8	6.2	−3.08	45.0	10.7
−7.39	−4.0	4.2	−2.60	43.4	7.0
−7.04	−7.3	7.0	−2.34	46.6	4.3
−6.60	−9.2	7.4	−1.76	68.5	8.7
−6.03	4.4	4.9	−1.33	44.6	3.8
−5.72	5.7	7.6	−0.88	25.4	7.2
−5.31	5.8	5.4	−0.53	45.9	2.9
−4.91	−3.5	4.3	0.00	42.6	2.5
−4.31	4.0	4.3	0.54	42.8	2.8
−3.97	−1.7	3.9	0.88	43.7	6.0
−3.47	−3.2	3.9	1.30	44.2	3.3
−3.06	−3.2	4.4	1.76	46.1	7.0
−2.60	−4.4	2.9	2.34	44.5	4.1
−2.13	0.4	3.2	2.60	40.7	7.0
−1.68	0.7	3.5	3.08	41.2	10.5
−1.28	2.3	2.8	3.74	47.5	4.1
−0.83	1.1	2.7	4.17	34.9	12.2
−0.42	−4.5	1.5	4.72	50.7	7.1
0.00	−1.0	1.5	5.76	48.9	4.3
0.41	0.4	1.8	6.70	33.0	16.0
0.84	−2.8	2.5	7.80	41.1	13.7
1.27	−1.0	2.7	9.36	41.5	4.6
1.70	−0.1	3.1	11.78	40.1	11.9
2.14	2.9	2.9			
2.61	2.0	2.7			
3.04	−5.2	4.0			
3.44	−2.3	3.2			
3.97	5.6	4.9			
4.26	6.4	3.6			
4.94	−1.0	4.7			
5.32	5.7	5.4			
5.72	8.0	6.6			
6.04	9.1	4.9			
6.60	−8.9	8.4			
7.04	−7.3	10.6			
7.37	3.3	4.1			
8.13	8.3	8.2			
9.24	5.7	4.5			
9.90	−7.1	8.0			
10.61	4.4	6.6			
11.66	−1.6	10.6			
12.57	8.5	5.3			
14.07	0.1	11.5			
15.60	29.5	11.0			
17.56	6.8	9.2			
20.30	18.0	10.0			
24.84	−15.8	13.6			

Table D.12: Kinematic profiles for VCC1087.

R_v ($''$)	v (km s^{-1})	v_e (km s^{-1})	R_σ ($''$)	σ (km s^{-1})	σ_e (km s^{-1})
−23.37	16.5	17.3	−17.02	29.4	24.0
−18.40	7.9	17.6	−12.03	21.9	20.5
−15.21	9.9	8.5	−10.97	35.8	7.7
−14.07	6.2	11.5	−9.83	25.1	23.6
−12.75	15.6	15.6	−7.33	36.4	6.2
−11.52	19.7	4.7	−5.94	38.5	8.8
−10.33	10.6	12.6	−5.32	33.4	6.9
−9.39	13.3	9.0	−3.99	38.0	6.9
−8.58	−7.1	11.6	−3.45	35.6	7.2
−7.96	7.4	5.7	−2.75	36.0	4.6
−7.55	7.0	12.9	−2.20	28.4	10.9
−7.04	−12.4	12.4	−1.78	36.4	4.3
−6.75	13.2	6.3	−1.31	43.5	9.6
−6.16	12.7	7.9	−0.97	35.0	4.3
−5.76	7.6	4.6	−0.40	34.3	5.9
−5.28	−2.2	11.3	0.00	32.5	3.7
−4.95	8.7	5.8	0.40	28.7	4.4
−4.26	8.2	3.4	0.95	33.2	4.2
−3.95	5.9	9.2	1.31	33.5	9.1
−3.41	2.0	4.8	1.78	39.1	4.8
−3.08	17.4	8.3	2.20	53.1	19.8
−2.70	3.5	3.4	2.76	39.2	4.5
−2.29	1.7	3.3	3.40	40.4	5.9
−2.00	1.8	4.8	4.04	34.5	5.4
−1.68	2.4	3.0	5.30	35.1	6.5
−1.29	1.1	2.4	5.93	68.1	15.6
−0.84	2.0	2.6	7.29	37.9	5.5
−0.41	0.9	2.5	8.00	56.6	8.1
0.00	0.5	1.9	9.88	29.9	18.0
0.41	−0.3	2.1	10.96	37.3	7.7
0.85	−0.3	2.4	12.03	40.2	25.6
1.25	−0.2	3.3			
1.67	−1.5	3.1			
2.00	−1.7	5.3			
2.31	0.5	3.9			
2.71	−1.9	4.1			
3.08	−4.7	6.7			
3.43	−9.3	3.5			
3.95	−14.1	6.5			
4.27	−4.3	3.5			
4.93	−9.4	5.0			
5.32	−0.2	6.7			
5.76	−8.5	5.9			
6.16	−20.0	10.6			
6.75	−4.5	4.4			
7.04	−10.4	10.4			
7.53	−12.7	9.9			
7.96	−13.4	5.4			
8.57	−8.4	8.8			
9.41	−13.0	6.5			
10.33	−10.3	12.7			
11.50	−14.4	5.3			
12.74	−7.5	14.1			
14.07	−47.4	20.2			
15.37	−22.2	7.5			
18.39	−27.7	16.2			

Table D.13: Kinematic profiles for VCC1122.

R_v ($''$)	v (km s^{-1})	v_e (km s^{-1})	R_σ ($''$)	σ (km s^{-1})	σ_e (km s^{-1})
−4.91	−10.2	5.8	−3.08	40.8	3.8
−2.76	5.8	7.0	−0.97	43.6	4.6
−1.79	−0.2	4.7	−0.40	44.5	4.0
−1.20	−5.6	5.0	0.00	34.0	3.6
−0.80	−4.5	3.5	0.40	44.4	4.5
−0.40	−0.8	2.4	0.98	44.7	3.4
0.00	1.1	1.4	3.08	51.9	6.9
0.40	3.9	2.8			
0.80	5.3	4.3			
1.20	1.3	3.6			
1.78	3.1	6.0			
2.76	−5.8	4.9			
4.93	−10.6	7.4			

Table D.14: Kinematic profiles for VCC1183.

R_v ($''$)	v (km s^{-1})	v_e (km s^{-1})	R_σ ($''$)	σ (km s^{-1})	σ_e (km s^{-1})
−13.72	−40.1	11.2	−9.43	57.0	7.5
−9.34	−19.9	10.4	−5.14	87.9	6.5
−7.37	−5.2	10.7	−3.58	49.7	6.9
−5.98	−21.7	9.1	−2.59	51.4	9.7
−4.99	13.3	9.9	−1.78	54.5	5.6
−4.19	6.4	8.0	−1.20	61.1	6.0
−3.39	−3.9	11.4	−0.80	40.8	5.8
−2.80	−11.2	10.0	−0.40	43.1	2.9
−2.40	−7.5	9.3	0.00	44.3	4.9
−2.00	−9.7	6.3	0.40	44.7	2.6
−1.60	−0.1	6.3	0.80	47.0	3.9
−1.20	1.5	4.5	1.20	46.9	4.9
−0.80	0.7	2.6	1.79	53.9	4.8
−0.40	2.7	2.0	2.59	48.0	5.2
0.00	4.5	1.9	3.58	45.2	6.0
0.40	4.3	2.0	5.14	57.1	10.6
0.80	−4.9	2.9	9.48	70.5	7.8
1.20	−2.6	4.0			
1.60	−1.7	3.8			
2.00	−2.1	6.0			
2.40	−3.5	6.8			
2.80	−4.2	10.5			
3.39	−1.6	5.7			
4.19	−22.3	6.7			
4.99	−3.1	10.3			
5.98	−3.2	8.7			
7.37	0.3	10.6			
9.34	−8.0	15.7			
13.71	−6.5	16.4			

Table D.15: Kinematic profiles for VCC1261.

R_v ($''$)	v (km s^{-1})	v_e (km s^{-1})	R_σ ($''$)	σ (km s^{-1})	σ_e (km s^{-1})
-5.51	-0.2	9.6	-3.45	49.5	7.3
-3.16	-0.1	7.7	-1.38	63.3	8.8
-2.18	-4.7	7.8	-0.80	51.6	10.9
-1.60	-1.8	12.4	-0.40	49.4	3.5
-1.20	10.9	5.5	0.00	48.7	2.8
-0.80	5.5	4.4	0.40	57.2	7.9
-0.40	2.4	2.9	0.80	97.0	17.9
0.00	3.1	2.4	1.38	60.3	10.7
0.40	-8.5	3.6	3.46	49.0	4.8
0.80	-8.5	8.2			
1.20	6.2	8.5			
1.60	-1.8	9.4			
2.18	-8.5	7.3			
3.16	-17.6	7.9			
5.51	-7.4	8.3			

Table D.16: Kinematic profiles for VCC1431.

R_v ($''$)	v (km s^{-1})	v_e (km s^{-1})	R_σ ($''$)	σ (km s^{-1})	σ_e (km s^{-1})
-2.36	-15.2	5.4	-2.62	33.1	4.4
-1.38	-10.3	3.4	-0.57	38.6	3.0
-0.80	-5.5	3.8	0.00	35.3	4.2
-0.40	4.4	2.6	0.57	42.4	3.7
0.00	8.1	2.9	2.64	37.4	5.0
0.40	6.8	3.1			
0.80	2.0	7.7			
1.38	-2.4	5.3			
2.36	-5.5	4.6			

Table D.17: Kinematic profiles for VCC1549.

R_v ($''$)	v (km s^{-1})	v_e (km s^{-1})	R_σ ($''$)	σ (km s^{-1})	σ_e (km s^{-1})
−15.24	3.9	12.9	−7.85	28.6	18.2
−11.29	−9.1	5.9	−6.13	37.1	21.0
−9.87	−10.9	13.8	−4.89	26.5	5.7
−8.97	3.8	10.3	−3.73	23.7	11.8
−8.66	−16.2	10.6	−3.23	36.9	4.6
−7.36	−13.6	8.0	−2.78	20.1	8.6
−6.73	−9.9	7.8	−2.19	43.8	6.5
−6.37	−3.1	7.3	−1.87	37.3	5.1
−5.72	10.2	21.1	−1.36	29.8	4.2
−5.31	−5.2	4.7	−0.85	34.4	4.1
−4.84	3.4	7.8	−0.41	30.8	4.5
−4.27	−0.1	4.5	0.00	29.1	3.3
−3.96	−3.9	5.1	0.41	28.0	4.1
−3.44	−6.6	3.5	0.85	30.6	3.8
−3.04	0.0	4.5	1.37	25.9	4.0
−2.70	−1.0	3.7	1.89	36.3	7.6
−2.24	−2.2	2.9	2.19	31.2	5.2
−2.00	−4.3	5.7	2.80	27.6	9.0
−1.68	−6.3	2.5	3.26	37.9	4.5
−1.26	−3.0	2.3	3.73	20.1	12.5
−0.83	−2.7	2.1	4.17	33.2	20.3
−0.41	−2.4	2.0	4.92	36.6	4.8
0.00	−1.7	1.9	7.85	27.3	24.3
0.41	−2.8	2.0	12.59	20.4	25.8
0.83	0.0	2.2			
1.25	−0.2	2.4			
1.66	2.0	2.5			
2.00	2.5	4.4			
2.30	6.2	2.4			
2.70	5.8	3.9			
3.05	6.2	4.3			
3.43	6.0	3.4			
3.96	−2.1	4.5			
4.26	9.2	3.9			
4.84	14.0	6.8			
5.32	6.9	3.7			
5.72	−1.3	19.9			
6.56	11.9	5.0			
7.40	15.7	7.4			
8.72	15.7	5.3			
9.87	8.7	14.6			
11.26	16.7	5.6			
15.17	10.0	13.7			

Table D.18: Kinematic profiles for VCC1695.

R_v ($''$)	v (km s^{-1})	v_e (km s^{-1})	R_σ ($''$)	σ (km s^{-1})	σ_e (km s^{-1})
−18.69	0.8	15.9	−14.48	50.5	14.7
−14.71	22.8	9.3	−9.38	41.9	19.6
−13.66	−2.5	7.3	−7.44	36.7	4.2
−12.18	5.8	8.6	−5.70	51.3	13.2
−10.67	12.1	10.0	−4.41	38.8	4.2
−8.82	5.9	4.7	−3.62	40.1	5.4
−8.13	6.2	7.5	−2.81	40.4	4.0
−7.25	4.5	8.7	−2.20	35.8	9.3
−6.47	8.3	3.5	−1.61	44.2	3.1
−5.72	13.5	9.1	−1.33	34.5	5.5
−5.20	5.4	4.1	−0.88	39.9	9.5
−4.84	−5.6	6.6	−0.55	36.3	3.3
−4.25	2.5	3.5	0.00	34.9	3.0
−4.02	−0.6	4.0	0.55	32.6	3.5
−3.42	1.2	2.9	0.88	40.6	7.3
−3.08	10.6	5.9	1.33	39.1	4.9
−2.64	4.5	2.7	1.61	37.5	3.7
−2.20	5.7	5.1	2.20	30.2	10.7
−1.78	4.7	2.2	2.80	35.9	4.0
−1.26	−0.6	2.9	3.61	35.2	5.6
−0.87	0.0	2.5	4.38	39.5	4.3
−0.42	1.3	2.0	5.69	36.7	8.8
0.00	−0.9	1.7	7.45	44.5	4.9
0.41	−2.2	2.1	9.38	47.9	8.2
0.86	−1.3	2.3			
1.26	−1.6	3.0			
1.78	−2.3	2.4			
2.20	−8.7	5.0			
2.63	−1.2	2.7			
3.08	−0.9	5.0			
3.44	−6.4	3.5			
4.05	−2.2	4.1			
4.26	−4.0	3.7			
4.84	−10.4	6.8			
5.20	−2.6	3.7			
5.72	2.7	7.0			
6.41	−6.3	3.6			
7.25	−6.4	6.7			
8.13	8.5	9.2			
8.86	−6.6	4.2			
10.63	−1.8	6.5			
12.16	−1.5	9.4			
13.67	−3.0	6.6			
14.66	2.0	9.4			
18.86	−1.9	11.5			

Table D.19: Kinematic profiles for VCC1861.

R_v ($''$)	v (km s^{-1})	v_e (km s^{-1})	R_σ ($''$)	σ (km s^{-1})	σ_e (km s^{-1})
−7.88	−8.3	7.1	−5.28	23.6	5.4
−4.54	−2.1	4.5	−2.36	40.9	4.7
−3.39	−6.4	6.6	−1.38	40.8	3.0
−2.58	−3.3	3.6	−0.80	42.3	3.5
−2.00	−4.0	4.7	−0.40	39.8	3.0
−1.60	−8.8	3.5	0.00	44.1	2.3
−1.20	−0.6	2.8	0.40	41.3	3.3
−0.80	−4.1	2.4	0.80	49.5	4.8
−0.40	−3.3	1.9	1.38	43.6	3.1
0.00	5.4	2.0	2.36	44.0	4.2
0.40	5.3	2.1	5.29	29.3	4.4
0.80	1.4	3.0			
1.20	1.4	3.1			
1.60	1.5	3.6			
2.00	−0.6	4.2			
2.59	4.4	3.4			
3.39	−0.5	5.4			
4.55	−2.7	5.3			
7.89	10.8	9.1			

Table D.20: Kinematic profiles for VCC1910.

R_v ($''$)	v (km s^{-1})	v_e (km s^{-1})	R_σ ($''$)	σ (km s^{-1})	σ_e (km s^{-1})
−9.67	4.9	12.7	−7.92	25.5	8.5
−6.75	3.0	10.3	−3.74	37.3	7.3
−5.18	−4.9	8.3	−2.59	37.5	8.9
−4.19	7.8	8.2	−1.79	40.3	3.9
−3.39	5.9	8.0	−1.20	37.4	5.5
−2.80	0.2	5.7	−0.80	34.6	5.2
−2.40	1.4	8.3	−0.40	30.7	5.0
−2.00	1.2	5.2	0.00	30.5	3.4
−1.60	−0.9	4.5	0.40	37.8	4.1
−1.20	−5.9	4.7	0.80	24.2	6.3
−0.80	−6.4	3.4	1.20	33.5	6.4
−0.40	10.3	2.1	1.79	35.7	6.0
0.00	8.2	1.9	2.59	52.8	7.7
0.40	2.8	2.3	3.75	34.3	5.8
0.80	−10.4	3.4	7.88	37.4	5.7
1.20	−12.7	4.0			
1.60	−2.9	6.4			
2.00	−6.1	7.4			
2.40	5.4	10.3			
2.80	−20.9	8.2			
3.39	−5.1	6.2			
4.19	−17.8	6.7			
5.18	−10.1	8.9			
6.75	−25.7	7.1			
9.66	−33.1	8.6			

Table D.21: Kinematic profiles for VCC1912.

R_v ($''$)	v (km s^{-1})	v_e (km s^{-1})	R_σ ($''$)	σ (km s^{-1})	σ_e (km s^{-1})
-3.56	22.0	9.4	-3.46	51.2	3.9
-2.58	22.9	4.0	-1.38	42.0	5.3
-2.00	16.6	5.6	-0.80	59.8	5.7
-1.60	13.9	6.1	-0.40	42.2	2.4
-1.20	10.6	3.6	0.00	45.9	2.8
-0.80	4.3	3.2	0.40	52.5	4.4
-0.40	6.3	1.4	0.80	56.1	6.4
0.00	4.9	1.6	1.38	45.9	4.5
0.40	0.4	2.2	3.45	42.0	4.3
0.80	-5.6	4.4			
1.20	-16.7	5.3			
1.60	-35.4	4.1			
2.00	-23.6	4.0			
2.58	-31.7	3.4			
3.56	-23.0	6.0			

Table D.22: Kinematic profiles for VCC1947.

E

Photometric parameters measured in the optical and infrared of dwarf early-type galaxies

In this Appendix I show all the photometric parameters calculated in the different bands following the procedure explained in Section 6.2.

From the MAGPOP collaboration most of the galaxies observed at medium-resolution spectroscopy were also observed in the near-infrared in photometry (67% in H and/or K band). For the remaining 33%, H-band images were drawn from GOLDMine database (Gavazzi et al. 2003a). In order to carry out the studies in I and B bands presented in Sections 6.2 and 6.4 we also needed some optical bands to make the transformations accordingly. The photometry chosen for this purpose is SDSS (York et al. 2000) DR6 and DR7 (Adelman-McCarthy et al. 2008; **?**) because all of our target galaxies are observed by the Sloan Digital Sky Survey.

Tables E.1 and E.2 show all the parameters measured in the different bands. Note that for i band instead of showing the average surface brightness within the half-light radius, it is the surface brightness at the R_{eff}. All the magnitudes in these tables are in AB system but for K band that is in Vega.

In Section E.1 we defined an objective technique to measure the diskyness/boxyness parameter that has into account the variations of C_4 present along the radius of the galaxies and the quality of the images. In the published version of the paper we showed only three examples to justify our methodology, thus here we show these radial profiles of C_4 for all the galaxies in our sample.

Figure E.2 present the ellipticity profiles of the galaxies. The dashed black lines indicate the region between 3″ and the R_{eff}. The red line shows the mean value averaged between the dashed lines, which is the value assumed as ellipticity of the galaxy.

Galaxy	m_B mag	$< \mu_{eff,B} >$ mag arcsec^{-2}	m_g mag	ϵ_g	$R_{eff,g}$ arcsec	$< \mu_{eff,g} >$ mag arcsec^{-2}
PGC1007217	15.714± 0.019	22.958 ±0.019	15.539± 0.017	0.129± 0.054	12.02± 0.12	22.783± 0.072
PGC1154903	16.446± 0.021	22.788 ±0.021	16.245± 0.018	0.340± 0.024	9.11± 0.12	22.587± 0.050
NGC3073	13.630± 0.017	21.416 ±0.017	13.419± 0.015	0.142± 0.016	15.54± 0.13	21.205± 0.028
VCC0021	14.868± 0.017	22.091 ±0.017	14.667± 0.015	0.357± 0.029	13.86± 0.09	21.891± 0.051
VCC0308	13.996± 0.016	22.364 ±0.016	13.771± 0.014	0.035± 0.032	19.16± 0.04	22.139± 0.037
VCC0397	15.184± 0.017	22.406 ±0.017	14.968± 0.015	0.330± 0.027	13.56± 0.07	22.190± 0.045
VCC0523	13.473± 0.018	22.287 ±0.018	13.244± 0.015	0.252± 0.007	26.73± 0.23	22.059± 0.022
VCC0856	14.416± 0.017	22.362 ±0.017	14.137± 0.015	0.086± 0.031	16.21± 0.09	22.084± 0.039
VCC0917	15.431± 0.016	21.789 ±0.016	15.208± 0.014	0.406± 0.021	9.68± 0.03	21.566± 0.040
VCC0990	14.599± 0.016	21.123 ±0.016	14.364± 0.014	0.336± 0.019	9.88± 0.03	20.888± 0.033
VCC1087	13.868± 0.017	22.663 ±0.017	13.591± 0.014	0.281± 0.034	27.02± 0.15	22.387± 0.053
VCC1122	14.881± 0.017	21.885 ±0.017	14.642± 0.014	0.504± 0.041	14.26± 0.07	21.646± 0.092
VCC1183	14.171± 0.017	22.589 ±0.017	13.938± 0.015	0.223± 0.117	21.85± 0.14	22.356± 0.165
VCC1261	13.611± 0.016	21.985 ±0.016	13.343± 0.014	0.369± 0.045	23.76± 0.10	21.717± 0.078
VCC1431	14.544± 0.016	21.568 ±0.016	14.248± 0.014	0.033± 0.009	10.31± 0.02	21.272± 0.011
VCC1549	14.879± 0.016	22.270 ±0.016	14.606± 0.014	0.159± 0.014	13.09± 0.04	21.997± 0.020
VCC1695	14.323± 0.020	23.254 ±0.020	14.101± 0.017	0.220± 0.049	27.61± 0.37	23.032± 0.075
VCC1861	14.163± 0.017	22.787 ±0.017	13.906± 0.015	0.036± 0.015	21.57± 0.14	22.530± 0.023
VCC1910	14.281± 0.016	22.014 ±0.016	14.021± 0.014	0.142± 0.040	14.24± 0.12	21.617± 0.055
VCC1912	14.117± 0.016	22.129 ±0.016	13.891± 0.014	0.539± 0.061	23.53± 0.09	21.903± 0.146
VCC1947	14.493± 0.016	21.462 ±0.016	14.225± 0.014	0.230± 0.007	11.26± 0.04	21.194± 0.013

Table E.1: Photometric parameters of the sample of dwarf early-type galaxies analysed in Chapter 6 in B and g bands.

NOTES: m is the total apparent magnitude, $< \mu_{eff} >$ is the average effective surface brightness within the half-light radius, μ_{eff} is the surface brightness measured at the half-light radius (only for i band), R_{eff} is the effective radius. B band was obtained from g and r bands as explained in Section 6.4.

Galaxy	m_r mag	ϵ_r	$R_{eff,r}$ arcsec	$< \mu_{eff,r} >$ mag arcsec^{-2}	m_i mag	$\mu_{eff,i}$ mag arcsec^{-2}	m_K mag	ϵ_K	$R_{eff,K}$ arcsec	$< \mu_{eff,K} >$ mag arcsec^{-2}
PGC1007217	15.083± 0.0146	0.129± 0.054	10.01± 0.15	21.930± 0.075	14.66± 0.02	21.595± 0.026	12.66± 0.05	0.14± 0.03	8.52± 0.07	18.934± 0.042
PGC1154903	15.721± 0.0179	0.340± 0.024	8.74± 0.45	21.973± 0.119	15.49± 0.02	21.233±0.107	14.59± 0.05	0.26± 0.01	3.93± 0.05	17.900± 0.033
NGC3073	12.873± 0.0148	0.142± 0.016	17.31± 0.15	20.892± 0.028	12.73± 0.02	21.014±0.009	10.69± 0.05	0.14± 0.03	11.09± 0.03	17.536± 0.038
VCC0021	14.147± 0.0152	0.357± 0.029	14.72± 0.13	21.501± 0.053	13.86± 0.02	21.472±0.028	12.30± 0.05	0.35± 0.02	10.80± 0.19	18.814± 0.052
VCC0308	13.188± 0.0142	0.035± 0.032	18.68± 0.02	21.501± 0.037	12.82± 0.02	21.704±0.008	11.08± 0.05	0.06± 0.03	16.70± 0.03	18.832± 0.034
VCC0397	14.408± 0.0147	0.330± 0.027	12.54± 0.09	21.460± 0.046	13.98± 0.02	21.875±0.008	11.95± 0.05	0.37± 0.04	12.57± 0.03	18.730± 0.069
VCC0523	12.650± 0.0152	0.252± 0.007	24.62± 0.15	21.287± 0.017	12.48± 0.02	21.326±0.026	10.50± 0.05	0.27± 0.02	17.17± 0.18	18.327± 0.039
VCC0856	13.417± 0.0150	0.086± 0.031	17.06± 0.15	21.474± 0.042	13.16± 0.02	21.527±0.040	11.23± 0.05	0.11± 0.05	14.15± 0.11	18.682± 0.063
VCC0917	14.629± 0.0146	0.406± 0.021	9.04± 0.17	20.839± 0.057	14.25± 0.02	21.204±0.013	12.53± 0.05	0.37± 0.07	8.61± 0.04	18.488± 0.121
VCC0990	13.755± 0.0142	0.336± 0.019	9.31± 0.06	20.149± 0.035	13.37± 0.02	21.234±0.072	11.82± 0.05	0.36± 0.04	9.92± 0.08	18.103± 0.070
VCC1087	12.876± 0.0147	0.281± 0.034	27.32± 0.07	21.695± 0.052	12.69± 0.02	21.627±0.043	10.71± 0.05	0.32± 0.04	17.09± 0.35	18.450± 0.079
VCC1122	14.022± 0.0148	0.504± 0.041	13.99± 0.14	20.985± 0.094	13.70± 0.02	21.360±0.057	12.01± 0.05	0.55± 0.08	11.81± 0.09	18.269± 0.194
VCC1183	13.333± 0.0144	0.223± 0.117	19.19± 0.04	21.469± 0.164	13.05± 0.02	21.506±0.006	11.24± 0.05	0.31± 0.09	13.92± 0.04	18.240± 0.142
VCC1261	12.651± 0.0148	0.369± 0.045	24.21± 0.11	21.065± 0.078	12.42± 0.02	21.276±0.004	10.51± 0.05	0.41± 0.06	20.54± 0.03	18.285± 0.110
VCC1431	13.483± 0.0142	0.033± 0.009	10.15± 0.09	20.474± 0.022	13.09± 0.02	20.701±0.004	10.85± 0.05	0.02± 0.02	9.22± 0.02	17.647± 0.022
VCC1549	13.900± 0.0144	0.159± 0.014	12.85± 0.06	21.251± 0.021	13.46± 0.02	21.491±0.010	11.57± 0.05	0.19± 0.01	11.83± 0.04	18.361± 0.015
VCC1695	13.524± 0.0166	0.220± 0.049	26.14± 0.22	22.336± 0.072	13.48± 0.02	22.267±0.046	11.86± 0.05	0.16± 0.07	15.15± 0.48	19.238± 0.114
VCC1861	13.240± 0.0153	0.036± 0.015	21.52± 0.12	21.859± 0.022	12.99± 0.02	21.411±0.006	10.99± 0.05	0.01± 0.01	12.01± 0.02	18.162± 0.011
VCC1910	13.347± 0.0151	0.142± 0.040	13.57± 0.17	20.838± 0.058	12.92± 0.02	21.436±0.008	10.74± 0.05	0.17± 0.01	14.43± 0.05	18.119± 0.015
VCC1912	13.304± 0.0144	0.539± 0.061	23.57± 0.03	21.319± 0.146	13.02± 0.02	21.232±0.013	11.06± 0.05	0.59± 0.08	19.71± 0.06	18.350± 0.211
VCC1947	13.530± 0.0144	0.230± 0.007	10.92± 0.09	20.433± 0.020	13.18± 0.02	20.497±0.016	10.92± 0.05	0.23± 0.01	8.56± 0.02	17.294± 0.015

Table E.2: Photometric parameters of the sample of dwarf early-type galaxies analysed in Chapter 6 in r, i and K bands.

m is the total apparent magnitude, $< \mu_{eff} >$ is the average effective surface brightness within the half-light radius, R_{eff} is the effective radius. B band was obtained from g and r bands as explained in Section 6.4.

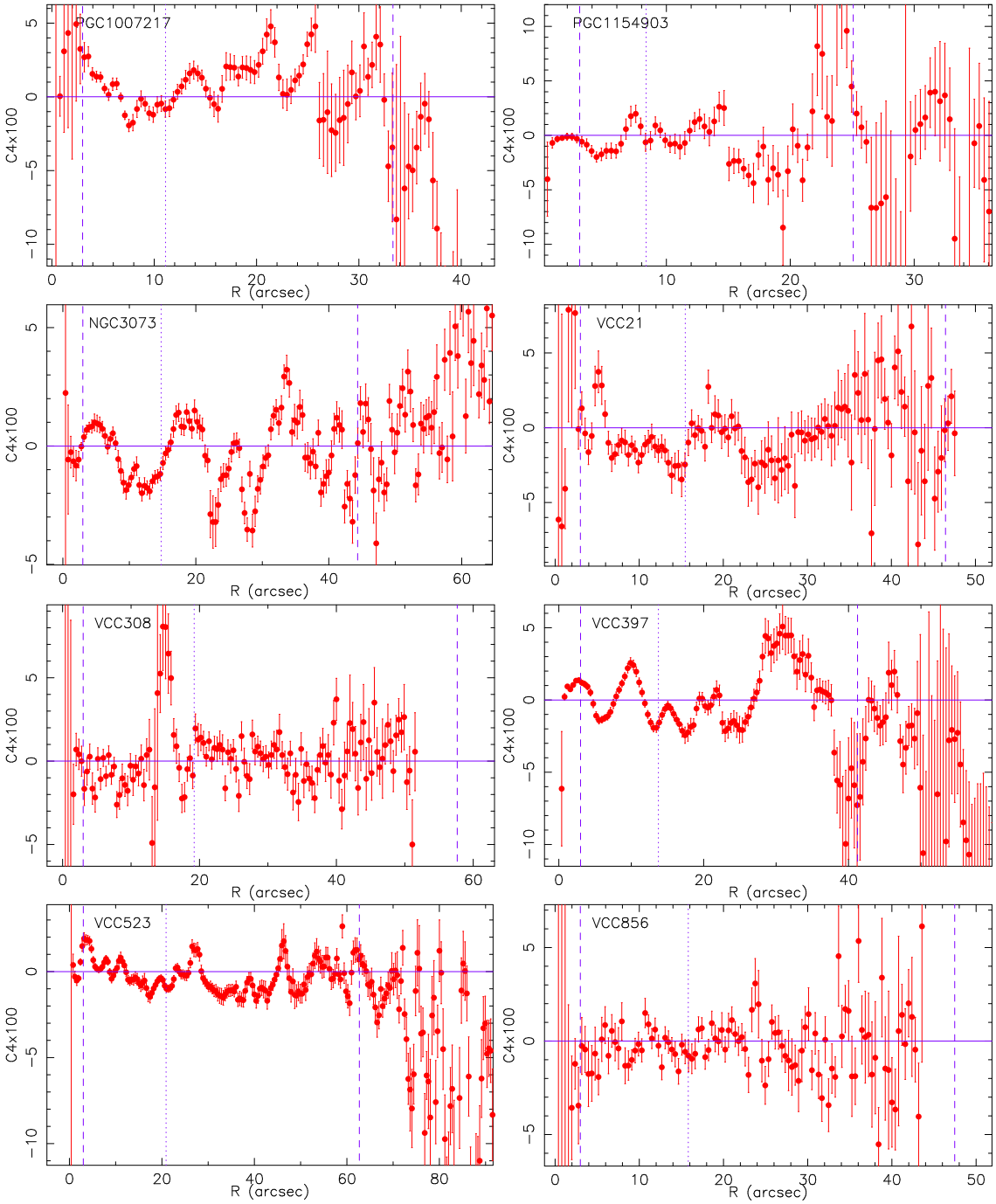

Figure E.1: Radial variation of the C_4 parameter in i band. The dashed purple lines indicate the region between 3" and the R_{eff}. The dotted purple line shows the R_{eff}.

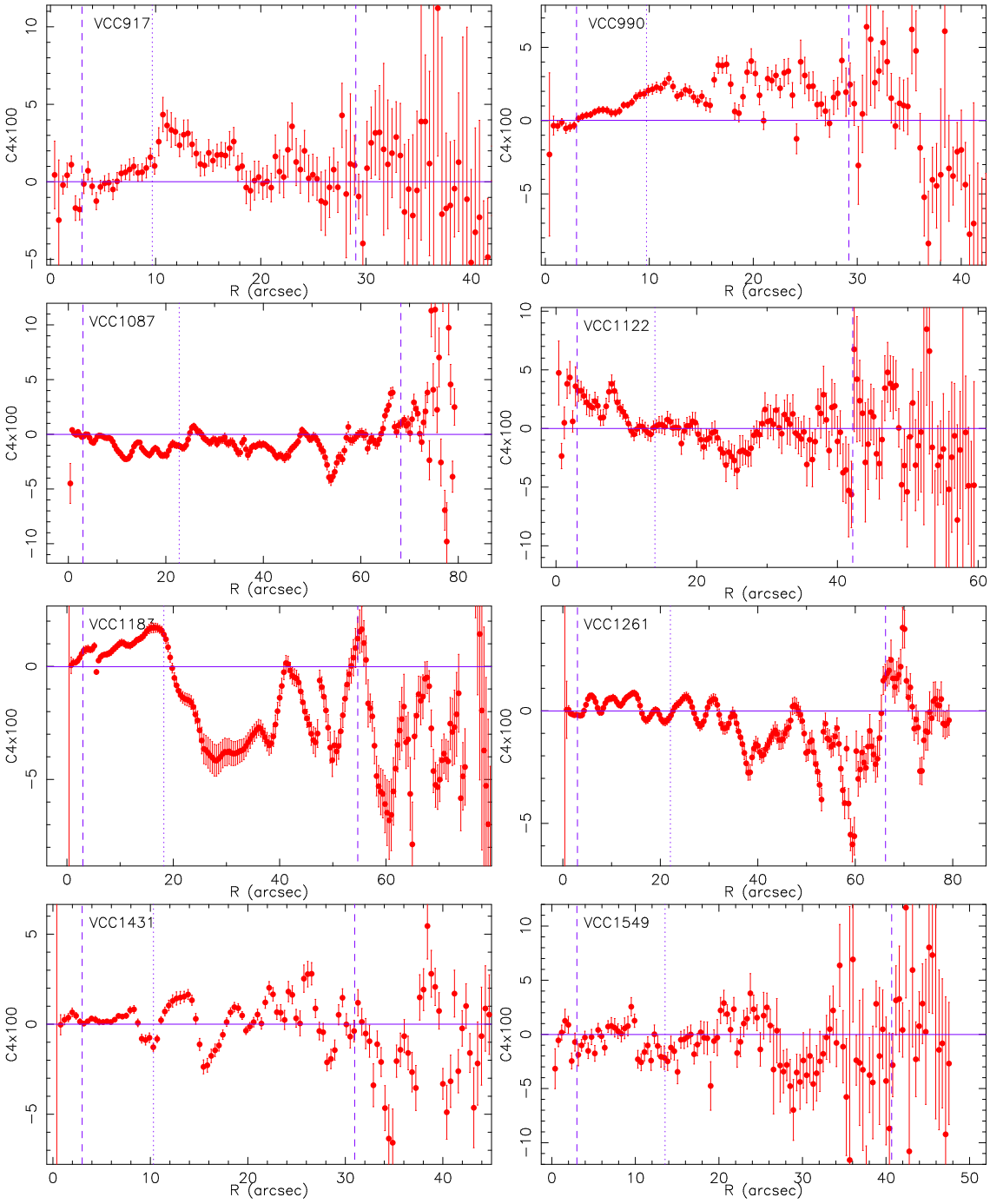

Figure E.1: Continued.

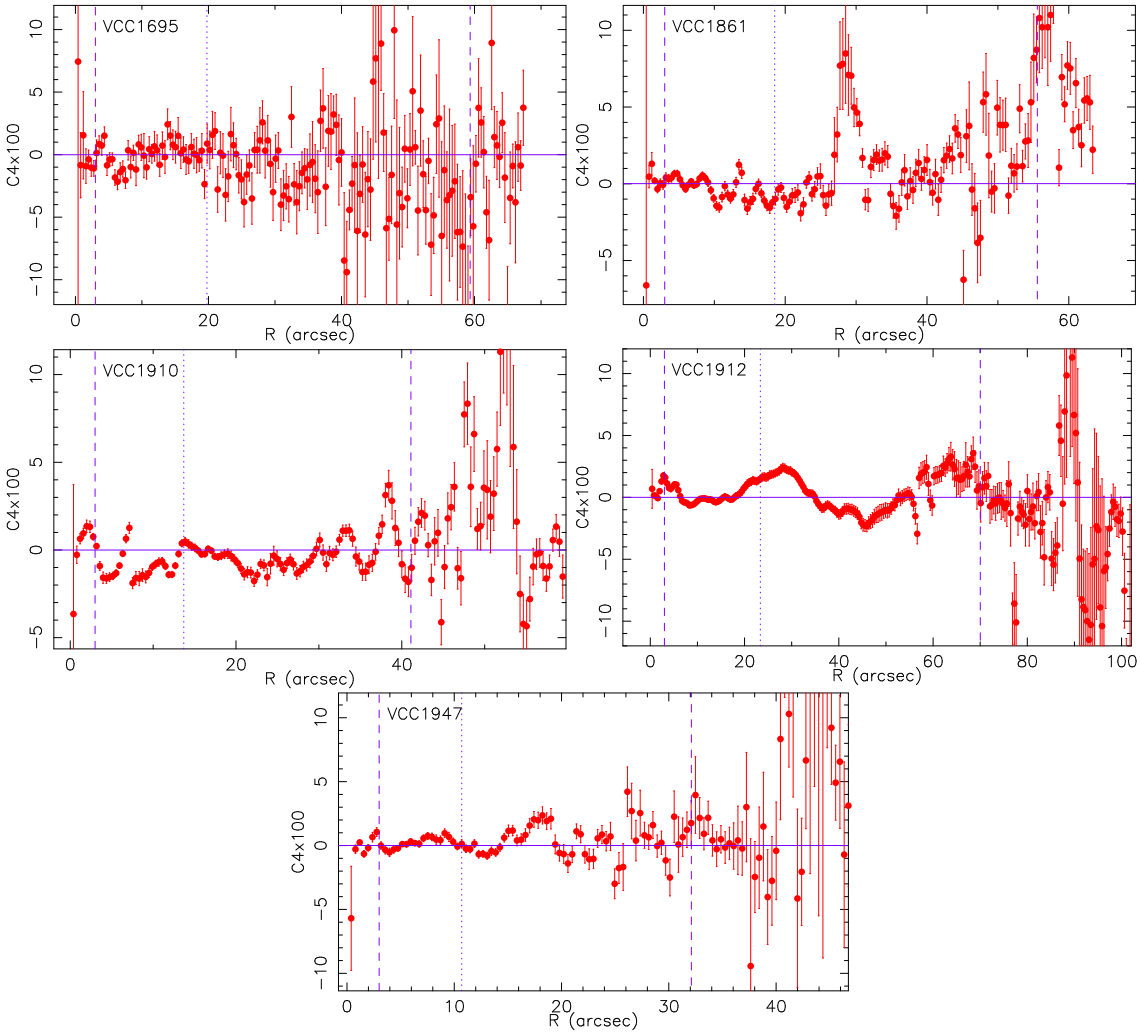

Figure E.1: Continued.

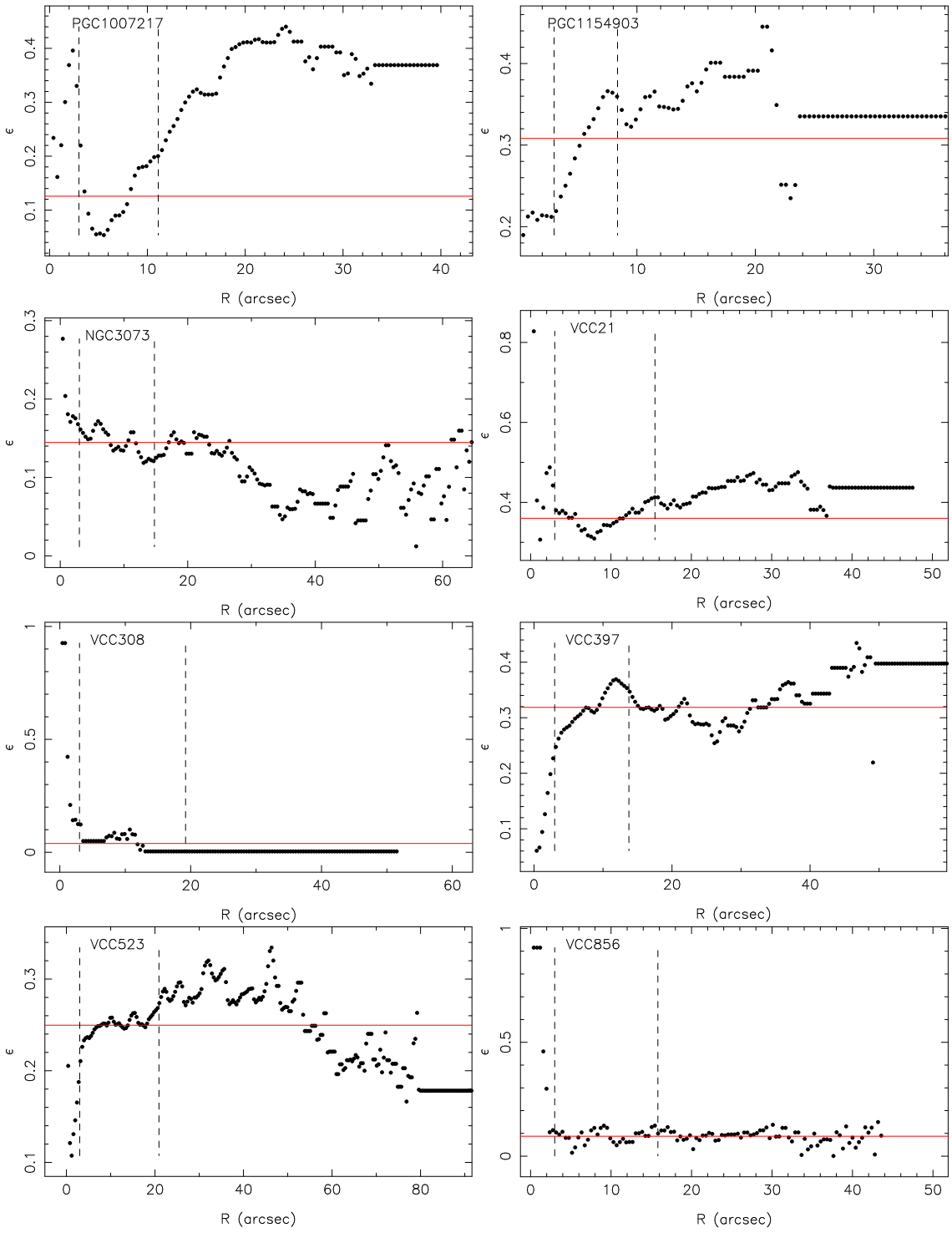

Figure E.2: Radial variation of the ellipticity in i band. The dashed lines indicate the region between 3" and the R_{eff}. The red solid line shows the mean value within the dashed lines.

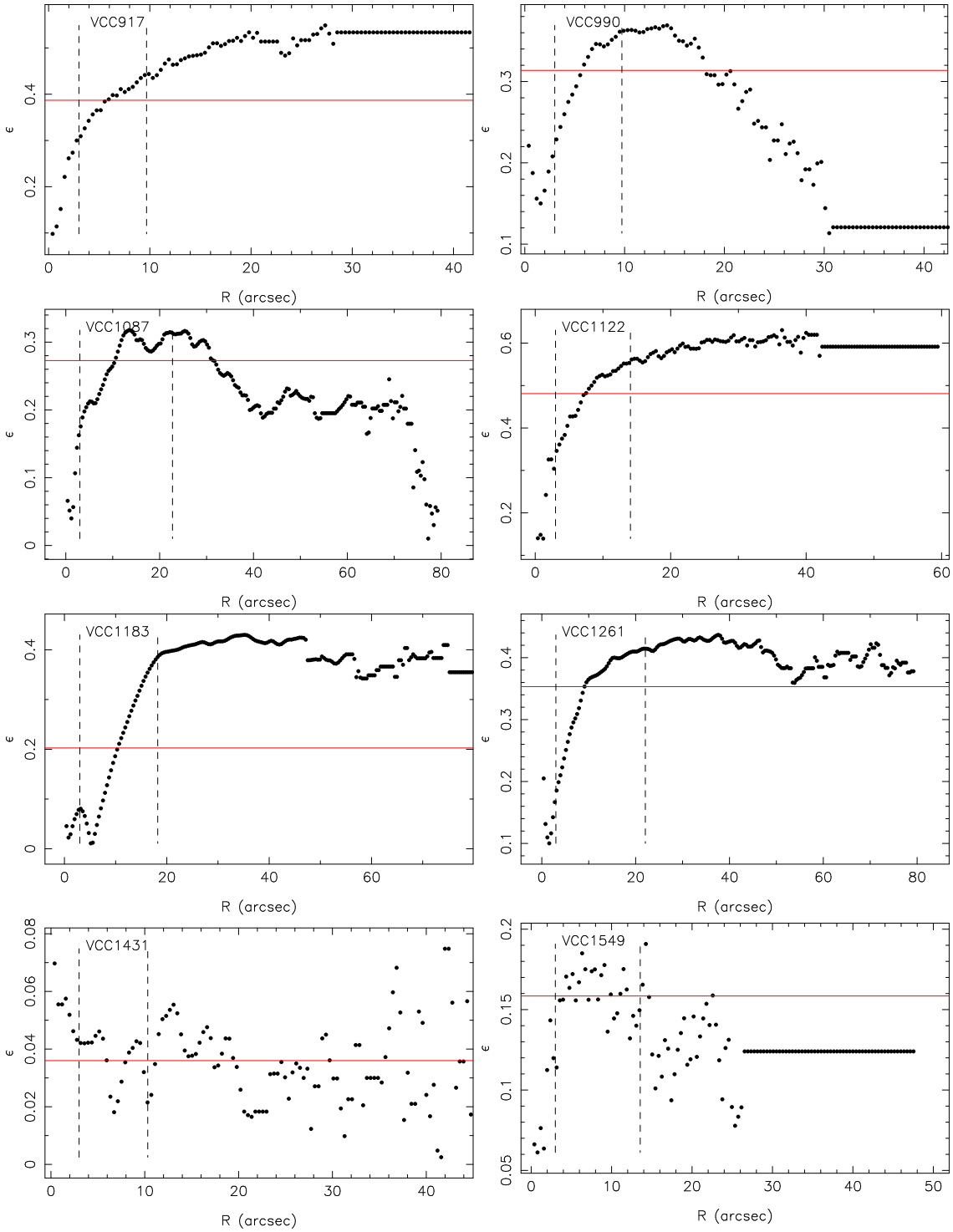

Figure E.2: Continued.

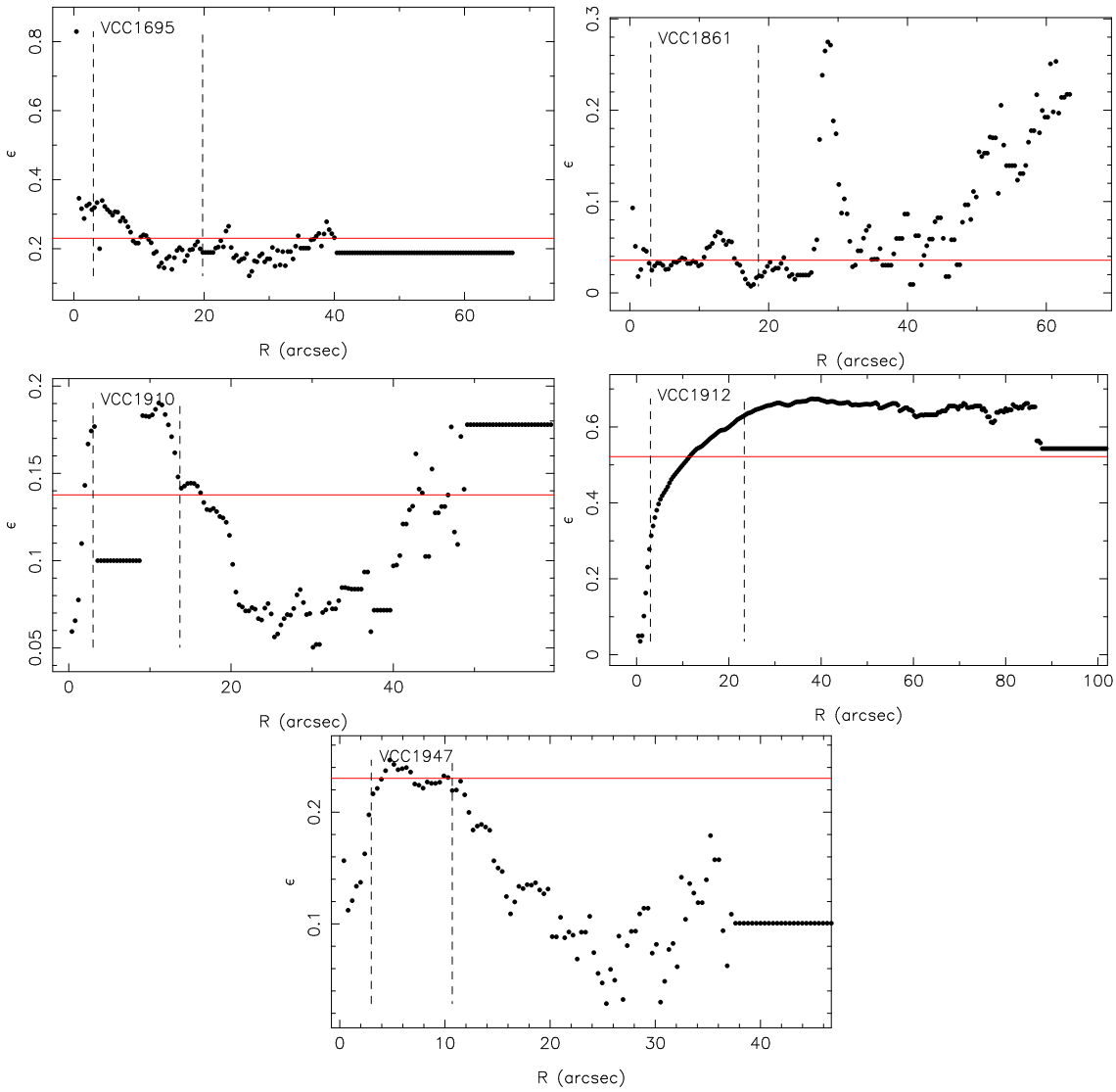

Figure E.2: Continued.

Bibliography

Aaronson, M. 1978, ApJL, 221, L103

Abazajian, K., Adelman-McCarthy, J. K., Agüeros, M. A., et al. 2003, AJ, 126, 2081

Abazajian, K. N., Adelman-McCarthy, J. K., Agüeros, M. A., et al. 2009, ApJS, 182, 543

Adelman-McCarthy, J. K., Agüeros, M. A., Allam, S. S., et al. 2008, ApJS, 175, 297

Andreon, S., Cuillandre, J., Puddu, E., & Mellier, Y. 2006, MNRAS, 372, 60

Arimoto, N. & Yoshii, Y. 1987, A&A, 173, 23

Babul, A. & Ferguson, H. C. 1996, ApJ, 458, 100

Baldry, I. K., Glazebrook, K., Brinkmann, J., et al. 2004, ApJ, 600, 681

Ballero, S. K., Matteucci, F., Origlia, L., & Rich, R. M. 2007, A&A, 467, 123

Balsara, D., Livio, M., & O'Dea, C. P. 1994, ApJ, 437, 83

Baum, W. A. 1959, PASP, 71, 106

Beasley, M. A., Cenarro, A. J., Strader, J., & Brodie, J. P. 2009, AJ, 137, 5146

Beasley, M. A., Strader, J., Brodie, J. P., Cenarro, A. J., & Geha, M. 2006, AJ, 131, 814

Bender, R., Burstein, D., & Faber, S. M. 1992, ApJ, 399, 462

Bender, R., Doebereiner, S., & Moellenhoff, C. 1988, A&AS, 74, 385

Bender, R. & Nieto, J. 1990, A&A, 239, 97

Bernardi, M., Sheth, R. K., Nichol, R. C., et al. 2006, AJ, 131, 2018

Bessell, M. S. & Norris, J. 1982, ApJL, 263, L29

Beuing, J., Bender, R., Mendes de Oliveira, C., Thomas, D., & Maraston, C. 2002, A&A, 395, 431

Binggeli, B. & Cameron, L. M. 1991, A&A, 252, 27

Binggeli, B. & Jerjen, H. 1998, A&A, 333, 17

Binggeli, B., Sandage, A., & Tammann, G. A. 1985, AJ, 90, 1681

—. 1988, ARA&A, 26, 509

Binggeli, B., Sandage, A., & Tarenghi, M. 1984, AJ, 89, 64

Binney, J. 1978, MNRAS, 183, 501

Binney, J. & Merrifield, M. 1998, Galactic astronomy (Princeton Series in Astrophysiscs)

Blakeslee, J. P., Jordán, A., Mei, S., et al. 2009, ApJ, 694, 556

Blakeslee, J. P., Lucey, J. R., Barris, B. J., Hudson, M. J., & Tonry, J. L. 2001, MNRAS, 327, 1004

Blanton, M. R., Dalcanton, J., Eisenstein, D., et al. 2001, AJ, 121, 2358

Blanton, M. R., Lupton, R. H., Schlegel, D. J., et al. 2005, ApJ, 631, 208

Blanton, M. R. & Roweis, S. 2007, AJ, 133, 734

Bonanos, A. Z., Stanek, K. Z., Szentgyorgyi, A. H., Sasselov, D. D., & Bakos, G. Á. 2004, AJ, 127, 861

Boselli, A., Boissier, S., Cortese, L., & Gavazzi, G. 2008a, ApJ, 674, 742

—. 2008b, A&A, 489, 1015

Boselli, A., Cortese, L., Deharveng, J. M., et al. 2005, ApJL, 629, L29

Boselli, A. & Gavazzi, G. 2006, PASP, 118, 517

Boselli, A., Gavazzi, G., Donas, J., & Scodeggio, M. 2001, AJ, 121, 753

Boulade, O., Rose, J. A., & Vigroux, L. 1988, AJ, 96, 1319

Bower, R. G., Lucey, J. R., & Ellis, R. S. 1992, MNRAS, 254, 601

Bressan, A., Chiosi, C., & Fagotto, F. 1994, ApJS, 94, 63

Bruzual, G. & Charlot, S. 2003, MNRAS, 344, 1000

Bundy, K., Ellis, R. S., Conselice, C. J., et al. 2006, ApJ, 651, 120

Burstein, D. 2003, in Astronomical Society of the Pacific Conference Series, Vol. 297, Star Formation Through Time, ed. E. Perez, R. M. Gonzalez Delgado, & G. Tenorio-Tagle, 253–+

Burstein, D., Bender, R., Faber, S., & Nolthenius, R. 1997, AJ, 114, 1365

Burstein, D., Bertola, F., Buson, L. M., Faber, S. M., & Lauer, T. R. 1988, ApJ, 328, 440

Burstein, D., Faber, S. M., Gaskell, C. M., & Krumm, N. 1984, ApJ, 287, 586

Burstein, D., Faber, S. M., & Gonzalez, J. J. 1986, AJ, 91, 1130

Byrd, G. & Valtonen, M. 1990, ApJ, 350, 89

Caldwell, N., Rose, J. A., & Concannon, K. D. 2003, AJ, 125, 2891

Caon, N., Capaccioli, M., & D'Onofrio, M. 1993, MNRAS, 265, 1013

Capaccioli, M., Caon, N., & D'Onofrio, M. 1992, MNRAS, 259, 323

Cappellari, M., Bacon, R., Bureau, M., et al. 2006, MNRAS, 366, 1126

Cardiel, N. 1999, PhD thesis, Universidad Complutense de Madrid, Spain

Carigi, L., Peimbert, M., Esteban, C., & García-Rojas, J. 2005, ApJ, 623, 213

Carrera, R., Aparicio, A., Martínez-Delgado, D., & Alonso-García, J. 2002, AJ, 123, 3199

Carter, D. 1978, MNRAS, 182, 797

Catinella, B., Giovanelli, R., & Haynes, M. P. 2006, ApJ, 640, 751

Cenarro, A. J., Cardiel, N., Gorgas, J., et al. 2001, MNRAS, 326, 959

Cenarro, A. J., Peletier, R. F., Sánchez-Blázquez, P., et al. 2007, MNRAS, 374, 664

Chiappini, C., Hirschi, R., Meynet, G., et al. 2006, A&A, 449, L27

Chiappini, C., Romano, D., & Matteucci, F. 2003, MNRAS, 339, 63

Chilingarian, I. V. 2009, MNRAS, 394, 1229

Ciardullo, R., Feldmeier, J. J., Jacoby, G. H., et al. 2002, ApJ, 577, 31

Ciotti, L. 1991, A&A, 249, 99

Ciotti, L. & Lanzoni, B. 1997, A&A, 321, 724

Ciotti, L., Lanzoni, B., & Renzini, A. 1996, MNRAS, 282, 1

Clemens, M. S., Bressan, A., Nikolic, B., et al. 2006, MNRAS, 370, 702

Coelho, P., Bruzual, G., Charlot, S., et al. 2007, MNRAS, 382, 498

Colless, M., Dalton, G., Maddox, S., et al. 2001, MNRAS, 328, 1039

Conselice, C. J., Gallagher, III, J. S., & Wyse, R. F. G. 2001, ApJ, 559, 791

Conselice, C. J., O'Neil, K., Gallagher, J. S., & Wyse, R. F. G. 2003, ApJ, 591, 167

Cowie, L. L., Songaila, A., Hu, E. M., & Cohen, J. G. 1996, AJ, 112, 839

Croton, D. J., Farrar, G. R., Norberg, P., et al. 2005, MNRAS, 356, 1155

Crowl, H. H. & Kenney, J. D. P. 2008, AJ, 136, 1623

Davidge, T. J. & Clark, C. C. 1994, AJ, 107, 946

Davies, J. I., Baes, M., Bendo, G. J., et al. 2010, A&A, 518, L48+

Davies, J. I. & Phillipps, S. 1988, MNRAS, 233, 553

Davies, R. L., Efstathiou, G., Fall, S. M., Illingworth, G., & Schechter, P. L. 1983, ApJ, 266, 41

Davies, R. L., Sadler, E. M., & Peletier, R. F. 1993, MNRAS, 262, 650

De Lucia, G., Springel, V., White, S. D. M., Croton, D., & Kauffmann, G. 2006, MNRAS, 366, 499

de Rijcke, S., Michielsen, D., Dejonghe, H., Zeilinger, W. W., & Hau, G. K. T. 2005, A&A, 438, 491

De Rijcke, S., Zeilinger, W. W., Hau, G. K. T., Prugniel, P., & Dejonghe, H. 2007, ApJ, 659, 1172

de Vaucouleurs, G., de Vaucouleurs, A., Corwin, Jr., H. G., et al. 1991, Third Reference Catalogue of Bright Galaxies. Volume I: Explanations and references. Volume II: Data for galaxies between 0^h and 12^h. Volume III: Data for galaxies between 12^h and 24^h. (Springer, New York, NY (USA))

Djorgovski, S. & Davis, M. 1987, ApJ, 313, 59

D'Onofrio, M., Capaccioli, M., & Caon, N. 1994, MNRAS, 271, 523

Dressler, A. 1980, ApJ, 236, 351

Dressler, A., Lynden-Bell, D., Burstein, D., et al. 1987, ApJ, 313, 42

Eggen, O. J., Lynden-Bell, D., & Sandage, A. R. 1962, ApJ, 136, 748

Emsellem, E., Cappellari, M., Krajnović, D., et al. 2007, MNRAS, 379, 401

Faber, S. M. 1972, A&A, 20, 361

—. 1973, ApJ, 179, 731

Faber, S. M., Dressler, A., Davies, R. L., Burstein, D., & Lynden-Bell, D. 1987, in Nearly Normal Galaxies. From the Planck Time to the Present, ed. S. M. Faber, 175–183

Faber, S. M., Friel, E. D., Burstein, D., & Gaskell, C. M. 1985, ApJS, 57, 711

Faber, S. M. & Jackson, R. E. 1976a, ApJ, 204, 668

—. 1976b, ApJ, 204, 668

Faber, S. M., Tremaine, S., Ajhar, E. A., et al. 1997, AJ, 114, 1771

Faber, S. M., Willmer, C. N. A., Wolf, C., et al. 2007, ApJ, 665, 265

Faber, S. M., Worthey, G., & Gonzales, J. J. 1992, in IAU Symposium, Vol. 149, The Stellar Populations of Galaxies, ed. B. Barbuy & A. Renzini, 255–+

Falcón-Barroso, J., Peletier, R. F., & Balcells, M. 2002, MNRAS, 335, 741

Fenner, Y., Gibson, B. K., Lee, H.-c., et al. 2003, Publications of the Astronomical Society of Australia, 20, 340

Ferguson, H. C. & Binggeli, B. 1994, A&ARv, 6, 67

Ferrarese, L., Côté, P., Jordán, A., et al. 2006, ApJS, 164, 334

Fisher, D., Franx, M., & Illingworth, G. 1995, ApJ, 448, 119

Fitzpatrick, E. L. 1999, PASP, 111, 63

Forbes, D. A., Lasky, P., Graham, A. W., & Spitler, L. 2008, MNRAS, 389, 1924

Forbes, D. A. & Ponman, T. J. 1999, MNRAS, 309, 623

Forbes, D. A., Ponman, T. J., & Brown, R. J. N. 1998, ApJL, 508, L43

Fukugita, M., Hogan, C. J., & Peebles, P. J. E. 1998, ApJ, 503, 518

Fukugita, M., Shimasaku, K., & Ichikawa, T. 1995, PASP, 107, 945

Gallazzi, A., Charlot, S., Brinchmann, J., & White, S. D. M. 2006, MNRAS, 370, 1106

Gargiulo, A., Haines, C. P., Merluzzi, P., et al. 2009, MNRAS, 397, 75

Gavazzi, G., Boselli, A., Donati, A., Franzetti, P., & Scodeggio, M. 2003a, A&A, 400, 451

—. 2003b, A&A, 400, 451

Gavazzi, G., Boselli, A., Scodeggio, M., Pierini, D., & Belsole, E. 1999a, MNRAS, 304, 595

—. 1999b, MNRAS, 304, 595

Gavazzi, G., Donati, A., Cucciati, O., et al. 2005, A&A, 430, 411

Gavazzi, G., Franzetti, P., Scodeggio, M., Boselli, A., & Pierini, D. 2000, A&A, 361, 863

Gavazzi, G., Pierini, D., & Boselli, A. 1996, A&A, 312, 397

Geha, M., Guhathakurta, P., Rich, R. M., & Cooper, M. C. 2006, AJ, 131, 332

Geha, M., Guhathakurta, P., & van der Marel, R. P. 2002, AJ, 124, 3073

—. 2003, AJ, 126, 1794

Geha, M., van der Marel, R. P., Guhathakurta, P., et al. 2010, ApJ, 711, 361

Gibson, B. K., Loewenstein, M., & Mushotzky, R. F. 1997, MNRAS, 290, 623

Gil de Paz, A., Boissier, S., Madore, B. F., et al. 2007, ApJS, 173, 185

Giovanelli, R. & Haynes, M. P. 2002, ApJL, 571, L107

Giovanelli, R., Haynes, M. P., da Costa, L. N., et al. 1997a, ApJL, 477, L1+

Giovanelli, R., Haynes, M. P., Herter, T., et al. 1997b, AJ, 113, 22

Giovanelli, R., Haynes, M. P., Kent, B. R., et al. 2005, AJ, 130, 2598

González, J. J. 1993, PhD thesis, Thesis (PH.D.)–UNIVERSITY OF CALIFORNIA, SANTA CRUZ, 1993.Source: Dissertation Abstracts International, Volume: 54-05, Section: B, page: 2551.

Gorgas, J., Efstathiou, G., & Aragon Salamanca, A. 1990, MNRAS, 245, 217

Gorgas, J., Faber, S. M., Burstein, D., et al. 1993, ApJS, 86, 153

Gorgas, J., Pedraz, S., Guzman, R., Cardiel, N., & Gonzalez, J. J. 1997, ApJL, 481, L19+

Graham, A. W. & Guzmán, R. 2003a, AJ, 125, 2936

—. 2003b, AJ, 125, 2936

Graves, G. J. & Faber, S. M. 2010a, ApJ, 717, 803

—. 2010b, ApJ, 717, 803

Graves, G. J. & Schiavon, R. P. 2008, ApJS, 177, 446

Grebel, E. K., Gallagher, III, J. S., & Harbeck, D. 2003, AJ, 125, 1926

Greggio, L. & Renzini, A. 1983, A&A, 118, 217

Gunn, J. E. & Gott, III, J. R. 1972, ApJ, 176, 1

Gunn, J. E. & Stryker, L. L. 1983, ApJS, 52, 121

Gunn, J. E., Stryker, L. L., & Tinsley, B. M. 1981, ApJ, 249, 48

Guzmán, R., Graham, A. W., Matković, A., et al. 2003, in Astronomical Society of the Pacific Conference Series, Vol. 297, Star Formation Through Time, ed. E. Perez, R. M. Gonzalez Delgado, & G. Tenorio-Tagle, 271–+

Guzmán, R., Lucey, J. R., & Bower, R. G. 1993, MNRAS, 265, 731

Held, E. V., de Zeeuw, T., Mould, J., & Picard, A. 1992, AJ, 103, 851

Hudson, M. J., Lucey, J. R., Smith, R. J., Schlegel, D. J., & Davies, R. L. 2001, MNRAS, 327, 265

Hyde, J. B. & Bernardi, M. 2009, MNRAS, 396, 1171

Jacoby, G. H., Hunter, D. A., & Christian, C. A. 1984, ApJS, 56, 257

Janz, J. & Lisker, T. 2008, ApJL, 689, L25

—. 2009, ApJL, 696, L102

Jensen, J. B., Tonry, J. L., Barris, B. J., et al. 2003, ApJ, 583, 712

Jensen, J. B., Tonry, J. L., & Luppino, G. A. 1998, ApJ, 505, 111

Jerjen, H., Binggeli, B., & Barazza, F. D. 2004, AJ, 127, 771

Jerjen, H., Freeman, K. C., & Binggeli, B. 1998, AJ, 116, 2873

Jones, L. A. 1999, PhD thesis, Univ. of North Carolina, Chapel Hill

Jorgensen, I. 1997, MNRAS, 288, 161

Jørgensen, I. 1999, MNRAS, 306, 607

Jorgensen, I., Franx, M., & Kjaergaard, P. 1992, A&AS, 95, 489

—. 1993, ApJ, 411, 34

—. 1996, MNRAS, 280, 167

Karachentsev, I. D. & Makarov, D. A. 1996, AJ, 111, 794

Kauffmann, G. & Charlot, S. 1998, MNRAS, 297, L23+

Kauffmann, G., White, S. D. M., & Guiderdoni, B. 1993, MNRAS, 264, 201

Kelson, D. D., Illingworth, G. D., Franx, M., & van Dokkum, P. G. 2006, ApJ, 653, 159

Kelson, D. D., Illingworth, G. D., Tonry, J. L., et al. 2000, ApJ, 529, 768

Kirkpatrick, J. D., Henry, T. J., & McCarthy, Jr., D. W. 1991, ApJS, 77, 417

Kodama, T. & Arimoto, N. 1998, MNRAS, 300, 193

Koleva, M., de Rijcke, S., Prugniel, P., Zeilinger, W. W., & Michielsen, D. 2009a, MNRAS, 396, 2133

—. 2009b, MNRAS, 396, 2133

Kormendy, J. 1977, ApJ, 218, 333

—. 1985, ApJ, 295, 73

Kormendy, J. & Bender, R. 1996a, ApJL, 464, L119+

—. 1996b, ApJL, 464, L119+

Kormendy, J., Fisher, D. B., Cornell, M. E., & Bender, R. 2009, ApJS, 182, 216

Kuntschner, H. 1998, PhD thesis, AA(University of Durham, Department of Physics, South Road, Durham DH1 3LE)

Kuntschner, H. & Davies, R. L. 1998, MNRAS, 295, L29+

Kurucz, R. L. 1992, in IAU Symposium, Vol. 149, The Stellar Populations of Galaxies, ed. B. Barbuy & A. Renzini, 225–+

Larson, R. B., Tinsley, B. M., & Caldwell, C. N. 1980, ApJ, 237, 692

Lawrence, A., Warren, S. J., Almaini, O., et al. 2007, MNRAS, 379, 1599

Le Borgne, J.-F., Bruzual, G., Pelló, R., et al. 2003, A&A, 402, 433

Lee, H., Worthey, G., Dotter, A., et al. 2009, ApJ, 694, 902

Lejeune, T., Cuisinier, F., & Buser, R. 1997, A&AS, 125, 229

Lin, D. N. C. & Faber, S. M. 1983, ApJL, 266, L21

Lisker, T. 2009, Astronomische Nachrichten, 330, 1043

Lisker, T., Glatt, K., Westera, P., & Grebel, E. K. 2006a, AJ, 132, 2432

Lisker, T., Grebel, E. K., & Binggeli, B. 2006b, AJ, 132, 497

—. 2008, AJ, 135, 380

Lisker, T., Grebel, E. K., Binggeli, B., & Glatt, K. 2007, ApJ, 660, 1186

Lisker, T., Janz, J., Hensler, G., et al. 2009, ApJL, 706, L124

Mackey, A. D. & Gilmore, G. F. 2003, MNRAS, 345, 747

Maraston, C., Greggio, L., Renzini, A., et al. 2003, A&A, 400, 823

Martin, D. C., Fanson, J., Schiminovich, D., et al. 2005, ApJL, 619, L1

Mastropietro, C., Moore, B., Mayer, L., et al. 2005, MNRAS, 364, 607

Mateo, M., Hurley-Keller, D., & Nemec, J. 1998, AJ, 115, 1856

Mateo, M. L. 1998, ARA&A, 36, 435

Matković, A. & Guzmán, R. 2005, MNRAS, 362, 289

Matković, A. & Guzmán, R. 2007, in Revista Mexicana de Astronomia y Astrofisica, vol. 27, Vol. 29, Revista Mexicana de Astronomia y Astrofisica Conference Series, ed. R. Guzmán, 107–109

Matteucci, F. 1986, MNRAS, 221, 911

—. 1994, A&A, 288, 57

Matteucci, F. & Greggio, L. 1986, A&A, 154, 279

McElroy, D. B. 1995, ApJS, 100, 105

Mehlert, D., Noll, S., Appenzeller, I., et al. 2002, A&A, 393, 809

Mei, S., Blakeslee, J. P., Côté, P., et al. 2007, ApJ, 655, 144

Meynet, G. & Maeder, A. 2002, A&A, 390, 561

Michielsen, D., Boselli, A., Conselice, C. J., et al. 2008, MNRAS, 385, 1374

Moore, B., Ghigna, S., Governato, F., et al. 1999, ApJL, 524, L19

Moore, B., Katz, N., Lake, G., Dressler, A., & Oemler, A. 1996, Nature, 379, 613

Moore, B., Lake, G., & Katz, N. 1998, ApJ, 495, 139

Moore, S. A. W., Lucey, J. R., Kuntschner, H., & Colless, M. 2002, MNRAS, 336, 382

Mori, M. & Burkert, A. 2000, ApJ, 538, 559

Murakami, I. & Babul, A. 1999, MNRAS, 309, 161

Navarro, J. F., Frenk, C. S., & White, S. D. M. 1997, ApJ, 490, 493

Nelan, J. E., Smith, R. J., Hudson, M. J., et al. 2005, ApJ, 632, 137

Nieto, J., Davoust, E., Bender, R., & Prugniel, P. 1990, A&A, 230, L17

Nomoto, K., Thielemann, F., & Wheeler, J. C. 1984, ApJL, 279, L23

Norris, J. E., Ryan, S. G., Beers, T. C., Aoki, W., & Ando, H. 2002, ApJL, 569, L107

O'Connell, R. W. 1976, ApJ, 206, 370

—. 1980, ApJ, 236, 430

Pahre, M. A. 1999, ApJS, 124, 127

Pahre, M. A., de Carvalho, R. R., & Djorgovski, S. G. 1998a, AJ, 116, 1606

—. 1998b, AJ, 116, 1606

Paturel, G., Petit, C., Prugniel, P., et al. 2003, A&A, 412, 45

Paudel, S., Lisker, T., Kuntschner, H., Grebel, E. K., & Glatt, K. 2010, MNRAS, 570

Pedraz, S., Gorgas, J., Cardiel, N., Sánchez-Blázquez, P., & Guzmán, R. 2002, MNRAS, 332, L59

Peletier, R. F., Balcells, M., Davies, R. L., et al. 1999, MNRAS, 310, 703

Peletier, R. F., Davies, R. L., Illingworth, G. D., Davis, L. E., & Cawson, M. 1990, AJ, 100, 1091

Peletier, R. F. & Valentijn, E. A. 1989, Ap&SS, 156, 127

Persic, M., Salucci, P., & Stel, F. 1996, MNRAS, 281, 27

Peterson, R. C. 1976, ApJL, 210, L123

Pickles, A. J. 1985, ApJS, 59, 33

—. 1998, PASP, 110, 863

Poggianti, B. M., Bridges, T. J., Mobasher, B., et al. 2001, ApJ, 562, 689

Ponder, J. M., Burstein, D., O'Connell, R. W., et al. 1998, AJ, 116, 2297

Prugniel, P. & Simien, F. 1996, A&A, 309, 749

Prugniel, P. & Soubiran, C. 2001, A&A, 369, 1048

Prugniel, P., Soubiran, C., Koleva, M., & Le Borgne, D. 2007, ArXiv Astrophysics e-prints

Quilis, V., Ibáñez, J. M., & Sáez, D. 2000, A&A, 353, 435

Rabin, D. 1982, ApJ, 261, 85

Rabin, D. M. 1981, PhD thesis, California Inst. of Tech., Pasadena.

Renzini, A. 2006, ARA&A, 44, 141

Renzini, A. & Voli, M. 1981, A&A, 94, 175

Roediger, E. & Brüggen, M. 2008, MNRAS, 388, 465

Rose, J. A. 1985, AJ, 90, 1927

—. 1994, AJ, 107, 206

Sánchez-Blázquez, P. 2004, PhD thesis, Universidad Complutense de Madrid, Spain

Sánchez-Blázquez, P., Gorgas, J., & Cardiel, N. 2006a, A&A, 457, 823

Sánchez-Blázquez, P., Gorgas, J., Cardiel, N., Cenarro, J., & González, J. J. 2003, ApJL, 590, L91

Sánchez-Blázquez, P., Gorgas, J., Cardiel, N., & González, J. J. 2006b, A&A, 457, 787

Sánchez-Blázquez, P., Peletier, R. F., Jiménez-Vicente, J., et al. 2006c, MNRAS, 371, 703

Sánchez-Janssen, R., Méndez-Abreu, J., & Aguerri, J. A. L. 2010, MNRAS, 406, L65

Sandage, A., Binggeli, B., & Tammann, G. A. 1985, AJ, 90, 1759

Sandage, A. & Visvanathan, N. 1978a, ApJ, 225, 742

—. 1978b, ApJ, 223, 707

Sargent, W. L. W. & Turner, E. L. 1977, ApJL, 212, L3

Schechter, P. L. 1980, AJ, 85, 801

Schechter, P. L. & Gunn, J. E. 1979, ApJ, 229, 472

Schiavon, R. P. 2007, ApJS, 171, 146

Schlegel, D. J., Finkbeiner, D. P., & Davis, M. 1998, ApJ, 500, 525

Serote Roos, M., Boisson, C., & Joly, M. 1996, A&AS, 117, 93

Sérsic, J. L. 1968, Atlas de galaxias australes (Cordoba, Argentina: Observatorio Astronomico, 1968)

Serven, J., Worthey, G., & Briley, M. M. 2005, ApJ, 627, 754

Serven, J., Worthey, G., Toloba, E., & Sánchez-Blázquez, P. 2010, ArXiv e-prints

Silich, S. & Tenorio-Tagle, G. 2001, ApJ, 552, 91

Silva, D. R. & Cornell, M. E. 1992, ApJS, 81, 865

Simien, F. & Prugniel, P. 2002, A&A, 384, 371

Simon, J. D. & Geha, M. 2007, ApJ, 670, 313

Skrutskie, M. F., Cutri, R. M., Stiening, R., et al. 2006, AJ, 131, 1163

Smith, R., Davies, J. I., & Nelson, A. H. 2010, MNRAS, 405, 1723

Sneden, C. 1973, ApJ, 184, 839

Soubiran, C., Katz, D., & Cayrel, R. 1998, A&AS, 133, 221

Spinrad, H. 1962, ApJ, 135, 715

Spinrad, H. & Taylor, B. J. 1971, ApJS, 22, 445

Stevens, I. R., Acreman, D. M., & Ponman, T. J. 1999, MNRAS, 310, 663

Stiavelli, M., Miller, B. W., Ferguson, H. C., et al. 2001, AJ, 121, 1385

Terlevich, R., Davies, R. L., Faber, S. M., & Burstein, D. 1981, MNRAS, 196, 381

Thielemann, F., Nomoto, K., & Hashimoto, M. 1996, ApJ, 460, 408

Thomas, D., Brimioulle, F., Bender, R., et al. 2006, A&A, 445, L19

Thomas, D., Greggio, L., & Bender, R. 1998, MNRAS, 296, 119

Thomas, D., Maraston, C., & Bender, R. 2003, MNRAS, 339, 897

Thomas, D., Maraston, C., Bender, R., & Mendes de Oliveira, C. 2005, ApJ, 621, 673

Thomsen, B., Baum, W. A., Hammergren, M., & Worthey, G. 1997, ApJL, 483, L37+

Tinsley, B. M. 1978, ApJ, 222, 14

Toloba, E., Boselli, A., Cenarro, A. J., et al. 2011, A&A, 526, A114+

Toloba, E., Boselli, A., Gorgas, J., et al. 2009a, ApJL, 707, L17

Toloba, E., Sánchez-Blázquez, P., Gorgas, J., & Gibson, B. K. 2009b, ApJL, 691, L95

Tomkin, J. & Lambert, D. L. 1984, ApJ, 279, 220

Tonry, J. L. & Davis, M. 1981, ApJ, 246, 680

Tonry, J. L., Dressler, A., Blakeslee, J. P., et al. 2001, ApJ, 546, 681

Toomre, A. 1977, in Evolution of Galaxies and Stellar Populations, ed. B. M. Tinsley & R. B. Larson, 401–+

Trager, S. C., Faber, S. M., Worthey, G., & González, J. J. 2000, AJ, 120, 165

Trager, S. C., Worthey, G., Faber, S. M., Burstein, D., & Gonzalez, J. J. 1998, ApJS, 116, 1

Trujillo, I., Burkert, A., & Bell, E. F. 2004, ApJL, 600, L39

Valdes, F., Gupta, R., Rose, J. A., Singh, H. P., & Bell, D. J. 2004, ApJS, 152, 251

van Zee, L., Barton, E. J., & Skillman, E. D. 2004a, AJ, 128, 2797

van Zee, L., Skillman, E. D., & Haynes, M. P. 2004b, AJ, 128, 121

Vazdekis, A., Kuntschner, H., Davies, R. L., et al. 2001, ApJL, 551, L127

Vazdekis, A., Peletier, R. F., Beckman, J. E., & Casuso, E. 1997, ApJS, 111, 203

Vazdekis, A., Sánchez-Blázquez, P., Falcón-Barroso, J., et al. 2010, MNRAS, 404, 1639

Visvanathan, N. & Sandage, A. 1977, ApJ, 216, 214

White, S. D. M. & Frenk, C. S. 1991, ApJ, 379, 52

White, S. D. M. & Rees, M. J. 1978, MNRAS, 183, 341

Wolf, J., Martinez, G. D., Bullock, J. S., et al. 2010, MNRAS, 406, 1220

Woosley, S. E. & Weaver, T. A. 1995, ApJS, 101, 181

Worthey, G. 1994, ApJS, 95, 107

—. 1998, PASP, 110, 888

Worthey, G., Faber, S. M., & Gonzalez, J. J. 1992, ApJ, 398, 69

Worthey, G. & Ottaviani, D. L. 1997, ApJS, 111, 377

Wuyts, S., van Dokkum, P. G., Kelson, D. D., Franx, M., & Illingworth, G. D. 2004, ApJ, 605, 677

York, D. G., Adelman, J., Anderson, Jr., J. E., et al. 2000, AJ, 120, 1579

Yoshii, Y. & Arimoto, N. 1987, A&A, 188, 13

Zaritsky, D., Gonzalez, A. H., & Zabludoff, A. I. 2006, ApJ, 638, 725

List of Figures

List of Tables